Civil Engineering ETDs   Engineering ETDs

9-3-2013

Detection and characterization of impact damage in carbon fiber aircraft fuselage structure

Stephen Neidigk

Follow this and additional works at: https://digitalrepository.unm.edu/ce_etds

Stephen O. Neidigk
Candidate

Civil Engineering
Department

This thesis is approved, and it is acceptable in quality and form for publication:

Approved by the Thesis Committee:

Mahmoud Reda Taha, Chairperson

Arup Maji

Timothy Ross

DETECTION AND CHARACTERIZATION OF IMPACT DAMAGE IN CARBON FIBER AIRCRAFT FUSELAGE STRUCTURE

BY

STEPHEN O. NEIDIGK

B.S. CIVIL ENGINEERING, UNIVERSITY OF NEW MEXICO
2009

THESIS

Submitted in Partial Fulfillment of the
Requirements for the Degree of

Master of Science
Civil Engineering

The University of New Mexico
Albuquerque, New Mexico

July, 2013

DEDICATION

I would like to dedicate this work to my loving and supportive wife, Nicole.

ACKNOWLEDGEMENTS

First and foremost, I would like to acknowledge my Master's advisor and committee chair, Dr. Mahmoud Reda Taha. You inspired me to pursue a Master's degree through challenging courses, fascinating lectures and a civil engineering undergraduate assistantship, which led me to a career at Sandia National Labs. Thank you for providing me with opportunities to perform hands-on testing in multiple engineering disciplines, the recommendation to attend the Los Alamos Dynamics Summer School, as well as guidance and encouragement throughout my college education. I would also like to thank my committee members, Dr. Arup Maji and Dr. Timothy Ross and the rest of the civil engineering faculty at the University of New Mexico for their contributions to my education.

I would like to thank my colleague and mentor, Dennis Roach for his guidance, direction and council throughout this project. The knowledge I have gained from you in the fields of experimental testing, nondestructive inspection, and structural health monitoring greatly enhanced my ability to perform this work. In addition, I would like to thank Mike Bode for his technical review of this thesis. I also appreciate his and Tom Rice's support and encouragement to "hurry-up" and complete my Master's degree.

I would like to further thank Dr. Hyonny Kim and Jacqui Le at the University of California San Diego for their ice impact testing contributions. This part of the testing would not have been possible without the high velocity impact cannon you developed and your experience and expertise with simulated hail impact in composite laminates.

Also, I would like to recognize Randy Duvall for teaching me how to operate the various nondestructive inspection hardware used in this study. His hands-on experience with the equipment and participation in this study made it possible to obtain the highest quality inspection results. Similarly, thanks to Dr. Sandie Klute, Matt Reaves, and Matt Castellucci at Luna Innovations for helping develop and execute the methods used to embed and bond the fiber optics used in this study. Also, thanks for supplying the OBR for fiber optic strain interrogation and training me how to use it and collect data.

I would also like to acknowledge Dave Galella at the FAA's William J. Hughes Technical Center for funding this work. It's not everyday someone wants to fabricate a full-scale, advanced carbon fiber fuselage structure only to destroy it.

DETECTION AND CHARACTERIZATION OF IMPACT DAMAGE IN

CARBON FIBER AIRCRAFT FUSELAGE STRUCTURE

by

Stephen O. Neidigk

B.S. Civil Engineering, University of New Mexico, 2009

M.S. Civil Engineering, University of New Mexico, 2013

ABSTRACT

As the use of advanced composite materials continues to grow in the aviation industry, damage detection techniques need to be developed and tested. Impact damage on aluminum aircraft structures can be detected from obvious surface indications. This is not the case in composite aircraft structure. Large interply delaminations and substructure disbonding may occur as a result of an impact, often leaving no visual indications of damage.

This research investigates the use of conventional hand-deployed ultrasonic (UT) inspection techniques and more advanced UT pulse-echo and resonance scanning techniques to detect and characterize damage in full-scale carbon fiber fuselage structure. It also examines embedded and bonded methods of deploying an in-situ fiber optic (FO) Swept Wavelength Interferometry (SWI) strain sensing system for damage detection. The hypothesis is that the more advanced scanning nondestructive inspection (NDI) techniques used in the study will more effectively detect and characterize damage modes in the fuselage panels than hand-deployed UT techniques. It is further hypothesized that impact damage created by both simulated hail and steel spherical tip impacts will create a permanent, detectable strain change that can be detected by the FO strain measurement system.

Two fuselage panels representative of structures seen on advanced composite transport category aircraft were fabricated. They each measured approximately 56" x 76". The structural components consisted of a 16 ply skin, co-cured, hat-section stringers, fastened shear ties and frames. The material used to fabricate the panels was T800 unidirectional, carbon pre-preg and was processed in an autoclave. Simulated hail impact testing was conducted on the panels using a high velocity gas gun with 2.4" diameter ice balls. The ice impact tests were performed in collaboration with the University of California San Diego (UCSD). In addition to the simulated hail impact testing, 2" diameter spherical tip steel impacts were conducted to simulate impact damage introduced during heavy ground maintenance operations.

The extent of 16 ply skin damage induced on the panels ranged from less than 1 in^2 to 55 in^2 of interply delamination. Substructure damage on the panels included shear tie cracking, delamination of the built-up pad sections behind the fastened shear ties, and stringer-to-flange disbonding.

Substructure damage away from the site of high energy ice impacts was often not detected with hand-deployed UT, which can be attributed to failure to inspect far enough away from the impact site. This additional damage was detected using the more advanced scanning techniques. Data collection from the embedded FO was not possible due to light attenuation caused by micro-bending induced in the fiber. It was determined that increasing both the numerical aperture of the FO and the diameter, in combination with adjusting the layout orientation used, may make it possible to measure strain change using this technique. Detectable strain indications were obtained using the backside bonded FO in 15 of the 25 interrogated steel tip impacts. Increasing the robustness of this deployment method could provide a means for in-situ damage detection.

CONTENTS

LIST OF TABLES

LIST OF FIGURES

1   INTRODUCTION

As the use of advanced composite materials continue to grow in the aviation community, methods of damage inspection and detection have become increasingly more important. There is a greater need to understand the response of composite structures to various types of impacts. The typical composite aircraft structure that is vulnerable to an impact event is not a simple, single element structure. These assemblies often consist of skins, co-cured stiffeners or stringers, fastened shear ties and frames. Unlike metallic aircraft structures that often dent and deform during an impact event, carbon fiber aircraft structures leave little-to-no visual indication of damage on the external surface of the aircraft. Depending on the type of impact event experienced by a composite structure, significant, widespread substructure damage, interply delamination and disbonding may occur.

Until recently, typical inspections used to detect damage in solid laminate composite aircraft structure have consisted primarily of visual inspection and hand-deployed pulse-echo ultrasonic techniques. Today there are more advanced technologies capable of inspecting large areas and presenting inspection results as two dimensional images which minimize the use of single point measurement signals. This thesis seeks to assess the use of conventional and advanced nondestructive inspection (NDI) techniques to detect simulated hail damage and steel, spherical type impact damage in full-scale aircraft fuselage composite structure. It also investigates the use of a fiber optic (FO) based distributed strain sensing system to detect and locate damage.

1

To investigate a variety of inspection and damage detection techniques, as well as assess impact damage characteristics in carbon fiber aircraft structure, two full-scale composite fuselage sections representative of structure seen on advanced transport category aircraft were fabricated. Each panel measured approximately 56" x 76" and consisted of a 16 ply skin, co-cured stringers, fastened shear ties and frames. Simulated hail impact testing was conducted on both panels using a high velocity gas gun and 2.4" diameter ice balls. Damage was mapped onto the surface of the panel using conventional hand-deployed ultrasonic inspection techniques as well as more advanced ultrasonic and resonance scanning techniques. In addition to the simulated hail impact testing performed on the panels, 2" diameter spherical steel tip impacts were conducted on one of the panels to simulate potential impact damage introduced during heavy ground maintenance operations. The damage type and extent was characterized and documented at each impact location.

Nondestructive inspection is typically used to inspect for damage based on required scheduled inspections, or when an event of concern happens to the aircraft. Aircraft maintenance depots must consider impact damage that occurs to an aircraft but is not reported. For example, a baggage handling conveyor is bumped into the fuselage near the cargo loading door. In-situ damage detection techniques are desirable for impact detection that may occur between scheduled inspections. In addition to the NDI performed on the two panels, methods of deploying a FO strain detection system were investigated.

The hypothesis is that most of the impact damage induced on the carbon fuselage panels will not be visually detectable from the surface and that scanning NDI techniques will provide more accurate damage characterization than hand-deployed methods. It is also hypothesized that when damage occurs, there will be some level of permanent strain change created in the panel that will be detected by the FO sensors nearest to the impact damage.

1.1 OUTLINE OF THE THESIS

The thesis begins by providing background information and a literature review on impact damage in composite structures, NDI methods for damage detection in composites and strain sensing techniques using fiber optics. It also discusses the difference between NDI and Structural Health Monitoring (SHM).

Chapter 3 provides details on the experimental methods and describes the NDI techniques and the FO strain sensing system used in the study. This chapter also describes the fabrication of the two full-scale carbon fiber fuselage panels and the methods used to deploy the FO sensors. This section also includes details regarding the simulated hail impact and spherical tip impact testing performed on the panels.

Chapter 4 describes the results obtained from hand-deployed ultrasonic inspections, ultrasonic pulse-echo scanning and resonance scanning techniques. It also describes how damage characterization was performed using the NDI and details the types of damage associated with ice and steel spherical tip impacts. It then goes on to describe the

3

challenges associated with embedded FO strain sensing and provides results obtained from the multiple FO deployment methods tested.

Finally, conclusions are drawn in Chapter 5. These conclusions are based on the experimental impact testing conducted and subsequent inspections performed. Recommendations for future work are also discussed.

2   LITERATURE REVIEW

2.1   INTRODUCTION

This chapter provides a literature review detailing composite materials and manufacturing practices, impact damage and damage tolerance in composite structures, an introduction to structural health monitoring (SHM), NDI, and FO sensing along with their relationship to composite structures. This chapter begins by providing an overview of composite materials and introduces some of their mechanical properties and failure modes. It continues with a review of work associated with hail induced impact damage as well as other impact threats and how they relate to aircraft. Then it provides an introduction to SHM and discusses the differences between SHM and NDI. Conventional methods of NDI are presented along with applications to composite materials. Finally, methods of using fiber optics for damage sensing are discussed and a history of the technology is reviewed.

2.2   COMPOSITE MATERIALS

Composite materials such as fiber reinforced polymers (FRP) are becoming a common material that are used in applications that require low weight and high strength and stiffness such as military and commercial aircraft, satellite, automotive and civil structures. Composite materials are comprised of multiple different materials, each with its own unique structural properties that work together resulting in a combined material who's global properties are superior to the individual materials that make it up. Advanced FRP materials used in the aircraft industry differ from conventional composite materials in that they are constructed using advanced fiber reinforcements such as Kevlar,

5

carbon and high strength treated polymer fiber. Dorworth [1] describes typical applications of advanced composites in the transport industry such as:

- **Large components of commercial airplanes** - such as the Boeing 777 and the 787 Dreamliner, the Airbus A330/340, and the A380 aircraft

- **Large primary structures on military aircraft –** such as the Airbus A400 and the Boeing C-17 transports, the B-2 Spirit Stealth Bomber, and the V-22 Osprey tilt-rotor

- **Many other components on modern airliners** – such as radomes, control surfaces, spoilers, landing gear doors, wind-to-body fairings, and interiors

- **Large marine vessels and structures** – including military and commercial vessels, as well as composite masts

- **Primary components on helicopters** – including rotor blades and hubs. Composites make up 50 to 80 percent of a rotorcraft's airframe by weight.

The matrix in a composite laminate acts to bond the structural fibers together allowing them to share loads applied to the composite. The matrix is typically an epoxy, vinyl ester, or polyester resin system[1], but other resins used to fabricate composites can be seen in Table 2-1. The matrix in an FRP also protects the fibers form moisture ingress, ultraviolet and environmental degradation, abrasion and impacts. Without the matrix, a composite structure would be nothing more than a sheet of fibers, with little to no shear strength, resisting only tensile loads. Thermoset resins are primarily used for highly loaded structures because of their high strength, availably and ease of processing compared with other resin systems [2]. When high toughness and or impact resistance is desired, thermoset resins are commonly used. They are also commonly used in high

volume production applications. Other types of composites can be fabricated using metallic and ceramic matrices, but these are primarily considered in very high temperature applications such as brake pads on race cars [3].

Depending on the application for a composite structure, there are many different types of reinforcing fiber which can be integrated into a lay-up. Common fibers include glass, carbon, aramid, polyethylene (PE), polyphenylene benzobisoxazole (PBO), and other ceramic fibers. The Composite Materials Handbook [4] shows other fibers that can be used in composite fabrication. Some of these are listed in Table 2-1.

Table 2-1: Fiber and Matrix Materials That Can be Used for Composite Fabrication[4]

Fiber Systems	Matrix Materials
Alumina	Bismaleimide
Aramid	Cyanate Ester
Boron	Epoxy
Carbon	Fluorocarbon
D-Glass	Phenolic
E-Glass	Polyamide-Imide
Glass	Polybenzimidazole
Graphite	Polyetheretherketone
Lithium	Polyetherimide
Polyacrylonitrile	Polyethersulfone
Polybenzothiazole	Polyimide
Quartz	Polyphenylene Sulfide
Silicone	Polysulfone
Silicone Carbide	Silicone
S-Glass	Thermoplastic Polyester
Titanium	
Tungsten	

7

In addition to strength and other mechanical property tailorability, Clemson University is producing and researching cross-sectional shaped fibers[5]. Similarly, Sang-Yong produced differently shaped cross-sectional carbon fibers prepared form melt-spinning [6]. The mechanical properties of conventional carbon fiber laminates and laminates made using various shaped fibers were investigated. It was shown that the tensile strength of carbon composites increased as the ratio of perimeter to cross-sectional area increased. It was found that an X-shaped fiber made a composite five times stronger than a composite made with circular fiber. Challenges associated with shaped fiber composites is fully wetting the fiber material with resin and manufacturing the shaped fibers.

2.3   IMPACT DAMAGE IN COMPOSITE MATERIALS

Impact damage can occur on aircraft structures from a variety of different objects. They can range from low velocity, high mass impacts caused by baggage handling vehicles and dropped equipment during maintenance, to high velocity light weight hail impacts and runway debris. Table 2-2 shows where impact damage can occur on an aircraft during maintenance, what can cause the impact damage, and what level of energy may be induced to the structure [7]. It can be seen that a significant impact event can occur on fuselage structure while heavy equipment is being mounted to the aircraft as well as the range of impact energy that can be delivered to a structure from hail impact while on the ground.

Impact damage caused by hail has been known to severely cripple a fleet of aircraft. Recently, American Airlines had 80 airplanes removed from service as a result of damage caused by hail in a storm at Dallas Fort Worth Airport [8]. It was reported that over 100

8

aircraft were damaged by baseball-sized hail, causing at least 500 cancelations [9]. Although baseball-size hail is not a common occurrence, an understanding of the effect and detectability of this type of damage in solid laminate composite structures will assist engineers with estimating what damage will occur to an aircraft in this type of event.

Table 2-2: Impact Threats to Aircraft Structure[7]

Section / Area		Impact Risk	Energy (J)	ft·lbs
Upper Wing Skin:	near fuselage	Falling Tools	4	5.4
	(inboard)	Aircraft Lifting Equipment	20	27.1
		Refueling by Gravity	20	27.1
Lower Wing Skin:	Outboard	Falling Tools	4	5.4
	Outboard+Inboard	Hail Impact	30 to 35	40.7 to 47.4
	Outboard	Loading of Pylons	16	21.7
Rear Fuselage	Inboard	Runway Debris	12 to 22	13.2 to 29.9
	Top	Mounting of:		
		1. Fin	57	77.3
		2. Rudder	10	13.6
		3. Hyd. Reservoir	29	39.3
		4. Hyd. Accumulator	28	38.0
		5. Air Break	6	8.1
		6. Precooler	62	84.1
		Engine Lifting Equipment	44	59.7
		A/C Lifting Equipment	57	77.3
	Sides	Ramming of Service Platform	19	25.8
		Mounting of:		
		1. Hyd. Reservoir	5	6.8
		2. Precooler	11	14.9
		3. Air break	6	8.1
		Engine Lifting Equipment	8	10.8
		A/C Lifting Equipment	20	27.1

In the severest month of any given year, the maximum hail stone size that reaches the ground is estimated to average slightly over one inch diameter, and has a 10 percent chance of exceeding two inches. A three inch diameter hail stone has a 10 percent probability of reaching the ground, at a terminal velocity of around 50 meters per second.

9

For flights at 10,000 to 20,000 feet altitude, over an area of the United States with the most severe hail, there is a 0.1 percent chance an aircraft will encounter hailstones as large as 1.9 inches in diameter in a 100 mile span and 2.4 inches in 200 miles [10]. Impact velocity at higher altitudes can reach 200 to 250 meters per second.

When a foreign object impacts a composite structure there are several damage modes that can occur including delaminations, disbonds, fiber breakage, matrix cracking and several other mixed failure modes. The damage mode that is most prevalent depends on the parameters of the impactor and the material properties of the composite [11]. Composites made with fiberglass or carbon are more susceptible to damage during impact because of their brittle characteristics, as opposed to Kevlar, which can absorb significant amounts of energy [11].

Damage induced from impact in composite materials consists of multiple fracture modes which combine to produce a complex three-dimensional pattern. Experiments indicate that a Failure Threshold Energy (FTE) exists, which is the impact energy level at which damage is first produced in a composite laminate. Impacts below this energy threshold do not produce damage. Impacts above the FTE level produce matrix cracks generated by shear or tensile flexural stresses around the indentation area. They develop mainly in the intermediate and back face layers [12]. Matrix cracks are then followed by interface delaminations growing from the crack tips. Delaminations occur between plies of different orientations and are elongated along the fiber direction of the lower layer interface, with the largest delaminations developing between layers with the highest

10

orientation mismatch. As impact energy is increased, superficial fiber fractures initiate at the tensile side of the impacted sample and may propagate through the remaining layers leading to total perforation of the laminate.[12].

Impact damage of high velocity hail on woven carbon/epoxy composites was studied by Kim [13]. Spherical, simulated hail balls were created using a spherical split mold. They were fired from a high velocity gas gun at carbon composite plates held in an aluminum picture-frame fixture at speeds ranging from 30 to 200 m/s, and varying angles of 90, 45 and 20 degrees. Numerous panels were tested and some were tested multiple times following a no-damage test result. It was found that the FTE of composites scaled linearly with the panel thickness. It was also found that small diameter simulated hail produced a lower FTE than larger due to the more localized impact area. A damage mode progression for high velocity ice impact was provided by Kim and can be seen in Figure 2-1. The figures shows that internal damage (not visual) can be induced at much lower impact velocity and be more severe than damage created at much higher impact velocity that penetrates the structure.
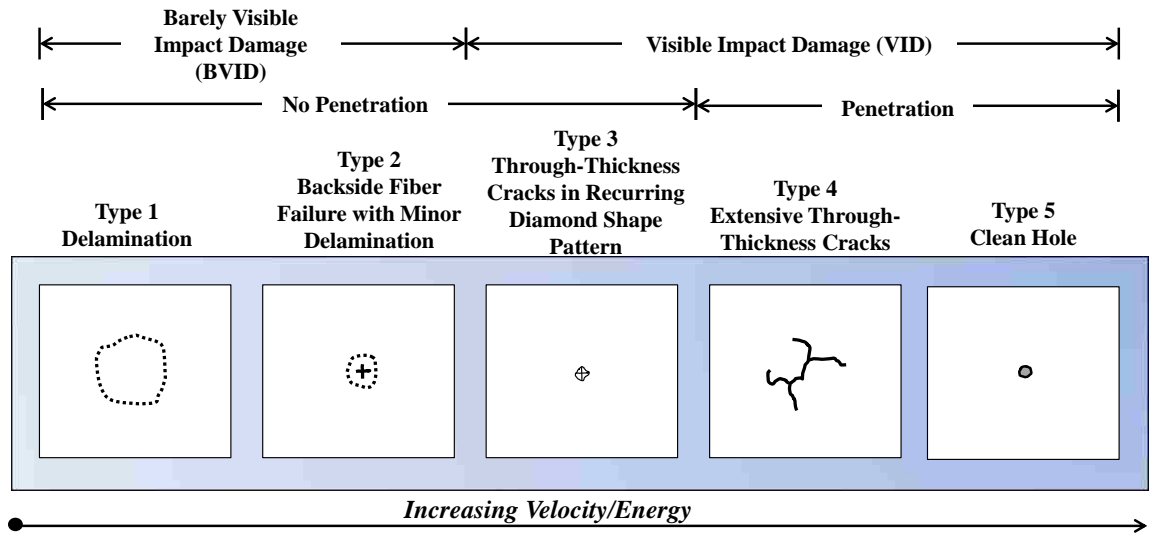
Figure 2-1: Damage Mode Progression for High Velocity Ice Impacts [13]

More recently, Rhymer determined the FTE of 12"x12", square composite laminates fabricated using T800/3900-2 carbon/epoxy pre-preg tape, as opposed to woven fabric [14]. The study employed a high velocity gas gun and used three different diameter ice balls (38.1, 50.8, and 61.0 mm.), as well as three different thicknesses of composite panels. Table 2-3 shows the FTE values for 8, 16 and 24 ply laminates. To determine FTE, a panel was first impacted at an energy level where no damage was expected. The specimen was then inspected in-situ with an ultrasonic inspection method and if no damage was detected the panel was impacted a second time at a higher energy level where damage may occur. If no damage was detected, the process was repeated, increasing the energy roughly 10% each time. The impact energy was calculated using the mass of the simulated hail and the velocity measured just before impact using equation 2.1.

$$E = \frac{1}{2}mv^2 \tag{2.1}$$

12

A comparison of the data was performed with similar results from woven fabrics [13].

This showed that the failure threshold of the two materials was almost the same.

Table 2-3: Simulated Hail Impact (SHI) Failure Threshold Energy on T800 Carbon Tape Panels

Panel Type (Thickness)	Ice Ball Diameter (mm)	Mean FTE Value (J)	FTE Value (10% threshold) (J)	FTE Value (10% threshold) (m/s)
8 Ply (1.59 mm)	38.1	211	172	115
	50.8	259	258	91
	61	226	223	65
16 Ply (3.11 mm)	38.1	369	311	154
	50.8	456	456	121
	61	507	489	96
24 Ply (4.66 mm)	38.1	415	413	178
	50.8	736	733	154
	61	938	865	127

2.4 DAMAGE TOLERANCE OF COMPOSITE STRUCTURES

As defined by the FAA in Advisory Circular 25.571-1D [15] for transport aircraft, damage tolerance is the attribute of the structure that permits it to retain its required structural strength for a period of use after the structure has sustained a given level of fatigue, corrosion, accidental or discrete source damage. It is the ability of an aircraft structure to sustain damage, without catastrophic failure, until such time that the component can be repaired or replaced.

The effect of impact damage on the strength of composite structures, also known as damage tolerance has been extensively studied. It was shown that impact damage ranging in size from 200 mm^2 to 300 mm^2 in 3 mm thick CFRP panels (approximately 16 plies of uniaxial tape) decreases the strength of the laminate approximately 30% in

13

compression loading [16]. Typically the larger the damage size in a composite structure the more significant the decrease in ultimate strength and durability of the structure.

Detectable damage size and damage tolerant design go hand-in-hand. A critical flaw that significantly decreases the strength of a structure should be within the detectable limits of the inspection technology being used. Alternatively, the damage tolerance of the structure needs to be increased such that damage of concern can be reliably detected by nondestructive inspection methods. The relationship between damage detectability and accidental impact energy can be seen in Figure 2-2 [17]. The damages falling in Zone 1 are undetectable, lower-energy damages and must be able to withstand ultimate load for the life of the structure. Damage falling in Zone 2 is detectable at scheduled inspection intervals and must be able to withstand the design limit load (considered ultimate). Damage in Zone 3 is undetectable higher-energy damage such as blunt ground vehicle impact.
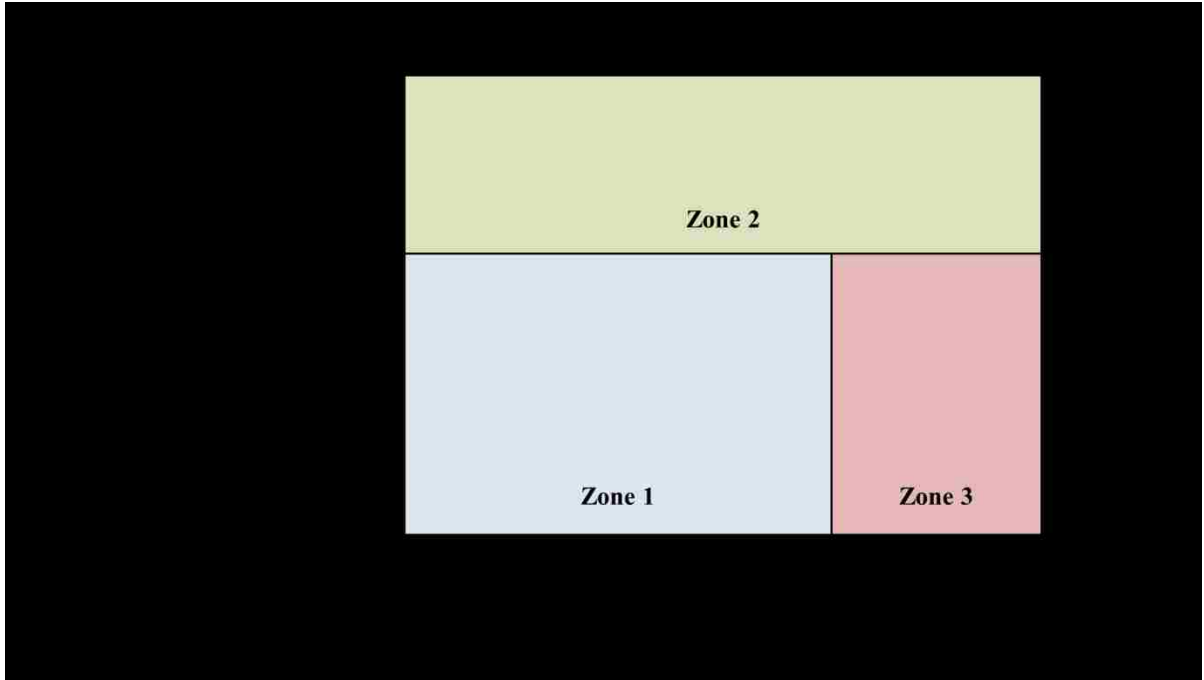
Figure 2-2: Damage Tolerant Design [17]

2.5   STRUCTURAL HEALTH MONITORING - INTRODUCTION

SHM, which is often closely associated with NDI but utilizes in-situ sensors instead of human-deployed inspection devices, has been defined in a wide variety of ways. A definition of NDI is provided below along with a definition of SHM to provide a basis of comparison.

Nondestructive Inspection (NDI) – examination of a material to determine geometry, damage, or composition by using technology that does not affect its future usefulness.

- High degree of human interaction
- Local, focused inspections
- Requires access to area of interest
- Applied at select intervals

15

The use of in-situ sensors for real-time health monitoring of aircraft structures can be a viable option to overcome inspection impediments stemming from accessibility limitations, complex geometries, and the location and depth of hidden damage.

<u>Structural Health Monitoring</u> (SHM) is the use of in-situ, mounted or embedded sensors and analysis to aid in the assessment of structural or mechanical condition or system operation including the direct detection of structural flaws. Parameters to be monitored could indicate flaws directly or could be physical properties such as load, strain, pressure, vibration, or temperature from which damage, malfunction, mechanical problems, or the need for additional investigation can be inferred [18] Potential benefits that SHM offers regarding airplane maintenance and operation include:

- Reduction of inspection time

- Early flaw detection to enhance safety and allow for less drastic and less costly repairs

- Overcome impediments associated with accessibility limitations, complex geometries, depth of hidden damage

- Ensure safety by identifying problems (aircraft operations, diminished structural integrity) that could threaten airworthiness

- Deferred maintenance and repair

- Maintenance on demand

- Minimized human factors concerns due to automated, uniform deployment of SHM sensors and automated data analysis

Fiber based composites have been a desirable application for SHM because of the need for wide area monitoring and the unique range of failure modes associated with

16

composite structures including delamination, fiber fracture, matrix cracking and environmental degradation . Moreover, fiber based composite structures are primary candidates for embedded sensors because they are laid up using multiple plies of fiber material and then infused or pre-impregnated with resin.

2.6   NONDESTRUCTIVE INSPECTION OF COMPOSITE STRUCTURES

Damage assessment in aircraft composite structures is critical to ensure their safe operation. The size and location of damage must be accurately determined in order to determine the type and size of repair that needs to be performed. If the size of damage is over estimated the amount of the material removed from the structure may exceed what is necessary. Visual inspection is typically the first and most rapid inspection performed after a suspected impact. The smallest damage size likely to be found visually is discussed by Armstrong [19]. Using a number of experienced and inexperienced operators, viewing the surface from a distance of approximately 2 meters and using a flashlight to illuminate the area, surface damage with an area of 1.4 mm square and a depth of 0.3 mm was readily detectable with a probability of 95%. Visual inspection is not only dependent on the distance and the amount of light available during an inspection, but also the angle that the light is glancing off of the part under interrogation. Traditional tap tests, where a small metal hammer or coin is used to tap the structure under investigation and variations in pitch are detected by the inspector, and ultrasonic-based inspection methods have been commonly used to inspect composite structures.

2.6.1 NONDESTRUCTIVE INSPECTION TECHNIQUES

Recently, alternative methods have increased the number of available inspection options. Over the last several years, a series of experiments, designed and implemented by Sandia National Laboratories, have been used to assess how well both conventional and advanced NDI techniques can detect anomalies in composite aerospace structures [20]. The following nondestructive inspection (NDI) sources were identified and participated in NDI activities with the FAA/Airworthiness Assurance NDI Validation Center (AANC) in composite flaw detection experiments:

Computer-Aided Tap Testing (CATT) System [21], designed to significantly improve the classic tap testing method by eliminating reliance on the technician's auditory interpretation skills. The impact duration of an instrumented tapper is measured and fed into a spreadsheet to produce two-dimensional images that reveal structural flaws.

Mobile Automated Scanner (MAUS) is a portable, scanning inspection system that integrates ultrasonic (pulse-echo, through-transmission, or shear wave) via resonance, pitch-catch, or mechanical impedance; with single and dual-frequency eddy current inspection [22]. The system can achieve inspection speeds up to 100 ft² (9.3m²) per hour.

Motionless Laminography X-Ray System (MLX), unlike conventional X-ray systems, the MLX is capable of capturing 1,000 X-ray slices, each 1 mil thick, with a single exposure [23]. It reportedly produces fog-free, high-resolution digital images, even with low-density materials, such as composites. Large-area inspection can be performed without moving the object, the detectors or the X-ray source.

Evisive Scan is a microwave nondestructive examination technology [24]. Microwaves are radiated from a transducer to the test specimen. A detectable signal is returned at each

18

interface where the dielectric constant changes (e.g., where there are defects). The transducer may be moved at any speed. Data is displayed as a digitized image.

Terahertz Composite Inspection System, which is nonionizing sub-millimeter microwave radiation technique (wavelengths between 0.1 mm and 1 mm) in the electromagnetic spectrum between 300 gigahertz and 3 terahertz [25]. Radiation at these wavelengths can penetrate composites, returning a signal that can establish a baseline for accurately "fingerprinting" a variety of anomalies.

Digital Acoustic Video (DAV) is an ultrasound imaging modality. The system features an ultrasound camera technology that generates real-time images that are said to eliminate the uncertainty associated with conventional ultrasound [26]. The hand-held camera type device is coupled to the part being inspected and an ultrasonic 2-dimensional scan is viewed with a monitor.

High-speed **Laser Shearography** system detects changes in test part surface deformation down to 5 nm [27]. The device applies small stress changes, such as a 1° increase in temperature or a 1 psi/0.07 bar increase in pressure. This alters the structure's surface elevation, but the elevation change differs over a defect. It detects these changes in real time as phase shifts in the reflected light.

Laser Ultrasonic Technology (Laser UT) uses laser energy to detect defects in composite materials and is reportedly 10 times faster than water-coupled ultrasonic inspection machines [28].

Woodpecker automated tap testing device which uses a solenoid hammer to produce a controlled impact on a structure's surface, while built-in sensors gauge the differences in

19

the speed of the hammer rebound and uses that data to display quantified information about defects [29].

AIRSCAN is an air-coupled ultrasonic technology. For structures that cannot tolerate water, it overcomes attenuation issues by using specialized transducers, with frequencies from 50 kHz to 400 kHz, to produce 2-dinentional scans in either through-transmission or pitch-catch modes [30].

RapidScan2 is a phased-array ultrasonic system that is said to be capable of generating high-resolution scans in a fraction of the time required by existing techniques [31]. The device uses a wheel probe that contains an array of up to 128 elements, typically 10 cm/4 inches long, which enables the user to scan larger areas more efficiently.

Thermographic Signal Reconstruction (pulsed thermography) which in its simplest terms observes an object with an infrared camera while subjecting the object to a heat impulse. Variations in the infrared radiation are sensed by the camera and converted to a video image, which maps the laminate interior [32]. A very short, uniform pulse of light is used to heat the sample surface.

Rapid Damage Detection Device (RD3), which uses a lightweight hammer and an accelerometer that measures the speed at which the hammer bounces back (slower bounces occur on relatively softer structures which can indicate damage) [33]. The device is cable-linked to a liquid crystal display, where numeric readouts correlate to flaws.

2.7   FIBER OPTIC SENSING

Fiber optics work on the principal that light can be guided by an interface between materials of different indices of refraction. The components of a fiber optic line consist of a core with a higher index of refraction surrounded by a cladding with a lower index of

20

refraction. The differences in the index of refraction in the core and the cladding cause light to be guided through the core.

As early as the 1980s, fiber optic (FO) sensors were used to measure strain fields embedded in composite structures. Udd used a single mode optical fiber integrated into a carbon epoxy coupon to take strain measurements with a Sagnac interferometer [34]. These early tests were performed to monitor strains developed in composites during and after curing. In very early tests using embedded fibers, the fibers were coated with an epoxy acrylate jacket which did not properly transfer strain to the optical fiber. Other tests on stripped fibers were performed. This method of embedding fibers provided adequate strain transfer to the fiber, but careful attention had to be taken during stripping and handling the fiber as to not damage the fiber. It was discovered that a fiber coated with a polyimide material that has properties similar to resins found in organic composite materials properly transferred strain and protected the fiber during handling.

Also discussed by Udd is the response of the fiber optic sensor to post curing strain in a woven composite part. Depending on the fiber's diameter, placement and orientation relative to the composite fibers, fiber optic sensors could be used to determine the interply strain state of varying tow sizes [35]. Cross sections of fiber optic sensors were also taken to determine how they affect the composite structure. It was determined that when an optical fiber is embedded perpendicular to the fiber tows, a resin pocket formed into an eye pattern that was a structural concern that may result in the onset of failure. Many tests were conducted by multiple institutions and it was concluded that the fibers,

21

could under certain conditions, be placed perpendicular to the fiber tows without affecting the overall strength of the part.

Fiber Bragg grating sensors and interrogation systems have come a long way since early testing in the 1980s. Gupta presents an airworthy Fiber Bragg Grating (FBG) based SHM system that was used to monitor the health of Unmanned Aerial Vehicles [36]. The SHM instrumentation consisted of a FBG interrogator, on-board computer, battery, electrical and fiber optic connectors, and mounting fixtures. The system had the capability to interrogate the sensors and store the data. In validation testing, it passed multiple vibration, shock and temperature tests. An artificial neural network was developed to estimate flight loads during different flight regimes. The system was flight tested and successfully demonstrated the ability to monitor 16 FBG sensors starting from launch to recovery.

In addition to using local FBG sensors with narrow gage length, Optical Frequency Domain Reflectometry (OFDR) can be used to interrogate distributed strain sensors that return strain values as a function on linear position along an optical fiber. Murayama developed a distributed strain sensing system using long-length FBGs based on OFDR [37]. In this work, 100 mm. sensing length was achieved by serially-cascading long-length FBGs and the system had spatial resolution of less than 1 mm. In order to demonstrate the system in an SHM application, single lap joint aluminum plates were investigated. The long-length FBG was set in a V-shaped grove within the bonded joint and was used to measure the strain distribution along the interface between the adherend

22

and the adhesive. The sample was then subjected to tensile loading and was failed.

Strains were successfully measured and correlated well with finite element analysis. The

system was also demonstrated on the 6 meter composite wing box shown in Figure 2-3.

**Figure 2-3: Composite Wing Box (Right) and Structural Testing Equipment Used
by Murayama**

Multiple long length FBGs were bonded along the length of the wing box structure and

were effectively used to measure the overall deformation to the wing box during loading.

Another example of OFDR distributed sensing being used to monitor structural fatigue in

a full scale test is described by Duncan [38]. Optical fibers containing high density FBG

sensors were applied to the surface of a Lockheed Martin P-3C Orion full-scale fatigue

test article. The purpose of the test was to assess the long-term structural damage

detection and monitoring of the system and investigate unique 3-D visualization tools

composed through wide area strain mapping. Results indicated good agreement with

conventional resistance based strain gages and the test demonstrated the potential for

supplementing conventional NDI with the FO SHM technique.

Swept wavelength interferometry (SWI) is another method to measure Rayleigh backscatter as a function of length in a telecom-grade single mode optical fiber. This can then be used to measure strain and temperature [39]. A sensor element is formed by transforming a spatial segment of the Rayleigh backscatter pattern into the optical frequency domain and measuring the induced shift in the reflected spectrum.

Fiber Bragg Gratings are a commonly used tool to assess strain in fiber optics but they are not the only method. By using OFDR and standard poly (methyl methacrylate) POF fiber, strain can be measured by evaluating local backscatter within a fiber as demonstrated by Liehr [40]. Using baseline scans, the authors were able to show that strained fiber sections could be detected with a special resolution of a few centimeters by evaluating the backscatter increase of POF fiber with increased strain. By applying a cross-correlation algorithm to the backscatter signal of the fiber, a length change occurring in the fiber relative to a reference measurement could be measured with a resolution better than 1 mm. The interrogation and evaluation techniques provide a reliable distributed strain sensor with a maximum measurement of more than 500 meters.

In addition to directly measuring strain to detect damage using optical fibers, a coil of fiber can be used as an acoustic sensor to collect ultrasonic waves produced by piezo-actuators [41]. Testing was conducted on a 1585 x 790 x 2.8 mm^3 CFRP quasi-isotropic plate, placing the piezo-actuators on one side of the plate and the FO sensors on the other. Waves generated by the actuators are picked up by the FO sensors. If a defect is in the path of the ultrasonic waves they are deflected or attenuated when detected by the FO

24

sensors, causing a change in response. It was shown that impact damage can be detected and located in CFRP plates, but with less clarity than in aluminum plates. Signal attenuation in composites, which is higher than in metallic structures, is an issue that is still being addressed.

Brillouin optical correlation domain analysis (BOCDA) is another method to use optical fibers for damage sensing. This measurement technique is based on the principal that when a strain is applied to the fiber, the fluctuation of density changes the acoustic wavelength, making the Brillouin frequency change [42]. Bearing damage tests were conducted around holes drilled through quasi-isotropic 16 ply laminates to determine if Brillouin frequency shifts (BFS) could be monitored to detect the onset of damage during tension loading. Micro-damage, such as out –of-plane shear cracking and interlaminar delamination could be detected by the BFS distribution changes.

3 EXPERIMENTAL METHODS

3.1 NONDESTRUCTIVE INSPECTION TECHNIQUES USED

3.1.1 SINGLE ELEMENT ULTRASONIC INSPECTION

Conventional single element ultrasonic inspection uses a piezoelectric transducer with a specific frequency to transmit ultrasonic waves into the part being inspected. Probe frequency is selected based on the attenuation, ultrasonic velocity of the material being inspected and the size of the defect intended to detect. The relationship between frequency, velocity and wave length are shown in Equation 3.1. The minimum defect detectable is half the wavelength.

$$f = \frac{v}{\lambda} \tag{3.1}$$
$$d = \frac{\lambda}{2} \tag{3.2}$$

Where f is the frequency, v is the ultrasonic velocity of the material being inspected, λ is the wavelength, and d is the minimum detectable defect size.

Ultrasonic waves propagate through the part and reflect off of the back wall or are interrupted by discontinuities with in the part. An ultrasonic inspection can be performed with a single, send and receive transducer, also known as pulse-echo, or separate sending and receiving transducers, also known as pitch-catch or through transmission. In most ultrasonic based techniques a coupling medium needs to be used to transmit the ultrasonic waves into the part. As an inspection is being performed, the inspector typically monitors the amplitude and position of the returned sound waves. This is done at a single point with an A-scan, or a two-dimensional, wide area C-scan, where a

position encoding device is used to track the position of the transducer. A color pallet associated with high and low amplitude is used to produce an image of the part. Example A-scans and a C-scan of a carbon fiber laminate impacted with simulated hail can be seen in Figure 3-1. The peak in the A-scan shown on the left side of Figure 3-1 represents a point measurement on a good area of the plate where the reflection is seen at the back wall. The second A-scan on the left represents a point measurement over a region that has an interply delamination. This flaw produces a new reflection which shows up earlier in time in the A-scan than the back wall reflection. A-scans show signal amplitude (y-axis) verses time of signal travel (x-axis) for the point of transducer placement. The red horizontal bar in the two A-scans is a gate that was set at the time location corresponding to the back wall of the part. The C-scan in the center is produced by the set of the maximum amplitude measurements under the gate at every point on the panel. In this particular scan, red or orange colors are high amplitude and blues, yellows and greens are low amplitude.

In addition to amplitude C-scans, time of flight (TOF), or the position of the reflected signal can be tracked to inspect for changes in thickness. The A-scan taken at the good area in the figure is an example of a full thickness measurement. As the transducer is moved over the delaminated area the reflected sound signal shifts to the left indicating a decrease in thickness.

27

| 1 A-Scan Good Area | C-Scan Impact Damage on 16 ply Carbon Laminate | 2 A-Scan Bad Area |
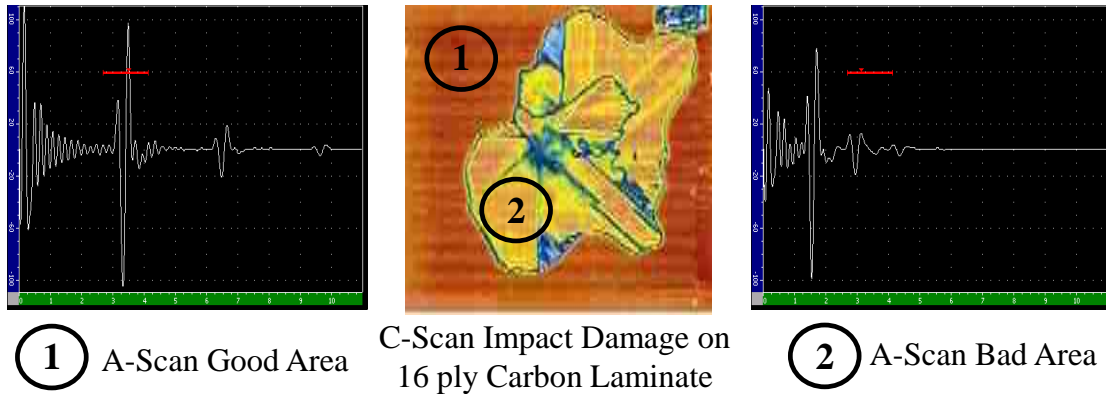
Figure 3-1: Examples of an A-Scan Over a Good Area, C-Scan, and an A-Scan over a Bad Area on A 16 Ply Carbon Composite Plate

The ultrasonic hardware used in this study was the General Electric USM Go for spot check A-scans, Boeing MAUS V Scanning system for C-scan collection using a 5 MHz single element transducer.

3.1.2 ULTRASONIC RESONANCE INSPECTION

Resonance testing is also known as high frequency bond testing. It is similar in application to conventional ultrasonic testing in that a resonance transducer is acoustically coupled to the sample being inspected using liquid couplant. Resonance testing utilizes special narrowband frequency transducers that can be excited at their natural resonant frequency by an oscillator in the instrument [43]. When the transducer is coupled to the test article it produces a tuned, continuous standing sound wave in the material. The test material, in turn, provides a mass loading on the transducer increasing the transducer bandwidth which, in turn, changes the transducer's resonant frequency. Flaws in the material or changes in the material thickness result in significant changes to the transducer loading that cause changes in the transducer resonant frequency. These changes are subsequently detected as differences in phase and amplitude. A flying dot or

28

curser is displayed on the resonance testing unit on an X-Y plot. The X-axis corresponds to the signal amplitude and the Y-axes corresponds to the signal phase. The magnitude of the amplitude and phase are tracked and position data can be collected using a scanner. T information can be displayed in a C-scan image.

In order to use resonance testing, the probe needs to be calibrated in an area where there is no defect. The probe is then nulled, or zeroed to establish a baseline signal. If it is not possible to locate an area with no defect the probe can be nulled in air for the starting point. Then the scan is performed.

An example of resonance inspection results performed on a 24 ply carbon laminate impacted with a steel, 2" diameter impactor can be seen in Figure 3-2. The figure shows an A-scan taken at a pristine location on the panel along with an A-scan at a large damage (A), a small damage (B), and a medium damage (C) area. The flying dot chart to the right of each resonant frequency plot shows the magnitude of the phase and amplitude change at each location in an X-Y chart. The two C-scans at the top of the figure visually show the changes in the amplitude and phase.

29
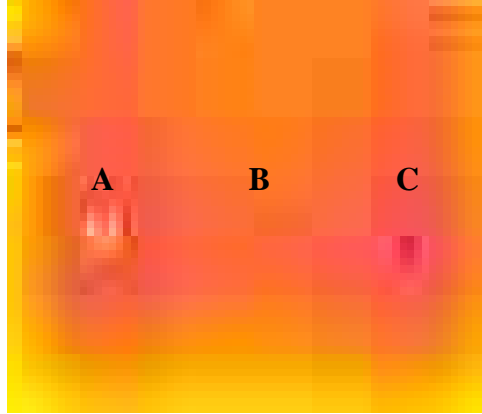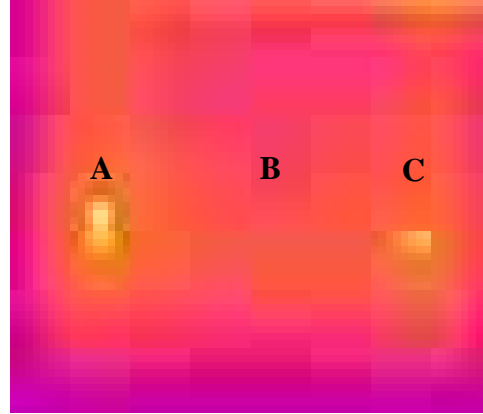
X-Plot (Amplitude)   **Y-Plot (Phase)**
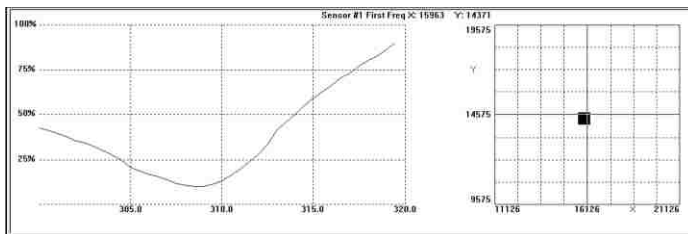
CAL IN (No Damage)
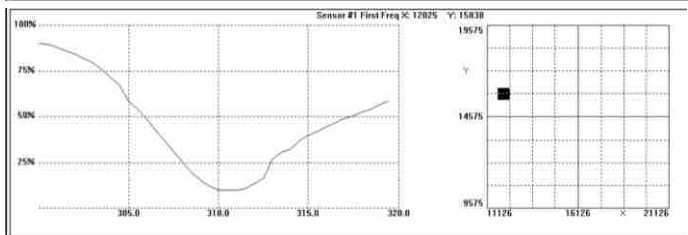
Impact **Point A**: Large Shift
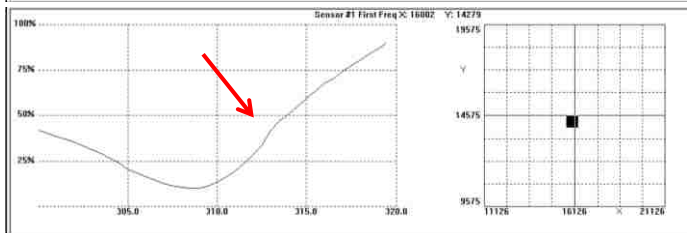
Impact **Point B**: Small Shift
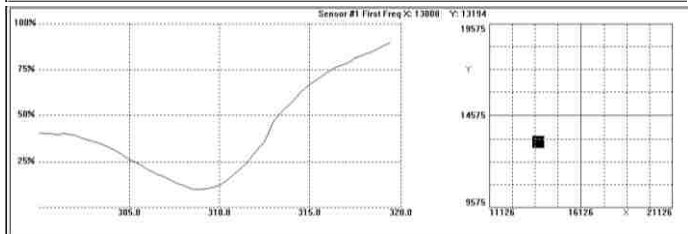
Impact **Point C**: Medium Shift

Figure 3-2: Resonance Testing Results for a 24 Ply Impact Damage Panel Showing Amplitude and Phase Shift Plots (C-scans and A-scans)

3.2 CARBON FIBER FUSELAGE PANEL FABRICATION

This thesis seeks to assess the use of conventional and advanced NDI techniques to detect simulated hail damage and hardened, spherical type impact damage in full-scale aircraft composite structure and investigate the use of a FO strain sensing system to detect and localize damage. To test the FO strain sensing system and various NDI techniques to detect damage, two full-scale carbon fiber fuselage sections were fabricated with co-cured stringers, fastened shear ties and frames. The composite panels were painted using an aircraft grade epoxy primer and JetGlo Express paint and instrumented with bonded or embedded FO. Figure 3-3 shows the 56" high by 76" long carbon fiber fuselage sections after fabrication. The panels were designed to be representative of structure found on large, advanced composite commercial transport category aircraft. The intention was to generate varying levels of impact damage in the panels to assess the sensitivity of various NDI techniques and the fiber optic system. Since testing was focused on localized impact damage, the normal carbon fiber frames used in an actual aircraft were replaced with aluminum frames with similar global stiffness properties and are not shown in this figure.

31
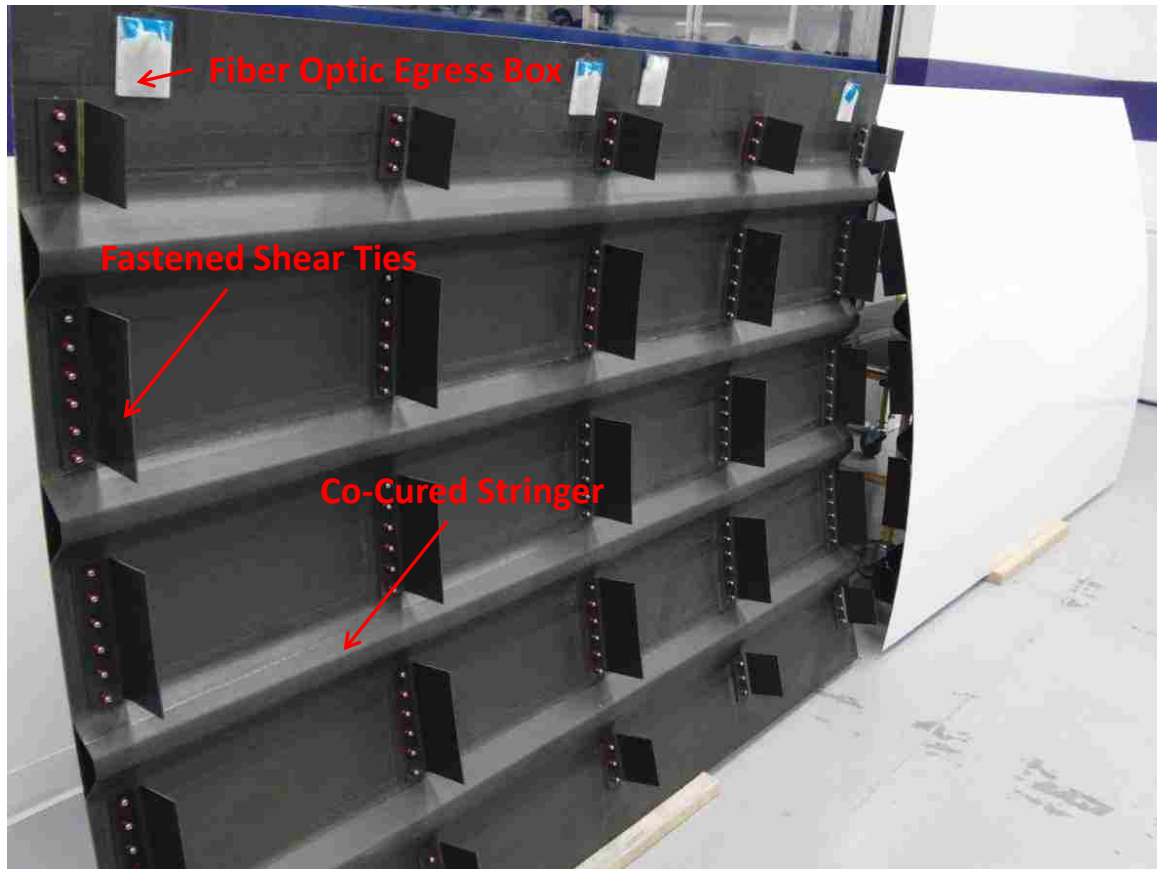
Figure 3-3: Backside and Front Side View of Carbon Fiber Fuselage Sections

The skin layup of the panels was a 16 ply quasi-isotropic, symmetric $[0,+45,90.-45]_{2(s)}$ layup with a fiberglass cover ply. The material used for the skin, stringers and shear ties was T800 unidirectional pre-preg tape with a 3900 series resin system made by Cytec (Boeing specification BMS8-276). A schematic of the layup for the skin of the panel can be seen in Figure 3-4. The glass cover ply material was a thin woven bidirectional glass also with a 3900 series pre-preg resin system also made by Cytec. All edges of the unidirectional taper were butt spliced with a maximum allowable gap of 0.020". A curved aluminum caul plate was custom designed and fabricated to construct representative fuselage curvature.

32

3.2.1 EMBEDDED FIBER OPTIC

The fiber optic used for both the embedded and bonded panels was an 80 micron polyimide clad telecom grade fiber. The fiber optic was embedded 11 plies deep in the 16 ply skin which is approximate ¾ depth of the skin thickness. This location was selected because the fiber would have less of a chance of being crushed near the surface of the skin when impacted and has a higher chance of maintaining residual strain after impact since it is on the other side of the neutral axis, or the mid-plane, of the skin.

Tool Plate

Glass Coverply
Ply 1: 0˚
Ply 2: +45˚
Ply 3: 90˚
Ply 4: -45˚
Debulk
Ply 5: 0˚
Ply 6: +45˚   ¾ Thickness
Ply 7: 90˚
Ply 8: -45˚
Debulk
Ply 9: -45˚
Ply 10: 90˚
Ply 11: +45˚
Veil and Fiber Optic
Ply 12: 0˚
Debulk
Ply 13: -45˚
Ply 14: 90˚   ¼ Thickness
Ply 15: +45˚
Ply 16: 0˚
Debulk
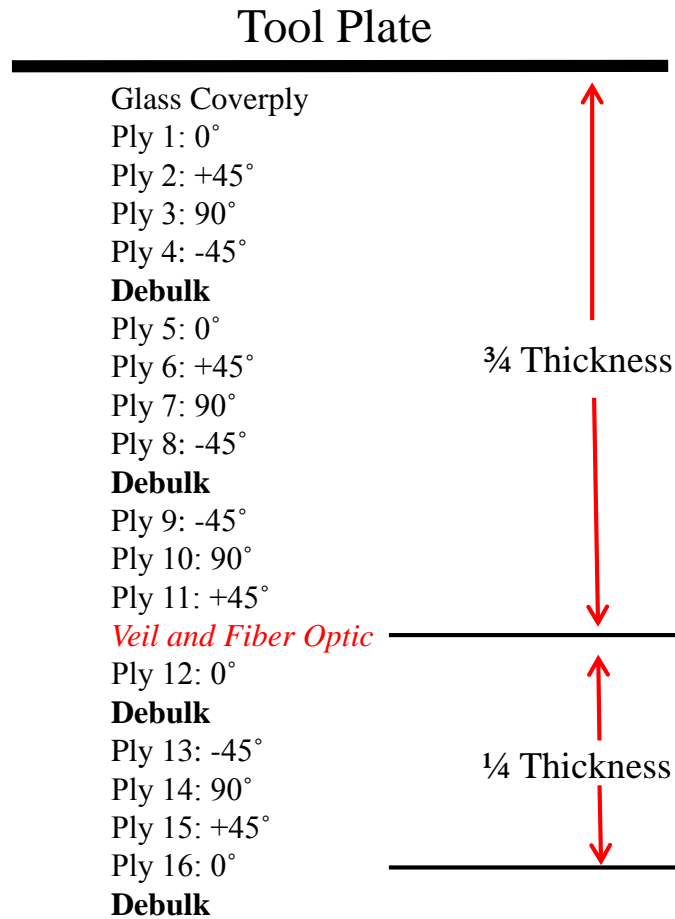
Figure 3-4: Skin Layup Schematic Showing Where in the Skin the Fiber Optic was Embedded

In order to embed the fiber optic in the panel during fabrication, a FO layout was designed to provide some redundancy if a fiber was broken during testing and would also avoid the areas where the shear ties would be fastened to the skin of the panel. To easily lay out the fiber onto the layup during manufacturing, the fiber was attached to a thin veil made of carbon weave. Details regarding the carbon veil cannot be discussed at this time.

3.2.2 EFFECT OF FIBER OPTIC CARRIER ON NDI

To determine if the veil material would have an adverse effect on the structural integrity of the fuselage skin, a section of veil material with a short section of fiber was embedded in half of a 12"x12" carbon T800 layup, and was laid up and processed in the same way as the full scale panels. A picture of the test panel with the layout of the veil and fiber optic can be seen on the left side of Figure 3-5. The veil/fiber optic side is shown in red. Also in the figure are ultrasonic C-scans of the test panel showing that there is little change in ultrasonic amplitude between the veil and non-veil sides of the panel. The center scan was taken using the Boeing MAUS V system with a 5 MHz contact probe and the right ultrasonic C-scan was taken using a 5 MHz Through Transmission (TTU) probe in an immersion tank. The contact probe test indicated some areas of decreased amplitude, but the TTU did not. This discrepancy was due to surface demarcations on the panel causing the contact probe to rock and loose contact with the part. There were no disbonds or resin flow issues shown in the NDI that indicated that the veil/fiber was an impediment to subsequent inspections.

34

Tool Side · Ultrasonic Amplitude C-Scan (5 MHz Contact Probe) · Ultrasonic Amplitude C-Scan (5 MHz Through Transmission)
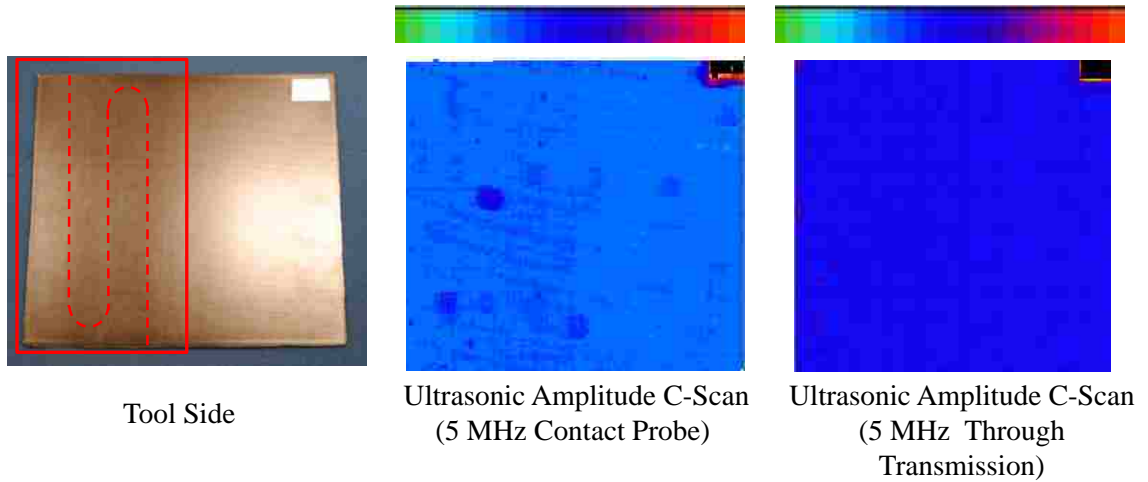
Figure 3-5: Embedded Veil and Fiber Optic NDI Test Panel with Contact and Through Transmission C-Scans

In addition to ultrasonic C-scans, conventional A-scan amplitudes were compared on the NDI test panel. Representative A-scans from both the veil and non-veil sides of the panel can be seen in Figure 3-6. The scans indicate that there was very little loss of amplitude caused by the veil, but there was an additional signal reflected by the veil layer. This may have been caused by the lower fiber density and higher resin content in the layer.

A-Scan 1 – Veil Side   A-Scan 2 – No Veil Side

Fiber Optic-79% Amplitude   Non-Fiber Optic-80% Amplitude
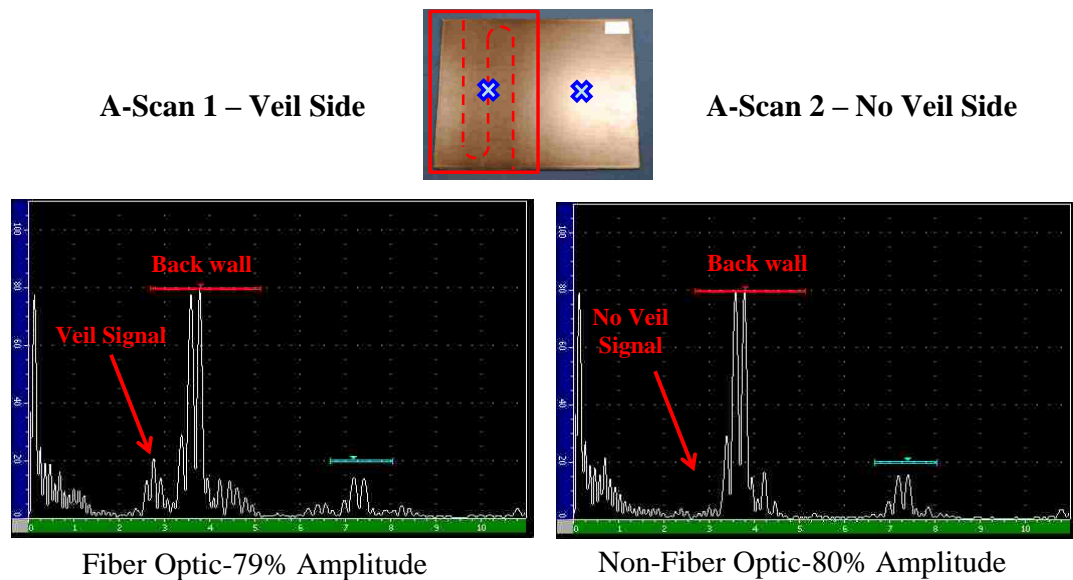
Figure 3-6: A-Scan Showing Amplitude of Veil and Non -Veil Side of Test Panel

35

Two fibers were embedded in one of the two full-scale fuselage panels. Each fiber had two egress points. A schematic showing the fiber layout can be seen in Figure 3-7. Initially, the spatial resolution of the system was not known in these conditions. It was also unclear how large of a permanent residual strain change would be maintained in the carbon after impact and if the impact would occur in the vicinity of a fiber. Because of this unknown, a two inch spaced serpentine pattern of the fiber was used. In total there was approximately 130 feet of fiber optic embedded in the panel. Two egress locations on each fiber were used so that the fiber could be interrogated from either side in case there was a break in the fiber due to an impact or if a connector failed.
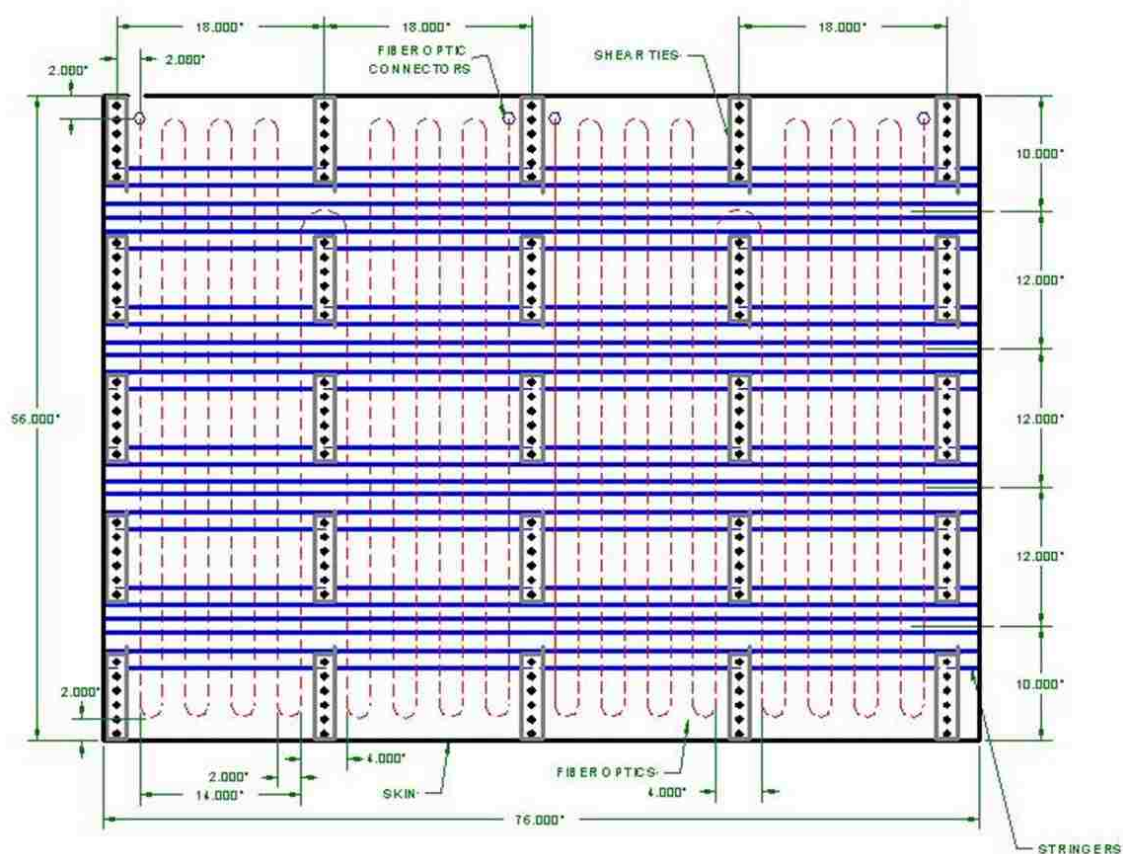
Figure 3-7: Embedded Fiber Optic Layout Showing Location of Embedded Fibers in Panel A

To begin fabrication of the skin of the panel the custom aluminum caul plat was cleaned and the first fiberglass cover ply layer was laid down. The layup shown in Figure 3-4 was then followed until the 11th ply was placed. Then the veil with the fiber optic attached was set in place. Figure 3-8 shows the carbon pre-preg being laid up on the caul plate to construct the skin.

Figure 3-8: Carbon Pre-Preg Skin Plies Being Laid Up on Caul Plate

The veil material was rolled out and pressed by hand to the room temperature, tacky pre-preg. The position of the fiber optic was verified and subsequent layers (plies) of carbon were placed. The two fibers each attached to their own veil are shown in Figure 3-9 being placed on the layup.

Figure 3-9: Fiber Optic Placed on Skin Layup and Subsequent Layer of Carbon Being Applied

As described in the layup schematic of the panel, a vacuum debulk was performed each time four plies of carbon were placed. Release film was positioned over the pre-preg and then a layer of breather to properly distribute the vacuum pressure. At each debulk approximately 506.5 Torr (20 inHg, 67.5 KPa) was applied for 20 minutes. The debulk process can be seen in Figure 3-10.

Figure 3-10: Skin Layup Bagged and Being Debulked

When all 16 plies of the skin were in place and debulked, silicone molds for the hat

section stringers were placed. One of the silicone molds used for the hat section stringers

(Figure 3-11) is shown in Figure 3-12. Four stringers were cured to each panel and were

12 inches apart. The flange portion of the stringer was co-cured to the skin. The flange

is 1.5 inches long and tapered at a ply drop rate of two plies per 0.02" of an inch.

Tapered stringers are used to provide better stress distribution at the stringer to skin

interface, decreasing the chance of disbonding. They also help to minimize the shear

stress that develops in the skin when an impact occurs near the edge of a stringer. There

is also a tapered built-up section in the skin under each shear tie which consists of 12

additional plies. This is known as a pad build-up and provides more material for

fastening the shear ties to the skin.

39

Tapered Region   **Hat Section Stringer**

Disbonded Flange Region
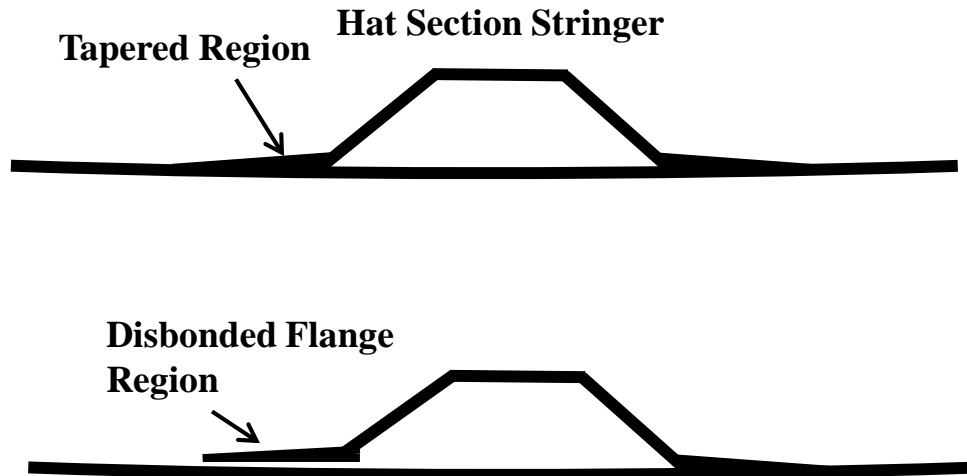
Figure 3-11: Tapered Hat Section Stringer Geometry and Disbonded Stringer Flange Example

Once the full layup was complete, a vacuum line was attached to the bagged part in a similar process that occurred during the debulk. Vacuum was applied to the panel and it was loaded into an autoclave. A cure profile was then programed into the autoclave which consisted of a heating and pressurization ramp. The temperature in the autoclave was raised at 5°F per minute until a final temperature of 350°F was reached. This temperature was held for two hours and 20 minutes. Simultaneously, a pressure ramp was applied to reach a max external pressure of 90 psi at which time the vacuum pressure within the bag was released to atmosphere.

Figure 3-12: Autoclave and Silicone Stringer Molds used to Cure Panels

3.2.3 BONDED FIBER OPTIC

Two different methods of deploying fiber optic strain sensing to the panels was investigated in this work: embedded and bonded. Embedding a fiber optic in any composite structure would have to be performed during the manufacturing of the composite part. Also, embedding sensors or any type of material in the skin of an aircraft would have to be accompanied by stringent certification testing to show that the sensors do not degrade the structural integrity of the aircraft or affect any other part of the structure. Because of this and due to manufacturing reasons, external bonding or applying sensors to the inside skin of the aircraft has more potential in the near future than embedded sensors. To bond the fiber optic to the backside of the panel, three orientations of fiber layout were investigated. They included:

41

1) Bonded to the panel perpendicular to the stringers with the fiber being bonded to each skin and stringer. This fiber had the same orientation and layout as the embedded fiber and was applied to all bays on panel B.

2) Bonded to the backside of the panel to only the skin and parallel to the stringers (bays 1 and 2 on panel A).

3) Bonded to the backside of the panel perpendicular to the stringers, but not bonded to the stringers, only the skins (bays 3 and 4 on panel A).

The surface of the backside of the panels was prepared and cleaned for bonding. When the panels were cured under high pressure in the autoclave the breather material left a slight, rough indention pattern on the backside of the panels. This was lightly sanded down with a 240 grit sand paper in order to remove the bumpy cured resin. Once the surface was sanded it was conditioned using M-Prep conditioner-A then neutralized using M-Prep Neutralizer 5A. The process of conditioning and neutralizing on the sanded panel is shown in Figure 3-13. The fiber optic was then carefully laid out onto the prepared surface and taped with small pieces of Kapton tape to hold the fiber flush to the surface. In order to lay out the fiber on the backside of the panel, short lengths of fiber were unrolled from the spool and taped into place until the full serpentine pattern was laid out. M-Bond GA-2 strain gage adhesive was placed under the fiber with a syringe and squeegeed smooth around the fiber with a sponge.

Figure 3-13: Conditioning and Neutralizing the Backside of the Panel for Bonding FO Lines

Figure 3-14 shows the fiber taped in place with a thin line of adhesive squirted under the fiber. The adhesive is being smoothed out with the sponge, removing any excess adhesive. Many small pieces of tape were needed to keep the fiber optic in close contact with the surface of the panel. Laying out the fiber and bonding it to the surface in the three different orientations was a time consuming and tedious process.

43

Figure 3-14: Thin Line of M-Bond GA-2 Adhesive Being Squeegeed Smooth Around Fiber Optic

Both the embedded and bonded fiber optics needed to have connectors mated to the bare fiber. The process of splicing two fibers together involved using a fiber optic cleaver to cut a flat end face perpendicular to the longitudinal axis of the sensing fiber. An FC connector with a short length of fiber already attached to the connector was cleaved and spliced to the sensing end. To join the two ends of cleaved fiber a Fujikura Arc Fusion Splicer was used. After each splice performed, the splicer unit analyzed the light attenuation loss based on the geometry of the splice. If this loss was greater than 0.1 dB the splice had to be redone. The hardware used is shown in Figure 3-15.

44

Figure 3-15: Fiber Optic Cleaver and Fujikura Arc Fusion Splicer

3.3 SWEPT WAVELENGTH INTERFEROMETRY DISTRIBUTED STRIAN SENSING

Luna Innovation's Optical Backscatter Reflectometer (OBR) was used to measure the strain in the fiber optics. The OBR uses swept wavelength interferometry (SWI) to measure the Rayleigh backscatter as a function of length in optical fiber and is shown in Figure 3-16. An external stimulus (like a strain or temperature change) causes temporal and spectral shifts in the local Rayleigh backscatter pattern. The OBR measures these shifts and scales them to give a distributed temperature or strain measurement. The SWI approach enables robust and practical distributed temperature and strain measurements in optical fiber with sub-centimeter-scale spatial resolution up to 70 meters of fiber with strain and temperature resolution as fine as 1 µstrain and 0.1 °C [44].

Figure 3-16: Luna Innovations Optical Backscatter Reflectometer used in the Study

Rayleigh backscatter in a fiber optic is caused by random fluctuations in the index profile along the fiber length [39]. The scatter amplitude as a function of distance is a random but static property of an individual fiber and can be modeled as a long, weak Fiber Bragg Grating with a random period. Changes in the local period of the Rayleigh scatter caused by an external stimulus (like strain or temperature) in turn cause shifts in the locally reflected spectrum. These local spectral shifts can then be calibrated and assembled to form a distributed strain or temperature measurement [39].

3.4   SIMULATED HAIL IMPACT TEST SETUP

The first set of tests imposed on the panels was high velocity simulated hail impact testing which was performed in collaboration with the University of California San Diego (UCSD). A schematic of the UCSD gas gun test facility can be seen in Figure 3-17. The gas gun was used to fire 2.4 inch diameter ice balls at high velocity into the panels. The hail velocity to be considered was the relative velocity of the hail, or speed of the airplane plus the speed of the hail. Glancing blows were not considered.

The test facility consisted of the following (see Figure 3-17 labels):

1) Gas gun composed of high pressure gas tank filled with Nitrogen to a specified pressure depending on the intended ice ball velocity, helium actuated pneumatic ball valve, breach and barrel

2) Nitrogen gas storage tanks

3) Laser diode and photo detector in trajectory path of projectile to trigger lights and high speed camera measurements

4) Sabot stopper used to disengage the sabot from the ball of ice prior to impact

5) Two laser diodes and photo detector contained in an aluminum housing whose laser path is broken and used to measure ice ball velocity

6) High speed cameras used to measure velocity and determine if the ice ball was still intact at time of impact

7) Panel being tested secured with a frame constructed with 80/20 aluminum structure

8) Luna Innovations OBR fiber optic interrogator

47

UCSD Gas Gun Test Facility
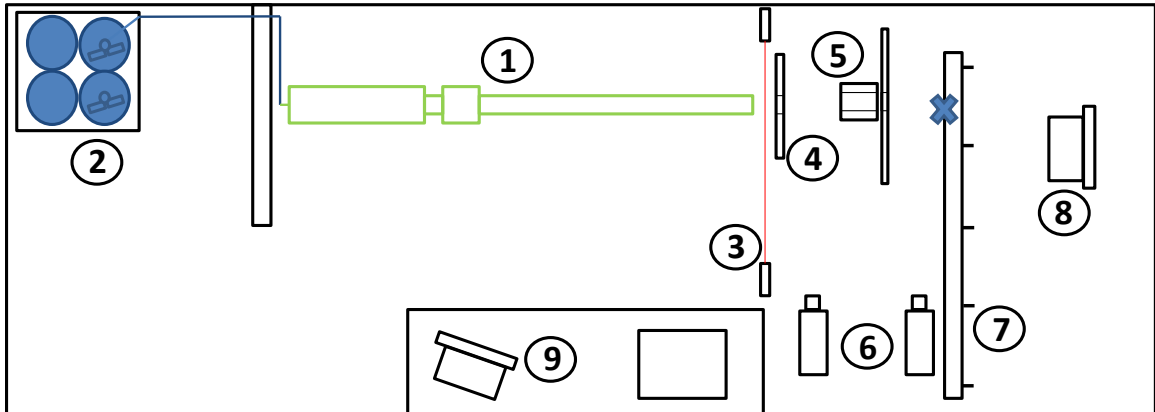
Figure 3-17: Schematic of the UCSD Gas Gun Test Facility

The nitrogen propellant gas is used to fill the high pressure storage tank on the gas gun.

Based on previous testing data, a tank pressure vs. exit velocity chart was used to

determine the pressure level needed to achieve a desired impact velocity. Simulated hail

balls are placed in sabots and then inserted into the breach. In order to launch the

simulated hail, helium gas is used to actuate the ball valve which opens and releases gas

from the propellant gas tank. The gas expands and exerts pressure onto the sabot and

projects the ice ball and sabot through the 79.300 mm φ x 2286 mm (3.122 in φ x90 in)

barrel. After exiting the barrel, the sabot hits a stop plate and is removed from the ice

ball as it continues its trajectory through the laser velocity measurement system and high

speed cameras before impact with the target.

Figure 3-18: Gas Gun used for High Velocity Ice Ball Impacts Testing Showing the High Pressure Gas Tank, Pneumatic Actuator, Breach and Barrel

The test panel was mounted to an aluminum frame constructed out of 80/20 aluminum members. First the impact location of interest was identified and the panel was lifted into place with a jack and set against the frame. The desired impact location was marked on the surface of the panel and a laser was shined down the barrel of the gun and matched with the marking on the panel. Clamps were used to secure the panel to the frame by clamping the frame sections of the panel to the support frame. A digital level was used on the face of the panel to ensure that the panel was perpendicular in both the horizontal and vertical directions to the trajectory of the simulated hail. A backside view of the panel clamped to the frame and ready for impact is shown in Figure 3-19. The X in the figure indicates the impact location on the front side of the panel.

Figure 3-19: Panel Supported with Frame being Prepared for Impact Test

Multiple impact scenarios were tested with high velocity simulated hail. Impact areas of interest are shown in Figure 3-20 and consisted of:

- o Mid-bay impact between shear ties and stringers (1)

- o Stringer impact at start of stringer flange (2a)

- o Stringer impact at center of stringer flange (2c)

- o Stringer impact at end of stringer flange (on flange closest to mid stringer) (2c)

- o Mid-stringer (between flanges under hat section) (3)

- o Shear tie impact (4)

After each impact was induced, a visual inspection of the front and backside of the panel was performed. In the visual inspection, signs of damage to the surface of the panel such

50

as denting, chipping and marring were identified. On the backside of the panel,

disbonding of the stringer flange-to-skin interface were inspected.
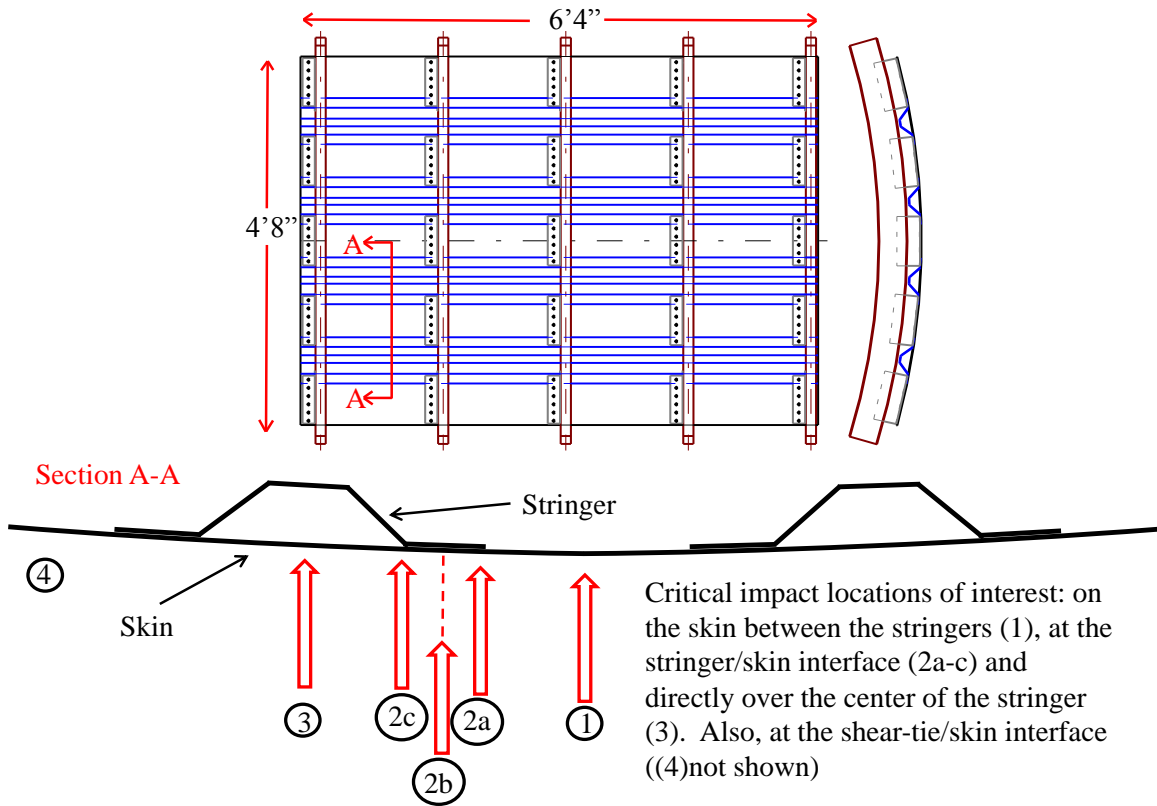
Figure 3-20: Schematic of Panel Showing Impact Areas of Interest

To ensure that the ice ball stayed intact during its trajectory high speed video was taken.

Example high speed images of an ice ball prior to and during impact are shown in Figure

3-21.

Figure 3-21: High Speed Image of Simulated Hail Impacting Fuselage Panel

After the visual inspection, an ultrasonic A-scan unit was used to determine the extent of damage as shown in Figure 3-22.

Figure 3-22: Ultrasonic A-Scan Inspection Being Performed After Impact to Determine Damage Extent

There were 22 different locations on the two panels that ice impact testing was performed. The 13 ice impact locations that were conducted on panel A are shown in Figure 3-23 and the 14 ice impact test locations conducted on panel B are shown in Figure 3-24. The naming convention used to describe each impact is discussed in Chapter 4.
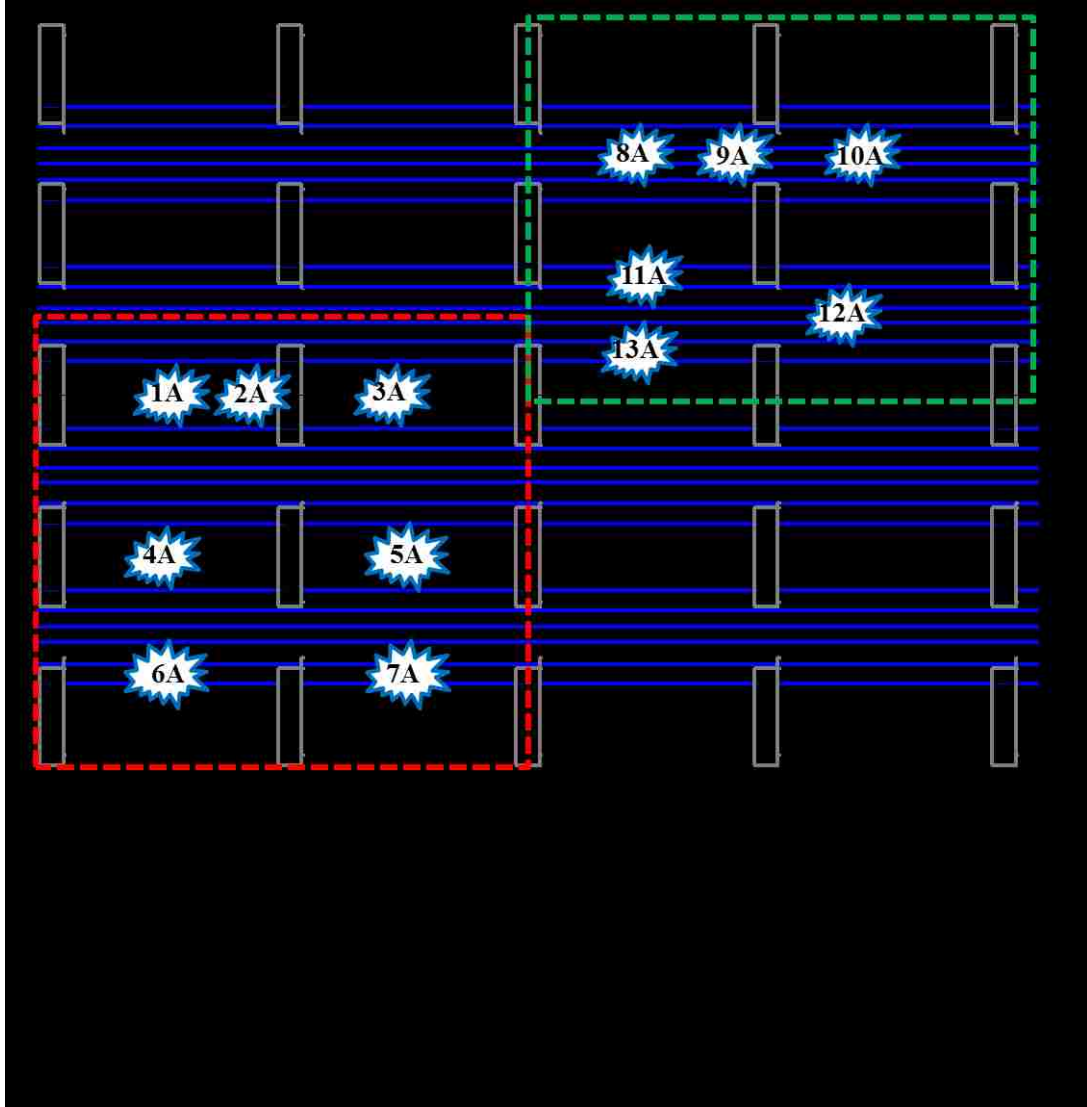
Figure 3-23: Ice Impact Test Locations on Panel A
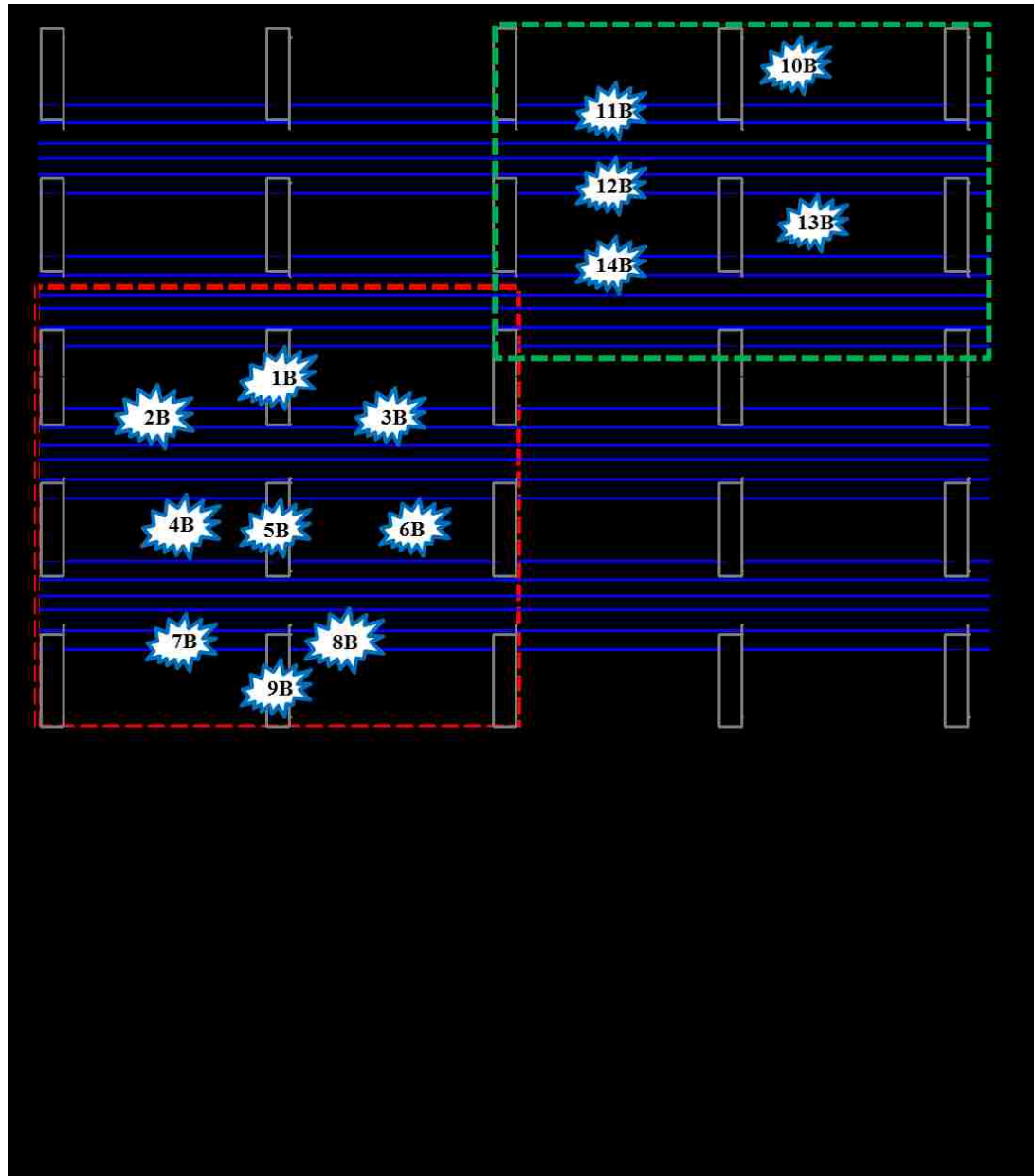
Figure 3-24: Ice Impact Test Locations on Panel B

3.5   SPHERICAL TIP DROP WEIGHT IMPACT TEST SETUP

To simulate impact damage related to ground based equipment, a drop weight, spear-type

impact device was designed and fabricated. The intention of these tests was to induce

varying levels of damage on the panels created by hard, spherical tipped impacts. The

intended levels of damage ranged from almost nonexistent to fairly severe.

The hemispherical shape was selected to represent a generalized solid object impacting the skin of the panel. A 2" diameter, spherical impact tip was selected to test panel A. The drop spear was constructed using a ¾" – 10 threaded rod. The threaded rod was used so that the weight of the spear could be easily adjusted using large washers secured to the rod with nuts. A 10 foot tall pipe was used to guide the drop spear to its target. Two larger diameter aluminum guide washers were fabricated with a diameter that is 1/8th" smaller than the inside diameter of the guide tube. The guide washers were sized to minimize rattling during the spear descent into its target. A smooth, sanded radius was integrated on the outside edge of the guide washers to minimize frictional energy loss. Figure 3-25 shows the drop tube and spear with the two inch diameter impact tip.

55

Figure 3-25: Guide Tube, Drop Spear with 2" Diameter Impact Tip and Quick Release Mechanism

To raise the drop spear to the desired height of impact, a steel cable loop was attached to

the top of the drop spear. A quick release mechanism attached to a cable was run through

a pulley secured above the top of the guide tube and attached to a manual winch. The quick release was attached to the drop spear through a rectangular access hole in the guide tube. The drop spear was suspended at the intended distance from the panel in the center of the drop tube. A string was run down through the top of the tube to the quick release. This is also shown in Figure 3-25. Prior to each drop test the tube was checked for vertical level to ensure the spear did not slide along the side of the tube.

To secure the panel during impact testing a steel frame was fabricated using 1"x2" steel tubing. The frame was welded together with two supports clamped to each frame on the panel (10 locations). Angled stiffeners were added to prevent any horizontal movement during impact testing. A picture of panel A clamped to the mounting fixture is shown in Figure 3-26. The vertical runs of bonded fiber can be seen in the lower left side of the figure and the horizontal runs of fiber can be seen in the upper right.

Figure 3-26: Panel A Clamped to the Steel Frame for Drop Weight Impact Testing

57

Each impact was performed perpendicular to the surface of the panel. Two brackets, one on each side of the frame, were used to secure the panel at the required angel to keep the impact site perpendicular to the spear guide tube. The two brackets clamped to the frame are shown in Figure 3-27.

Brackets used to adjust angle

Figure 3-27: Panel A Set Up for Drop Weight Impact Testing

Impact locations for the steel, spherical tip impacts that were performed on Panel A are in Figure 3-28. There were a total to 43 spherical tip impacts performed on the panel.
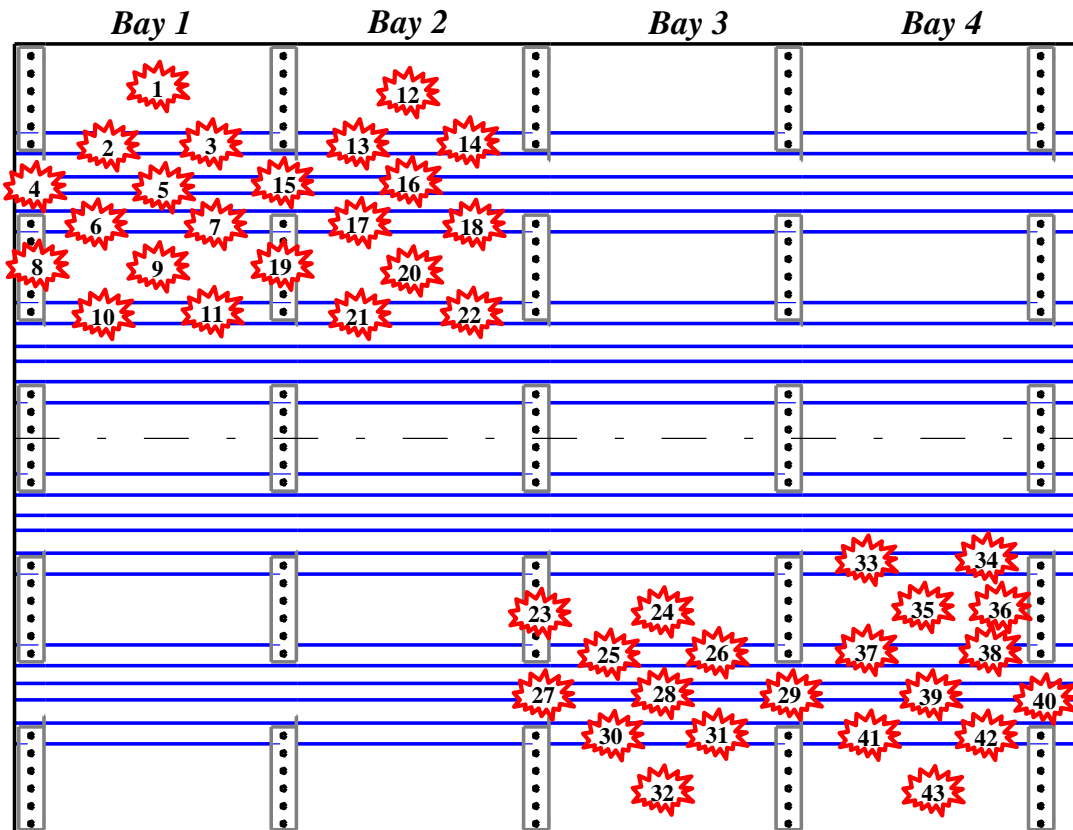
Figure 3-28: Impact Locations for Steel, Spherical Tip Impacts

4   RESULTS AND DISCUSSIONS

For this experimental investigation, 45 ice impacts were performed at 22 different

locations (some multiple impacts at the same location) on two full scale fuselage panels

and 69, 2" diameter spherical tip impacts were performed at 43 different locations on one

of the panels. The quantity of each type of impact on the different structural elements of

the panel is shown in Table 4-1.

Table 4-1: Number and Type of Impacts Conducted on Panels
(Some Multiple Impact at Same Location)

Number of Impacts Performed		
Structure Type	Simulated Hail	Hard Spherical
1 - Center Bay Over Skin	19	16
2a - Edge of Stringer Flange (Not Stringer Side)	6	13
2b - Center of Stringer Flange	9	14
2c - Edge of Stringer Flange (Stringer Side)	0	12
3 - Mid-Stringer	6	11
4 - On Shear Tie	5	3

Panels A and B were separated into quadrants for simulated hail and hard, spherical

impact testing. Simulated hail impact damage was induced in two quadrants of panels A

and B. Drop spear, spherical tip impacts were performed in two quadrants on panel A.

Strain data was collected on the embedded fiber optic during simulated hail impact

testing, but because of heat induced by the halogen lamps used to illuminate the panel

during testing for the high speed cameras, a majority of the data collected was not usable.

However, strain data was successfully collected during hard, drop spear impact testing

using two different bonded fiber optic layouts.

60

The naming convention used to describe each impact is made up of the bay number, skin number, stringer number and impact type. An example using this naming convention is B2-SK2-ST1L-H2c or Bay#-Skin#-Stringer# (Left or Right)-Impact Type (H for hard and I for ice). With the name and the panel schematic shown in Figure 4-1, each unique impact can be identified and located on the panel.
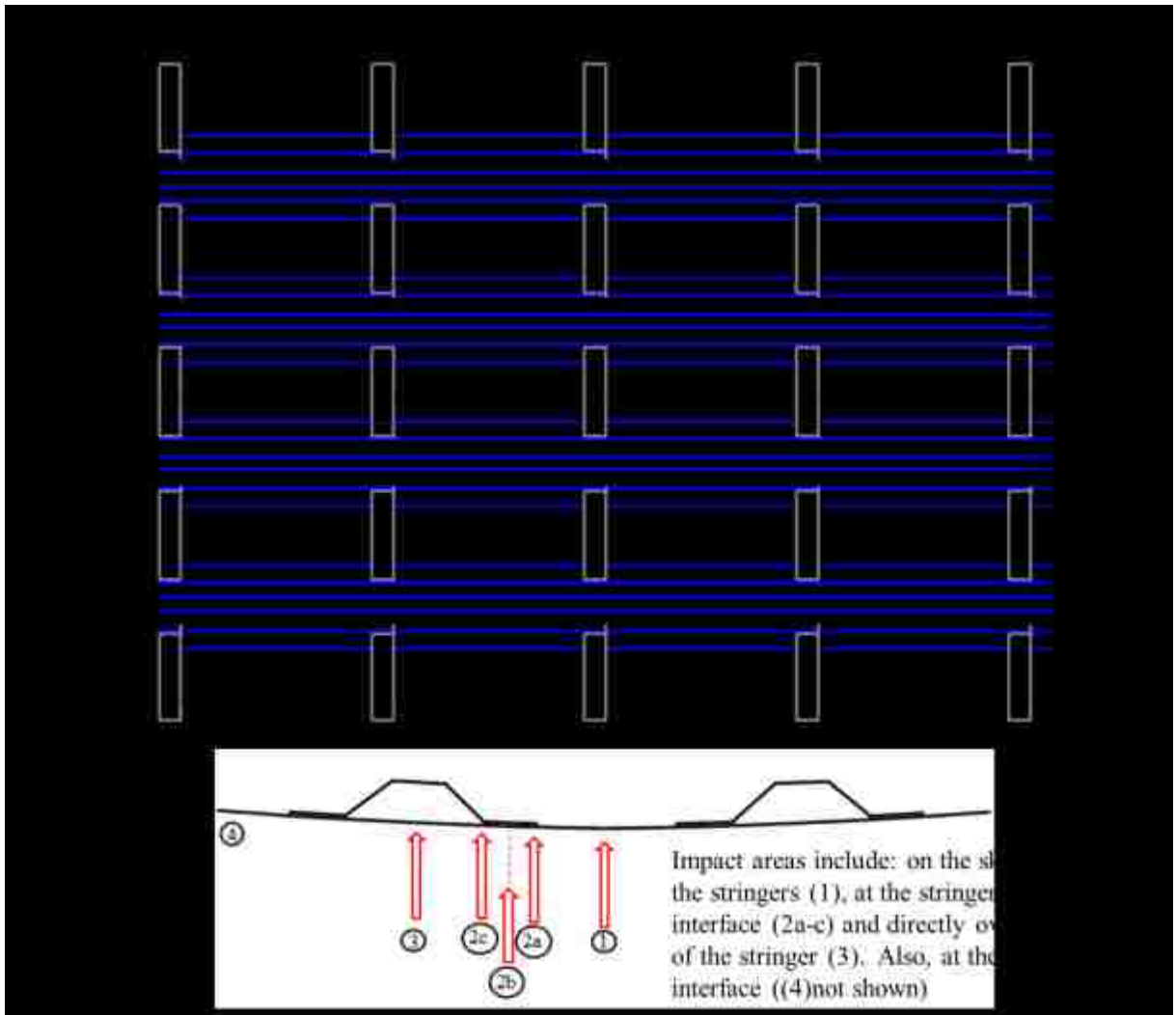
Figure 4-1: Schematic Used to Label and Locate Impact Damage

4.1 ULTRASONIC DAMAGE DETECTION

After each impact test was performed, a hand deployed 5 MHz ultrasonic transducer was used to determine if damage was induced during the impact. If the desired level of damage was not obtained, the panel was impacted again. Notes were taken during these initial hand deployed inspections and were documented and mapped out on the panels. Typical signal changes of interest were loss of back wall signal and a shift in the back wall signal. A less common signal change was a decrease in amplitude (not total loss of signal).

When the full set of impact tests was completed, each panel was inspected using the Boeing MAUS V system in both ultrasonic pitch-catch (5 MHz) and resonance (330 KHz) modes. Figure 4-2 shows the scanning system, mounted via vacuum suction inspecting one of Panel A. The inspections of the panels were split into 10 sections, five across the top of each panel and 5 across the bottom. The 10 scans were then reassembled to make up the inspection of the entire panel.

Figure 4-2: Boeing MAUS V Scanning System Conducting a UT Inspection

The C-scan inspections revealed significantly more information than the hand held pulse-echo inspections performed during impact testing. Flaws that were difficult to size using hand deployed UT were easily sized and mapped using a combination of amplitude and time of flight C-scan images. The difference in damaged mapping is illustrated on the top left side of panel B in Figure 4-3. The black mapped regions of damage were sized using hand held UT and the red mapped regions were mapped using a combination of UT amplitude, TOF and resonance.
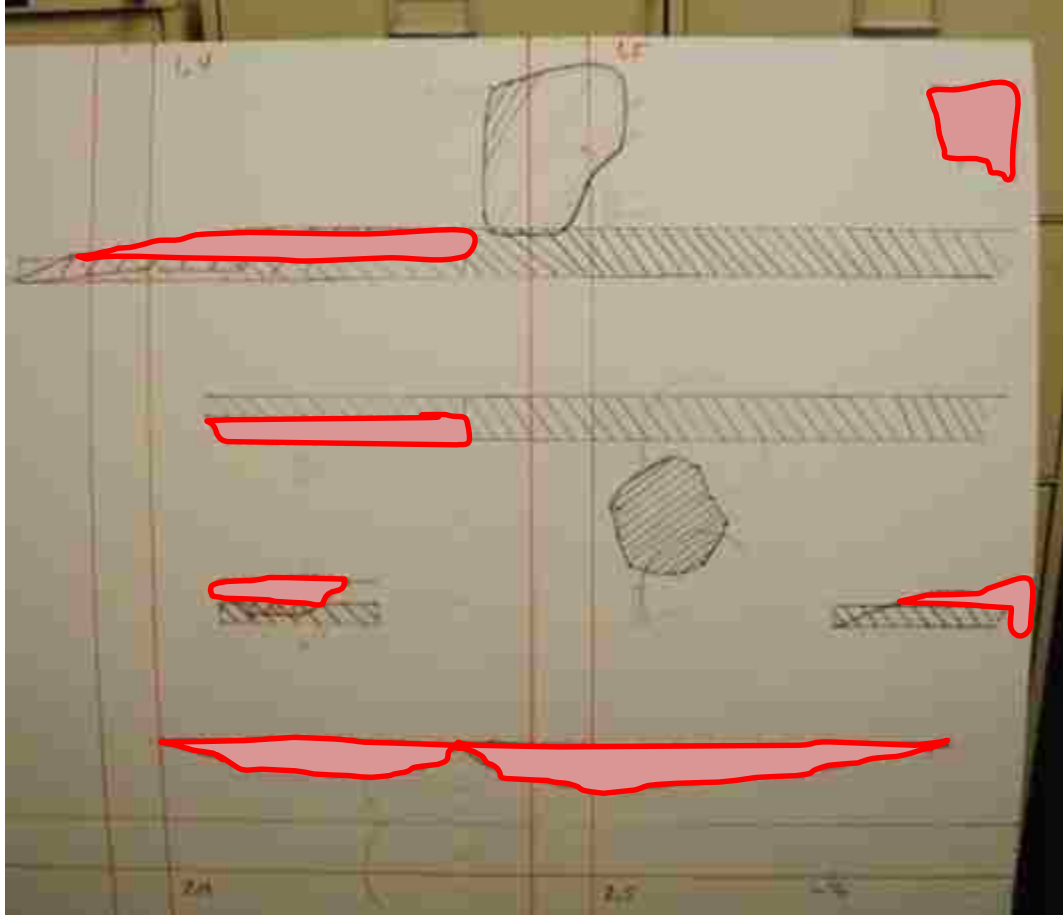
Figure 4-3: Top Right Side of Panel B - Black Mapped Damage Was Detected After Impact With Hand-Held UT and Red Mapped Damage was Additional Damage Detected and Sized Using the MAUS V Scanning System

Interply delaminations in the skin of the panels and stringer flange delaminations were the two most common damage modes observed in the post inspections of simulated hail impacts. The example C-scan shown in Figure 4-4 shows the difference between an interply delamination in the skin, and a stringer delamination which were both induced by a simulated hail impact. It was also noted that the impacts produce damage in regions that were farther from the impact location than anticipated. Some of this distant damage was not detected during initial A-Scan inspections. Also shown in the figure is the clear difference between a bonded and disbonded stringer flange. The scan on the left of the

figure has one fully bonded stringer flange, and one partially disbonded flange. The image on the right has two fully bonded flanges. These two images can be compared to the pristine area shown at the top of the figure.

Pristine Area

Fully bonded
stringer flange

Fully delaminated
stringer flange

Partially delaminated
stringer flange

Interply delamination
in the skin
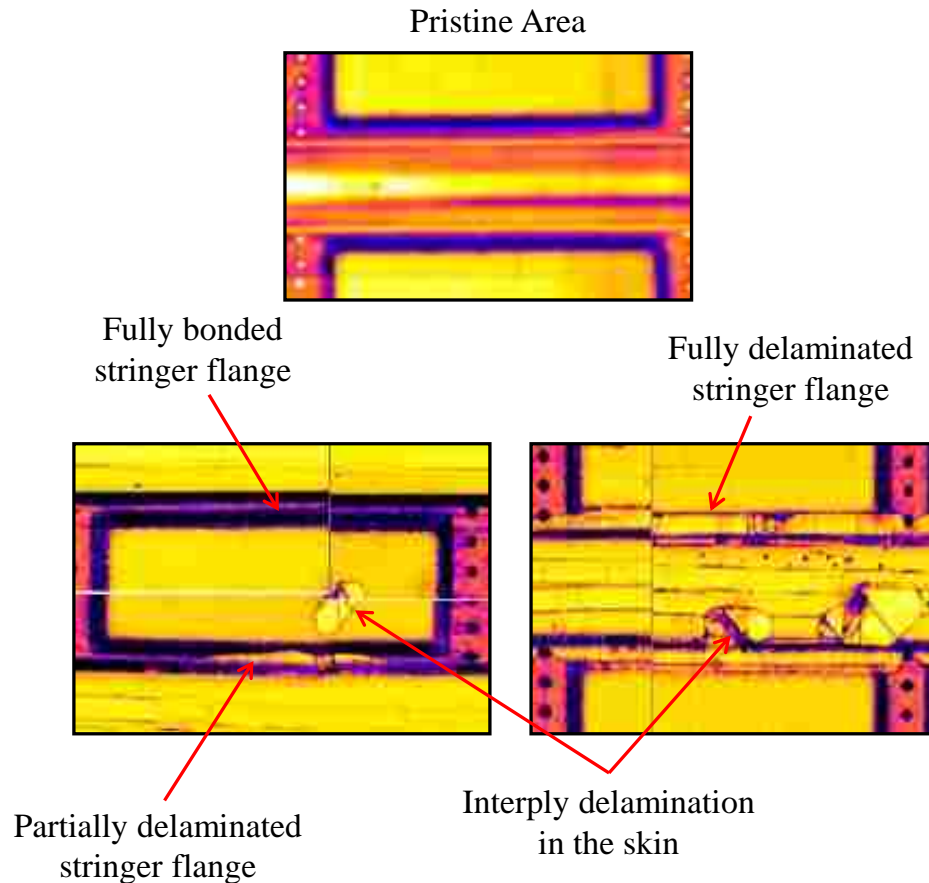
**Figure 4-4: Impact Damage Induced on Panel A Showing the Difference Between
Interply Delamination and Stringer Flange Delamination**

Although it is fairly clear to detect delaminated stringer flanges using the amplitude C-scans, additional, less obvious delaminations could be detected when analyzed side-by-side with time of flight C-scans. An example of a TOF C-scan demonstrating the clear difference between a bonded and delaminated stringer flange is shown in Figure 4-5. The purple areas in the figure are fully bonded flanges. The yellow/orange areas of the flange

are the same depth as the back wall of the skin of the panel, indicating a delamination at the skin-flange interface.

Pristine Area

Disbonded stringer flange

Bonded stringer flange
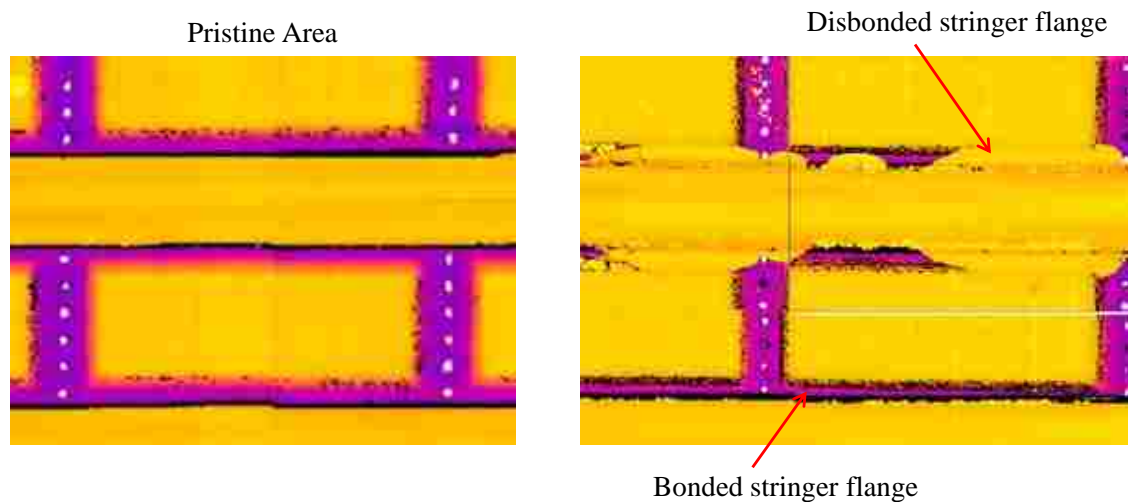
Figure 4-5: Ultrasonic Time of Flight (TOF) C-Scan Showing Delaminated Stringer Flanges

Full panel pulse echo ultrasonic inspections of panel A and B are shown in Figure 4-6 and Figure 4-7. The upper left and lower right sides of the panel inspections in Figure 4-6 show the two areas of panel A that were impacted with the drop weight, spherical tip impactor. The upper right and the lower left quadrants are the two areas that were impacted with simulated hail. Similarly, Figure 4-7 shows the pulse echo ultrasonic full panel inspection results for panel B. The top left and bottom right are pristine, untested areas of the panel and the upper right and lower left were quadrants tested with simulated hail. Much greater inspection detail including exact impact location, energy levels and damage area can be found in Appendix B for ice impact tests and Appendix C for the hard impact tests.
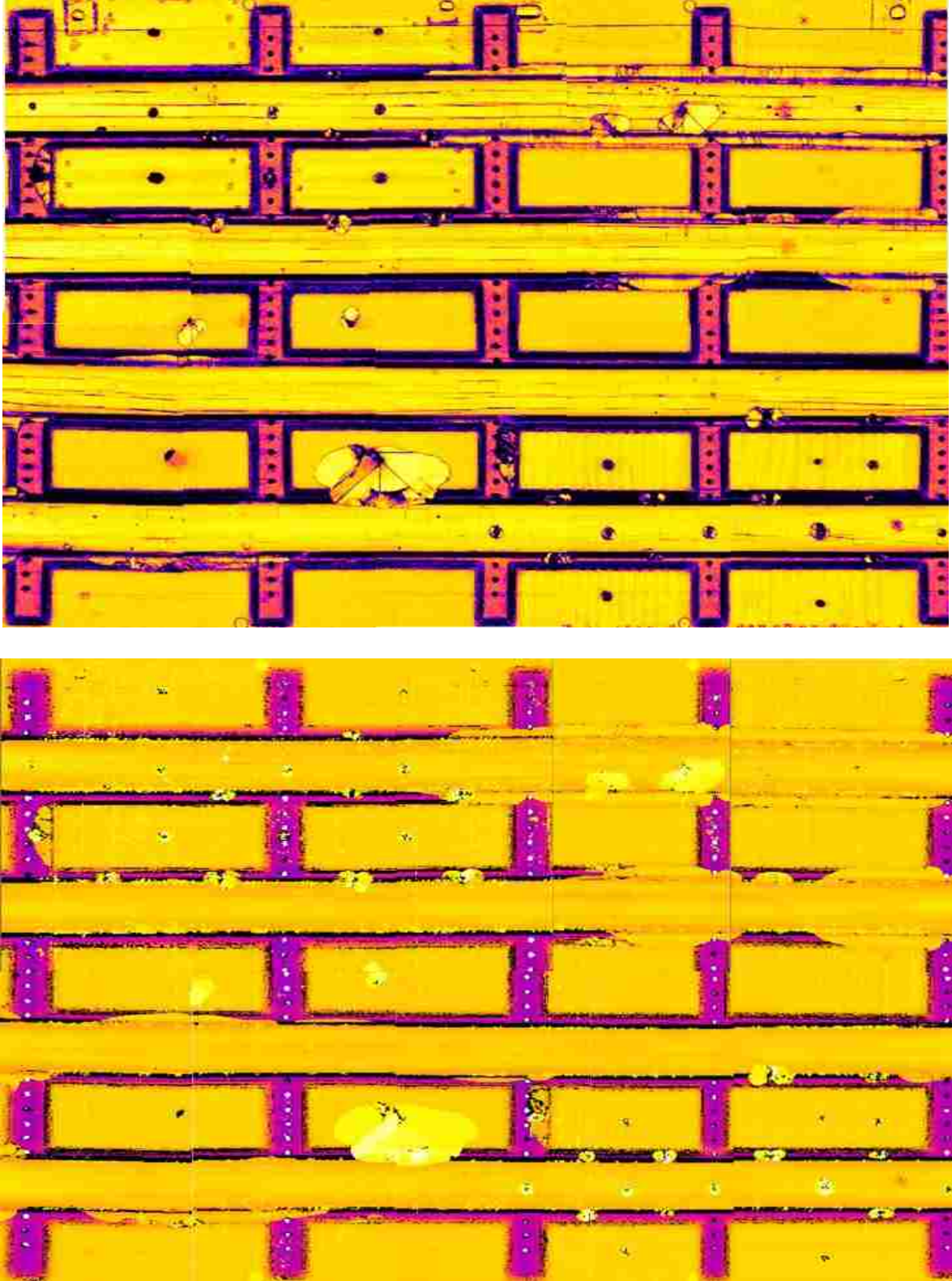
Figure 4-6: Panel A - Ultrasonic Amplitude (top) and Time-of-Flight C-Scans (bottom) C-Scans
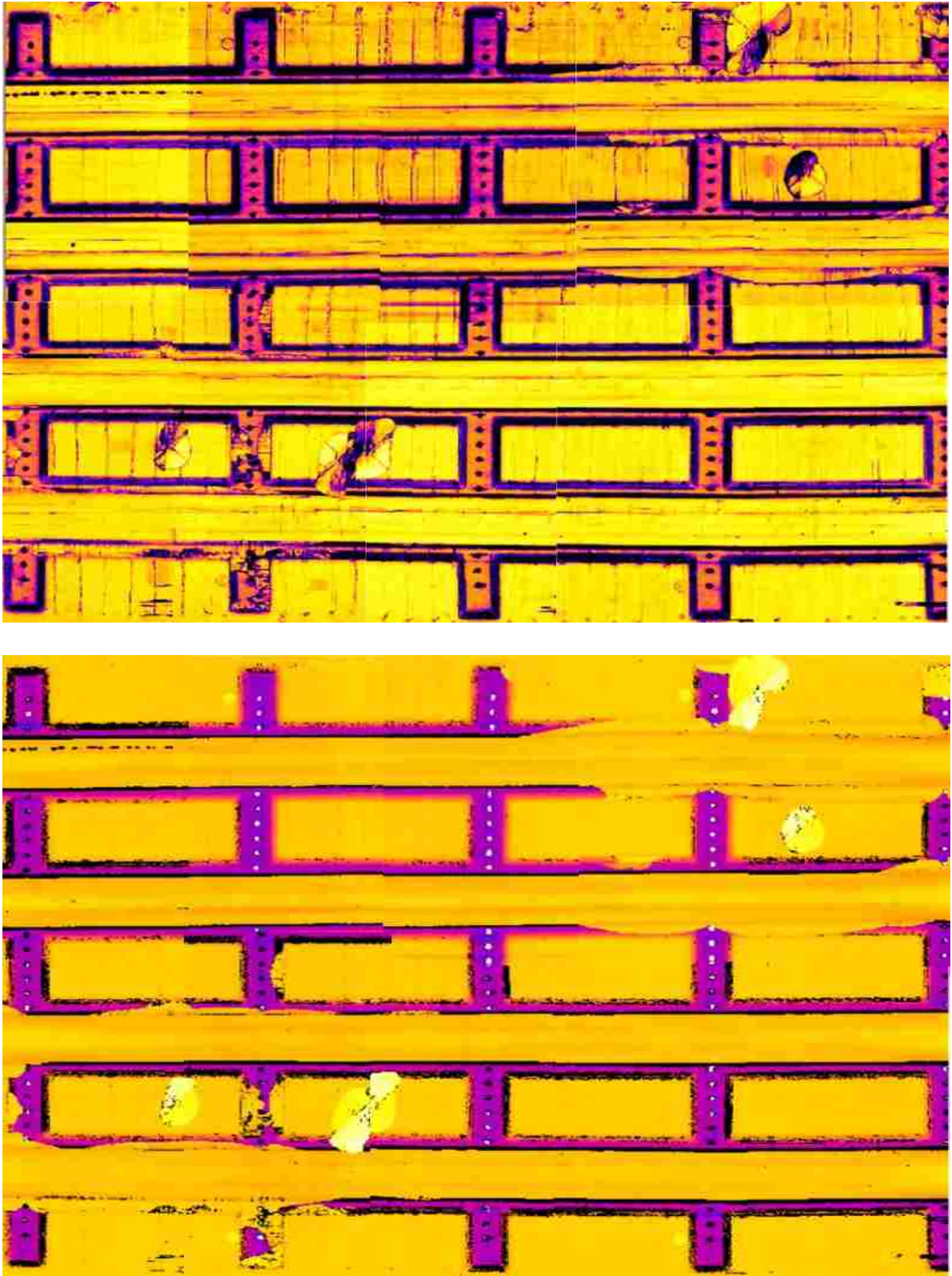
Figure 4-7: Panel B - Ultrasonic Amplitude (top) and Time-of-Flight C-Scans (bottom) C-Scans

4.2 ULTRASONIC RESONANCE DAMAGE DETECTION

Ultrasonic resonance C-scans were composed using the MAUS V scanning system with a 330 KHz resonance probe. In general, the resonance inspection technique detected the same damage as the pulse echo ultrasonic method. Similar to TOF scans, resonance indicated areas where substructure is disbonded from the skin more clearly than PE-UT amplitude. This can be observed in Figure 4-8, where the small stringer flange disbond in the circled area is detected in the TOF and resonance inspections, but not amplitude.
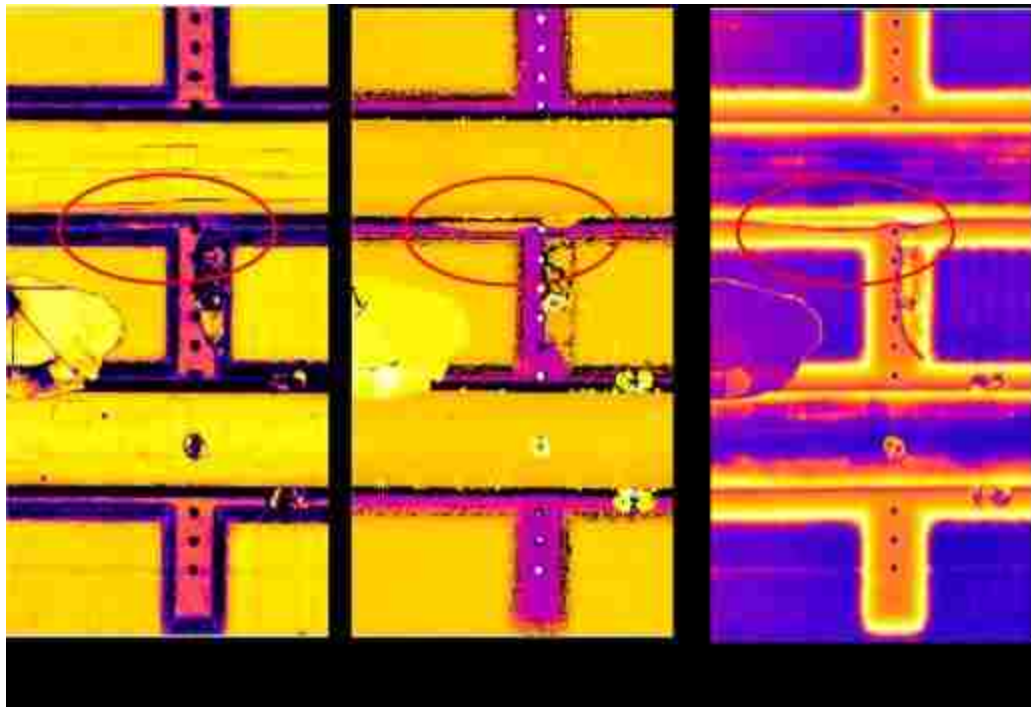
Figure 4-8: Comparison of UT Amplitude, TOF and Resonance

Fully assembled resonance scans of panels A and B are shown in Figure 4-9 and Figure 4-10, respectively. There is a slight difference in the color pallet between panel A and B because of the way the resonance inspection technique is zeroed, or nulled. The probe was nulled on a pristine location on each panel, then the inspection was performed. There was a slight difference in the initial null settings between the two panels creating the difference in pallet.

69

The clear difference between bonded and disbonded stringer flanges can be seen by comparing the upper right and upper left sides of panel B. The upper left side of the panel was not impact tested and all of the substructure elements are still bonded. By comparison, disbonded stringer flanges can easily be detected on the upper right and lower left sides of the resonance scans in Figure 4-10, as well as interply delaminations in the skin.
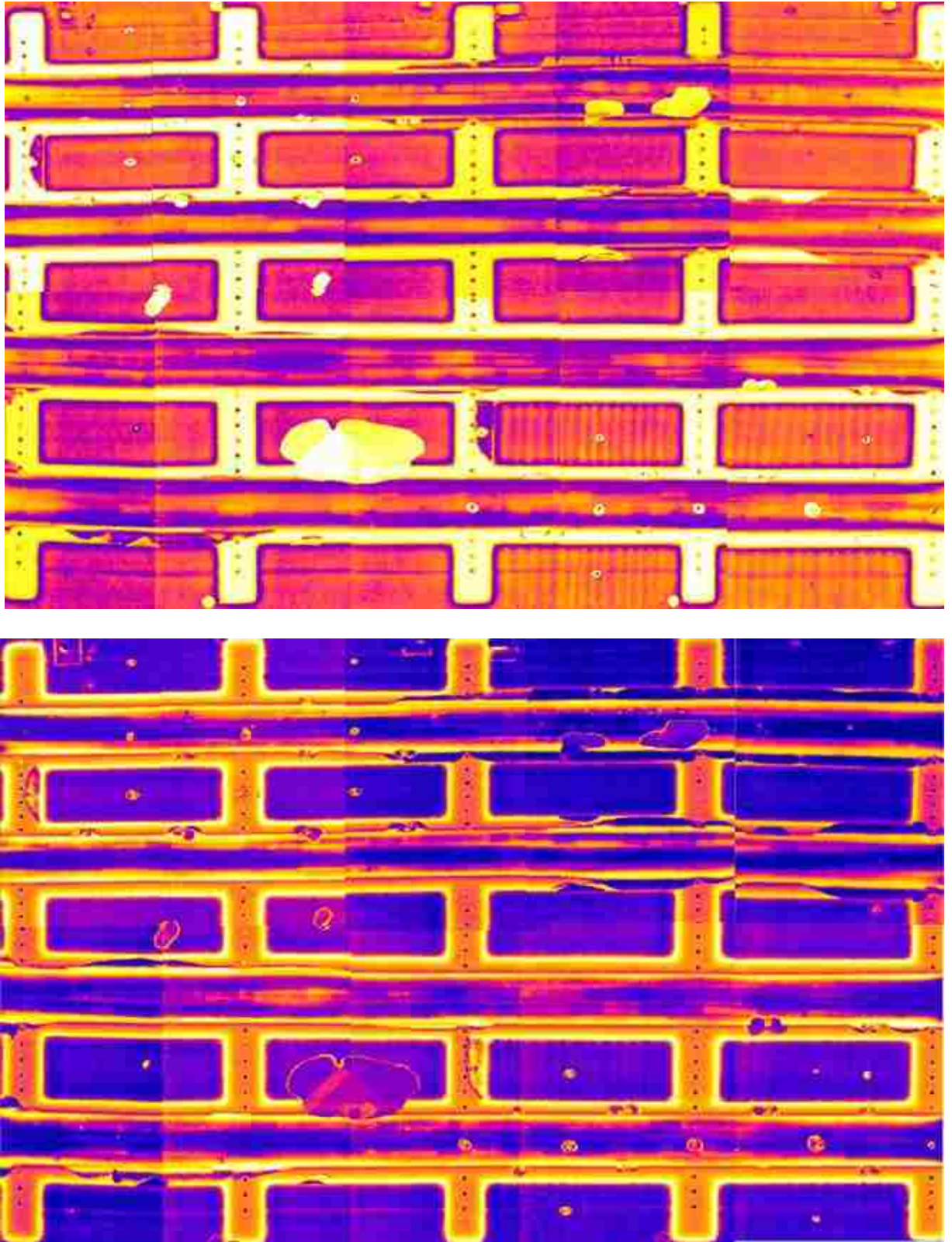
Figure 4-9: Panel A - Resonance Amplitude X plot (top) and Phase Y plot (bottom) C-Scans
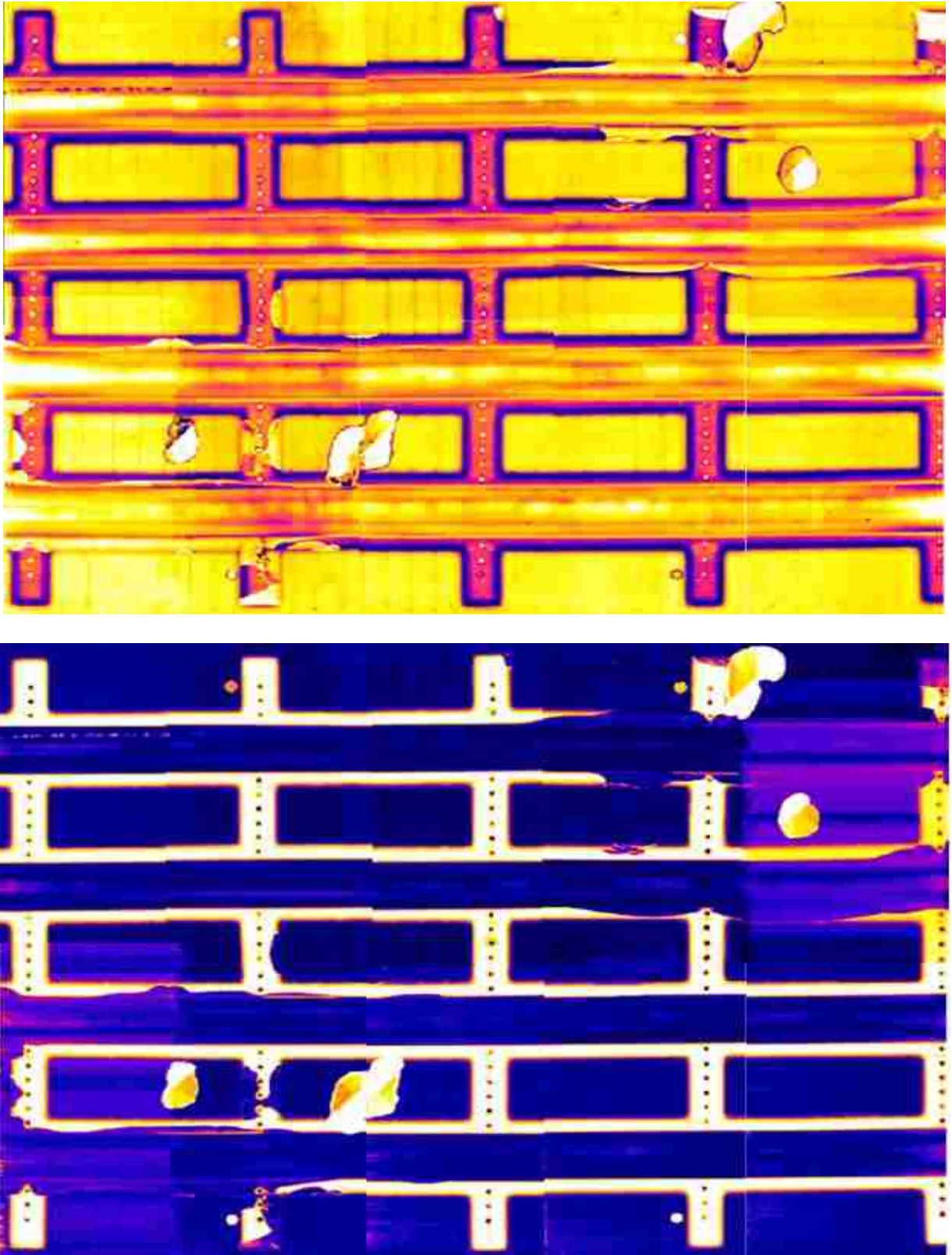
Figure 4-10: Panel B - Resonance Amplitude X plot (top) and Phase Y plot (bottom) C-scans

The information gathered from the scans was assembled and analyzed at each impact location.   The ice impact damage created from a 721 Joule, mid-bay skin impact is shown in Figure 4-11. The information shown in the figure is an example of the data assembled for each test location and is provided for each impact location in the appendices. The damage shown in Figure 4-11is an example of a large interply skin delamination. The first part of information that is provided in the top of the figure is a schematic depicting what type of structure was impacted. Two up-close C-scans of the damage are shown in the middle of the figure (ultrasonic amplitude and resonance). The green dashed line in the close-up amplitude scan indicates where on the backside of the panel there was a visual indication of damage. In this case it was a 2 in crack in the stringer flange. The bottom two C-scans are the quadrant where the damage is located. The green dashed box in the quadrant scan show where the close-up was taken. The damage induced during this impact also provides a good example a small stringer flange disbond that was difficult to detect in the amplitude C-scan, but is easily visible in the resonance scan.
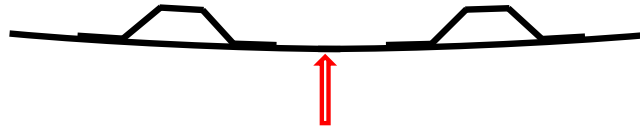
Skin Impact
Max Impact Energy: 977.7 ft lbs, 721.1 Joules
Max Impact Velocity: 382.9 ft/s, 116.7 m/s
Visual Indication: No front side visible indication, small 2" stringer flange crack detectable on backside
Damage Area: Interply Delamination 54.97 in^2, Stringer Disbond 1.70 in^2
Type of Damage: Mostly interply delamination, small stringer disbond to the upper right of the impact area not detected in amplitude scan

Stringer Delamination

Interply Delamination

UT Resonance Y-Plot

UT Amplitude C-Scan

UT Time of Flight C-Scan
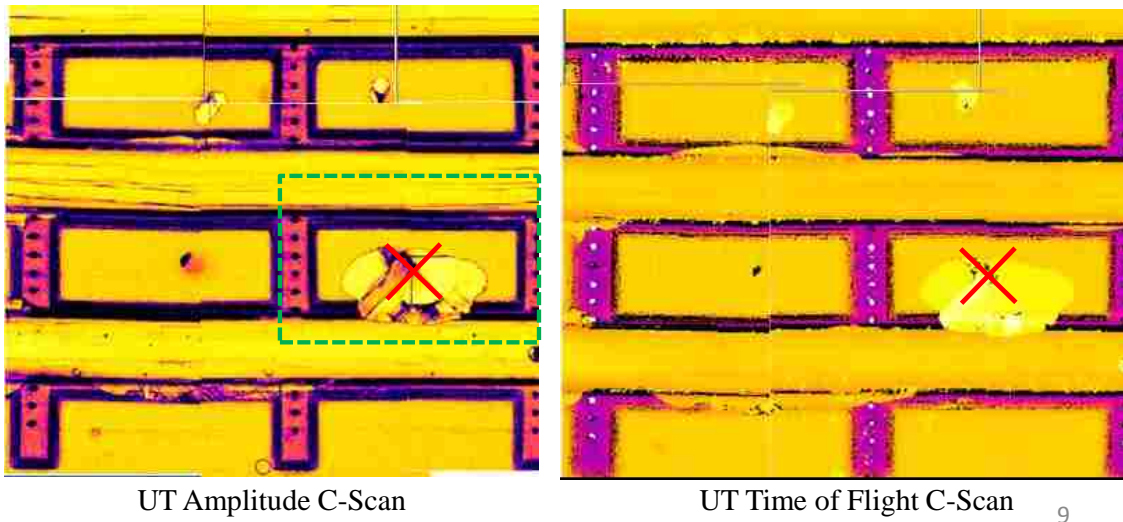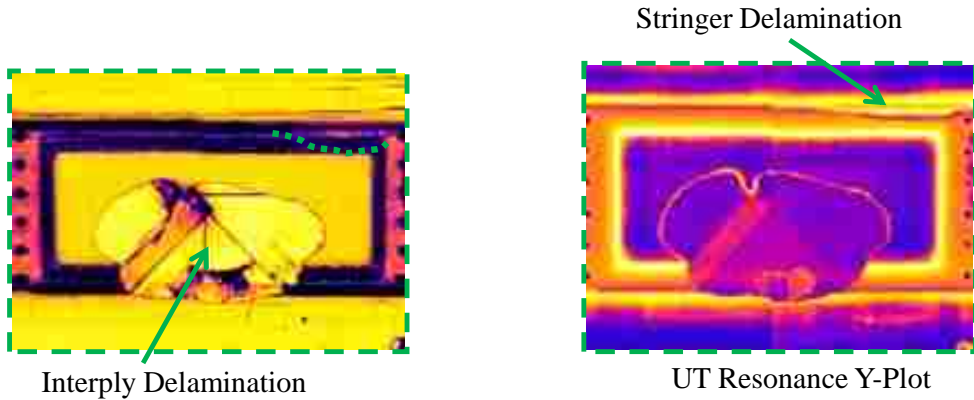
✗ Impact Location

Quadrant 3

Figure 4-11: Damage Created by Ice Impact at Location 5A (Mid-Bay Skin Impact) on Panel A

An example of a damage induced by an ice impact at the edge of stringer flange is shown in Figure 4-12. It can be seen in the quadrant view C-scan at the bottom of the figure that the impact was directed mid-way between two shear ties at the edge of a stringer flange. The impact energy of the ice ball was 278.9 Joules and caused the stringer flange to fully disbond. The two shear tie built-up pad sections helped to resist the flange disbonding from continuing farther. Additionally, there was a visible crack at the flange-skin interface along the length of the stringer. This is indicated in the center UT amplitude scan with a green dashed line on the stringer.
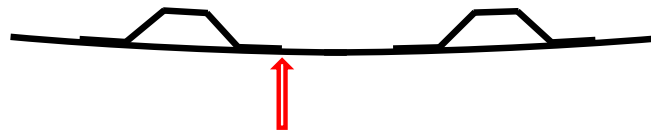
Edge of Stringer Flange (Not Stringer Side)
Max Impact Energy: 378.1 ft lbs, 278.9 Joules
Max Impact Velocity: 235.6 ft/s, 71.8 m/s
Visual Indication: No front side surface visual indication, 17.5" stringer flange crack visible
Damage Area: Interply Delamination 0.0 in^2, Substructure Disbond 23.16 in^2
Type of Damage: Full stringer disbond, no interply delamination detected
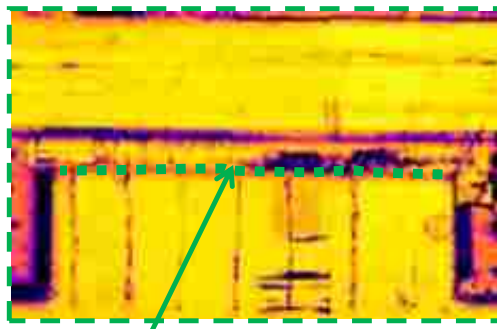
Full Stringer Disbond

UT Resonance X-Plot
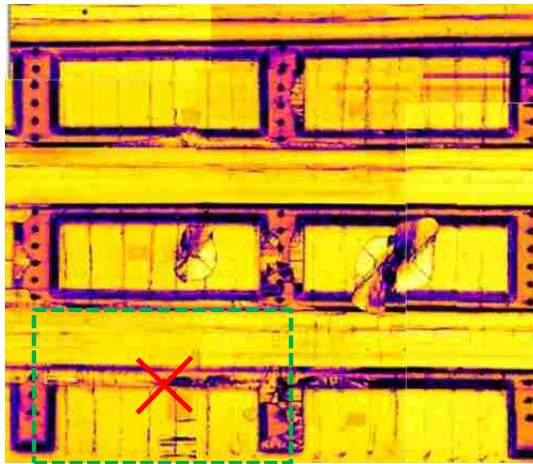
UT Amplitude C-Scan
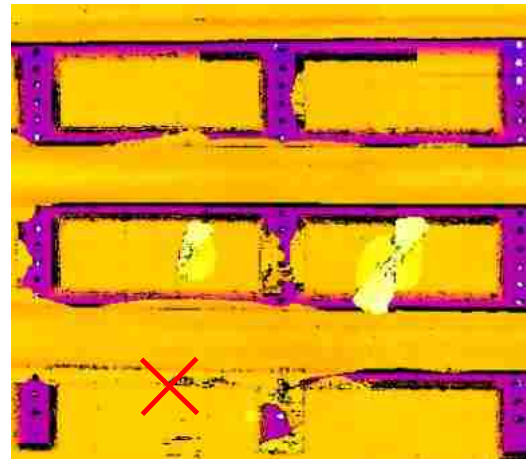
UT Time of Flight C-Scan

⊠ Impact Location

Quadrant 3

Figure 4-12: Damage Created by Ice Impact at Location 7B (Edge of Stringer Flange) on Panel B

4.3 DAMAGE CHARACTERIZATION

Damage characterization was accomplished through detailed visual inspection on both sides of the panels and through nondestructive inspection methods including ultrasonic amplitude analysis, time of flight (TOF) and resonance. A database was assembled containing pertinent impact information at each impact location and is presented in Appendices B and C. The database contains information on each impact damage including location of impact, maximum impact energy, maximum impact velocity, visual indications of impact damage, damage area, interpretation of type of damage, and C-scan images of the damage.

Damage was assessed by interpreting information gathered through the nondestructive inspection techniques on a structural level, not a materials failure level. Example A-scans showing how the return signals change depending on the type and depth of damage are shown in Figure 4-13. A clear back wall signal over the skin laminate is shown in A, an A-scan over a skin interply delamination is shown in B, a co-cured stringer flange disbond is shown in C, an interply delamination in the flange of the stringer is shown in D, and a near surface skin damage is shown in E. A complete loss of back wall signal with no appearance of an intermediate signal was interpreted as near surface fiber fracture or matrix crushing and was typically observed in hard impacts.
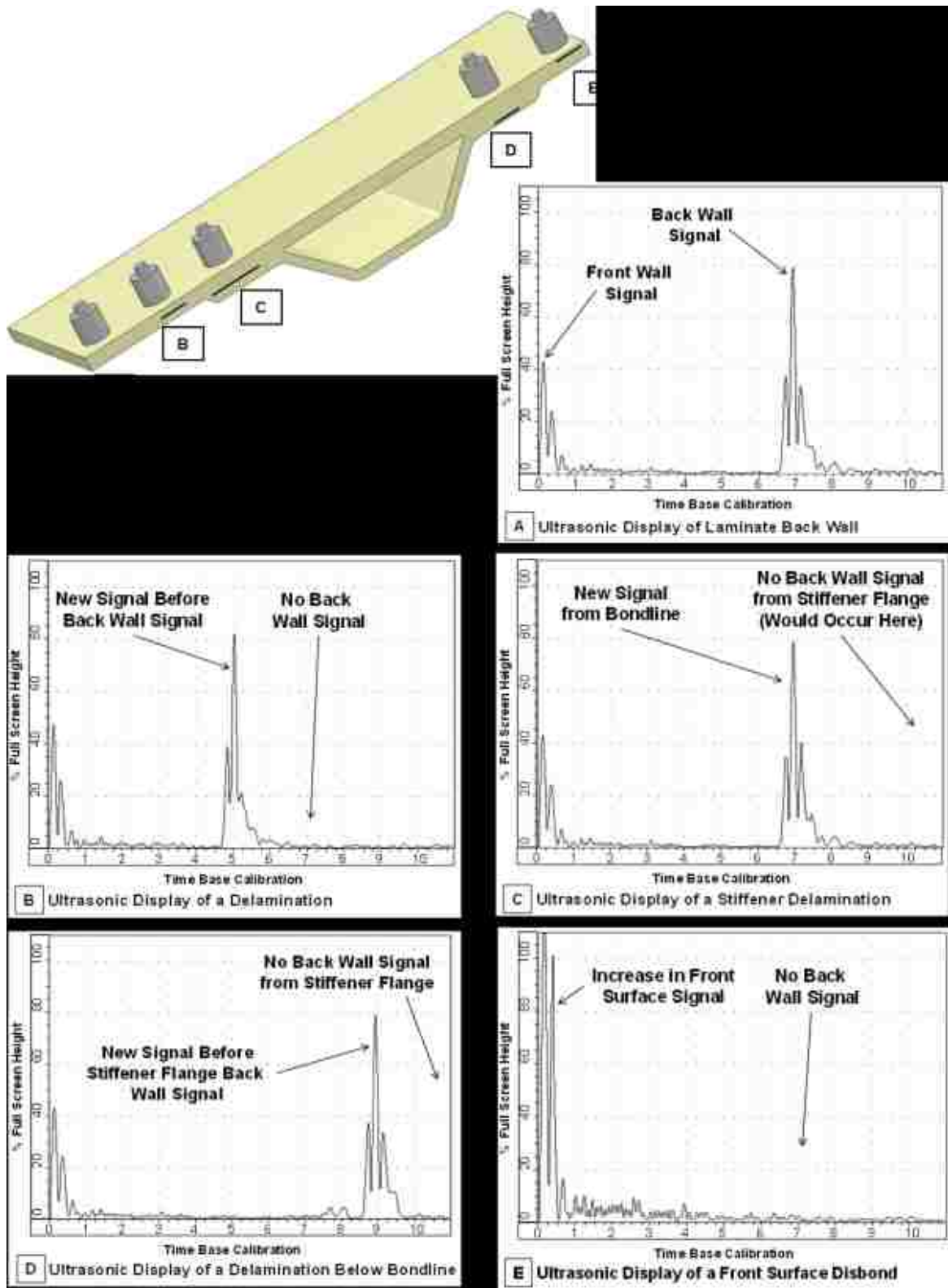
Figure 4-13: Example A-Scan Signals Over Different Structural Elements and Damage

78

4.3.1 DAMAGE AREA DETERMINATION

The area of damage induced by simulated hail impact damage was determined using time of flight C-scan images generate during pulse-echo UT inspections. The TOF C-scans were imported into SolidWorks and scaled to the physical dimensions of the panel. The damage was traced and the area was calculated using a Solid Works surface area calculation feature. The traced areas used to calculate the damage area on panel B are shown in Figure 4-14.
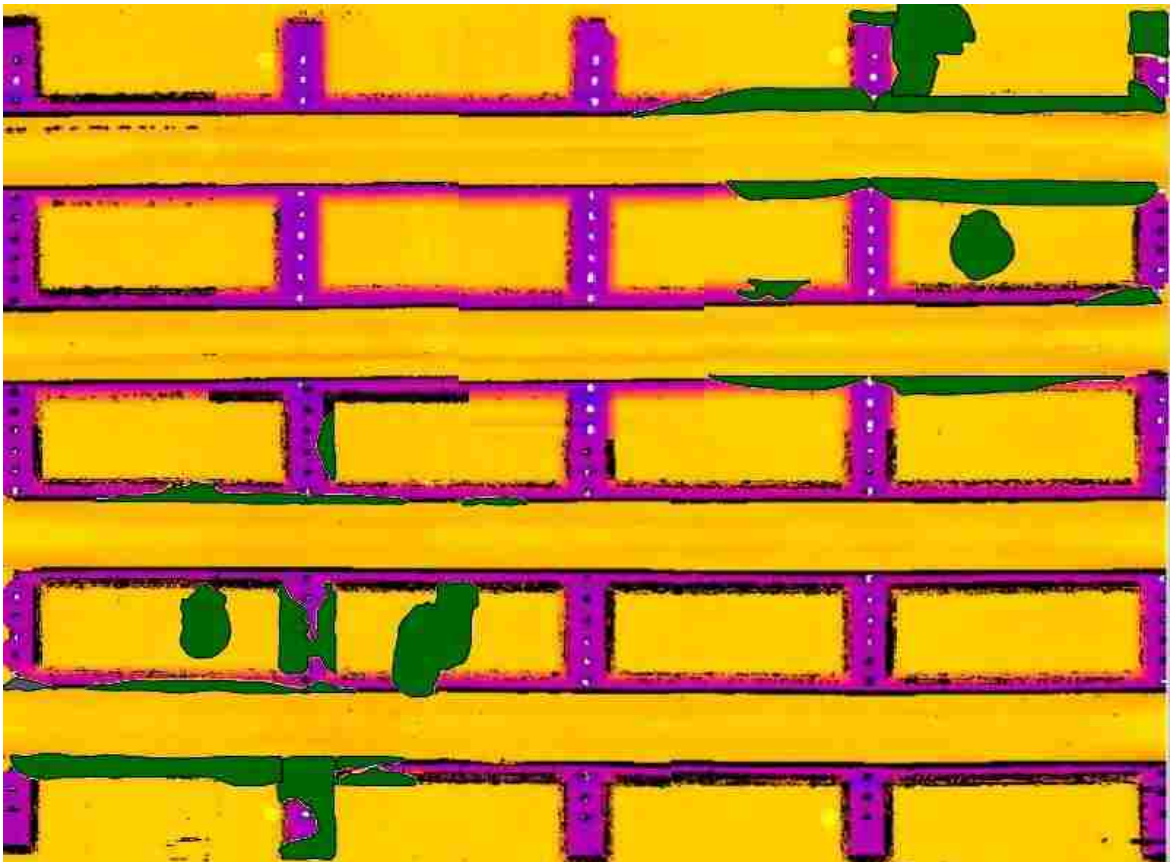
Figure 4-14: Green Tracings Used to Determine Damage Area on Panel B

4.3.2 DAMAGE ASSOCIATED WITH HAIL IMPACT

There were three main types of damage associated with the hail impact damage imparted on the panels. Depending on the location of the impact, the corresponding damage could be interply delamination in the 16 ply skin, disbonding at the skin-to-stringer flange interface (substructure delamination), delamination between the plies of the built-up shear tie pad and shear tie cracking. Interply skin and substructure delamination were detectable with the surface based NDI techniques used, but shear tie cracking was only detectable visually from the backside of the panels. An example of a visually detectable disbonded stringer flange is shown in Figure 4-15, and an example of a cracked shear tie is shown in Figure 4-16. The fractures in the shear ties were observed to occur in the vertical flange at the radius. Thus, UT inspections from the skin side could not detect this damage.

Figure 4-15: Stringer Flange Delamination Detectable from Backside of Panel A

Figure 4-16: Crack on Shear Tie Bend Radius Not Detectable Using NDI from Front Side of Panel

4.3.2.1 MID-BAY IMPACTS (TYPE I1)

Damage created by mid-bay hail skin impacts included both substructure and interply skin delaminations. Figure 4-17 plots the hail impact energy verses the resulting damage size. The calculated damage area associated with each impact can be found in the tables in Appendix A, while the information for each impact and the corresponding inspection images are contained in Appendix B. It can be observed as a general trend that the interply delamination created by mid-bay skin impacts increases with impact energy, but not linearly (black diamonds), and is not a very strong trend. Sometimes mid-bay skin impacts caused stringer flange delamination, but not all the time.

It was observed at impact locations that were impacted multiple times starting with low energy levels, that damage onset is somewhat of a binary, bifurcation point. It either

81

happens or it doesn't. However, there may be some very subtle changes in the local make-up (e.g. micro changes in the resin matrix or a reorder in the distribution of residual strains). Thus, when the failure threshold energy is reached after multiple impacts at the same location, the resulting damage could be slightly different than if it had only been impacted once at the highest energy level.
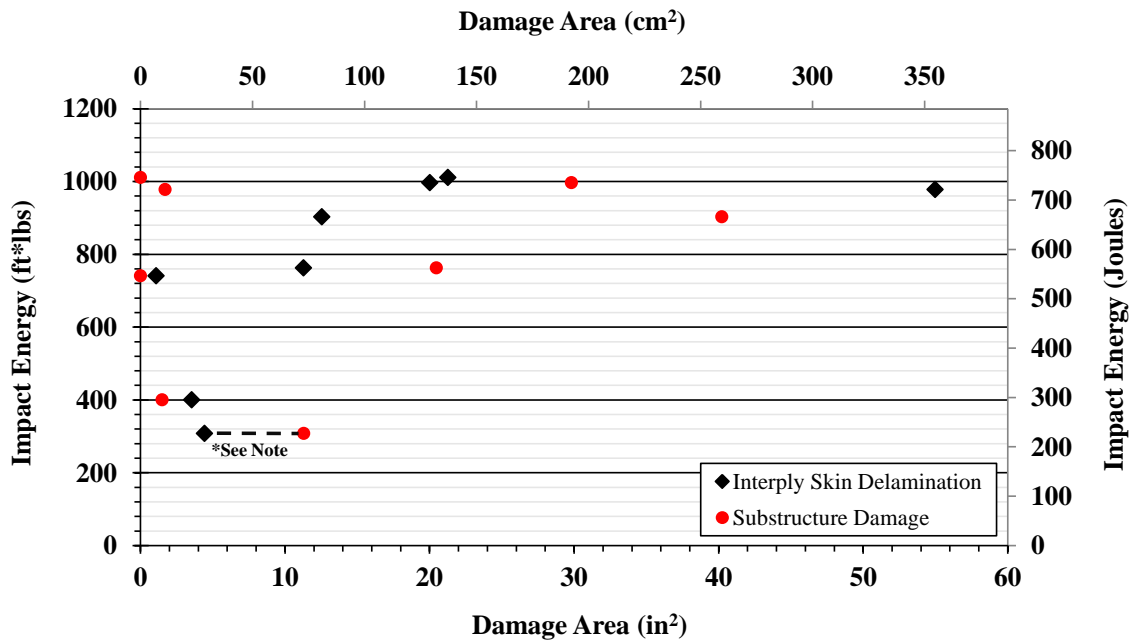
*Interply delamination and substructure damage on same horizontal line were produced by the same impact

Figure 4-17: Substructure and Skin Delamination Damage Area Created by Simulated Hail, Mid-Day Skin Impacts (Type I1)

The total damage area, or combination of substructure and interply delamination is charted in Figure 4-18. The black bar in the chart indicates the damage contributed by interply delamination in the skin and the red bar shows the damage contribution from substructure delamination. It can be observed in the chart that it is difficult to determine when substructure disbonding will occur. There is not a set energy threshold that when increased from this threshold substructure delamination will occur.

82
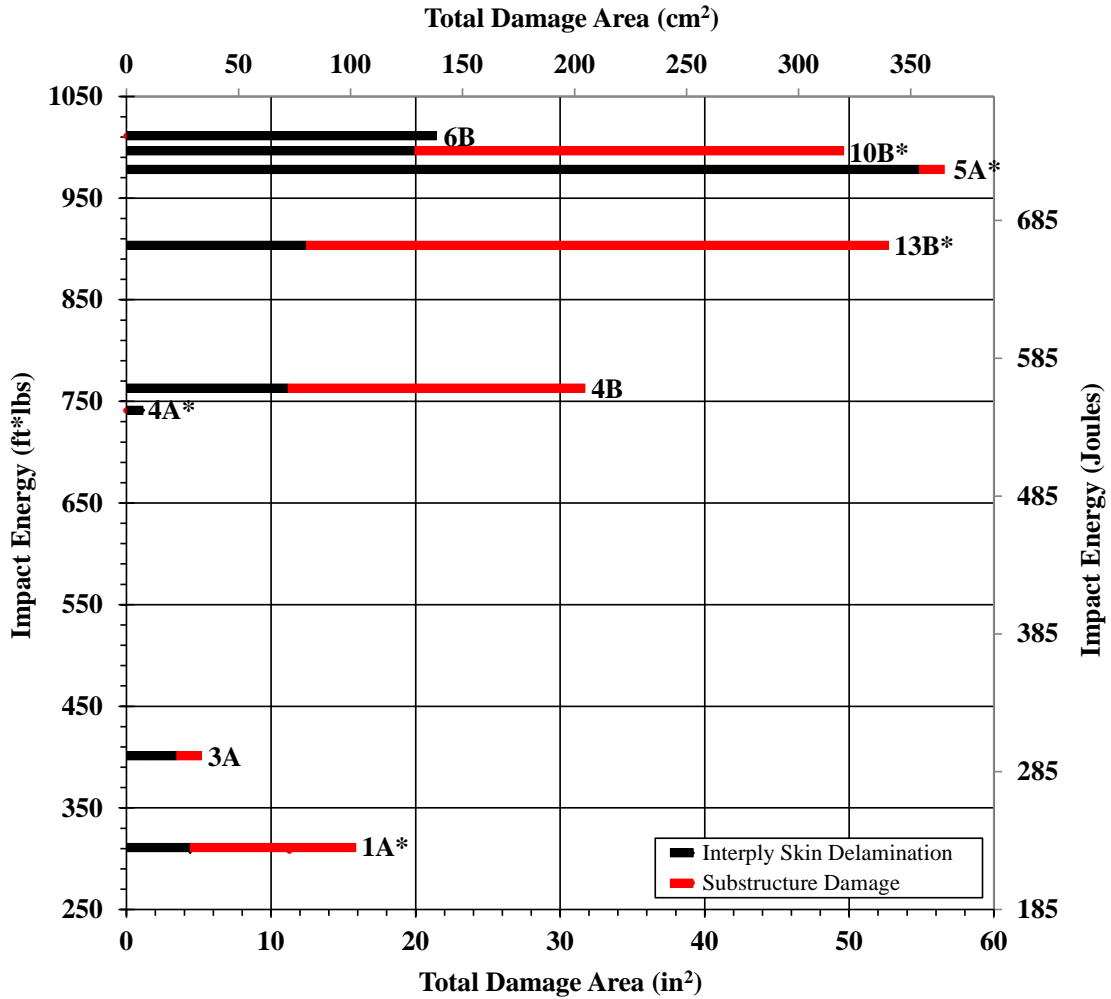
Figure 4-18: Total Damage Area Created by Simulated Hail, Mid-Day Skin Impacts (Type I1)

To illustrate the damage produced from mid-bay skin impacts, inspection results along with associated damage area and the associated impact energy levels are shown in Figure 4-19. The minimum energy level to achieve damage was (1A) 227.1 Joules.

83

1A 227.1 Joules
(4.43) / (11.29)

3A 295.1 Joules
(3.55) / (1.50)

4A 546.1 Joules
(1.09) / (0.0)

4B 562.3 Joules
(11.28) / (20.48)

13B 666.0 Joules
(12.55) / (40.23)

5A 721.1 Joules
(54.97) / (1.70)

10B 735.1 Joules
(20.01) / (29.82)

6B 745.6 Joules
(21.27) / (0.0)

Increasing Impact Energy

(Interply Delamination Area in²) / (Substructure Damage Area in²)
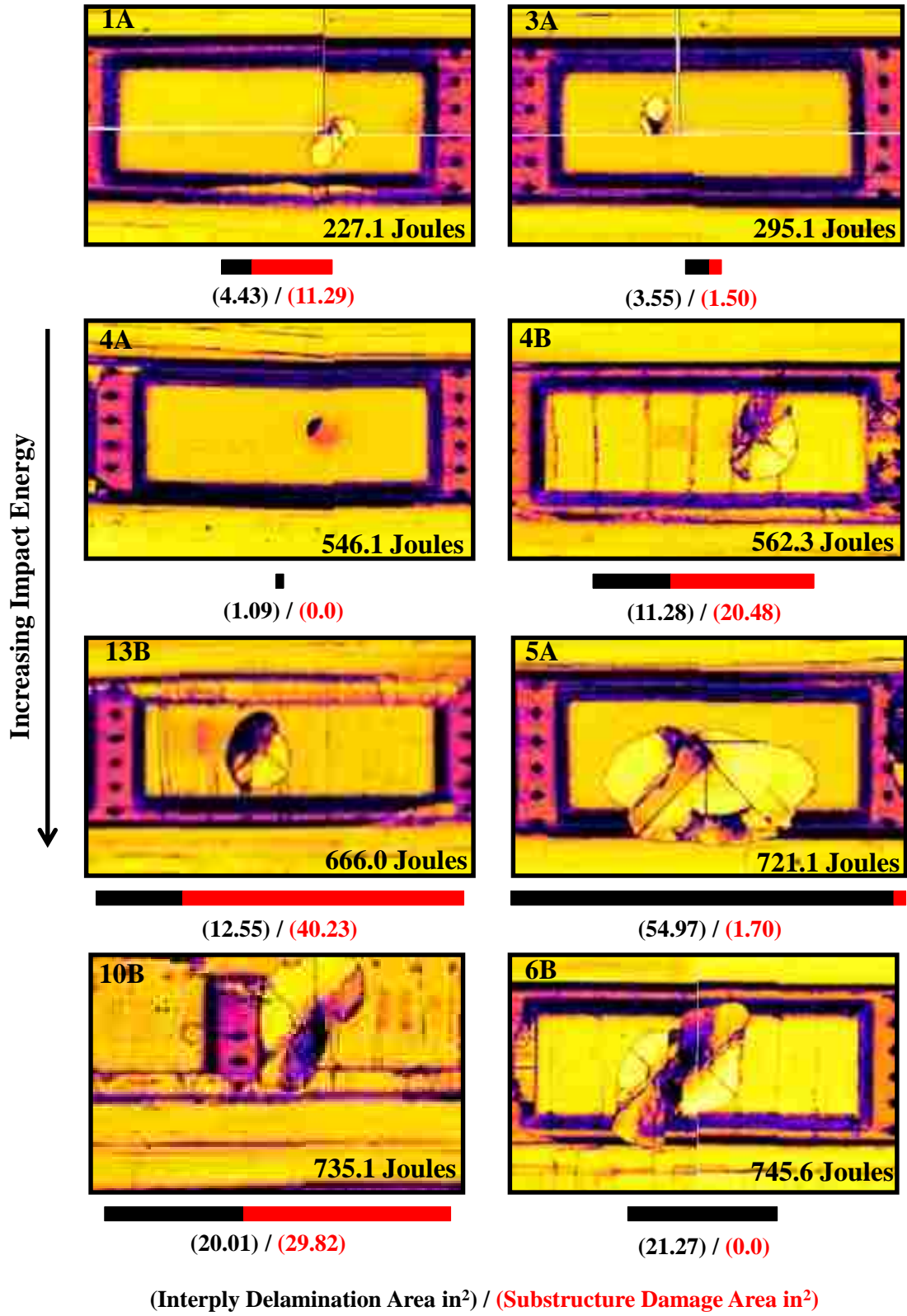
Figure 4-19: Amplitude C-Scan Results for Simulated Hail Mid-Bay Impacts (Type I1)

84

4.3.2.2 STRINGER FLANGE IMPACTS (TYPE I2)

This study investigated impact on both stiffened and unstiffened fuselage structural elements. Impacts conducted at locations over stringer flanges initiated damage at lower levels than impacts over unsupported skin impacts. Figure 4-20 plots the damage area in both substructure and skin elements induced by simulated hail impact over the stringer flange. The plot consists of both 2a and 2b type impacts and was combined for both panels. It was noted that none of the stringer flange impacts caused any type of interply delamination in the 16 ply skin. All of the damage area caused by these impacts was substructure disbonding and typically increased with impact energy. This most likely occurred because of the high peeling stresses that are generated at the edges of the flange when the skin of the panel bends during the impact event. The energy induced into the panel is absorbed through flange delamination and therefore does not lead to interply skin delamination. The total area damage plot for these impacts is not provided because it is the same as the substructure delamination area plot (red dots).
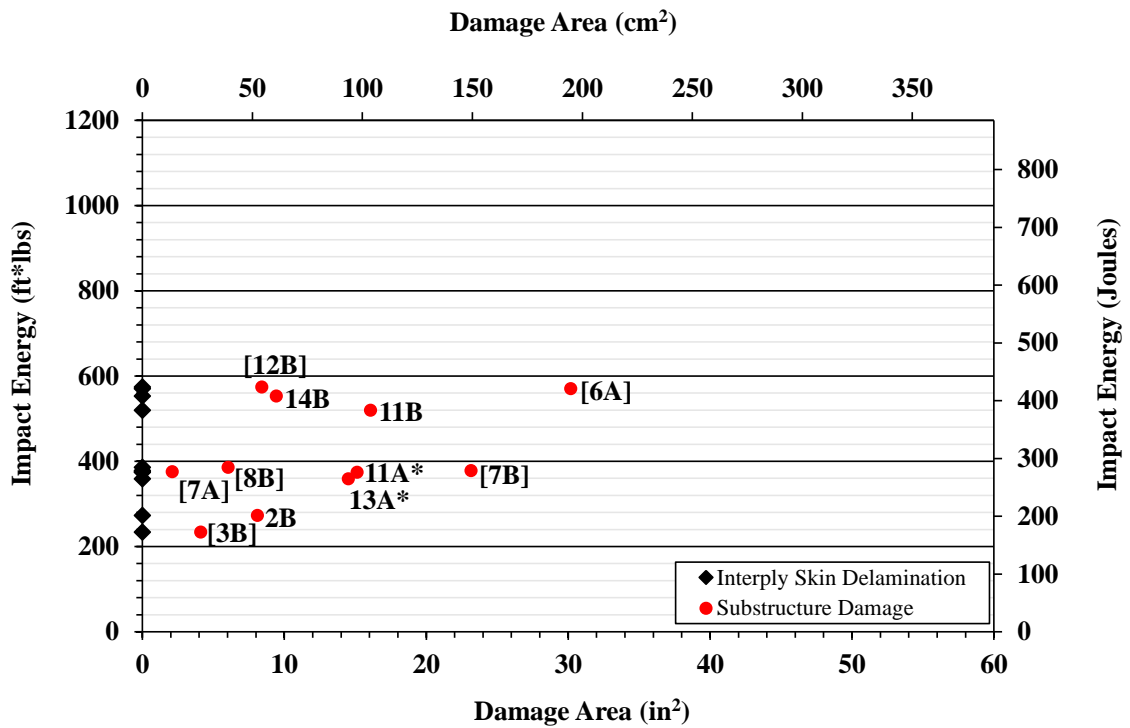
Damage Area (cm²)

Figure 4-20: Substructure and Skin Delamination Damage Area Created by Simulated Hail, Stringer Flange Impacts

Damage associated with edge of flange impacts (type 2a) is shown in the TOF images in Figure 4-21. TOF C-scans were selected to present this data because they were more sensitive to small delaminations in the stringer flanges than amplitude C-scans. Some of the damage in the TOF C-scans were initiated by other impacts that occurred in close proximity to the impact of interest and was not added in the area calculation for that particular impact. It can be seen at low impact energy levels, a small amount of damage occurs which does not span the width of the tapered flange. The minimum energy level to initiate damage was 172.2 Joules (impact 3B) in Figure 4-21. There was a very small difference in impact energy between impact 7A and 7B, but a significant difference in

86

substructure delamination area. This could potentially be due to the proximity of 7B to the edge of the panel, but this was not observed in other edge bay impacts.

(Interply Delamination Area in^2) / (Substructure Damage Area in^2)
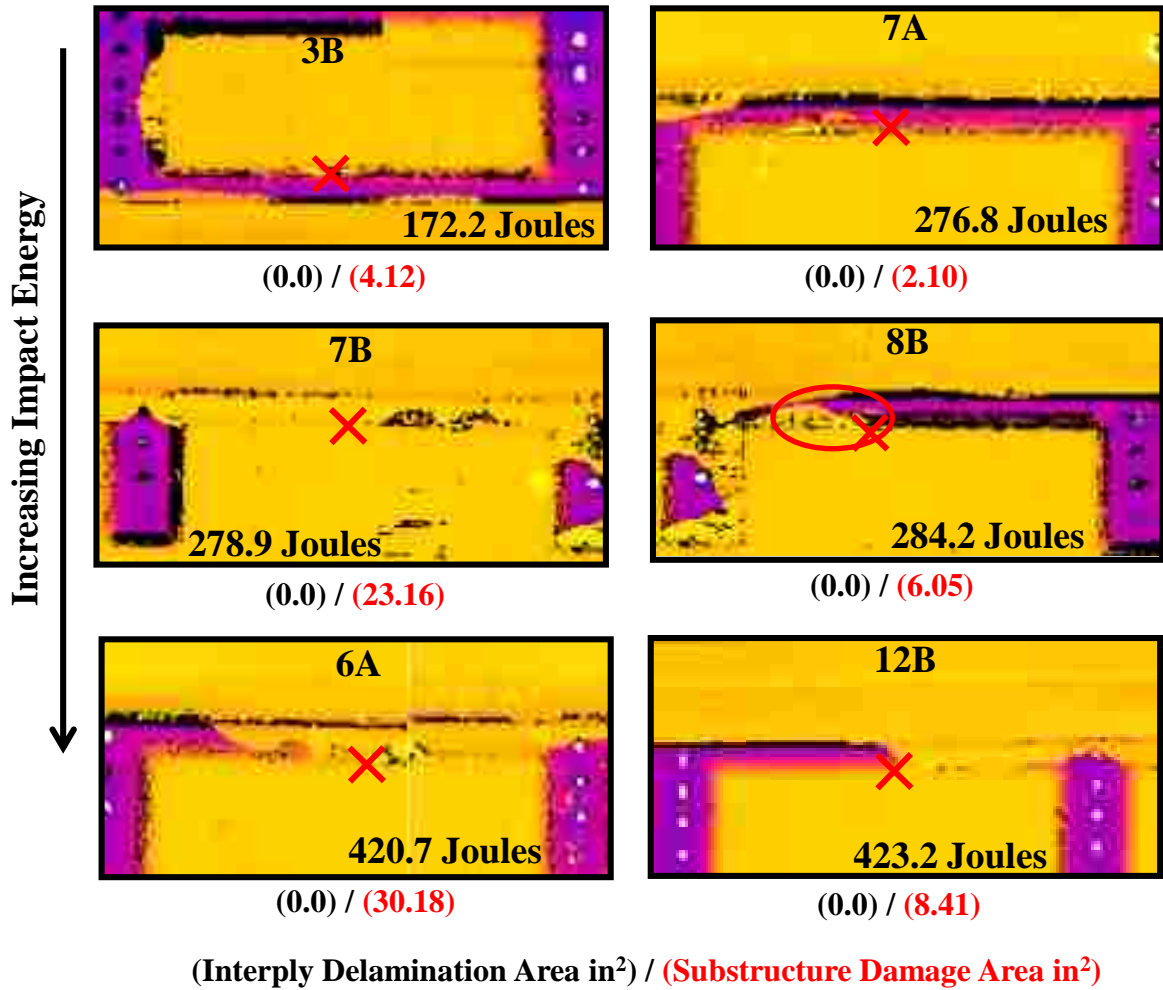
Figure 4-21: Ultrasonic TOF C-Scans of Stringer Flange Edge Impact Damage Produced by Impact at X (Type I2a)

Damage associated with center of flange impacts (type 2b) are shown in the TOF images in Figure 4-22. Interestingly, impact 14B was the highest energy impact of this type and showed fairly little delamination at the impact site, but did cause delamination of the adjacent stringer flange.

Increasing Impact Energy

2B — 201.0 Joules — (0.0) / (8.12)	**13A** — 264.6 Joules — (0.0) / (14.52)
11A — 275.8 Joules — (0.0) / (15.14)	**11B** — 383.2 Joules — (0.0) / (16.09)
14B — 407.8 Joules — (0.0) / (9.45)	

(Interply Delamination Area in^2) / (Substructure Damage Area in^2)
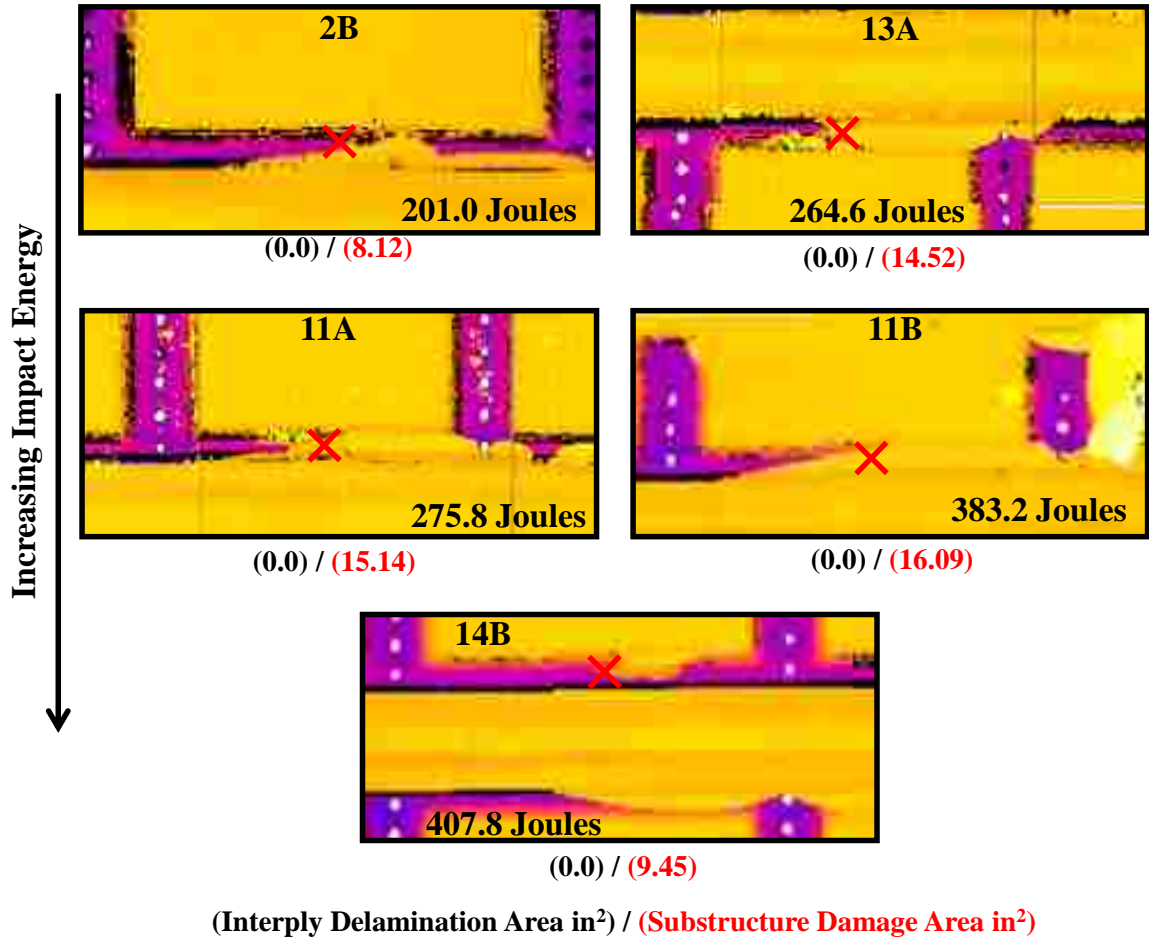
Figure 4-22: Ultrasonic TOF C-Scans of Center Stringer Flange Impact Damage Produced by Impact at X (Type I2b)

4.3.2.3 MID-STRINGER IMPACTS (TYPE I3)

Damage area induced from mid-stringer hail impacts for both substructure and skin delamination is plotted in Figure 4-23. Similar to mid-bay skin impacts, two of the four mid-stringer impacts generated both interply delamination and stringer flange delamination. To initiate damage at the mid-stringer location, more impact energy was needed than the energy level that produced damage for a mid-bay impact and direct stringer flange impact.
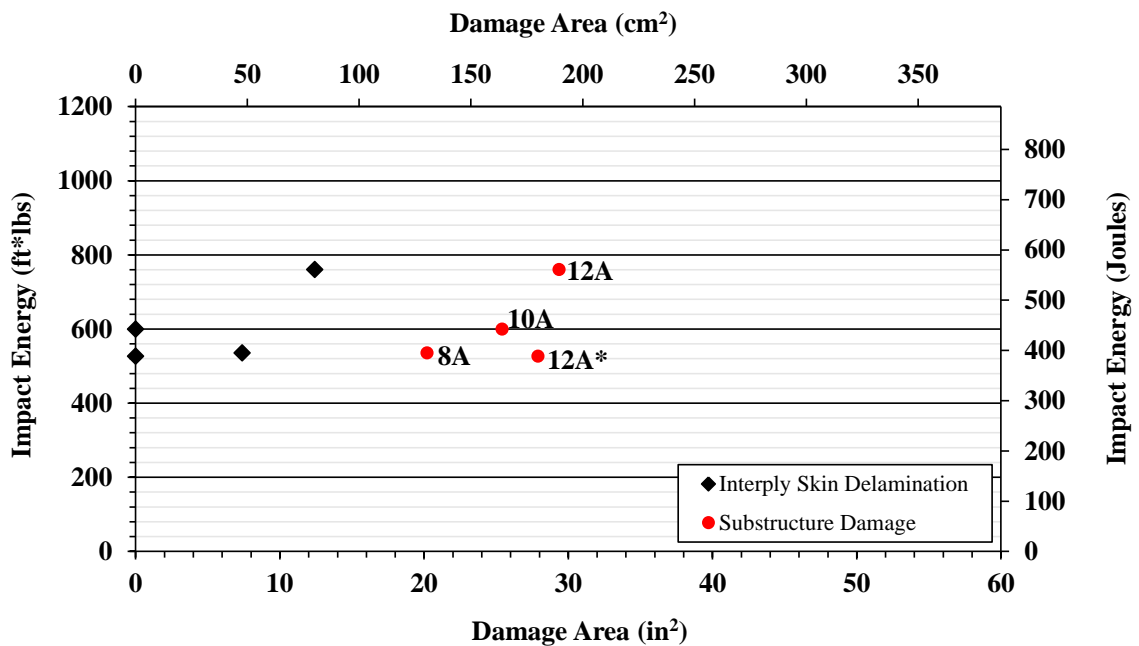
Figure 4-23: Substructure and Skin Delamination Damage Area Created by Simulated Hail, Mid-Stringer Impacts (Type I3)

The total damage generated by mid-stringer impacts is shown in Figure 4-24. Although interply skin delamination did occur in two of these impacts, a majority of the damage was caused at the skin to flange substructure interface. Because impacts 8A, 9A and 10A were conducted on the same stringer, the first damage-inducing impact may have had an effect on subsequent, nearby impacts.
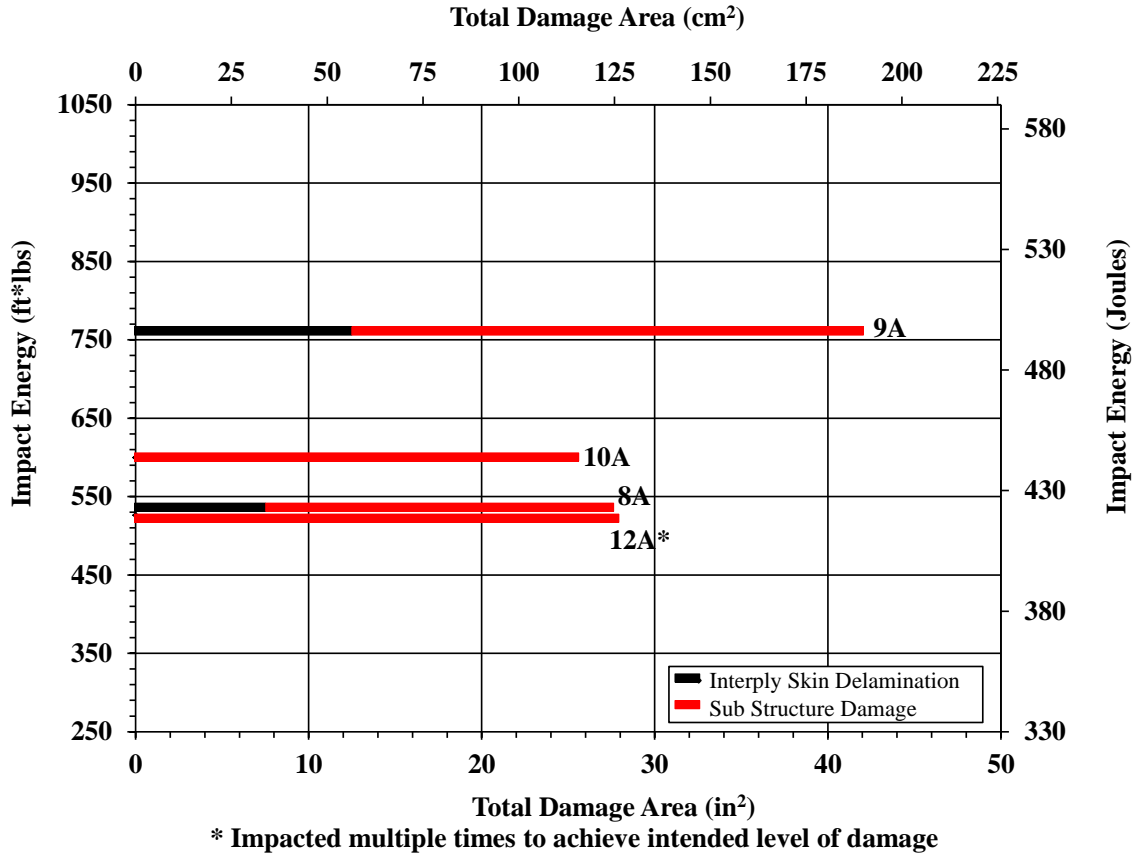
Figure 4-24: Total Damage Area Created by Simulated Hail, Mid-Stringer Impacts (Type I3)

It is evident from the UT amplitude C-scans in Figure 4-25, that all four of the mid-stringer impacts created some level of substructure delamination. There was some difficulty in the assessment of what damage area uniquely was associated with impacts 8A and 9A. Because the two impacts occurred closely to each other and both stringer flanges on either side of the two impacts were fully delaminated, the assigned substructure damage within the same bay was split between the two impacts at a line half way between them.

90

12A

388.1 Joules

(0.0) / (27.9)

8A

394.9 Joules

(7.39) / (20.21)

10A

442.2 Joules

(0.0) / (25.41)

9A

560.8 Joules

(12.42) / (29.37)

Increasing Impact Energy

(Interply Delamination Area in^2) / (Substructure Damage Area in^2)
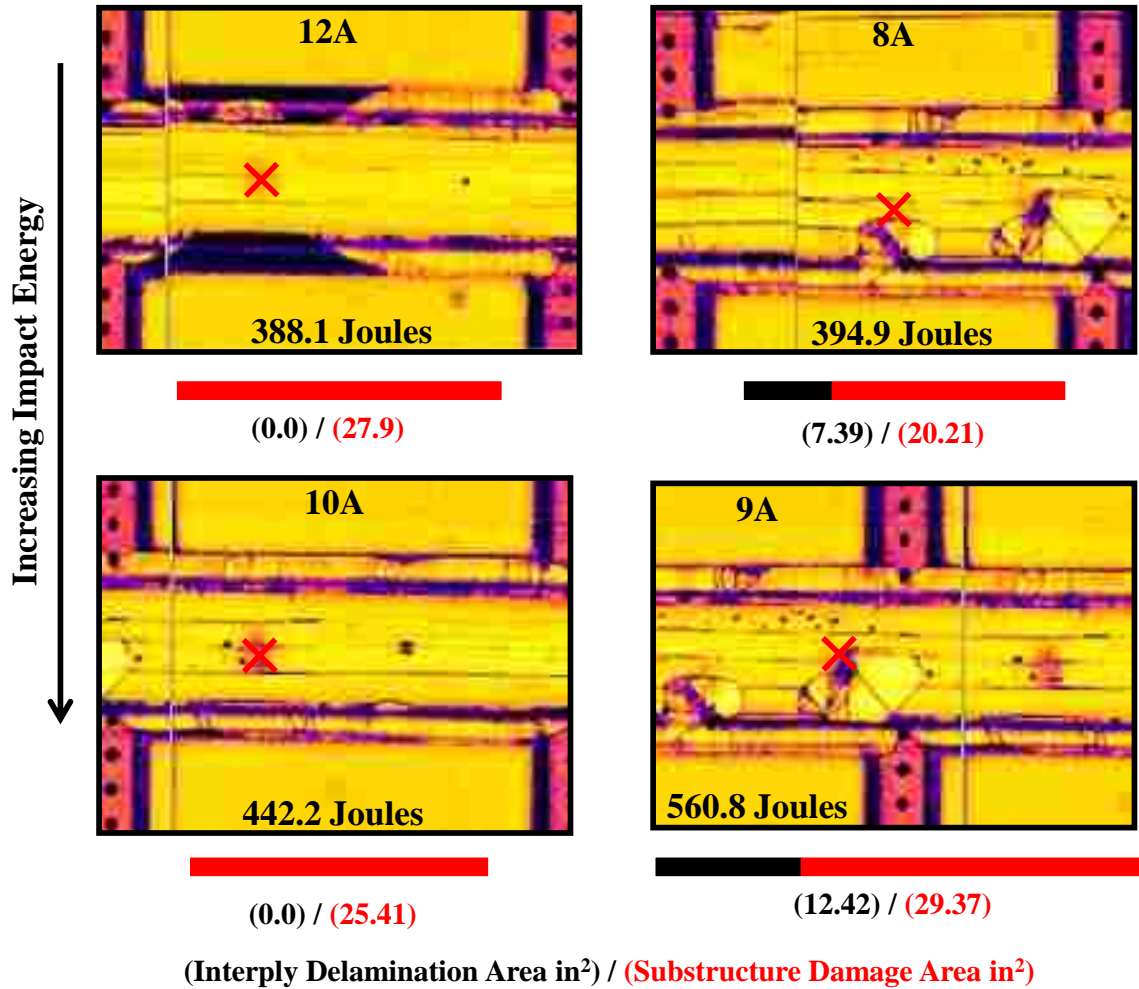
Figure 4-25: Ultrasonic Amplitude C-Scans of Mid-Stringer Impact Damage (Type I3)

4.3.2.4 SHEAR TIE IMPACTS (TYPE 4)

Damage induced by hail impacts directly on the shear ties consisted mainly of substructure damage or delaminations in the built-up pad sections. Figure 4-26 shows that there were no interply skin delaminations associated with direct shear tie impacts. Visual inspections revealed that all three of these impacts cracked the shear tie located beneath the impact location (see Figure 4-16). All three of the shear tie impacts also produced visually detectable indication of damage on the outer surface. These visual

91

indications were either paint scuffing, paint chipping, or cracking in the paint around the fasteners. Additional details regarding the cracked shear ties and visual indications are provided in Appendix B.
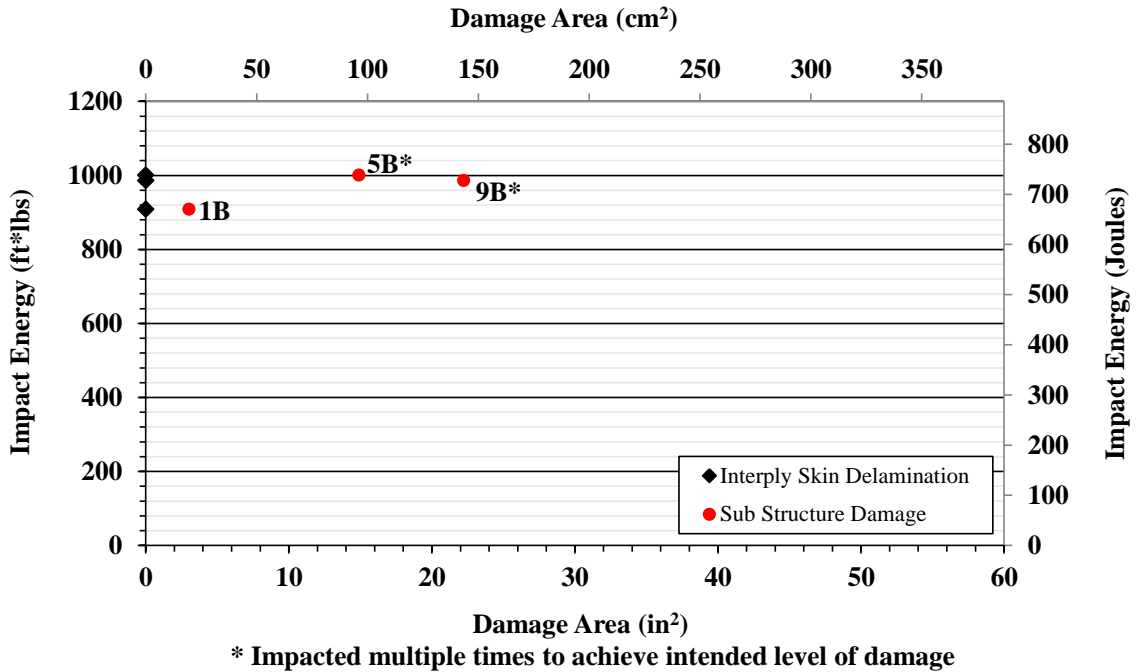
Figure 4-26: Substructure and Skin Delamination Damage Area Created by Simulated Hail, Shear Tie Impacts (Type I4)

Ultrasonic amplitude C-scans for direct shear tie impacts are shown in Figure 4-27. Shear tie damage poses three unique nondestructive inspection challenges: 1) the shear ties are fastened to the skin, not bonded or co-cured, so the ultrasonic signal cannot penetrate into the shear tie to detect damage, 2) the shear tie built-up pad section typically delaminated during the impact event thus any damage beneath this interface damage would not be detectable and 3) the share ties are bent at a 90 degree angle and damage in the shear tie manifests itself as cracking in the radius of bend which is not in contact with the backside of the panel. It may be possible to detect this damage if there was sealant or

92

other type of ultrasonic coupling medium between the shear tie and the built-up pad section or adhesive.

(Interply Delamination Area in^2) / (Substructure Damage Area in^2)
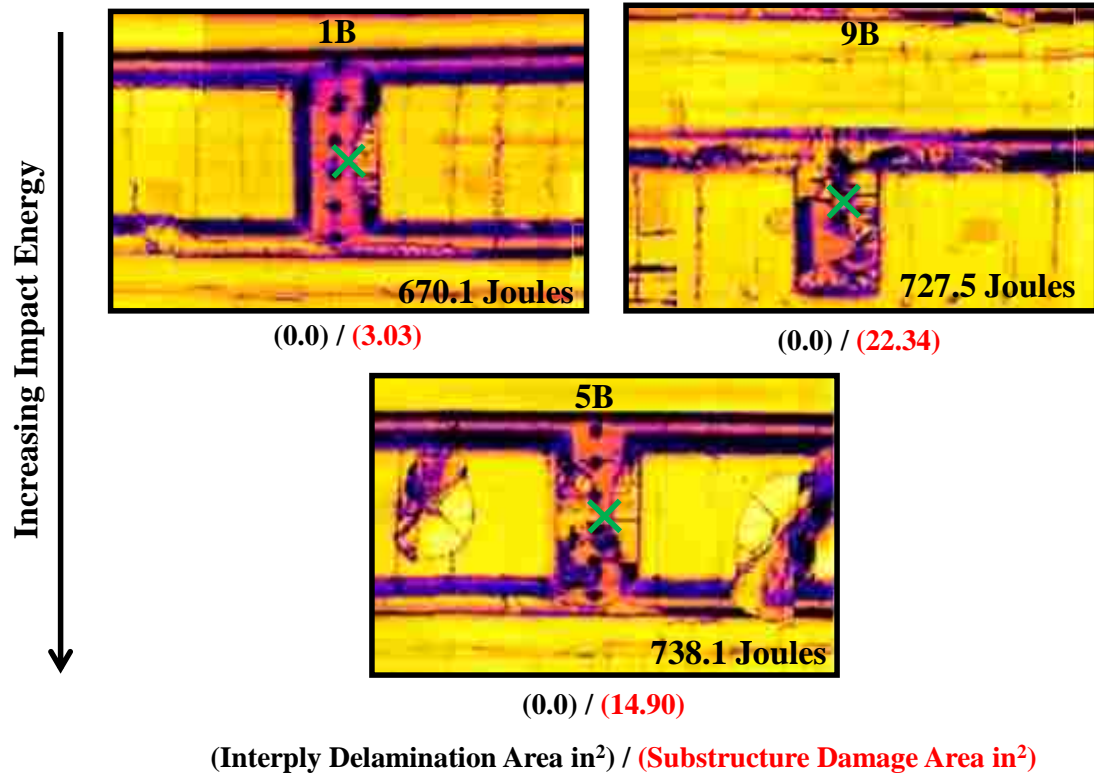
Figure 4-27: Ultrasonic Amplitude C-Scans of Shear Tie Impact Damage (Type I4)

4.3.3 DAMAGE ASSOCIATED WITH HARD SPHERICAL TIP IMPACT

For hard tip spherical impact tests, local loss of ultrasonic signal at the impact location primarily indicated crushed fibers near the surface and was typically accompanied by a visual dent at the impact site. Furthermore, damage created the by solid spherical tip was very localized such that it never initiated damage away from the impact location. Also, because the damage created by the hard tip was significantly smaller than the simulated hail, it was not possible to separate the area of substructure damage from the interply skin delamination area.

Damage created by mid-bay skin impacts with the 2" diameter spherical tip included near surface fiber crushing and some interply skin delamination. Damage area verses impact energy for these impacts is shown in Figure 4-28. About half of the impacts were conducted on skins that were stiffened by a single stringer on one side (outboard impacts). This resulted in decreased stiffness of the overall outboard skin and damage from impacts in these regions created less damage than mid-bay skin impacts, inboard of stringers two and four. This phenomena is shown in the Figure 4-28 plots and can be attributed to slightly different boundary conditions between the impacts.
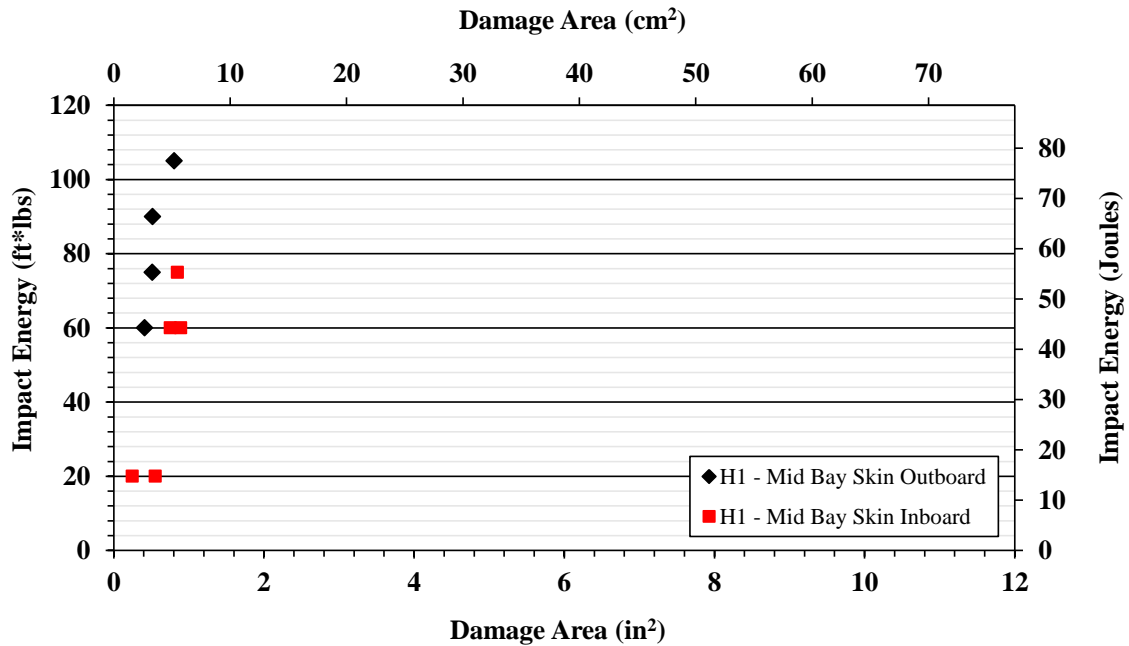
Figure 4-28: Damage Area Created by 2" Diameter Spherical Tip Mid-Bay Skin Impacts (Type H1)

One way to mitigate the dependency of boundary conditions and plot the impact damage data more consistently would be to plot impact force verses damage area as opposed to impact energy verses damage area. The damage area is more dependent on the impact force than it is on impact energy. For a given impact energy, the force imparted on the

94

structure is dependent on the stiffness at the location being impacted. The higher the stiffness, the higher the force induced. This measurement would be possible by integrating a force transducer onto the tip of the impactor.

Damage area produced by the 2" diameter, hard spherical impact tip at the three different stringer flange impact locations are shown in Figure 4-29. As discussed before, the plot is not divided into substructure damage and skin delamination damage because unlike hail impact damage, it was not possible to determine the amount of damage in the skin and the substructure separately. Instead, the plot displays the damage area as it relates to each stringer flange impact location (2a, 2b and 2c). In general, damage area increases with impact energy. Two obvious deviations from this are the two, 2b impacts (red squares) that produced zero damage. This may not actually be the case. These two impacts created very small visual dents, but in the C-scan images used to determine damage area did not indicate any damage. This may have been due to a masking effect caused by the stringer flange, hiding the very small level of damage.
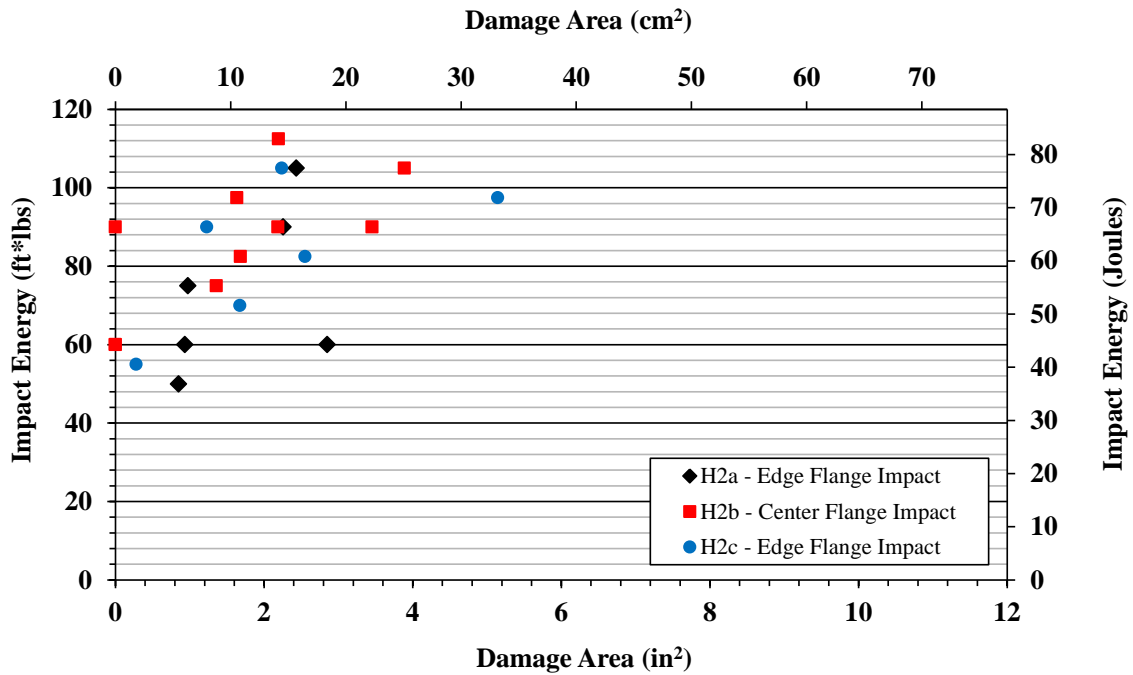
Figure 4-29: Damage Area Created by 2" Diameter Spherical Tip Stringer Flange Impacts (Type H2)

Figure 4-30 plots the mid-stringer impact (between stringer flanges – H3) damage area verses impact energy. These impacts created near surface fiber crushing and some interply delaminations in the skin. No substructure disbonds were observed as a result of these impacts. This particular impact location had the most consistent boundary conditions and therefore resulted in the best trending data.
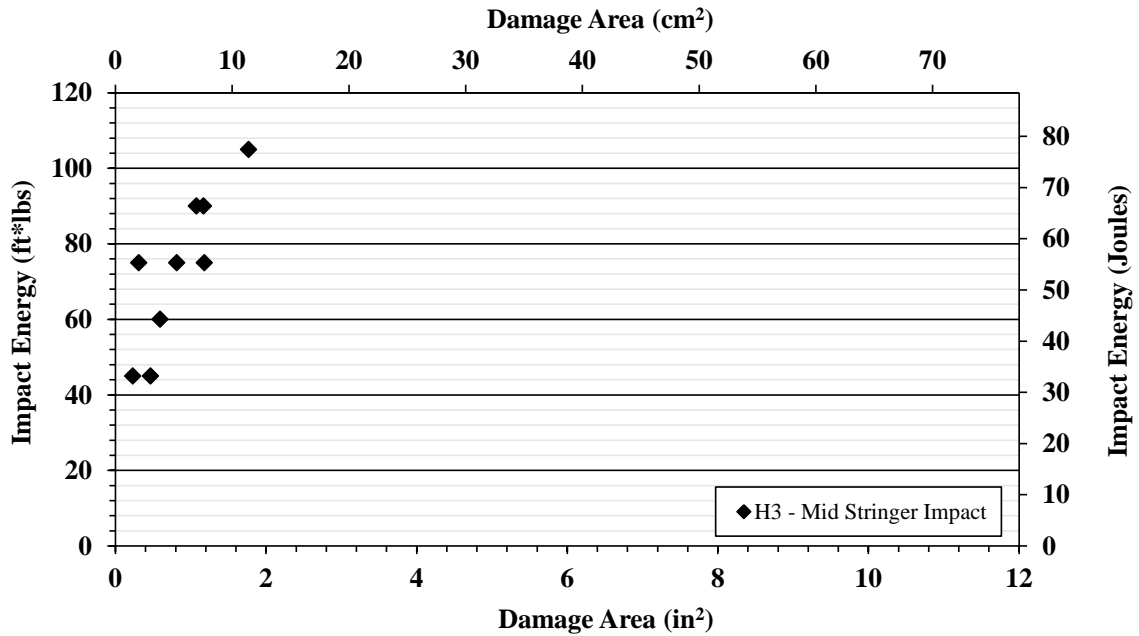
Figure 4-30: Damage area Created by 2" Diameter Spherical Tip Mid-Stringer Impacts (Type H3)

Damage area from the three shear tie impact tests (H4) are displayed in Figure 4-31. The two impacts that created approximately 4 in^2 and 10 in^2 of damage were located at the edge of the shear tie. The high shear stresses developed during the impact caused the tapered built-up section to delaminate from the skin. The inspection results from the shear tie edge impacts and shear tie center impact clearly show the difference in damage level (see impacts 8, 19, and 23 in Appendix C).

97
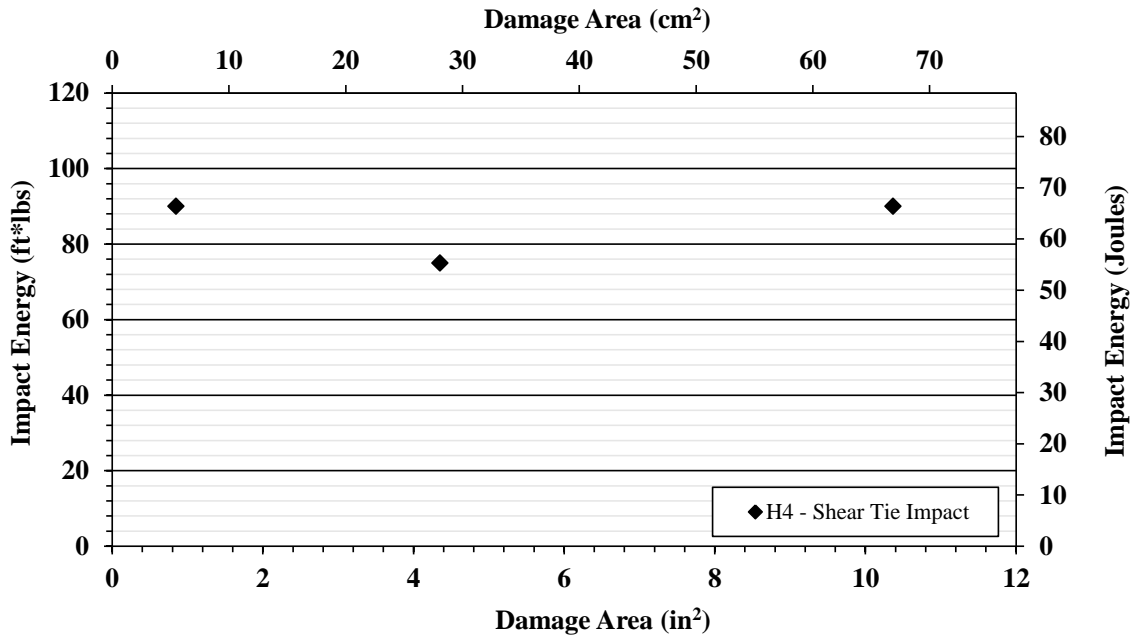
Figure 4-31: Damage Area Created by 2" Diameter Spherical Tip Shear Tie Impacts (Type H4)

Ultrasonic amplitude C-scan results from the top of bay 1 on panel A are shown on the right side of Figure 4-32. Most of the impact damage shows up as a dark spot on the scan. This is due the significant decrease in amplitude caused by the near surface fiber crushing. The UT signal does not make it past the first couple layers of carbon and the back wall signal is not detected under the set gate. The blue box in the figure indicates a damage that induced an interply delamination in the skin. The red circle indicates a damage area where the near surface fibers were crushed.

Pristine Area on Panel B Impacted Area on Panel A
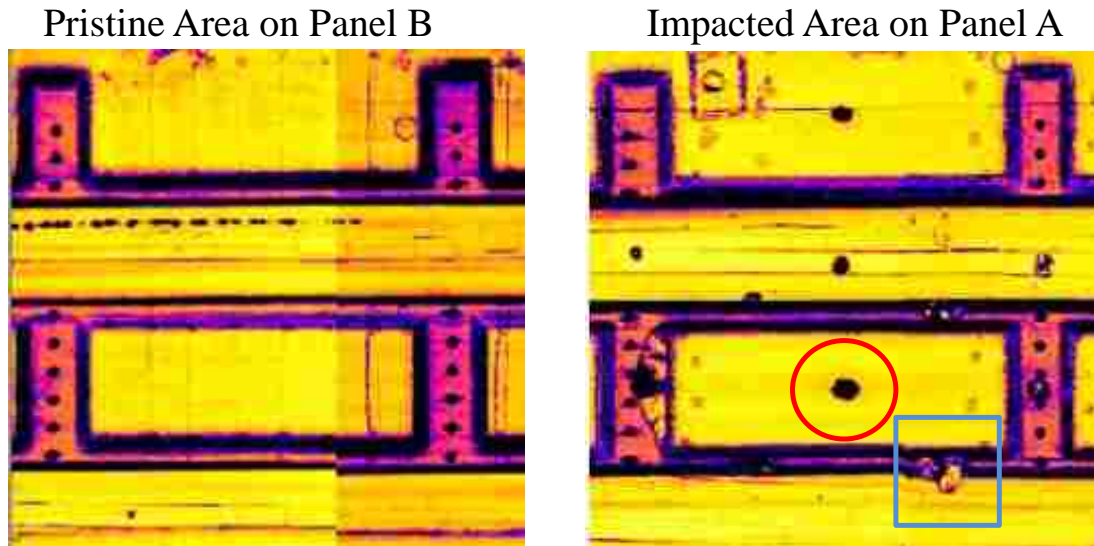
Figure 4-32: Example of Spherical Tip Impact Damage On Panel A

It is clear from the nondestructive inspection results and the damage area created by the

hard, non-crushable impact tip, the damage associated with simulated hail impact is much

more severe. Although impact energies for the hard impacts were much lower than the

simulated hail, higher hardened impact energies would still produce localized damage

until penetration of the panel occurred.

4.4   FIBER OPTIC DAMAGE DETECTION

There were four different methods used to deploy fiber optics for strain sensing on the

two panels. These were:

1) Embedded within the skin of the 16 ply laminate (panel A)

2) Bonded to the panel perpendicular to the stringers with the fiber being bonded to

    each skin and stringer in the same orientation and layout as the embedded

    fiber(panel B)

99

3) Bonded to the backside of the panel to only the skins parallel to the stringers (bays 1 and 2 on panel A)

4) Bonded to the backside of the panel perpendicular to the stringers, but not bonded to the stringers, only the skins (bays 3 and 4 on panel A).

An initial interrogation of the embedded fiber revealed that there was significant light attenuation within the fiber and that light could not be transmitted through the length of the fiber. The majority of the fiber optic was run in the 90 degree fiber direction and the fiber toes on either side of the embedded fiber were run at -45 degrees and 0 degrees. When the panel was cured under high pressure in the autoclave, the carbon fibers were pressed tightly inducing micro bending along the length of the fiber. Micro bending of the fiber optic is illustrated in Figure 4-33. The initial intention in selecting a fiber for this application was to select a fiber with a high numerical aperture. Fibers with a high numerical aperture are less susceptible to light attenuation due to micro bending. The particular fiber used may not have had as high of a numerical aperture as intended.

Carbon Fibers

Fiber Optic

Carbon Fibers
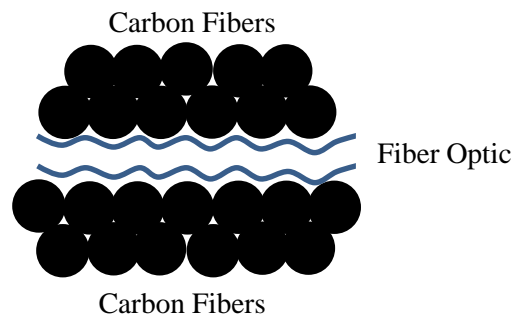
Figure 4-33: Micro Bending of Embedded Fiber Optic Causing Light Attenuation

Although there was significant light attenuation in the fiber optic and light could not pass all the way through the length of the fiber, there were two sections of fiber that could successfully be interrogated using the two fiber egresses connection points. Each side of

the fiber could be interrogated for approximately the first 5 vertical runs of fiber, but was only successful for the first impact test Figure 4-34. A major factor contributing to the lack of data obtained from the embedded fiber optic was the use of high power flash lamps during the impact tests. The lamps were used to illuminate the area for the high speed cameras to capture video during each impact. This had an inverse effect on the detection ability of the fiber optic strain sensing system because the flash lamps increase the surface temperature of the panel. Baseline measurements were taken prior to impact and were obtained at ambient temperature with the flash lamps off. When the data was later interpreted it was clear that the heat from the lamps induced global strain changes in the panel and swamped out any indication of impact damage. A color strain map result from the first impact test conducted on panel A is shown in Figure 4-34.
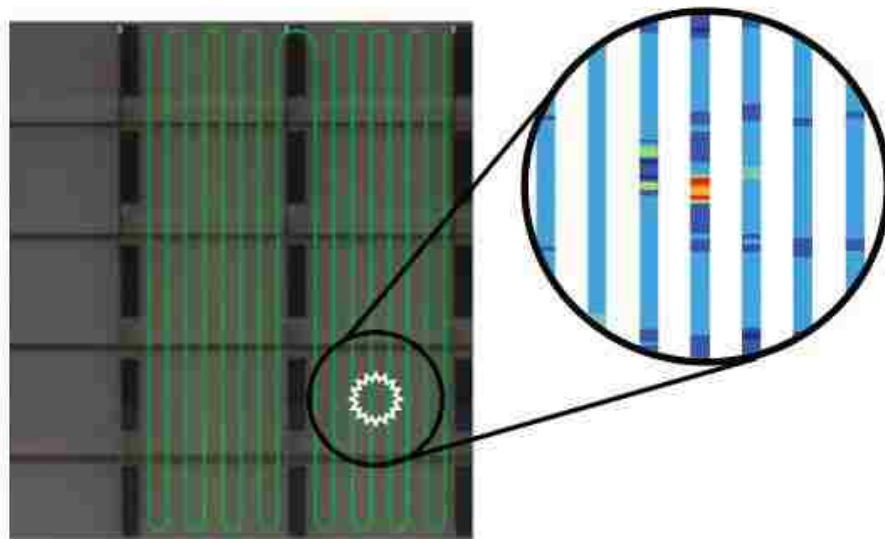
Figure 4-34: Strain Map of First Impact Damage Performed on Panel A, Only Result Obtained From Embedded Fiber Optic

Damage detection using the fiber optic that was externally bonded to the skins and stringers was equally unsuccessful during simulated hail impact testing. Because the fiber optic was bonded to both the skin and the stringers, when an impact occurred that

101

delaminated the stringer flange from the skin it broke the fiber optic. An example of a delaminated stringer flange shearing the fiber optic sensor (white line) is shown in Figure 4-35. No results were obtained using this method of fiber optic deployment due to extensive fiber breakage.

Figure 4-35: Broken Fiber Optic Due to Stringer Flange Delamination

In response to the ineffective method of fiber optic deployment used during simulated hail impact testing, two alternative methods were investigated that did not involve bonding the fiber over the stringer during hard impact testing. The two different layouts tested are shown in the schematic in Figure 4-36. In the fiber layout used in bays 1 and 2, the fiber was bonded parallel to the stringers. At each stringer flange, one strand of fiber was bonded just to the outside of each flange, and one was bonded just on the flange, but never bonded over the interface. In the fiber layout used in bays 3 and 4, the fiber was run perpendicular to the stringers, but the bond was stopped prior to the skin-to-flange

intersection. Both of these layouts left un-bonded sections of fiber leaving the fiber

exposed to potential breakage during handling.

Front Side View of Panel
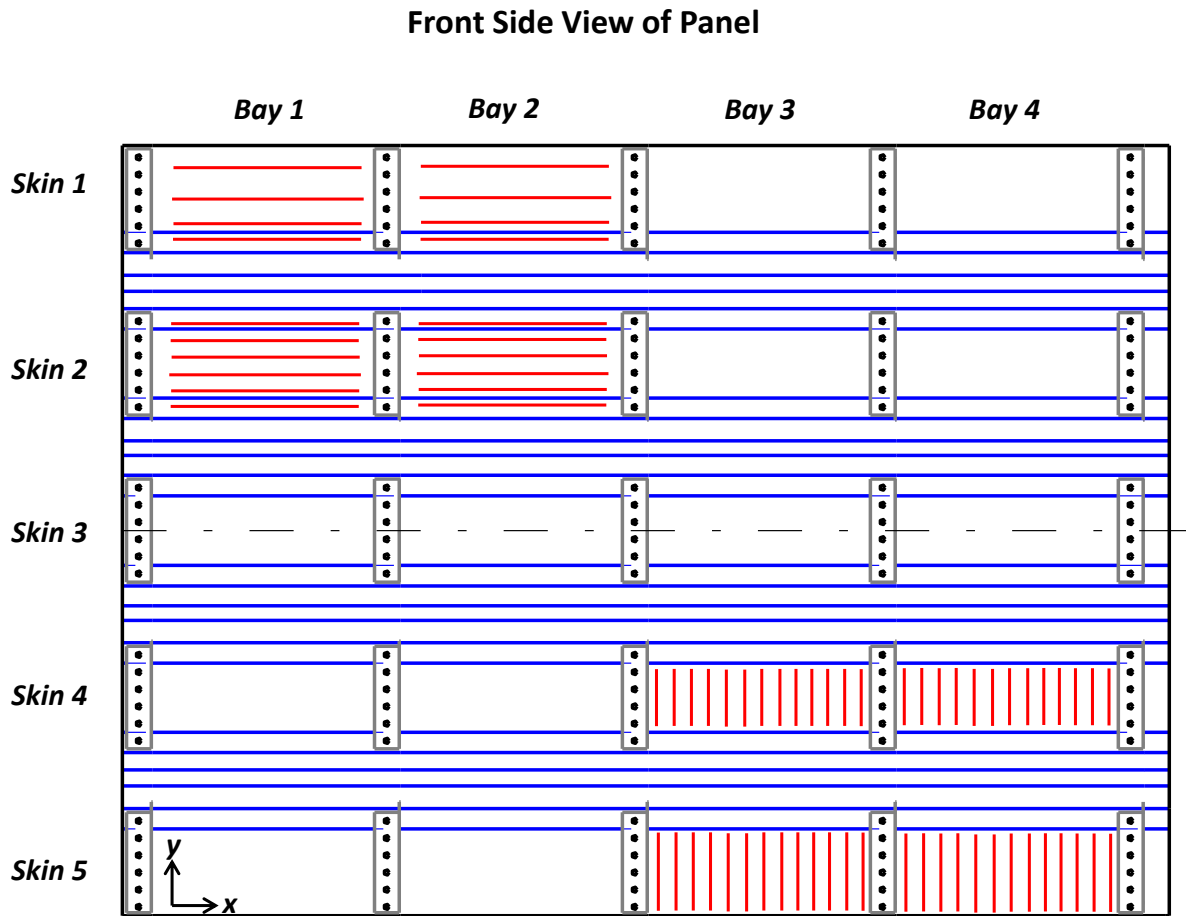
Figure 4-36: Bonded Fiber Optic Layouts Used During 2" Diameter, Spherical Tip Impacts

A picture of the two different fiber optic layouts is shown in Figure 4-37. Bay 2, on the

left of the figure shows the horizontal fiber runs that were unequally spaced apart. The

spacing between the two fibers at the edge of the stringer flange (one on the edge of the

flange and the other on the skin) were placed close together in order to better detect

stringer disbonding. There were a total of 20 bonded sections of fiber over the two skins.

The right side of the figure shows the fiber optic layout used in bays 3 and 4. There were a total of 26 bonded sections of fiber in 13 vertical runs.
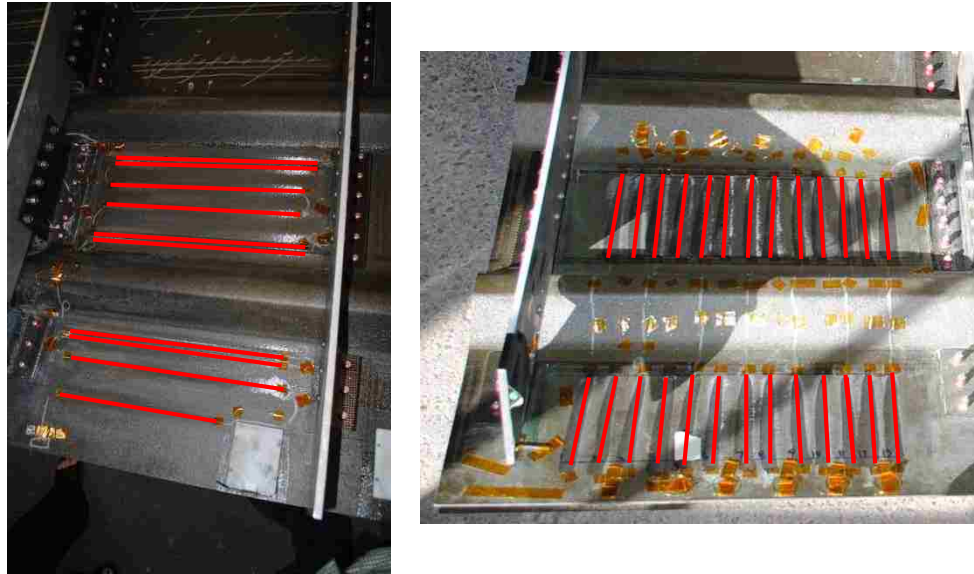
Figure 4-37: Picture of Bays 2 and 4 Showing Where the Fiber Optic was Bonded to the Panel

Baseline scans of the fiber optic were taken prior to each impact event and were collected within minutes of the impact test being performed. In order to calculate strain, the system measures minute changes in the Raleigh backscatter between the baseline and post-test scans. A 1 cm. strain resolution was used to interrogate the bonded fiber optics. The OBR recorded linear strain data every 1 cm. for the length of the entire fiber optic. As shown in the previous figures only certain portions of the fiber were bonded to the panel. The strain position date was used to determine the locations along the length of the fiber which were bonded and unbounded. Location calibration was accomplished by touching the fiber (changing the strain) at the beginning and end of each bonded section of fiber. Those specific fiber length positions were found in the data set and alternately plotted in a strain map. Because the data output from the OBR was linear strain-position

data, each strand of fiber need to be plotted in the opposite direction as the previous strand. This is illustrated in the fiber schematic in Figure 4-38.
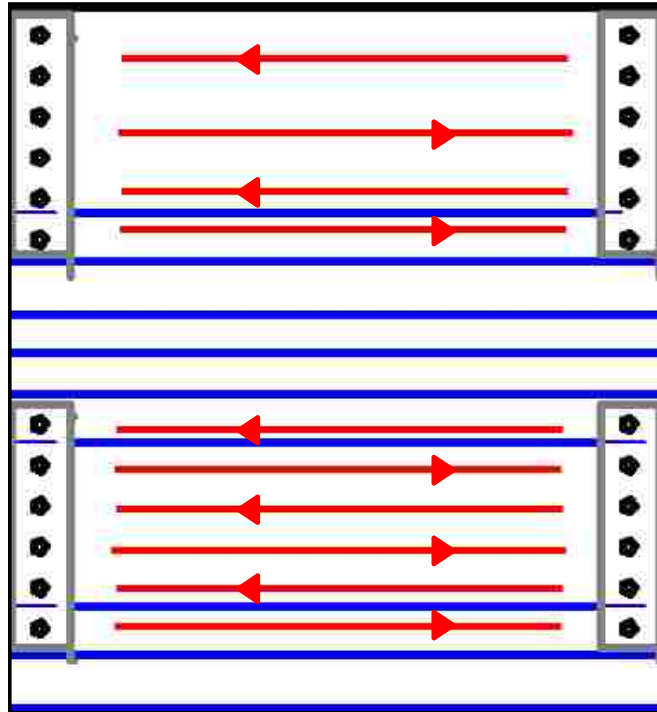
Figure 4-38: Linear Strain Position used for Data Plotting

A sample result constructed using the fiber orientation in bay 2 is shown in Figure 4-39. This particular impact was successfully detected using the bonded fiber optic. A noticeable strain indication of around 120 micro strain is shown in the 3D strain map at the bottom of the figure. It can also be seen in the 3D strain plot that there is a noticeable compressive strain on either side of the impact location, with a positive strain at the center of the impact. This is typical of a dent where the center of the impact corresponds to the peak positive strain of the dent and the compressive strains on either side correspond to the base (reverse bending) of the dent. The full set of strain map results for this fiber orientation and the vertical fiber orientations used in the hard tip spherical impact tests is contained in Appendix C.
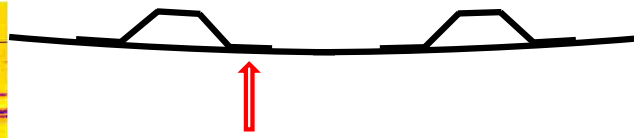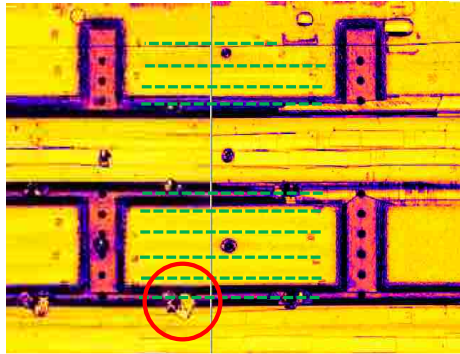
Impact Location
Fiber Optic

Center of Stringer Flange
Impact Energy: 90 Ft lbs
Damage Area: 3.46 in^2
Type of Damage: Interply delamination
Strain Indication: Yes, clear detectable strain indication

Ultrasonic Amplitude Scan

X Position (in.)
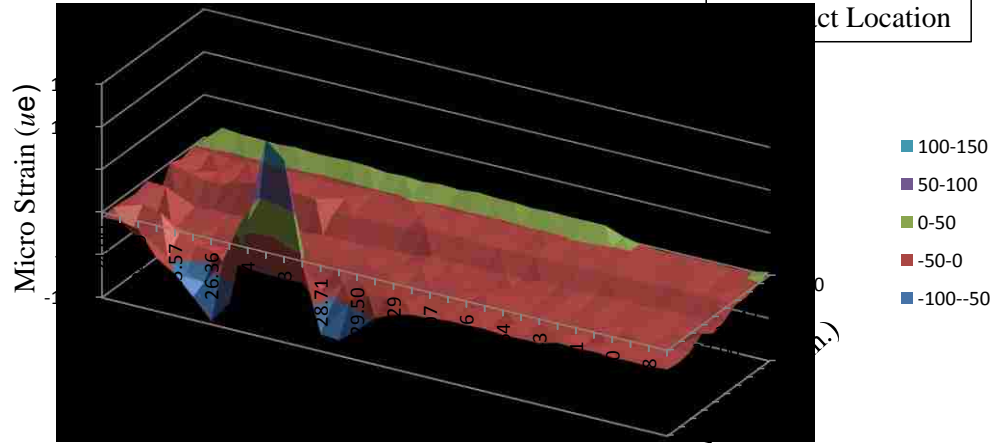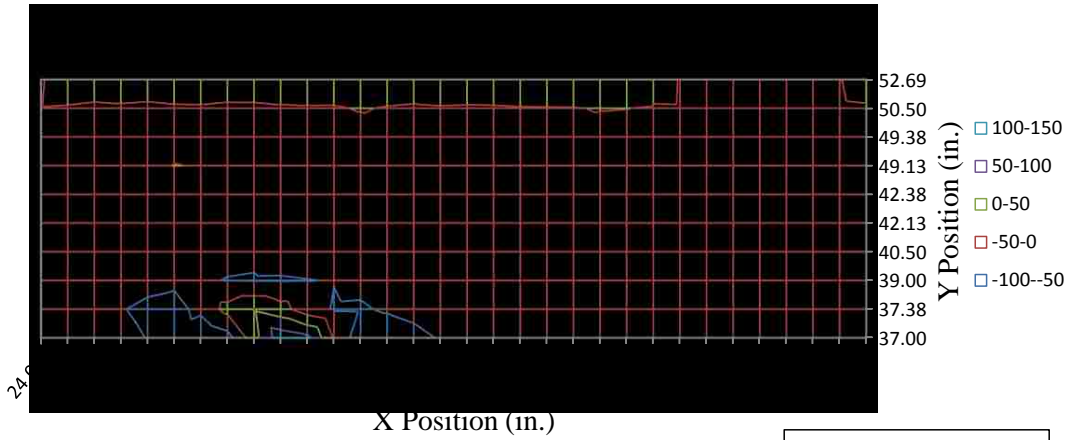
Figure 4-39: Example Fiber Optic Strain Map of Stringer Flange Impact

This set of results revealed that the vertical fiber orientation detected more impact damage than the horizontal fiber orientation. This was because the vertical fiber orientation (bays 3 and 4) was regularly spaced at approximately one inch, and the horizontal fiber runs were spaced at approximately 2.6, 1.1, and 0.25 inches. The closest spacing was placed on either side of the stringer flange-to-skin transition. In order for the fiber optic to detect any strain indication, deformation of the backside of the panel had to be in contact with the fiber. For example, skin impact damage generated between the stringer flanges (impacts H3) did not produce a detectable indication because the fiber was not bonded in this region.

Global changes in the strain field were occasionally noticed in some of the post impact strain plots. This may have been attributed to shifts in temperature between the initial baseline measurement and the post impact measurement, or movement of the panel during testing. Typically these were observed in tests where there was not a detectable strain indication of damage and the maximum strain over the length of the fiber was relatively low. An example of a non-detectable impact damage and the resulting strain field measurements is shown in Figure 4-40. This impact was conducted on the skin between the stringer flanges. It can be seen in the impact schematic in the top right of the figure that significant deformation at the impact site including stringer flange disbonding would have to occur in order for the FO to detect the strain change from this impact. It can also be seen in the ultrasonic amplitude C-scan at the top left side of the figure that there was very little damage induced by the impact (0.47 in^2 of near surface fiber crushing).
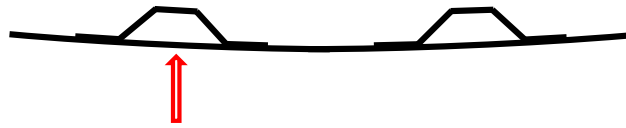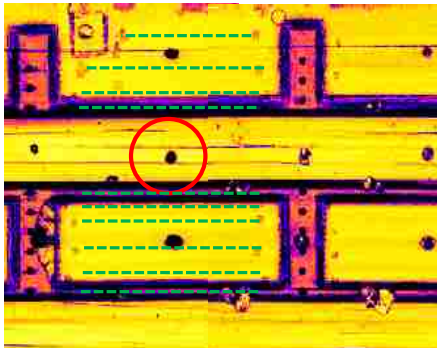
Impact Location

--- Fiber Optic

Ultrasonic Amplitude Scan

Mid-Stringer Between Flanges
Impact Energy: 45 Ft lbs
Damage Area: 0.47 in^2
Type of Damage: Near surface fiber crushing
Strain Indication: No, possible temperature shift or change in panel loading

Impact Location
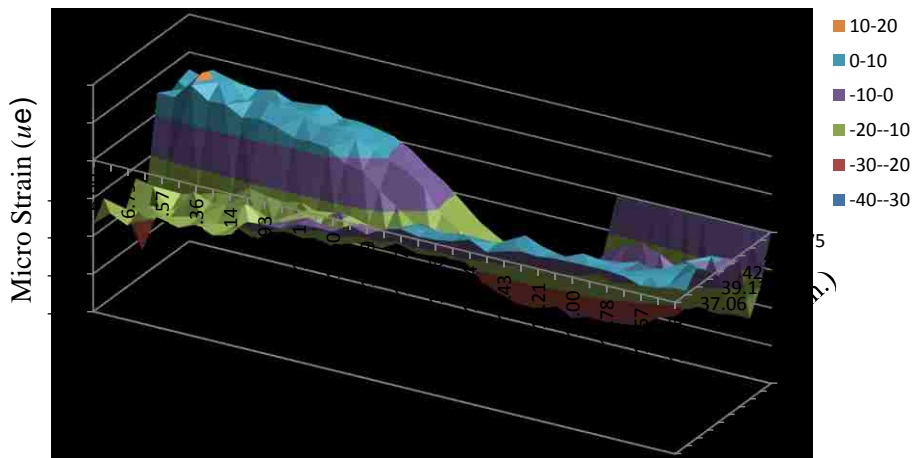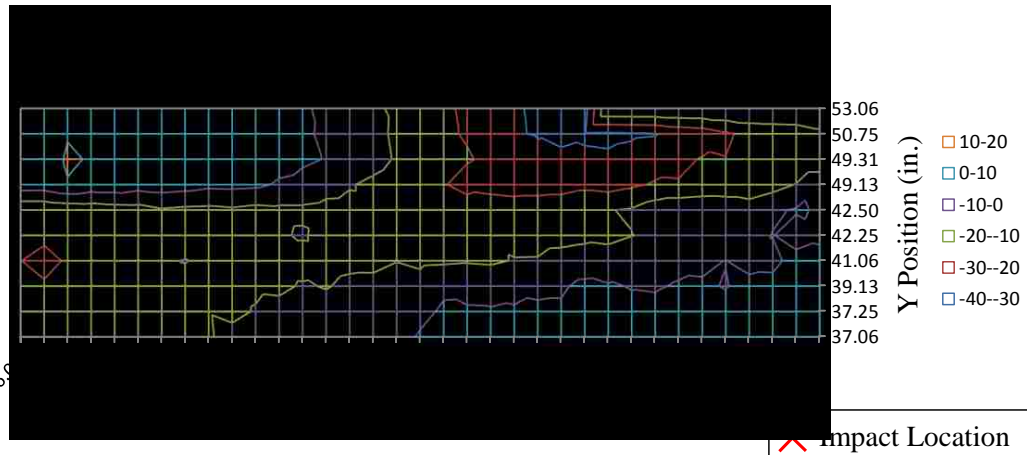
Figure 4-40: Impact at Mid-Stringer Between Flanges that was Not Detectable with the Fiber Optic

5   CONCLUSIONS AND RECOMMENDATIONS

Simulated hail and hard, spherical tip drop weight impact tests were conducted on full-scale carbon fuselage panels. Simulated hail impact on the panels at velocities up to 390 feet per second (118 meters/sec) left little to no surface visual indication of impact or damage, except at direct shear tie impacts. Simulated hail impacts located at the middle of the bays were capable of inducing extensive interply delamination and subsurface damage with no visual indication from the surface of the panel. Moreover, hail impacts directed at the stringer flange and shear tie only induced substructure disbonds but not interply delaminations in the 16 ply skin. Particular notes of interest during ice impact testing were:

- When a mid-bay impact occurred, there was no set energy threshold that when surpassed initiated substructure delamination away from the impact site. Sometimes it happened, sometimes it did not.

- Impacts conducted at locations over stringer flanges initiated damage at lower levels than impacts over unsupported skin impacts

- Increased impact energy was required to initiate damage at the mid-stringer location than at mid-bay and direct stringer flange impacts.

Conventional hand-deployed pulse-echo ultrasonic inspection methods were used to determine the extent of damage during impact testing. It was shown to be an effective method for locating and characterizing impact damage near the impact area. Substructure damage on stringer flanges away from the impact location was often not detected. This was due to not conducting inspections far enough away from the impact site to find all of

109

the damage. The additional damage area was subsequently revealed in full panel two-dimensional C-scan inspections.

Impact damage created with the drop weight, 2" diameter spherical, steel impact tip left localized, and often times, visually detectable damage. A majority of the damage was limited to the 16 ply skin of the panel, but stringer flange and shear tie edge impacts were capable of disbonding substructure. Due to the small size of this damage and its near surface nature it was difficult to characterize. Visual dents were observed on almost all of these impacts, even in cases where very little change in ultrasonic A-scans was observed. Moreover, damage initiated from these impacts never induced damage away from the impact site.

When the panel impact tests were completed, the MAUS V scanning system was used to inspect each panel with ultrasonic and resonance modes. Once the panels had been fully scanned with the MAUS V scanner and the damage accurately mapped out on the panels, additional damage characterization (determination of depth of damage) was accomplished using A-scan signal assessments in combination with C-scan analysis. Information gathered during the post impact assessment was assembled and put in an impact database (see Appendix B for the ice impacts and Appendix C for the hard tip impacts).

It was observed that ultrasonic time of flight C-scans and a combination of resonance phase and amplitude C-scans are capable of detecting substructure disbonds with higher

sensitivity than ultrasonic amplitude alone. The difference between ultrasonic amplitude and time of flight modes was that it was easier to visually observe the difference in color contrast corresponding to substructure disbonds in the time of flight C-scan images verses in the amplitude scans.

With resonance testing, changes to the transducer resonant frequency are caused by defects in the material being inspected or variations in material thickness. These changes in the resonant frequency are subsequently detected as differences in phase and amplitude. Because resonance testing is sensitive to slight changes in material stiffness, small areas where the substructure became disbonded from the skin resulted in detectable changes in the transducer resonant frequency and were reliably detected. This NDI method also accurately detected interply delaminations in the skin.

In addition to the inspections performed, there were four different methods used to deploy fiber optic strain sensing to the two panels. These included embedding the fiber in the skin of the panel, vertically bonding the fiber to the backside of the panel over the skins and stringers, bonding the fiber parallel to the stringers avoiding the flange-to-skin interface, and bonding the fibers vertically over the backside of the skins only (not over the stringer flanges). Embedding the fiber in skin must be performed in the factory when the laminate is being laid up. In order to minimize micro bending on the fiber optic, it should be laid parallel to the carbon material on either side of it. For example this could be done in the mid-plane of a quasi-isotropic lay-up, in the case of the panels used in this study, the -45 degree direction. Also, a larger diameter fiber optic with a high numerical

aperture is desired to minimize micro bending. Care needs to be taken not to embed the fiber where fastener holes may be drilled and special consideration should be taken to protect the fiber optic when egressing the fiber from the structure. With additional testing this could show to be a promising impact detection method.

When the fiber was continuously bonded to the entire backside of panel B over the stringers and skins, significant fiber breakage occurred at many locations due to stringer flange disbonding. To detect hard tip impacts, it was determined that avoiding the stringer flange-to-skin transition area prevented the fiber from being sheared when the flange disbonded from the skin. It was found that impact damage generated by the 2" diameter steel tip left a permanent dent in the panel that was detectable with the fiber optic method in 15 of the 25 interrogated tests. Two critical observations were made when fiber optics were used to detect impact damage: first the impact damage had to be in close proximity to the fiber optic in order to transfer strain to the fiber, secondly, the strain developed in the fiber could not be significantly high, approaching breakage of the fiber. If this did occur, other sections of fiber not related to the damage area showed very high levels of strain, or false detections.

Bonding the fiber optics to the backside of the panel was a time consuming and tedious operation. In order to utilize fiber optics for damage detection on real structures, a more advanced method of deploying the fiber to the surface of the structure would need to be developed. A possible solution to this would be to embed the fiber optic in the desired pattern in a sheet type carrier material that bonds to the structure of interest. The material

would need to be a robust, mechanically protective material as well as a high strain transfer material. If the fiber optics were embedded in this pre-manufactured sheet, the exact position of the fiber optic would be known and damage localization could be conducted. Multiple patches could be spliced together allowing wide area damage detection.

6 FUTURE WORK

To better understand the damage initiation using hard, spherical tip type impacts, a force transducer could be added to the drop spear impact test setup. Because of the various boundary conditions involved in testing complex, full-scale structures, it is desirable to plot maximum impact force verses the damage area. Also, additional tip diameters could be studied to determine the effect of impact tip diameter or contact pressure on carbon aircraft fuselage structure. Similarly, low velocity, hydraulic actuated blunt impacts simulating ground vehicles bumping the fuselage of an aircraft are of interest. These tests could be performed using protective rubber bumper devices with low velocity and large displacements.

To fully investigate the capabilities of modern nondestructive inspection technologies, the two panels impact tested in this study will be used to assess additional NDI techniques. Additional techniques could potentially include phased array ultrasonics, laser UT, air-coupled UT, vibro thermography, and flash thermography. The panels provide a realistic platform for NDI developers to test and validate their NDI technologies.

7 REFERENCES

[1]   Dorworth, L., Gardiner, G. and Mellema, G., *Essentials of Advanced Composite Fabricatio and Repair*. Newcastle, WA: Aviation Supplies & Academics, Inc., 2009.

[2]   *Polymer Matrix Composites: Guidelines for Characterization of Structural Materials* vol. 1: SAE International, 2012.

[3]   Papakonstantinou, C., Balaguru, P., and Lyon, R., "Comparative Study of High Temperature Composites," *Composites Part B: Engineering,* vol. 32, pp. 637-649, 12// 2001.

[4]   *Polymer Matrix Composites: Materials Properties* vol. 2: SAE International, 2012.

[5]   L. G. Fuller, "Production and Characterization of Novel Shaped Fibers for Fluid Sorption and Transport," Clemson University, Clemson2009.

[6]   Eom, S., Pyo, D. and Ryu, S., "Characterization of Differently Shaped Carbon Fiber Composites Prepared from Naphtha Cracking Bottom Oil," *Korean Journal of Chemical Engineering,* vol. 27, 2010.

[7]   Hosur, M., Murthy, C., Ramamurthy, T.and Shet, A., "Estimation of Impact-Induced Damage in CFRR Laminates Through Ultrasonic Imaging," *NDT & E International,* vol. 31, pp. 359-374, 10// 1998.

[8]   Myxter, J., American Airlines Cancels 296 More Flights Due to Hail-Damaged Planes. 2012.

[9]   Johanson, M., "Dallas Tornadoes 2012: DFW Airport Planes Damaged, Hundreds of Fights Canceled," in *International Business Times*, ed, 2012.

[10]   Gringorten, I., "Hailstone extremes for design," DTIC Document1971.

[11]   Aktas, M., Atas, C., Icten, B., and Karakuzu, R., "An Experimental Investigation of the Impact Response of Composite Laminates," *Composite Structures,* vol. 87, pp. 307-313, 2009.

[12]   Aymerich, F. and Meili, S., "Ultrasonic Evaluation of Matrix Damage in Impacted Composite Laminates," *Composites Part B: Engineering,* vol. 31, pp. 1-6, 1// 2000.

[13]   Kim, H., Welch, D., and Kedward, K., "Experimental Investigation of High Velocity Ice Impacts on Woven Carbon/Epoxy Composite Panels," *Composites Part A: Applied Science and Manufacturing,* vol. 34, pp. 25-41, 1// 2003.

[14]   Rhymer, J., Kim, H., and Roach, D., "The Damage Resistance of Quasi-Isotropic Carbon/Epoxy Composite Tape Laminates Impacted by High Velocity Ice,"*Composites Part A: Applied Science and Manufacturing,* vol. 43, pp. 1134-1144, 7// 2012.

[15]   Advisory Circular No. 25.571-1D, "*Damage Tolerance and Fatigue Evaluation of Structures,"* Federal Aviation Administration, 2011.

[16]   Herzberg, I., "An Engineering Aproach for Predicting Residual Strength of Carbon/Epoxy Laminates After Impact and Hygrothermal Cycling," in *Composite Structures*, December 1999, pp. 483-490.

[17]   CMH-17, *Polymer Matrix Composites: Materials Usage, Design and Analysis* vol. 3, 2012.

[18]   Roach, D. and Neidigk, S., "Industry Survey of Structural Health Monitoring Technology and Usage," 2012.

[19]   Armstrong, K. and Barrnett, R., *Care and Repair of Advanced Composites*: Society of Automotive Engineers Inc., 1998.

[20]   Roach, D., "Assessing Conventional and Advanced NDI for Composite Aircraft," *High Performance Composites,* vol. 16, p. 72, 2008.

[21]   Peters, J., Nielsen, Z., Hsu, D., "Comparison of Local Stiffness of Composite Honeycomb Sandwich Structures Measured by Tap Test and Mechanical Test," *AIP Conference Proceedings*, 2001, p. 1031.

[22]   Roach, D., Rackow, K, "Improving In-Service Inspection of Composite Structures–It'sa Game of CATT and MAUS," in *US Dept. of Defense/National Aeronautics and Space Administration/Federal Aviation Administration Aging Aircraft Conference*, 2003.

[23]   Malglaive, F. and Albert, R., "Reverse Feometry X-Ray Imaging," *Insight-Non-Destructive Testing and Condition Monitoring,* vol. 51, pp. 66-68, 2009.

[24]   Schmidt, K., Goitia, R., Ellingson, W., and Green, W., "Correlation of Scanning Microwave Interferometry and Digital X-Ray Images for Damage Detection in Ceramic Composite Armor," in *AIP Conference Proceedings*, 2012, p. 1129.

[25]   Shur, M., "Terahertz Sensing Technology," p. 27, 2006.

[26]   Davis, W., and Lasser, B., "Real-Time Ultrasonic Imaging Using CCD Camera Techniques," *NondestructiveCharacterization of Materials,* pp. 135-140, 2003.

[27]   Newman, J., "Aerospace NDT with Advanced Laser Shearography," in *17th World Conference on Nondestructive Testing*, 2008, pp. 25-28.

[28]   Toughiry, M., "Examination Of The Nondestructive Evaluation Of Composite Gas Cylinders," *United States Department of Transportation, NTIAC/A7621-18: CRC-CD8,* vol. 1, 2002.

[29]   Hsu, D., Barnard, D., Peters, J., and Dayal, V., "Physical Basis of Tap Test as a Quantitative Imaging Tool for Composite Structures on Aircraft," in *AIP Conference Proceedings*, 2000, p. 1857.

[30]   Peters, J., Barnard, D., and Hsu, D., "Development of a Fieldable Air-Coupled Ultrasonic Inspection System," in *AIP Conference Proceedings*, 2004, p. 1368.

[31]   La Delfa, G., Urso-Miano, V., and Gibson, A., "Characterisation and Modelling of Structural Integrity of Carbon Fibre Wing Box Laminate Subject to Fire," *Plastics, Rubber and Composites,* vol. 38, pp. 9-10, 2009.

[32]   Schroeder, J., Ahmed, T., Chaudhry, B., and Shepard, S., "Non-Destructive Testing of Structural Composites and Adhesively Bonded Composite Joints: Pulsed Thermography," *Composites Part A: Applied Science and Manufacturing,* vol. 33, pp. 1511-1517, 2002.

[33]   Georgeson, G., Hansen, J., Kollgaard, J, Lea, S., and J. R. Bopp, "Damage detection device and method," ed: Google Patents, 2004.

[34]   Udd, E., Winz, M., and Krege, S., "Failure Mechanisms of Fiber Optic Sensors Placed in Composite Materials," in *SPIE*, 2005, pp. 409-416.

[35]   Davol, K, Udd, E., Kreger, S., Kunzler, M., and Laylor, M., "Monitoring of Advanced Composite Weave Structures Using Multi-axis Fiber Grating Strain Sensors," in *Proceedings of SPIE*, 2003, p. 128.

[36]   Gupta, N., Augustin, M., Sathya, S., Sundaram, R., Prasd, M., Pillai, A.*, et al.*, "Flight Data from an Airworthy Structural Health Monitoring System for an Unmanned Air Vehicle Using Integrally Embedded Fiber Optic Sensors," *Structural Health Monitoring,* vol. 1, pp. 463-470, 2011.

[37]   Murayama, H., Igawa, H., Omichi, K., and Machijima, Y., "Distributed Sensieng with OFDR and its Applicatin to Dtructrual Health Monitoring," in *SPIE 21st International Conference on Optical Fiber Sensors*, 2011.

[38]   Duncan, R, Childers, B., Gifford, D., Pettit, D., Hickson, A., and Brown, T., "Distributed Sensing Technique for Test Article Damage Detection and Monitoring," in *SPIE Smart Structurs and Materials*, 2003.

[39]   Kreger, S., Gifford, D., Froggatt, M., Soller, B., and Wolfe, M., "High Resolution Distributed Strain or Temperature Measurements in Single- and Multi-Mode Fiber Using Swept-Wavelength Interferometry," 2006, p. ThE42.

[40]   Liehr, S., Wendt, M., and Krebber, K., "Distributed Strain Measurements in Perfluoinated Polymer Optical Fibers using Optical Frequency Domain Reflectometry," *Measurement Science Technology,* vol. 21, 2009.

[41]   Scheerer, M., Bockenheimer, C., Dantele, A., Djinovic, Z., Graf, F., Natschlager, T.*, et al.*, "Development and Testing of an Ultrasonic Phased Array System Based on Piezo Actuators and Fiber Optic Sensors," in *Structural Health Monitoring*, Landcaster, PA, 2011, pp. 447-454.

[42]   Saito, N., Yari, T., Nagai, K., and Emomoto, K., "Damage Detection Method for CFRP Bolted Joints Using Embedded BOCDA Optical Fiber Sensor," *Structural Helath Monitoring,* vol. 1, pp. 455-462, 2011.

[43]   *Technical Order 33B-1-1: Nondestructive Inspection Methods, Basic Theory*: USAF, 2007.

[44]   (2013). *Distributed Temperature and Strain Sensing*. Available: http://lunainc.com/products/fiber-sensing-solutions/distributed-temperature-and-strain-measurements/
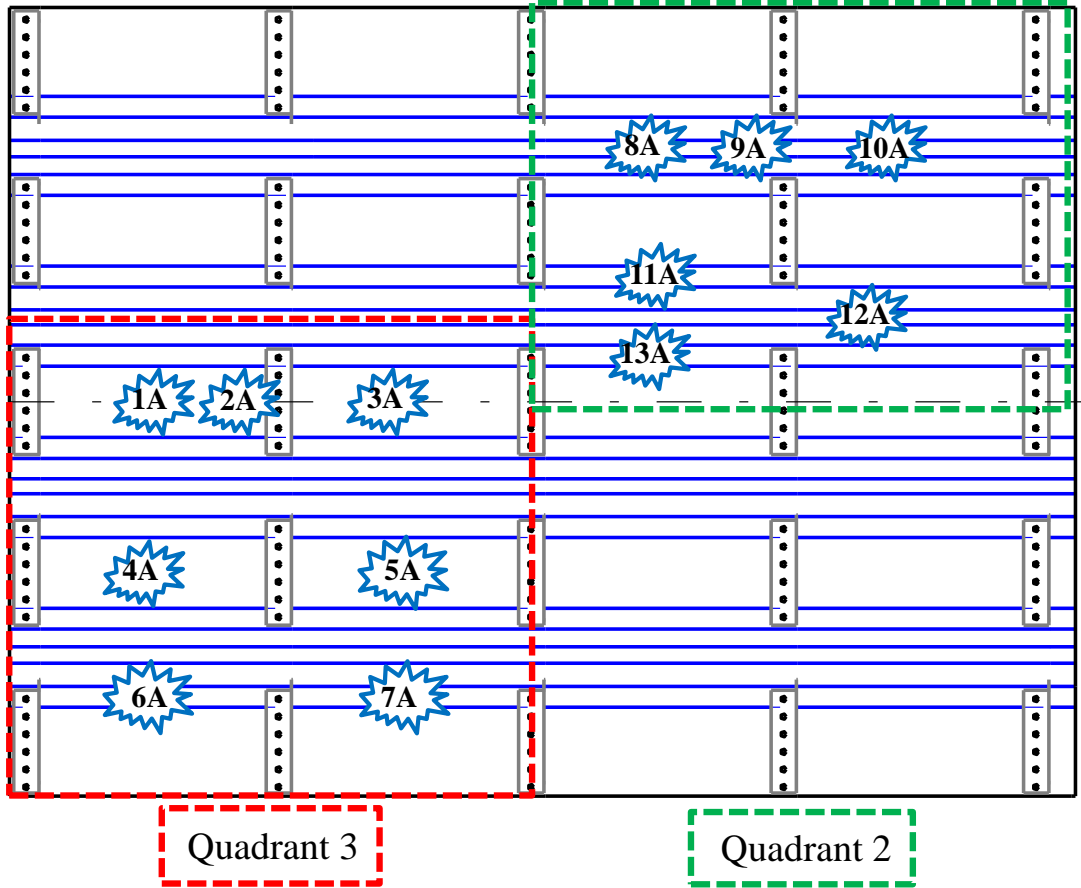
Panel A – Ice Impacts

Bays 1&2 Ice Impacts
(quadrant 3)

1A – B1-SK3-ST0-I1
2A – B1-SK3R-ST0-I1
3A – B2-SK3-ST0-I1
4A – B1-SK4-ST0-I1
5A - B2-SK4-ST0-I1
6A - B1-SK5-ST4-I2a
7A - B2-SK5-ST4-I2a

Bays 3&4 Ice Impacts
(quadrant 2)

8A – B3-SK0-ST1-I3
9A - B3/4-SK0-ST1-I3
10A - B4-SK0-ST1-I3
11A - B3-SK2-ST2-I2b
12A – B4-SK0-ST2-I3
13A –B3-SK3-ST2-I2b

Panel A - Ice Impacts (1A to 7A)

| Impact Location Number	Mass of Simulated Hail (g)	Velocity Before Impact (m/s)	(ft/s)	Energy Impact (Ft*lbs)	(Joules)	Visual Result	Damage Type	A-Scan Result	Resulting Damage Area (in²) Skin	Sub Structure
1A	107	54.9	180.1	218.6	161.2	No damage	No damage	No indication	4.43	11.29
	100.3	67.3	220.8	308.0	227.1	Not visible on front or backside	Interply delamination and stringer disbond	Visible shift in back wall signal		
2A	99.8	Not Obt.	Not Obt.	Not Obt.	Not Obt.	Not visible on front or backside	Stringer disbond	Visible shift in back wall signal over stringer.	0	0
3A	106.9	74.3	243.8	400.1	295.1	Not visible on front or backside	Interply delamination and stringer disbonding.	Shift in back wall over impact location, stringer disbond was not detected with A-scan.	3.55	1.5
4A	107	Not Obt.	Not Obt.	Not Obt.	Not Obt.	No damage, ice broke after sabot stop prior to impact	No damage	No damage		
	104.9	76.5	251.0	416.2	307.0	No damage	No damage	No indication		
	107.3	89.6	294.0	584.0	430.7	No damage	No damage	No indication	1.09	0
	109.1	91.9	301.5	624.6	460.7	No damage	No damage	No indication		
	108	100.6	330.1	741.0	546.5	Not visible on front or backside	Near surface fiber crushing, small interply delamination	Very small area of loss in amplitude		
	108.9	102	334.6	768.1	566.5	Not visible on front or backside	Interply delamination	Interply delamination detected		
5A	105.9	116.7	382.9	977.7	721.1	No front side visible indication, small 2" stringer disbond (crack) detectable on backside	Mostly interply delamination, small stringer disbond to the upper right of the impact	Large interply delamination detected, stringer disbond not detected in A-scan	54.97	1.7
6A	104.8	89.6	294.0	570.4	420.7	No front side visible indication, large, 11" long crack visually detectable on backside of stringer flange at impact location	Cracked through tapered flange at point of impact, un-zipped (disbonded) stringer flange from shear tie to shear tie	Shift in back wall over over stringer flange disbond	0	30.18
7A	106.8	72	236.2	375.3	276.8	No visual indication on front or backside of panel	Small stringer flange disbond	Stringer disbond not detected with A-scan	0	2.1
8A	103.4	87.4	286.7	140.2	394.9	No front side surface visual indication, 10.5" stringer disbond detectable on top stringer flange, full length bottom stringer flange disbond visually detectable	Full stringer disbond on both flanges, interply delamination at impact location	Shift in back wall signal at impact location as well as in both stringer flanges	7.39	20.21

Panel A - Ice Impacts (9A to 13A)

Impact Location Number	Mass of Simulated Hail (g)	Velocity Before Impact (m/s)	(ft/s)	Energy Impact (Ft*lbs)	(Joules)	Visual Result	Damage Type	A-Scan Result	Resulting Damage Area (in²) Skin	Sub Structure
9A	107.8	102	334.6	760.3	560.8	No front side surface visual indication, 3.5" stringer disbond detectable on top, left and right stringer flange	Disbonded stringers on both sides of impact, interply delamination at impact locatoin	Shift in back wall signal at impact location as well as in both stringer flanges	12.42	29.37
10A	106.8	91	298.6	599.6	442.2	No front side surface visual indication, 9" stringer disbond detectable on top stringer flange, two small visual cracks in the bottom stringer flange (1" and 4")	Stringer disbond, micro cracking in matrix at impact location	Slight loss in amplitude at impact location not detected in A-scans, stringer disbonds resulted in back wall shift	0	25.41
11A	103.2	56.3	184.7	221.8	163.6	No damage	No damage	No indication	0	15.14
	104.7	58.8	192.9	245.4	181.0	No damage	No damage	No indication		
	104.4	65.9	216.2	307.4	226.7	Very small tactile lip on backside at skin-flange interface	Small stringer delaminatin	No indication of delamination with A-scan		
	106.1	72.1	236.5	373.9	275.8	Very small tactile lip on backside at skin-flange interface	Stringer delamination	Shift in back wall signal at impact location at stringer-flange interface		
12A	105.5	72.4	237.5	374.9	276.5	No damage	No damage	No indication	0	27.9
	104.2	79.8	261.8	449.8	331.8	No damage	No damage	No indication		
	103.5	86.6	284.1	526.2	388.1	No front side surface visual indication, 10.5" stringer disbond detectable on bottom stringer flange	Stringer disbonding, micro cracking in matrix at impact location detected as drop in amplitude	A-scan shows slight drop in amplitude at impact location and shift in back wall signal at flange-skin interface		
13A	102.4	68.6	225.1	326.7	240.9	No damage	No damage	No indication	0	14.52
	107.4	70.2	230.3	358.8	264.6	No front side surface visual indication, 4.5" stringer disbond detectable on bottom stringer flange	Stringer disbond	Shift in back wall signal at impact location at stringer flange-to-skin interface		

119

Panel B – Ice Impacts

Quadrant 3

Quadrant 2

Bays 1&2 Ice Impacts

1B – B1/2-SK3-ST0-I4 – b7
2B – B1-SK3-ST3-I2b – b8
3B – B2-SK3-ST3-I2a – b9
4B – B1-SK4-ST0-I1 – b1
5B – B1/2-SK4-ST0-I4 – b6
6B – B2-SK4-ST0-I1 – b2
7B – B1-SK5-ST4-I2a – b4
8B – B2-SK5-ST4-I2a – b3
9B - B1/2-SK5-ST0-I4 – b5

Bays 3&4 Ice Impacts

10B – B4-SK1-ST0-I1 – b11
11B – B3-SK1-ST1-I2b – b12
12B – B3-SK2-ST1-I2a – b13
13B – B4-SK2-ST0-I1 – b10
14B - B3-SK2-ST2-I2b – b14

Panel B - Ice Impacts (1B to 8B)

Impact Location Number	Mass of Simulated Hail (g)	Velocity Before Impact (m/s)	(ft/s)	Energy Impact (Ft*lbs)	(Joules)	Visual Result	Damage Type	A-Scan Result	Resulting Damage Area (in²) Skin	Sub Structure
1B	108	111.4	365.5	908.6	670.1	Small paint crack around one fastener visible from front side, 2" crack in built-up section, 1" crack in corner bend radius of shear tie.	Shear tie built-up section delamination, cracked shear tie	Slight shift in back wall signal over small area of shera tie	0	3.03
2B	107.7	61.1	200.5	272.6	201.0	No visual indication on front or backside of panel	Small stringer disbond	Shift in back wall signal at stringer flange-to-skin interface	0	8.12
3B	107.9	56.5	185.4	233.5	172.2	No front side surface visual indication, 2.5" crack visible on backside of panel at the flange-skin interface	Interply delamination at impact location, edge of stringer disbond on stringer side.	No indication	0	4.12
4B	108.1	102	334.6	762.4	562.3	Not visible on painted or backside	Interply delamination	Interply delamination detected	11.28	20.48
5B	106.2	94.7	310.7	645.6	476.2	Slight paint cip on surface of panel	No damage	No indication		14.9
	107.1	117.4	385.2	1000.7	738.1	Paint crack around circumference of fastener, 4.5" crack at the skin to built-up section interface, 4" crack in the corner bend of the shear tie	Delamination of built-up section at shear tie, cracked shear tie	Back wall signal shift at shear tie built-up section to skin interface.	0	
6B	106.2	118.5	388.8	1011.0	745.6	Not visible on painted or backside	Extensive interply delamination	Some loss of back wall signal at impact locaiton, shift in signal	21.27	0
7B	108.2	71.8	235.6	378.1	278.9	No front side surface visual indication, 17.5" stringer flange crack visible	Full stringer flange disbond	Shift in back wall signal at stringer flange-to-skin interface	0	23.16
8B	105.5	73.4	240.8	385.3	284.2	No front side surface visual indication, multiple cracked plies in the tapered flange ranging from 1" to 2.5"	Partially disbonded stirnger flange	Shift in back wall signal at stringer flange-to-skin interface	0	6.05

121

Impact Location Number	Mass of Simulated Hail (g)	Velocity Before Impact (m/s)	(ft/s)	Energy Impact (Ft*lbs)	(Joules)	Visual Result	Damage Type	A-Scan Result	Resulting Damage Area (in²) Skin	Sub Structure
	108.3	84.2	276.2	520.5	383.9	No damage	No damage	No damage		
9B	107.2	116.5	382.2	986.3	727.5	Paint chip on surface of panel, 1" diameter perminant paint scuff, 2" crack at the built-up pad-to-skin interface, 4.5" crack in the corner bend of the shear	Shear tie built-up pad section delamination, cracked shear tie	Shift in back wall signal at the built-up pad section-to-skin interface	0	22.23
	108.3	89.4	293.3	586.8	432.8	No Damge	No damage	No indication		
	108.5	100.7	330.4	745.9	550.1	No damage, ice broke after sabot stop prior to impact	No damage	No indication		
10B	107.4	117	383.9	996.7	735.1	No front side surface visual indication, 17.5" stringer disbond crack visible on backside	Interply delamination in the skin, full length stringer disbond, and partial delamination in the shear tie built-up pad section	Shift in back wall signal over skin at impact location, shift in back wall signal at stringer flange-to-skin interface	20.01	29.82
11B	102.2	86.6	284.1	519.6	383.2	No front side surface visual indication, 6" stringer flage crack visible on backside of panel	Stringer flange disbond	Shift in back wall signal at stringer flange-to-skin interface	0	16.09
12B	107.1	88.9	291.7	573.8	423.2	No front side surface visual indication, 4.5" stringer flange crack visible on backside of panel	Stringer flange disbond	Shift in back wall signal at stringer flange-to-skin interface	0	8.41
	106.7	91.3	299.5	602.9	444.7	No Damage	No damage	No indication		
	105.8	101	331.4	731.6	539.6	No Damage	No damage	No indication		
13B	108.1	111	364.2	902.9	666.0	No front side surface visual indication, 15.5" stringer flange crack visible on backside of panel	Interply delamination in the skin, full length stringer disbond	Shift in back wall signal at stringer flange-to-skin interface	12.55	40.23
14B	103.2	88.9	291.7	552.9	407.8	No front side surface visual indication, two, 2.5" stringer flange cracks visible on backside of panel	Stringer flange disbond	Shift in back wall signal at stringer flange-to-skin interface	0	9.45

Panel B - Ice Impacts (9B to 14B)

122

Panel A (Bay 1,2,3&4) – Hard Impacts
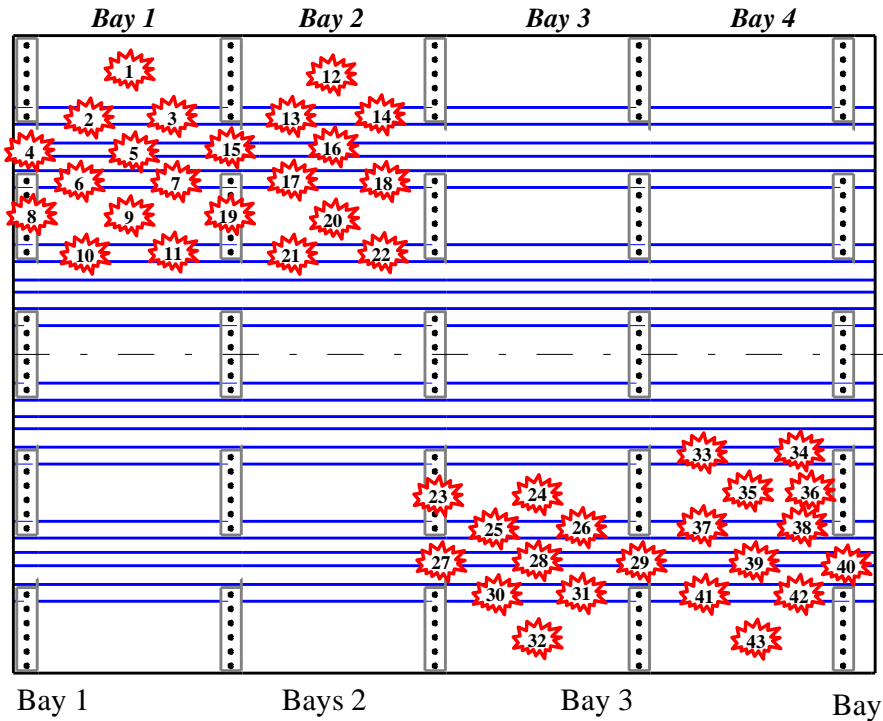
1 – B1-SK1-ST0-H1	12 – B2-SK1-ST0-H1	23 – B2/3-SK4-ST0-H4	33 – B4-SK4-ST3L-H2c
2 – B1-SK1-ST1L-H2b	13 – B2-SK1-ST1L-H2a	24 – B3-SK4-ST0-H1	34 – B4-SK4-ST3R-H2c
3 – B1-SK1-ST1R-H2b	14 – B2-SK1-ST1R-H2a	25 – B3-SK4-ST4L-H2a	35 – B4-SK4-ST0-H1
4 – B1-SK0-ST1L-H3	15 – B1/2-SK0-ST1-H3	26 – B3-SK4-ST4R-H2a	36 – B4-SK4R-ST0-H1
5 – B1-SK0-ST1-H3	16 – B2-SK0-ST1L-H3	27 – B2/3-SK0-ST3-H3	37 – B4-SK4-ST4L-H2a
6 – B1-SK2-ST1L-H2c	17 – B2-SK2-ST1L-H2c	28 – B3-SK0-ST4-H3	38 – B4-SK4-ST4R-H2a
7 – B1-SK2-ST1R-H2c	18 – B2-SK2-ST1R-H2c	29 – B3/4-SK0-ST4-H3	39 – B4-SK0-ST4-H3
8 – B1-SK2-ST0-H4	19 –B1/2-SK2-ST0-H4	30 – B3-SK5-ST4L-H2b	40 – B4-SK0-ST4R-H3
9 – B1-SK2-ST0-H1	20 – B2-SK2-ST0-H1	31 – B3-SK5-ST4R-H2b	41 – B4-SK5-ST4L-H2b
10 – B1-SK2-ST2L-H2b	21 – B2-SK2-ST2L-H2b	32 – B3-SK5-ST0-H1	42 – B4-SK5-ST4R-H2b
11 – B1-SK2-ST2R-H2b	22 – B2-SK2-ST2R-H2b		43 – B4-SK5-ST0-H1

Indicates strain results obtained and presented

Panel A - Hard Impacts (1-16)

Impact Location Number	Location BAY#.SKIN#.STRINGER#-Impact Type	Velocity (ft/sec)	(m/sec)	Highest Energy Impact (Ft*lbs)	(Joules)	Visual Result	Damage Type	A-Scan Result	Resulting Damage Area (in²)
1	B1-SK1-ST0-H1	19.6	6.0	90	122.0	Visible dent	Near surface crushed fibers	Local loss of back wall signal	0.52
2	B1-SK1-ST1L-H2b	19.6	6.0	90	122.0	No visual dent	No damage	Minor changes in back wall signal	0.00
3	B1-SK1-ST1R-H2b	16.0	4.9	60	81.3	Very small visible dent	No damage	No indication	0.00
4	B1-SK0-ST1L-H3	13.9	4.2	45	61.0	Visible dent	Near surface fiber crushing	Very local loss of back wall signal at impact location	0.23
5	B1-SK0-ST1-H3	13.9	4.2	45	61.0	Visible dent	Near surface fiber crushing	Very local loss of back wall signal at impact location	0.47
6	B1-SK2-ST1L-H2c	18.8	5.7	55	74.6	Very small visual dent	Near surface fiber crushing	No A-scan Change	0.28
7	B1-SK2-ST1R-H2c	17.3	5.3	70	94.9	Visible dent	Interply delamination	Shift of back wall signal	1.67
8	B1-SK2-ST0-H4	17.9	5.5	75	101.7	Visible dent	Delamination of shear tie tapered section build up to skin interface	Local loss of back wall signal	4.35
9	B1-SK2-ST0-H1	17.9	5.5	75	101.7	Visual dent	Near surface crushed fibers	Local loss of back wall signal	0.85
10	B1-SK2-ST2L-H2b	17.9	5.5	75	101.7	Visible dent	Stringer flange delamination	Shift in stringer back wall signal	1.36
11	B1-SK2-ST2R-H2b	19.6	6.0	90	122.0	Visible dent	Interply delamination	Shift of back wall signal in the skin	2.19
12	B2-SK1-ST0-H1	16.0	4.9	60	81.3	Small visual dent	Near surface fiber crushing	Local loss of back wall	0.41
13	B2-SK1-ST1L-H2a	16.0	4.9	60	81.3	Visual dent, very small crack on paint	Stringer flange delamination	A-scan shows delam on stringer	0.93
14	B2-SK1-ST1R-H2a	17.9	5.5	75	101.7	Small visual dent	Interply delamination, and near surface fiber crushing	Local loss of back wall signal, shift in back wall	0.98
15	B1/2-SK0-ST1-H3	16.0	4.9	60	81.3	Visual dent	Near surface crushed fibers and interply delamination	Local loss of back wall signal	0.59
16	B2-SK0-ST1L-H3	17.9	5.5	75	101.7	Visual dent	Near surface crushed fibers, small interply delamination	Loss of back wall signal at impact location, small area of shift in back wall signal	0.81

Panel A - Hard Impacts (17-33)

Impact Location Number	Location BAY#.SKIN#.STRINGER#-Impact Type	Velocity (ft/sec)	(m/sec)	Highest Energy Impact (Ft*lbs)	(Joules)	Visual Result	Damage Type	A-Scan Result	Resulting Damage Area (in^2)
17	B2-SK2-ST1L-H2c	19.6	6.0	90	122.0	Visible dent	Interply delamination	Shift in back wall signal	1.23
18	B2-SK2-ST1R-H2c	21.2	6.5	105	142.4	Visual crack parallel to stringer and visual dent	Stringer flange delamination	Local loss of back wall signal	2.24
19	B1/2-SK2-ST0-H4	19.6	6.0	90	122.0	Visual dent	Interply delamination	Shift of back wall signal	0.85
20	B2-SK2-ST0-H1	16.0	4.9	60	81.3	Visible dent	Near surface fiber crushing and slight interply delamination	Loss of back wall at impact location, partial shift in signal	0.75
21	B2-SK2-ST2L-H2b	19.6	6.0	90	122.0	Large, visual dent	Interply delamination	Shift of back wall signal	3.46
22	B2-SK2-ST2R-H2b	22.0	6.7	112.5	152.5	Large, visual dent	Interply delamination	Shift of back wall signal	2.19
23	B2/3-SK4-ST0-H4	19.6	6.0	90	122.0	Visual dent on front of panel. Back side visible crack at	Delamination at the shear tie built-up skin interface.	Shift in back wall signal over built-up section, much larger than usual	10.37
24	B3-SK4-ST0-H1	16.0	4.9	60	81.3	Visible dent	Near surface fiber crushing	Local loss of back wall signal	0.89
25	B3-SK4-ST4L-H2a	16.0	4.9	60	81.3	Visual dent	Flange delamination	Larger delam, 2 in sq est	2.85
26	B3-SK4-ST4R-H2a	21.2	6.5	105	142.4	Large visual dent, crack on paint surface	Flange delamination	Loss of back wall, possible delamination at stringer	2.43
27	B2/3-SK0-ST3-H3	19.6	6.0	90	122.0	Visual dent	Near surface fiber crushing and interply	Loss of back wall signal	1.07
28	B3-SK0-ST4-H3	19.6	6.0	90	122.0	Visual dent	Interply delamination	Loss of back wall signal, partial shift	1.17
29	B3/4-SK0-ST4-H3	17.9	5.5	75	101.7	Visual dent	Interply delamination	Loss of back wall signal	1.18
30	B3-SK5-ST4L-H2b	21.2	6.5	105	142.4	Visual dent	Interply delamination	Loss of back wall signal	3.89
31	B3-SK5-ST4R-H2b	20.5	6.2	97.5	132.2	Visual dent	Interply delamination	Local loss of back wall signal	1.63
32	B3-SK5-ST0-H1	21.2	6.5	105	142.4	Visual dent	Near surface fiber crushing	Local loss of back wall signal	0.81
33	B4-SK4-ST3L-H2c	20.5	6.2	97.5	132.2	Visual dent	Interply delamination	Shift in back wall signal	5.14

125

Impact Location Number	Location BAY#.SKIN#.ST RINGER#-Impact Type	Velocity		Highest Energy Impact		Visual Result	Damage Type	A-Scan Result	Resulting Damage Area (in²)
		(ft/sec)	(m/sec)	(Ft*lbs)	(Joules)				
						Panel A - Hard Impacts (34-43)			
34	B4-SK4-ST3R-H2c	18.8	5.7	82.5	111.9	Visual dent	Interply delamination	Local loss of back wall signal	2.55
35	B4-SK4-ST0-H1	11.3	3.5	20	27.1	Slight dent visible on surface	Near surface fiber crushing	No Change	0.25
36	B4-SK4R-ST0-H1	11.3	3.5	20	27.1	Slight dent visible on surface	Near surface fiber crushing	Some local loss of back wall at damage location	0.55
37	B4-SK4-ST4L-H2a	19.6	6.0	90	122.0	Visual dent, small crack in paint	Interply delamination	Local shift of back wall signal	2.26
38	B4-SK4-ST4R-H2a	17.9	5.5	50	67.8	Visual dent on paint, very small crack on paint	Interply delamination	Loss of back wall signal under damage location	0.85
39	B4-SK0-ST4-H3	21.2	6.5	105	142.4	Visual dent	Interply delamination	Local loss of back wall signal	1.77
40	B4-SK0-ST4R-H3	17.9	5.5	75	101.7	Visual dent	Near surface fiber crushing	Local loss of back wall signal	0.31
41	B4-SK5-ST4L-H2b	16.0	4.9	60	81.3	Small visual dent	No damage	Local loss of back wall signal	0.00
42	B4-SK5-ST4R-H2b	18.8	5.7	82.5	111.9	Visual dent, paint crack on surface	Interply delamination	Local loss of back wall signal	1.68
43	B4-SK5-ST0-H1	17.9	5.5	75	101.7	Visual dent	Near surface fiber crushing	Local loss of back wall signal	0.51
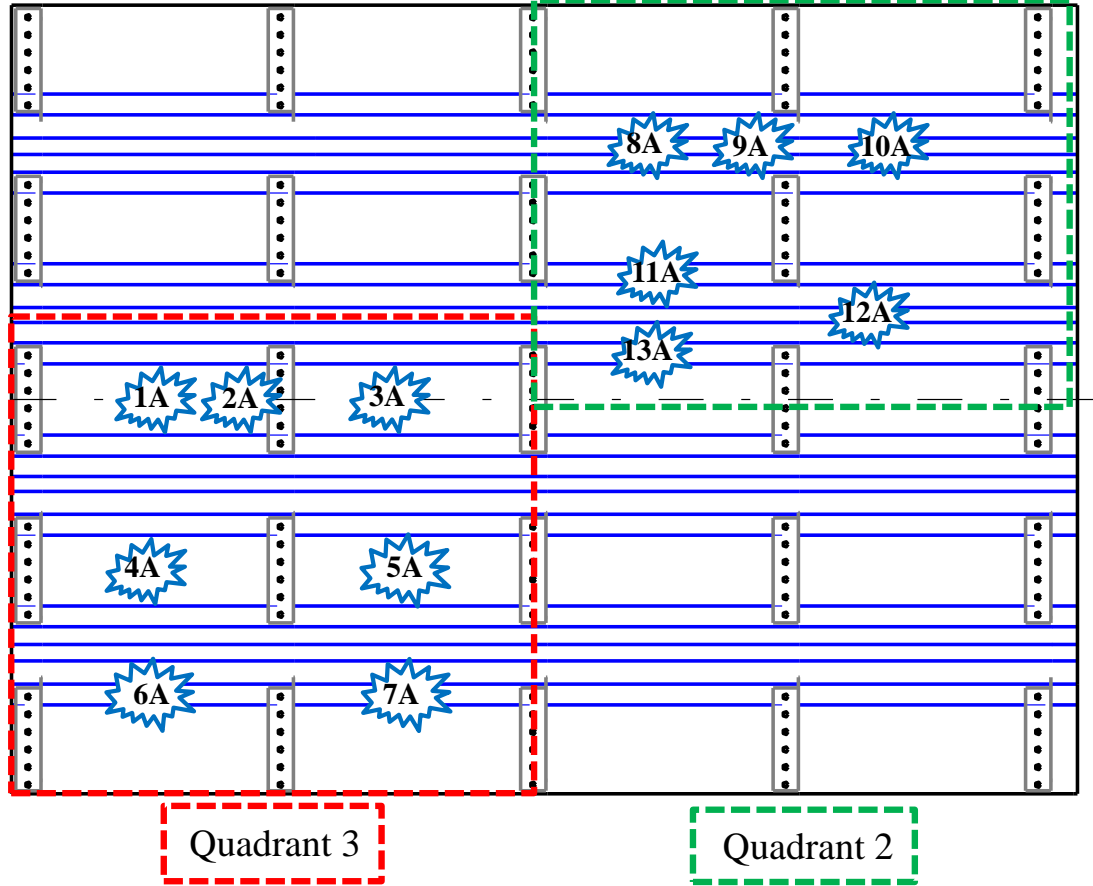
126

Panel A – Ice Impacts

Quadrant 3

Quadrant 2

Bays 1&2 Ice Impacts
(quadrant 3)

1A – B1-SK3-ST0-I1
2A – B1-SK3R-ST0-I1
3A – B2-SK3-ST0-I1
4A – B1-SK4-ST0-I1
5A - B2-SK4-ST0-I1
6A - B1-SK5-ST4-I2a
7A - B2-SK5-ST4-I2a

Bays 3&4 Ice Impacts
(quadrant 2)

8A – B3-SK0-ST1-I3
9A - B3/4-SK0-ST1-I3
10A - B4-SK0-ST1-I3
11A - B3-SK2-ST2-I2b
12A – B4-SK0-ST2-I3
13A –B3-SK3-ST2-I2b

Panel A – Full Panel Inspections

Ultrasonic Amplitude

Ultrasonic Time of Flight

128

Panel A – Full Panel Inspections

Resonance Amplitude X Plot

Resonance Phase Y Plot

Skin Impact
Max Impact Energy: 308 ft lbs, 227.1 Joules
Max Impact Velocity: 220.8 ft/s, 67.3 m/s
Visual Indication: No visual indication on front or back side of panel
Damage Area: I.D. 4.43, S.D 11.29 in^2
Type of Damage: Interply delamination, stringer flange disbonding

Interply Delamination

Stringer Disbond

UT Resonance Y-Plot

UT Amplitude C-Scan

UT Time of Flight C-Scan

× Impact Location   Quadrant 3

130

www.manaraa.com
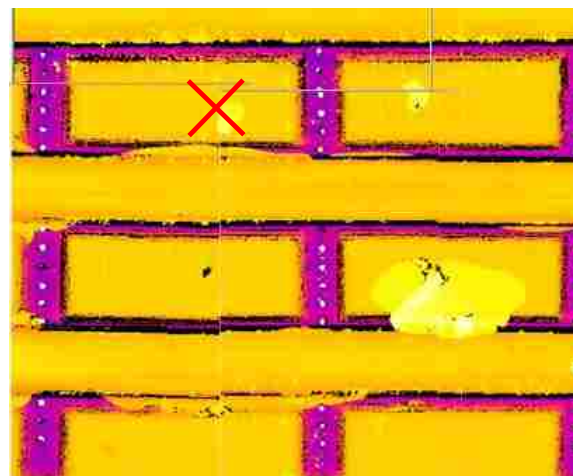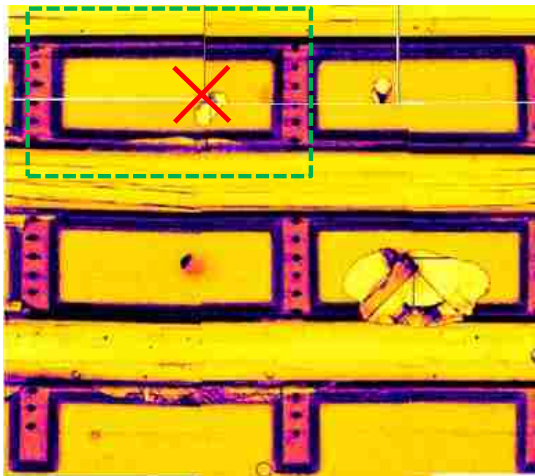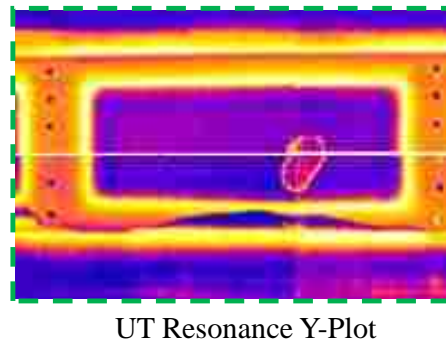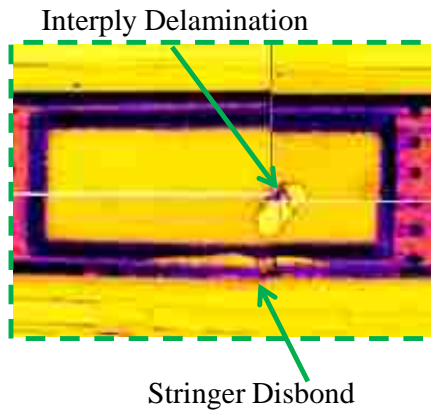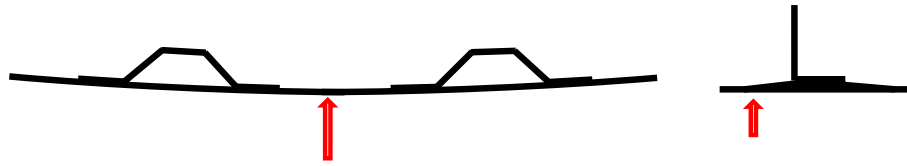
Skin Impact Near Shear Tie Tapered Build Up
Max Impact Energy: Not obtained
Max Impact Velocity: Not obtained
Visual Indication: No visual indication on front or back side of panel
Damage Area: None
Type of Damage: Slight loss in amplitude could indicate micro cracking in matrix at impact location

Slight Increase in Attenuation
(not noticeable in TOF)

No Indication
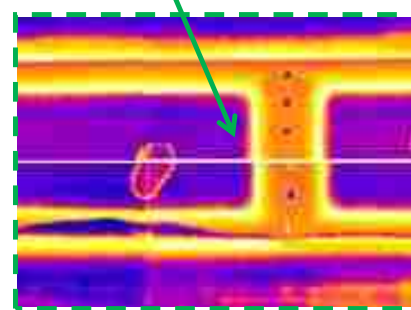
UT Resonance Y-Plot
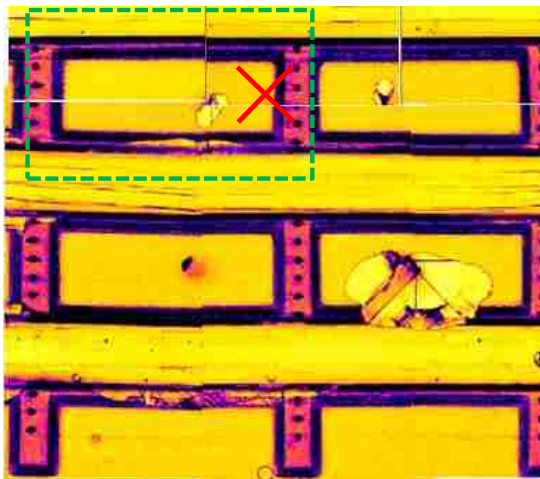
UT Amplitude C-Scan   UT Time of Flight C-Scan
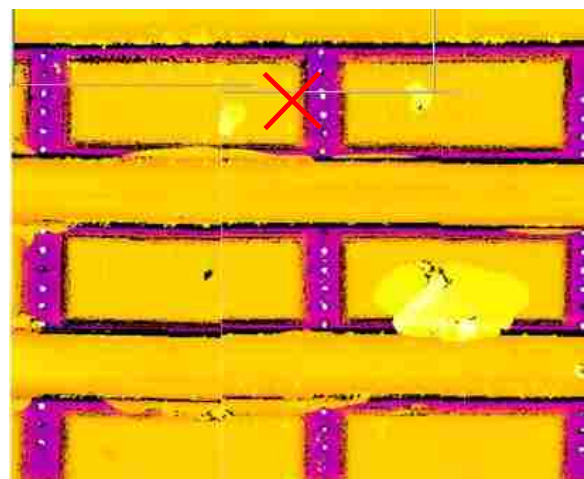
✕ Impact Location   Quadrant 3
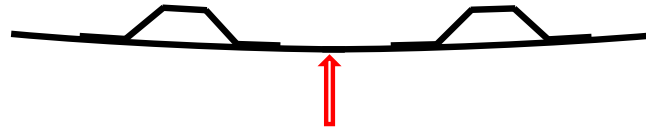
Skin Impact
Max Impact Energy: 400.1 ft lbs, 295.1 Joules
Max Impact Velocity: 243.8 ft/s, 74.3 m/s
Visual Indication: No visual indication on front or back side of panel
Damage Area: I.D. 3.55, S.D 1.50 in^2
Type of Damage: Interply delamination and stringer disbond. Stringer disbond was not detected in UT amplitude, but was in TOF and resonance.

Interply Delamination
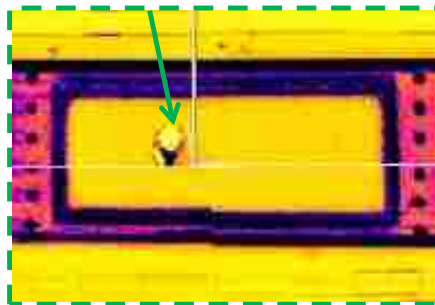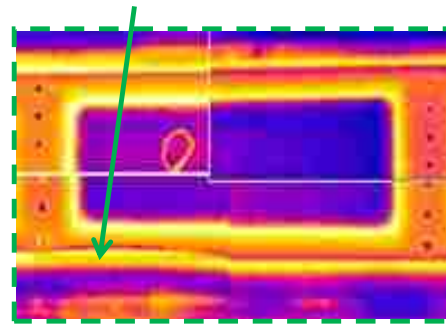
Stringer Delamination not detected in amplitude
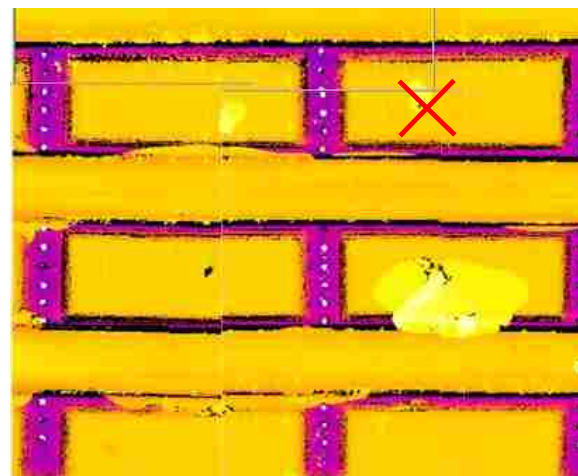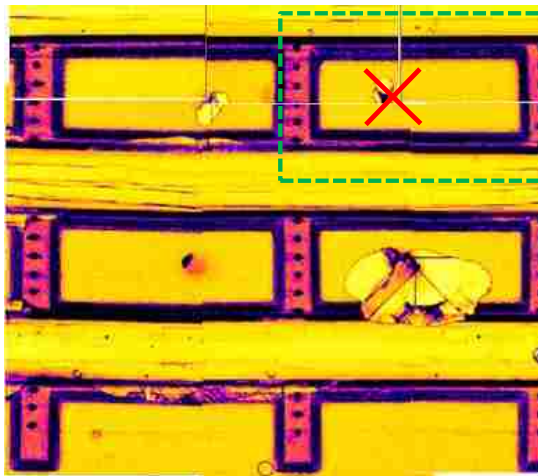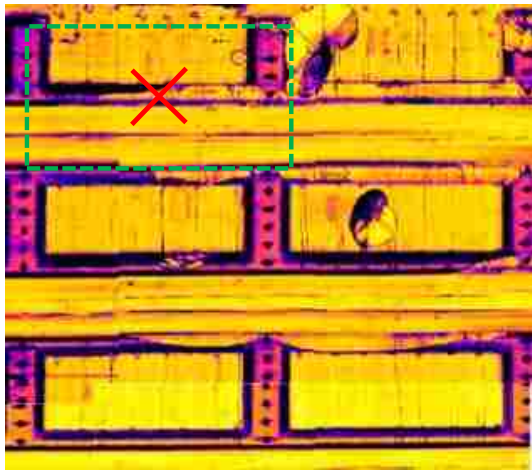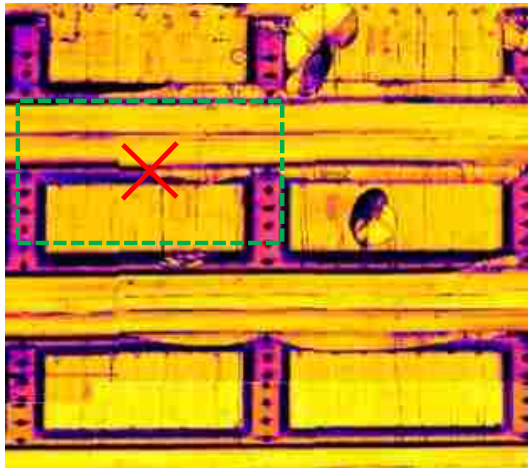
Stringer Disbond

UT Resonance Y-Plot

UT Amplitude C-Scan

UT Time of Flight C-Scan

✕ Impact Location

Quadrant 3
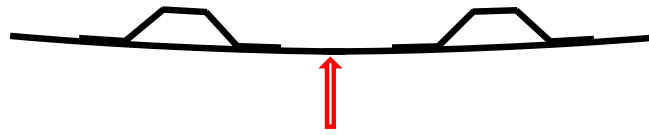
Skin Impact
Max Impact Energy: 741.0 ft lbs, 546.5 Joules
Max Impact Velocity: 330.1 ft/s, 100.6 m/s
Visual Indication: No visual indications
Damage Area: I.D. 1.09, S.D. 0.0 in^2
Type of Damage: Near surface fiber crushing, small interply delamination
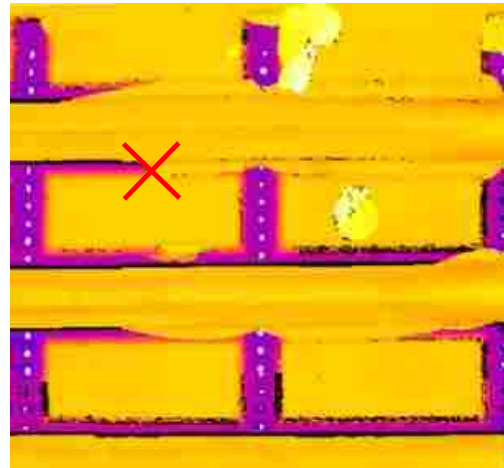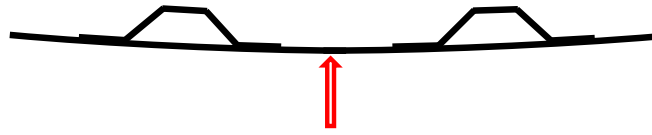
Small Interply Delamination

UT Resonance Y-Plot

UT Amplitude C-Scan

UT Time of Flight C-Scan

✕ Impact Location

Quadrant 3

Skin Impact

Max Impact Energy: 977.7 ft lbs, 721.1 Joules

Max Impact Velocity: 382.9 ft/s, 116.7 m/s

Visual Indication: No front side visible indication, small 2" stringer flange crack detectable on backside

Damage Area: Interply Delamination 54.97 in^2, Stringer Disbond 1.70 in^2

Type of Damage: Mostly interply delamination, small stringer disbond to the upper right of the impact area not detected in amplitude scan

Stringer Delamination

Interply Delamination

UT Resonance Y-Plot

UT Amplitude C-Scan

UT Time of Flight C-Scan

✕ Impact Location

Quadrant 3

134

Edge of Stringer Flange (Not Stringer Side)
Max Impact Energy: 570.4 ft lbs, 420.7 Joules
Max Impact Velocity: 294.0 ft/s, 89.6 m/s
Visual Indication: No front side e visible indication, large, 11" long crack visually detectable on back side of stringer at impact location
Damage Area: I.D. 0.0, S.D 30.18 in^2
Type of Damage: Cracked through tapered flange at point of impact, un-zipped (disbonded) stringer flange from shear tie to shear tie
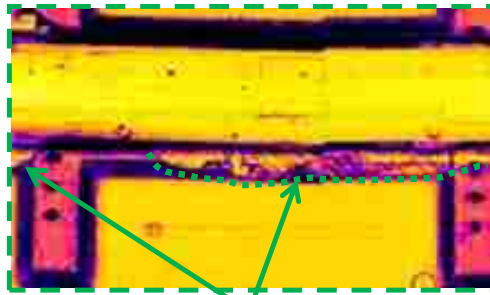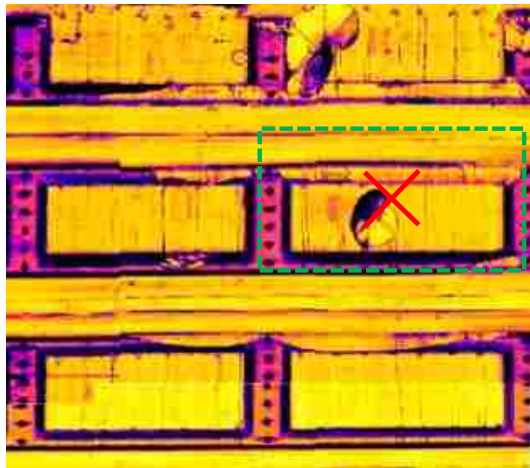
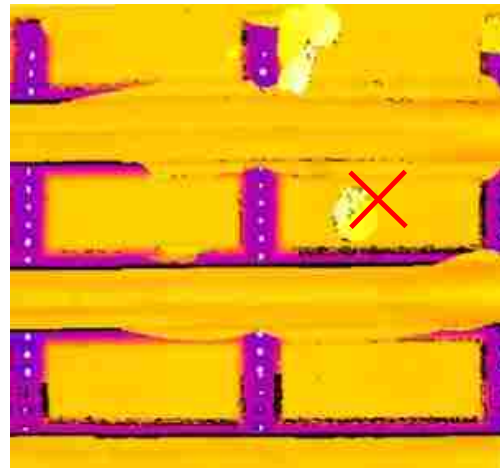

Stringer Disbond
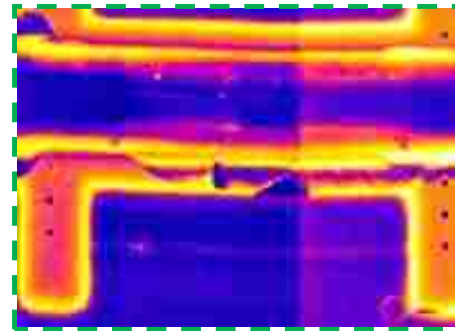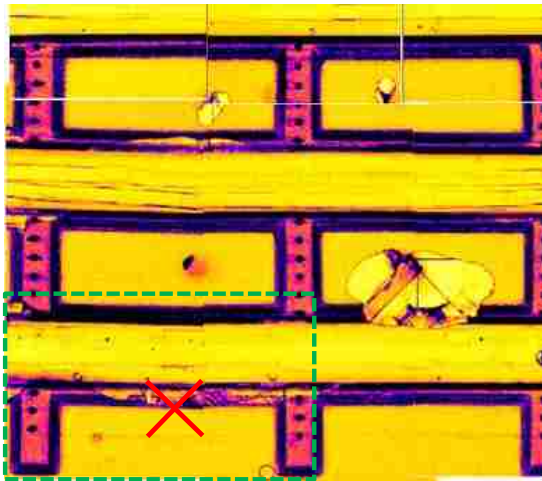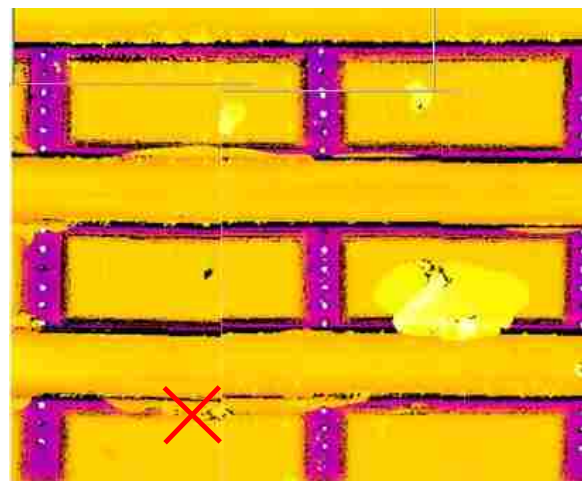
UT Resonance Y-Plot

UT Amplitude C-Scan

UT Time of Flight C-Scan

✕ Impact Location

Quadrant 3
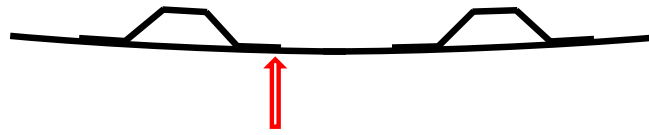
Edge of Stringer Flange (Not Stringer Side)
Max Impact Energy: 375.3 ft lbs, 276.8 Joules
Max Impact Velocity: 236.2 ft/s, 72 m/s
Visual Indication: No visual indication on front or back side of panel
Damage Area: I.D. 0.0, S.D. 2.10 in^2
Type of Damage: Small stringer disbond detected in resonance and TOF, but not amplitude
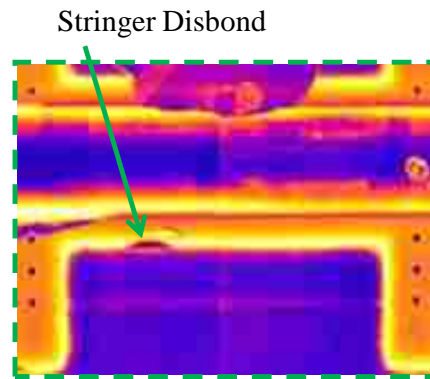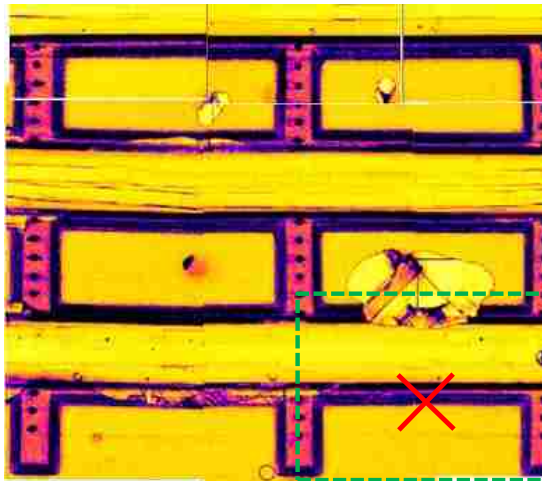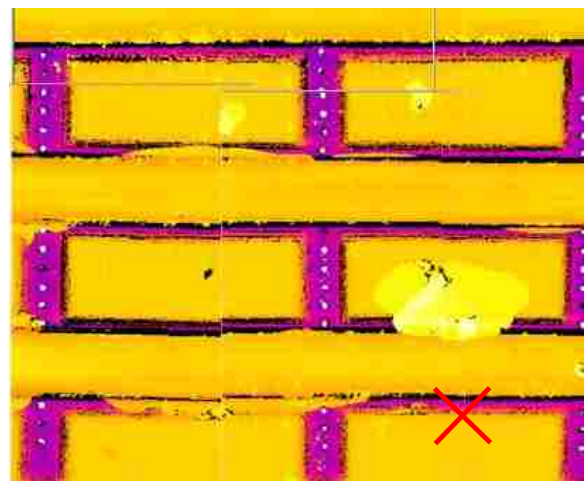
Stringer Disbond

UT Resonance Y-Plot

UT Amplitude C-Scan

UT Time of Flight C-Scan

$\times$ Impact Location

Quadrant 3

136

**Center of Stringer Between Flanges**
Max Impact Energy: 535.4 ft lbs, 394.9 Joules
Max Impact Velocity: 286.7 ft/s, 87.4 m/s
Visual Indication: No front side surface visual indication, 10.5" stringer delamination detectable on top stringer flange, full length bottom stringer flange delamination detectable
Damage Area: I.D. 7.39, S.D. 20.21 in^2
Type of Damage: Full stringer disbond on both flanges, interply delamination at impact location

Interply Delamination
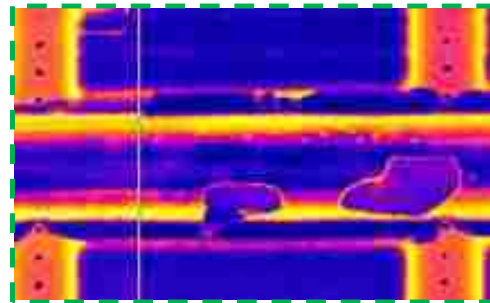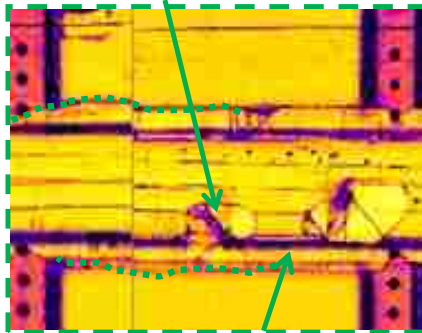
Full Stringer Disbonds
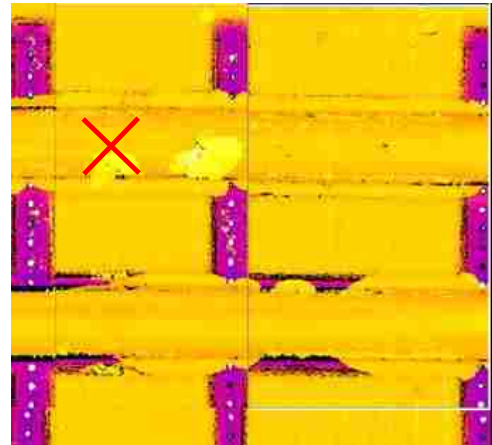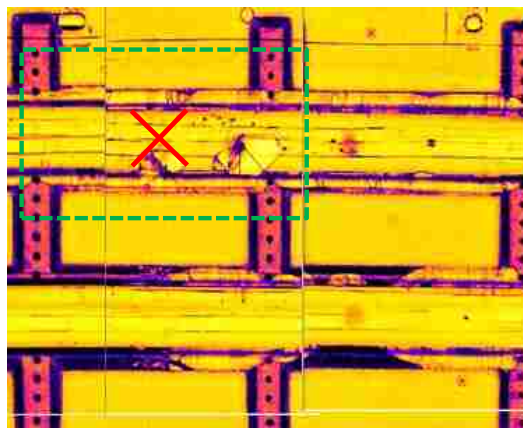
UT Resonance Y-Plot

UT Amplitude C-Scan

UT Time of Flight C-Scan

Quadrant 2

✗ Impact Location

Center of Stringer Between Flanges (Between Shear ties)
Max Impact Energy: 760.3 ft lbs, 560.8 Joules
Max Impact Velocity: 334.6 ft/s, 102 m/s
Visual Indication: No front side surface visual indication, 3.5" stringer delamination detectable on top, left and right stringer flange
Damage Area: I.D. 12.42, S.D. 29.37 in^2
Type of Damage: Disbonded stringers on both sides of impact, interply delamination

Interply Delamination
Stringer Disbonds
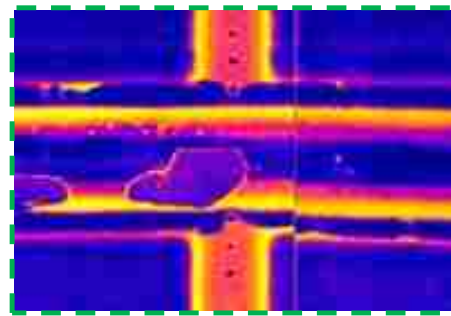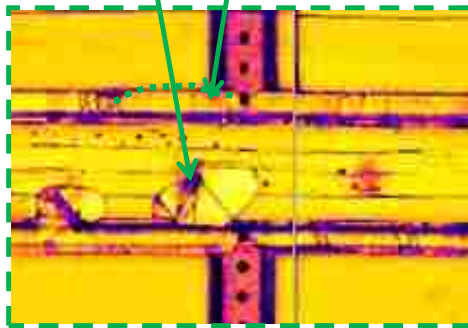
UT Resonance Y-Plot
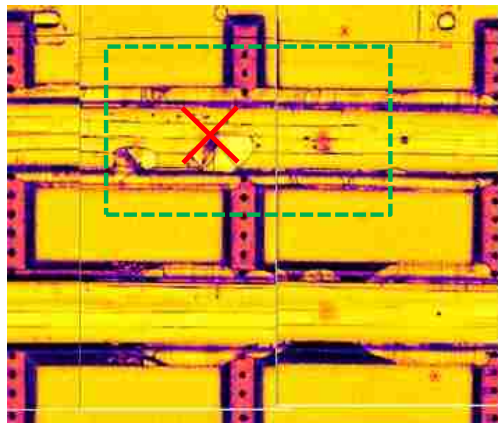
UT Amplitude C-Scan
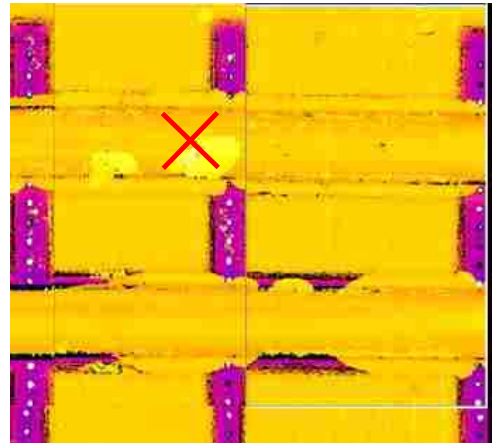
UT Time of Flight C-Scan

$\times$ Impact Location

Quadrant 2
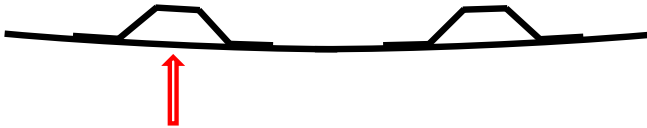
Center of Stringer Between Flanges
Max Impact Energy: 599.6 ft lbs, 442.2 Joules
Max Impact Velocity: 298.6 ft/s, 91 m/s
Visual Indication: No front side surface visual indication, 9" stringer delamination detectable on top stringer flange, two small visual cracks in the bottom stringer flange (1" and 4")
Damage Area: I.D 0.0, 25.41 S.D. in^2
Type of Damage: Stringer disbonds, micro cracking in matrix at impact location detected as drop in amplitude

Decrease in Amplitude
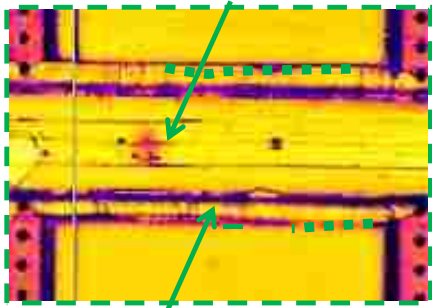
Full Stringer Flange
Disbondss
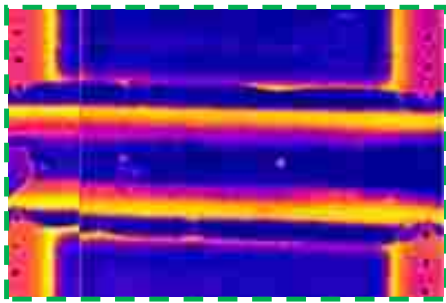
UT Resonance Y-Plot
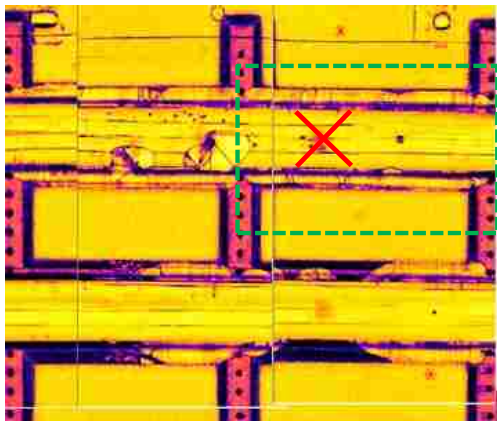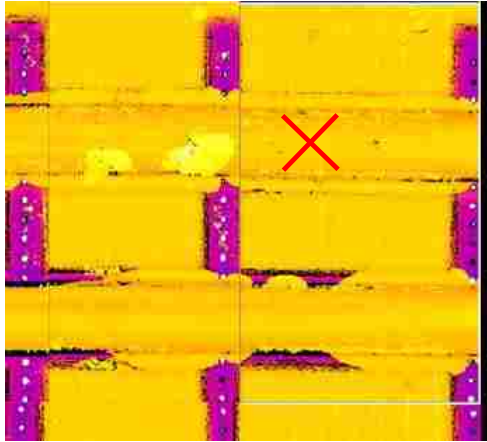
UT Amplitude C-Scan

UT Time of Flight C-Scan

$\times$ Impact Location

Quadrant 2

Center of Stringer Flange
Max Impact Energy: 373.9 ft lbs, 275.8 Joules
Max Impact Velocity: 236.5 ft/s, 72.1 m/s
Visual Indication: No visual indication on front or back side of panel, small tactile lip at the skin to string flange interface can be felt with hand at impact location
Damage Area: I.D. 0.0, 15.14 S.D. in^2
Type of Damage: Stringer disbonded detected in amplitude, TOF and resonance, no interply delamination detected in the skin
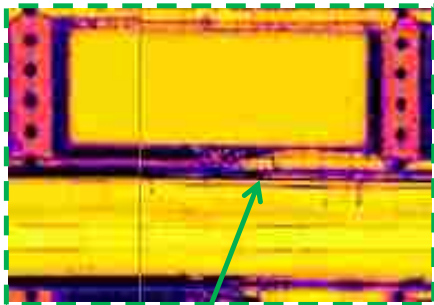
Stringer Disbond
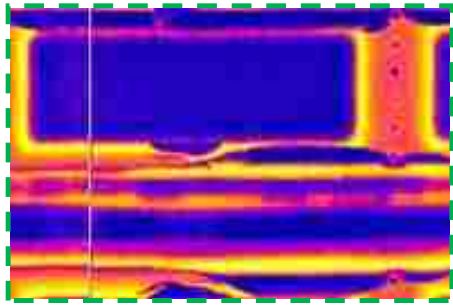
UT Resonance Y-Plot
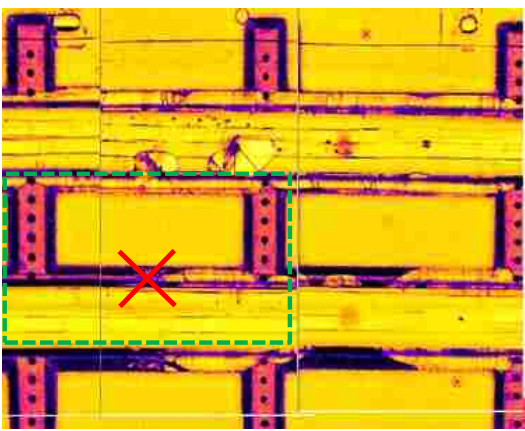
UT Amplitude C-Scan
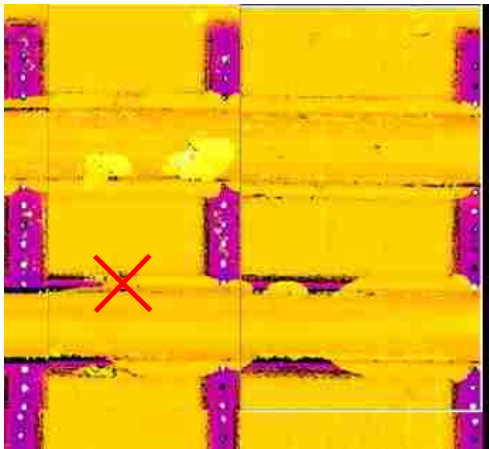
UT Time of Flight C-Scan

$\times$ Impact Location

Quadrant 2

Center of Stringer Between Flanges
Max Impact Energy: 526.2 ft lbs, 388.1 Joules
Max Impact Velocity: 284.1 ft/s, 86.6 m/s
Visual Indication: No front side surface visual indication, 10.5" stringer flange crack detectable on bottom stringer flange
Damage Area: I.D. 0.0, S.D. 27.90 in^2
Type of Damage: Stringer disbond, micro cracking in matrix at impact location detected as drop in amplitude

Decrease in Amplitude
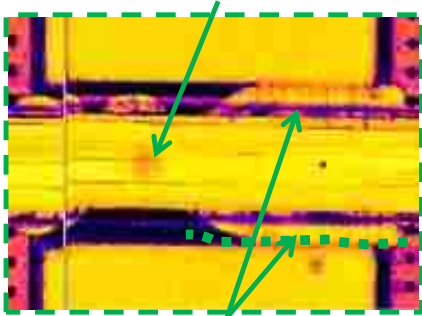
Stringer Disbonds
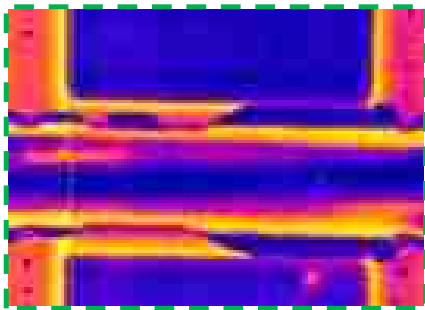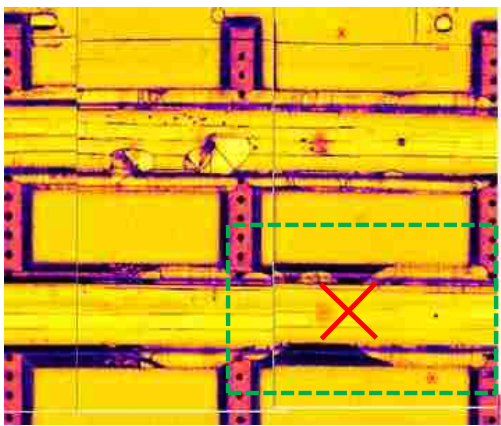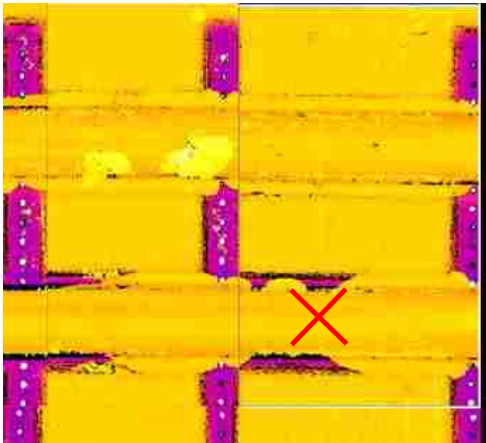
UT Resonance Y-Plot

UT Amplitude C-Scan

UT Time of Flight C-Scan

✕ Impact Location

Quadrant 2
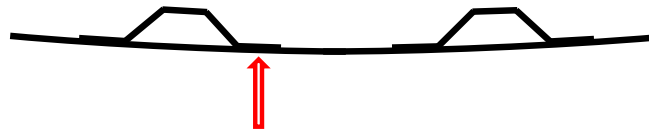
Center of Stringer Flange
Max Impact Energy: 358.8 ft lbs, 264.6 Joules
Max Impact Velocity: 230.3 ft/s, 70.2 m/s
Visual Indication: No front side surface visual indication, 4.5" stringer delamination detectable on bottom stringer flange
Damage Area: I.D. 0.0, S.D. 14.52 in^2
Type of Damage: Stringer disbond
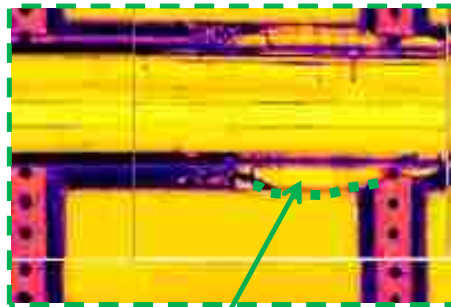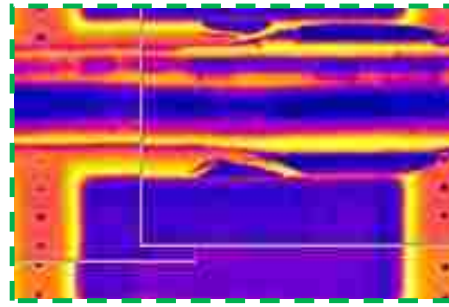
Stringer Disbond

UT Resonance Y-Plot
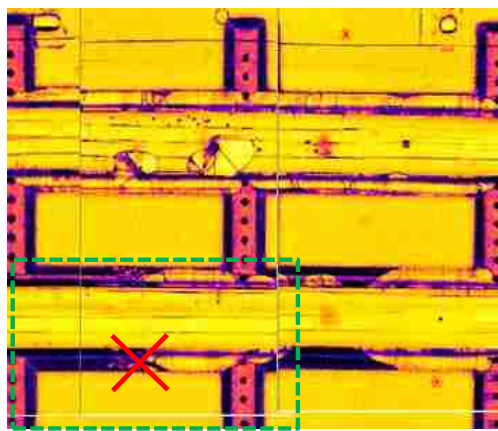
UT Amplitude C-Scan
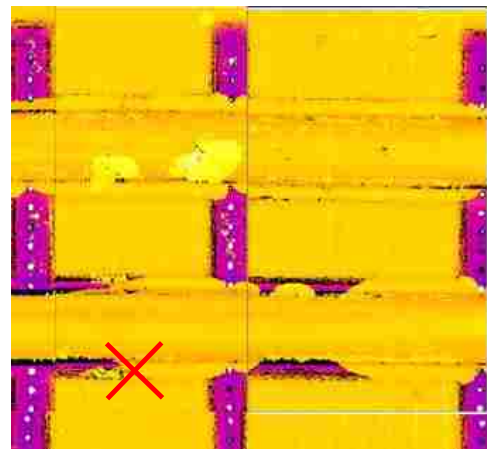
UT Time of Flight C-Scan

✕ Impact Location

Quadrant 2

142

Panel B – Ice Impacts
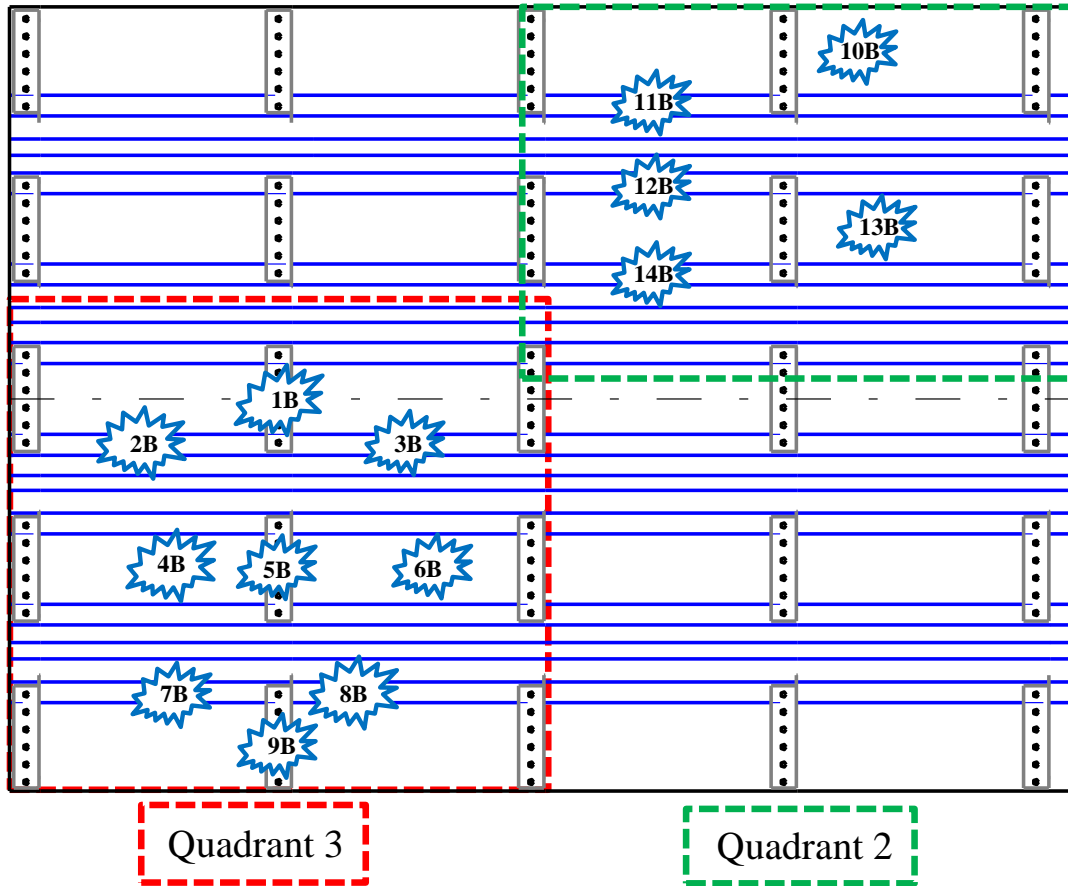
Quadrant 3

Quadrant 2

Bays 1&2 Ice Impacts

1B – B1/2-SK3-ST0-I4 – b7
2B – B1-SK3-ST3-I2b – b8
3B – B2-SK3-ST3-I2a – b9
4B – B1-SK4-ST0-I1 – b1
5B – B1/2-SK4-ST0-I4 – b6
6B – B2-SK4-ST0-I1 – b2
7B – B1-SK5-ST4-I2a – b4
8B – B2-SK5-ST4-I2a – b3
9B - B1/2-SK5-ST0-I4 – b5

Bays 3&4 Ice Impacts

10B – B4-SK1-ST0-I1 – b11
11B – B3-SK1-ST1-I2b – b12
12B – B3-SK2-ST1-I2a – b13
13B – B4-SK2-ST0-I1 – b10
14B - B3-SK2-ST2-I2b – b14

Panel B – Full Panel Inspections
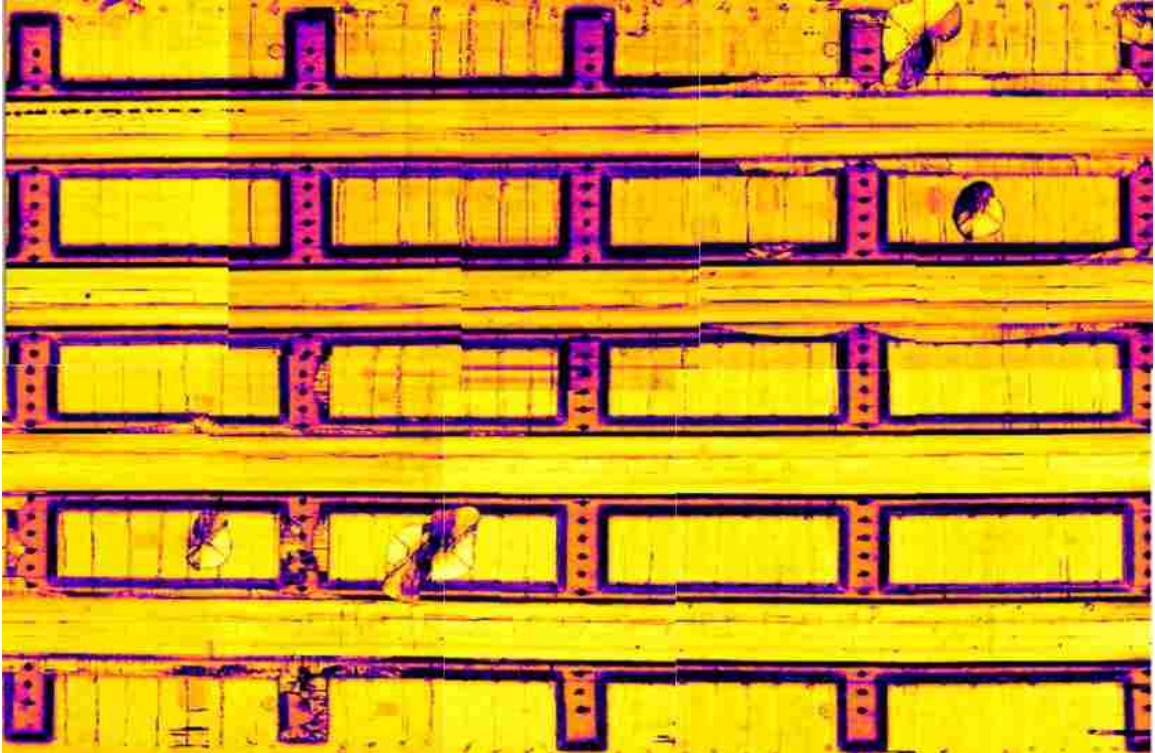
Ultrasonic Amplitude
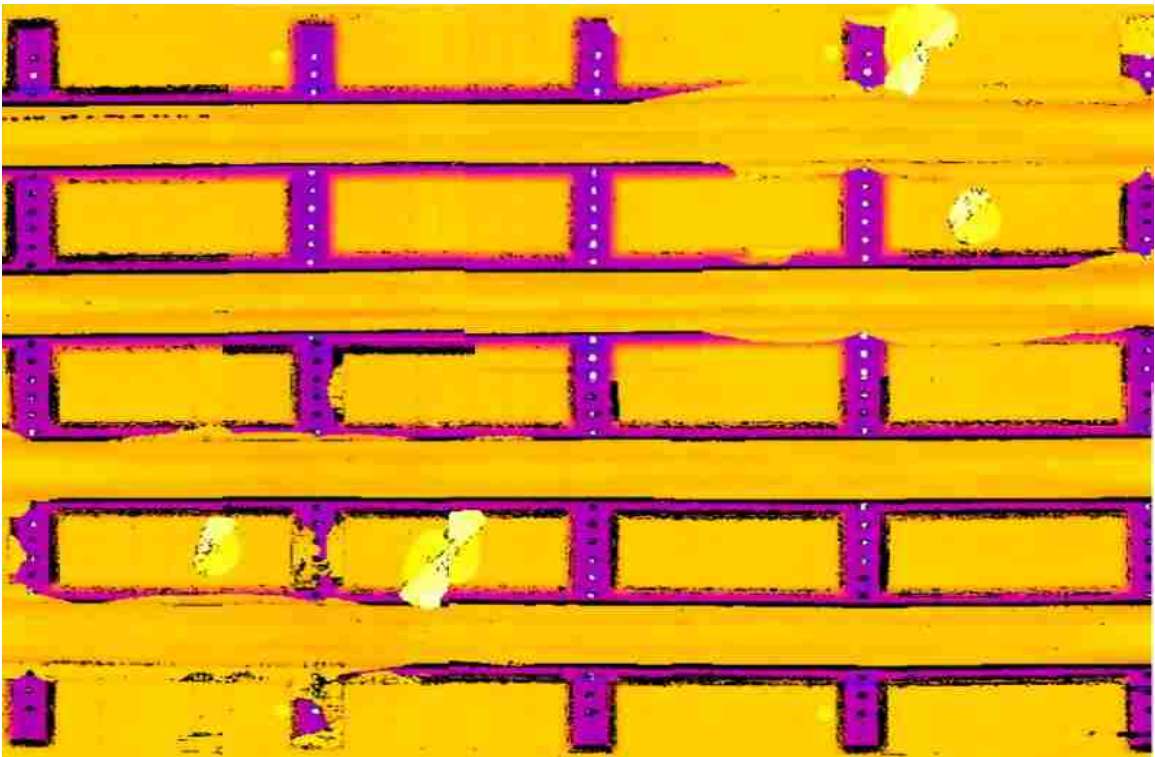
Ultrasonic Time of Flight

Panel B – Full Panel Inspections
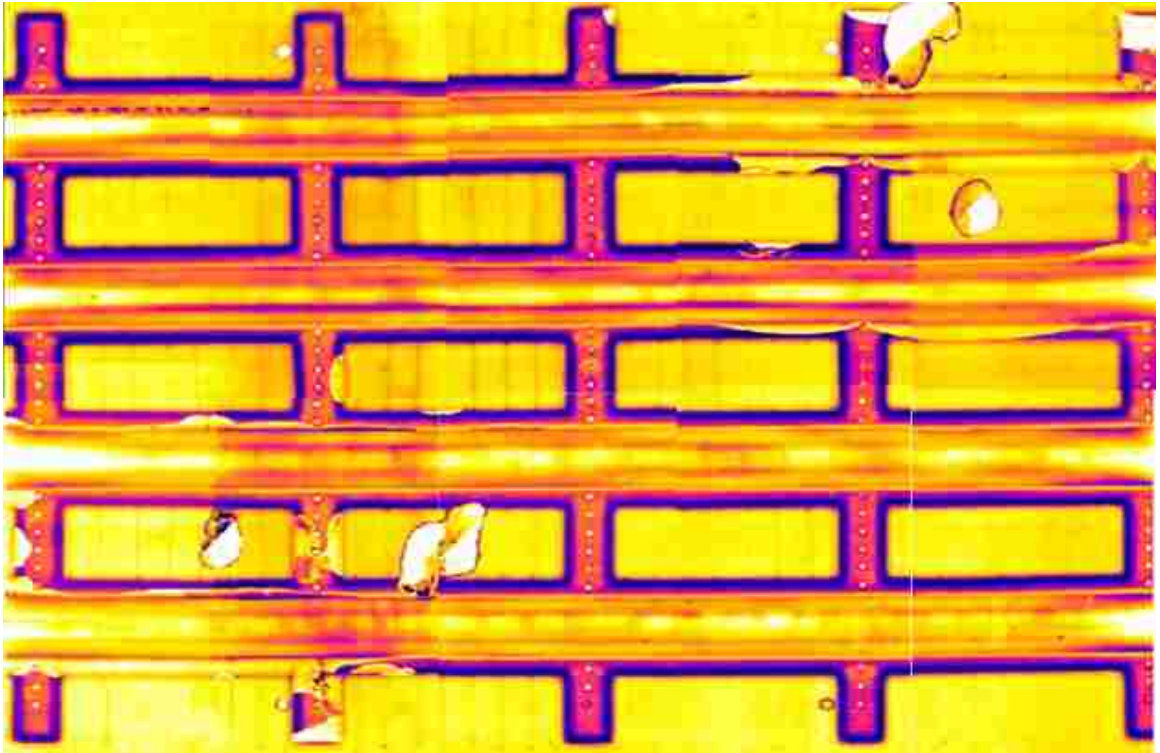
Resonance Amplitude X Plot
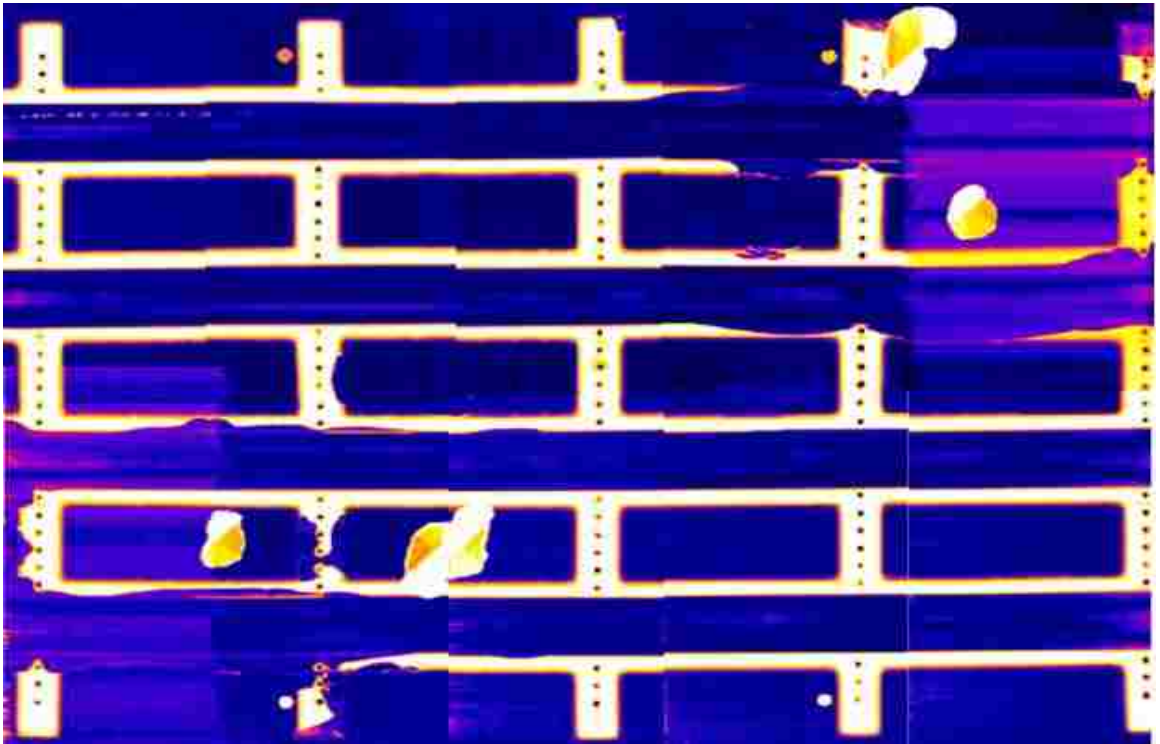
Resonance Phase Y Plot

1B – B1/2-SK3-ST0-I4
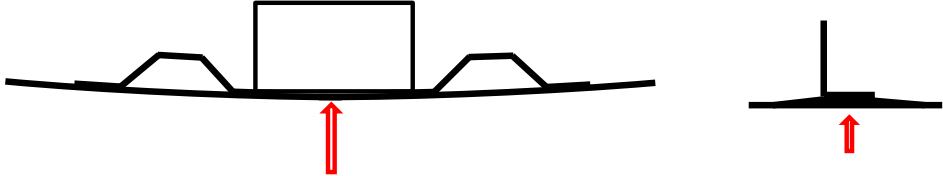
Center of Shear Tie
Max Impact Energy: 908.6 ft lbs, 670.1 Joules
Max Impact Velocity: 365.5 ft/s, 111.4 m/s
Visual Indication: Small paint crack around one fastener, 2" crack in built-up pad section, 1" crack in corner bend radius of shear tie.
Damage Area: I.D. 0.0, S.D 3.03 in^2
Type of Damage: Shear tie built-up pad section delamination, cracked shear tie
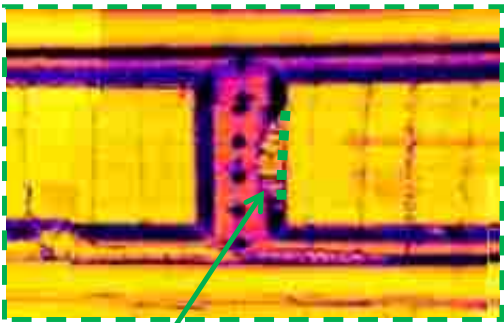
Delamination
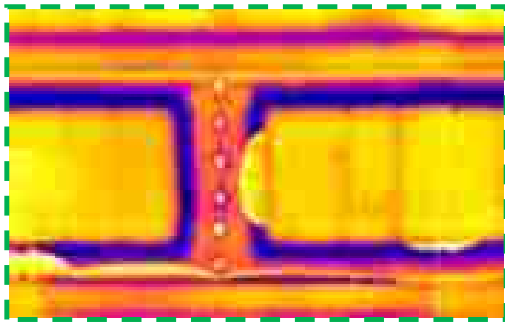
UT Resonance X-Plot
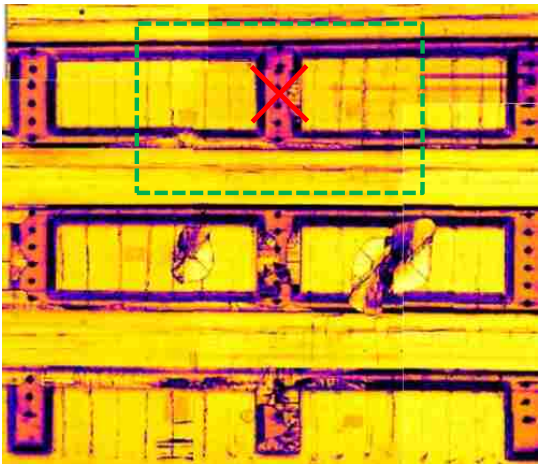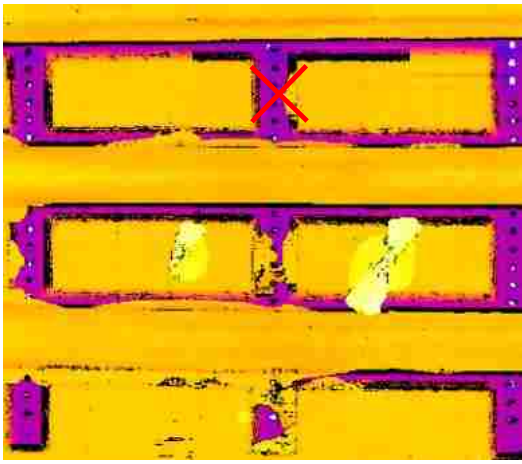
UT Amplitude C-Scan

UT Time of Flight C-Scan

✕ Impact Location

Quadrant 3

146
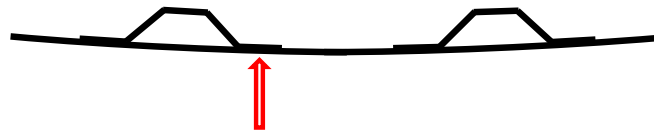
Center of Stringer Flange
Max Impact Energy: 272.6 ft lbs, 201.0 Joules
Max Impact Velocity: 200.5 ft/s, 61.1 m/s
Visual Indication: No visual indication on front or back side of panel
Damage Area: I.D. 0.0, S.D. 8.12 in^2
Type of Damage: Stringer disbond detected in amplitude, TOF and resonance, no interply delamination detected in the skin
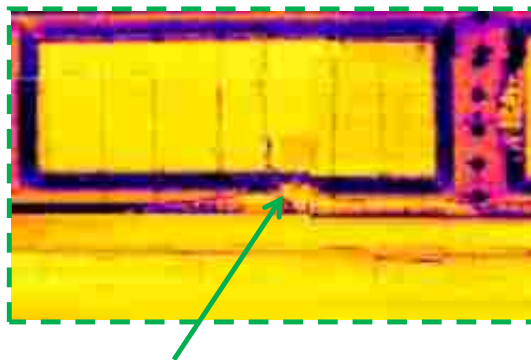
Stringer Disbond
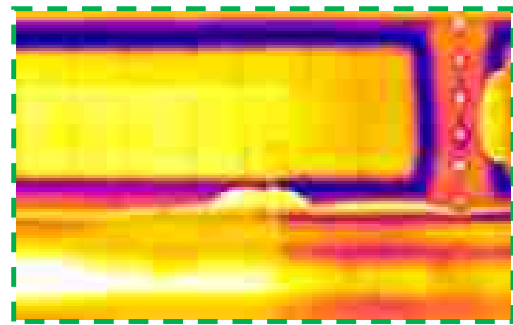
UT Resonance X-Plot
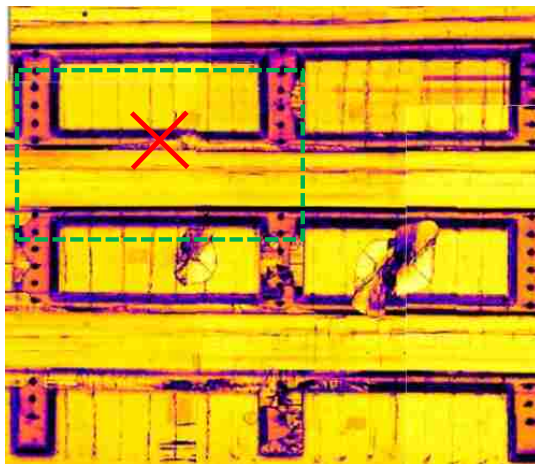
UT Amplitude C-Scan
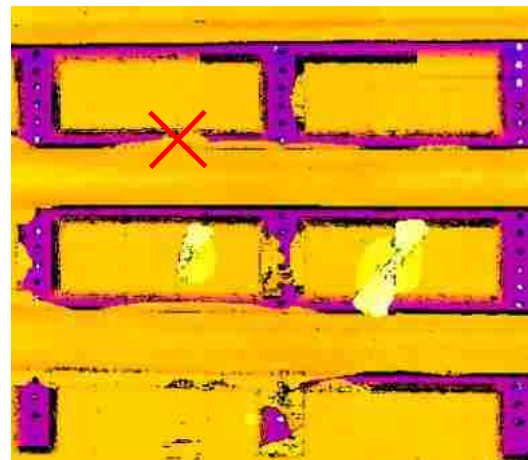
UT Time of Flight C-Scan

✕ Impact Location

Quadrant 3
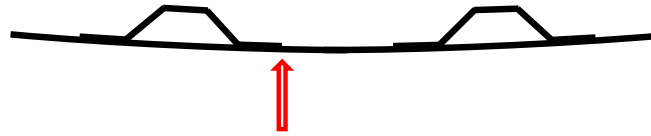
Edge of Stringer Flange (Not Stringer Side)
Max Impact Energy: 233.5 ft lbs, 172.2 Joules
Max Impact Velocity: 185.4 ft/s, 56.5 m/s
Visual Indication: No front side surface visual indication, 2.5" crack visible on backside of panel at the flange skin interface
Damage Area: I.D. 0.0, S.D. 4.12in^2
Type of Damage: Small stringer disbond detected in amplitude, TOF and resonance, no interply delamination detected in the skin

Small Stringer Disbond
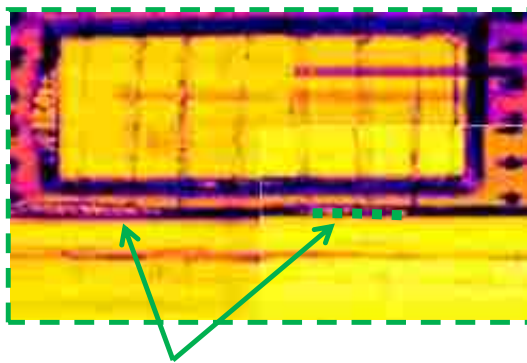
Small Stringer Disbond
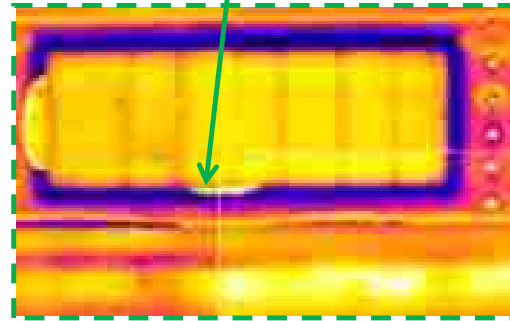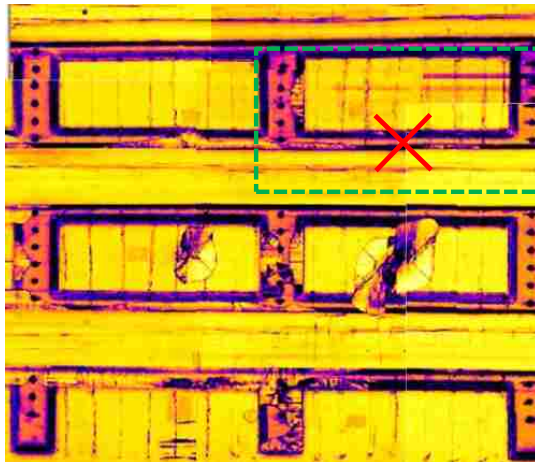
UT Resonance X-Plot

UT Amplitude C-Scan
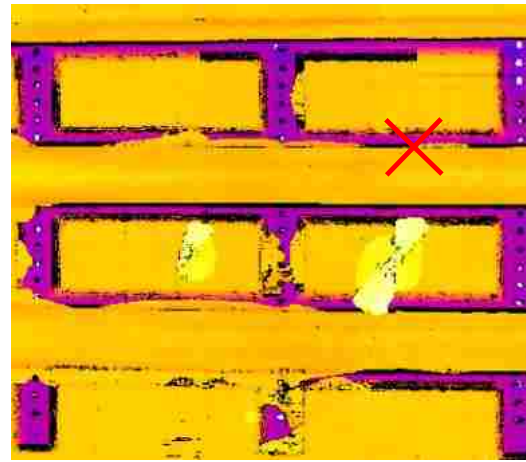
UT Time of Flight C-Scan

$\times$ Impact Location

Quadrant 3
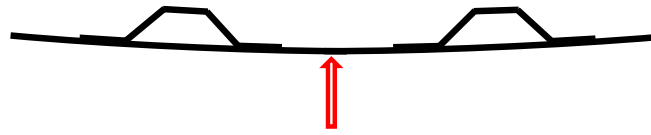
Skin Impact
Max Impact Energy: 762.4 ft lbs, 562.3 Joules
Max Impact Velocity: 334.6 ft/s, 102 m/s
Visual Indication: No visual indication on front or back side of panel
Damage Area: I.D. 11.28, S.D. 20.48 in^2
Type of Damage: Interply delamination at impact location, edge of stringer disbond on stringer side.

Interply Delamination
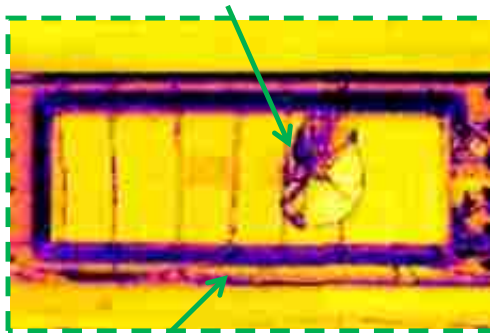
Stringer Disbond
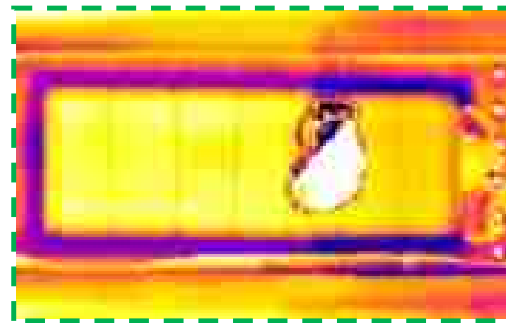
UT Resonance X-Plot
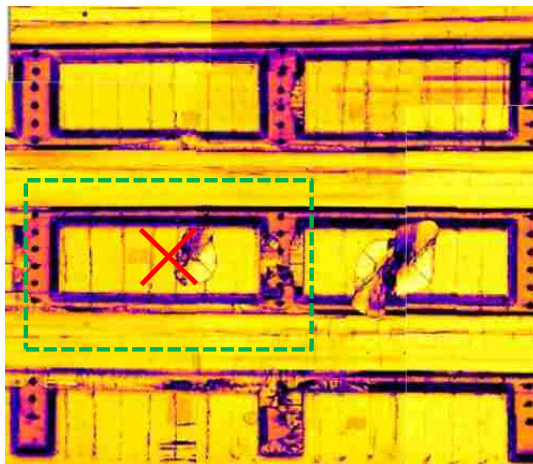
UT Amplitude C-Scan
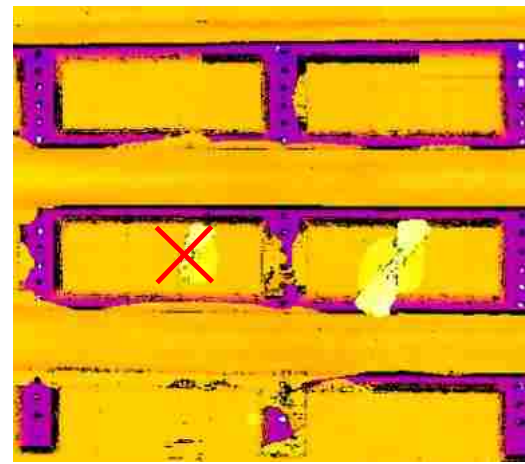
UT Time of Flight C-Scan

✕ Impact Location

Quadrant 3

5B – B1/2-SK4-ST0-I4
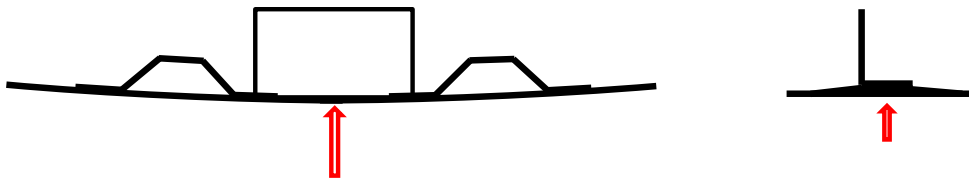
Center of Shear Tie
Max Impact Energy: 1000.7 ft lbs, 738.1 Joules
Max Impact Velocity: 385.2 ft/s, 117.4 m/s
Visual Indication: Paint crack around circumference of fastener, 4.5" crack at the skin to built-up pad section interface, 4" crack in the corner bend of the shear tie
Damage Area: I.D. 0.0, S.D. 14.90 in^2
Type of Damage: : Delamination of built-up pad section at shear tie, cracked shear tie
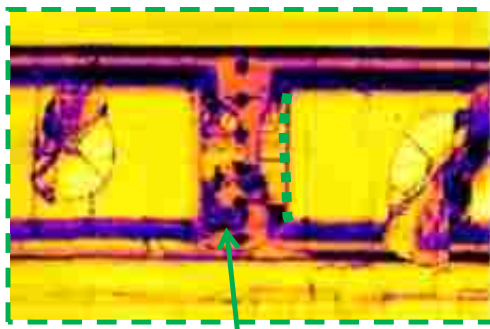
Built-up Section Delamination
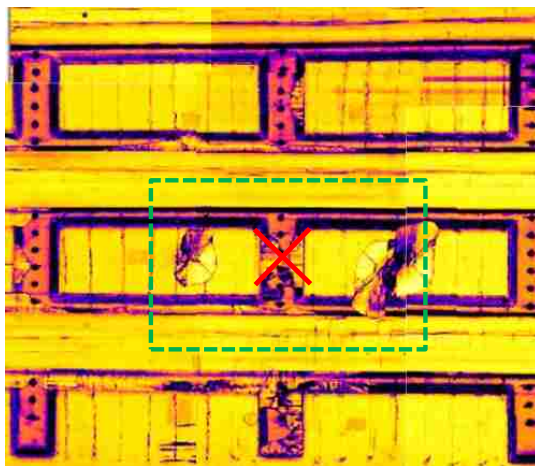
UT Resonance X-Plot

UT Amplitude C-Scan
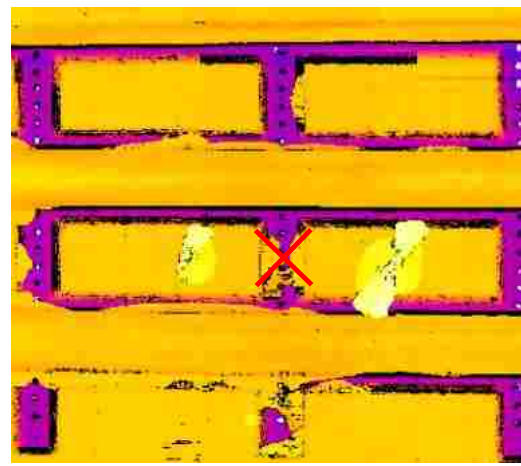
UT Time of Flight C-Scan

✕ Impact Location

Quadrant 3
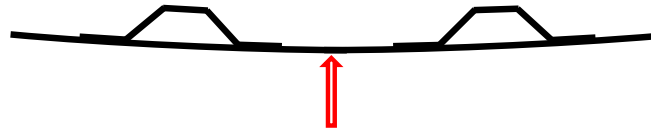
Skin Impact
Max Impact Energy: 1011.0 ft lbs, 745.6 Joules
Max Impact Velocity: 388.8 ft/s, 118.5 m/s
Visual Indication: No visual indication on front or back side of panel
Damage Area: I.D. 21.27, S.D. 0.0 in^2
Type of Damage: Interply delamination in the skin

Interply Delamination

UT Resonance X-Plot

UT Amplitude C-Scan

UT Time of Flight C-Scan

☒ Impact Location

Quadrant 3

Edge of Stringer Flange (Not Stringer Side)
Max Impact Energy: 378.1 ft lbs, 278.9 Joules
Max Impact Velocity: 235.6 ft/s, 71.8 m/s
Visual Indication: No front side surface visual indication, 17.5" stringer flange crack visible
Damage Area: Interply Delamination 0.0 in², Substructure Disbond 23.16 in²
Type of Damage: Full stringer disbond, no interply delamination detected

Full Stringer Disbond

UT Resonance X-Plot

UT Amplitude C-Scan

UT Time of Flight C-Scan

✕ Impact Location

Quadrant 3

Edge of Stringer Flange (Not Stringer Side)
Max Impact Energy: 385.3 ft lbs, 284.2 Joules
Max Impact Velocity: 240.8 ft/s, 73.4 m/s
Visual Indication: No front side surface visual indication, multiple cracked plies in the tapered flange ranging from 1" to 2.5".
Damage Area: I.D. 0.0, S.D. 6.05 in^2
Type of Damage: Partial stringer disbonding
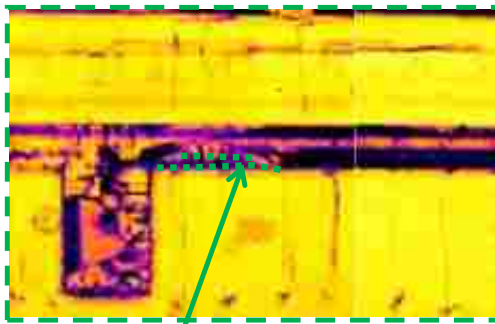
Partial Stringer Disbond

UT Resonance X-Plot
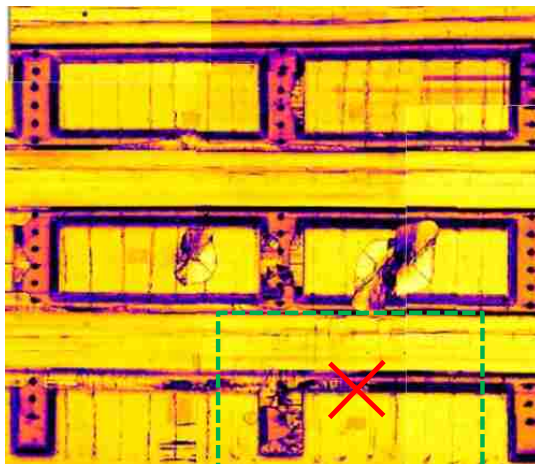
UT Amplitude C-Scan
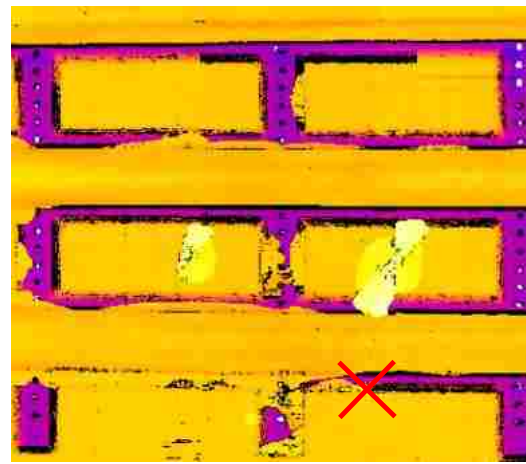
UT Time of Flight C-Scan

☒ Impact Location

Quadrant 3
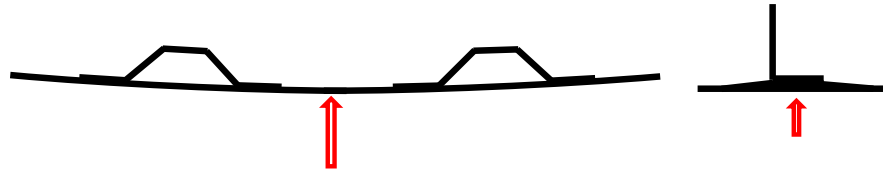
Center of Shear Tie
Max Impact Energy: 986.3 ft lbs, 727.5 Joules
Max Impact Velocity: 382.2 ft/s, 116.5 m/s
Visual Indication: Paint chip on surface of panel, 1" diameter perminant paint scuff, 2" crack at the built-up pad-to-skin interface, 4.5" crack in the corner bend of the shear tie
Damage Area: I.D. 0.0, S.D. 22.34 in^2
Type of Damage: Shear tie built-up pad section delamination
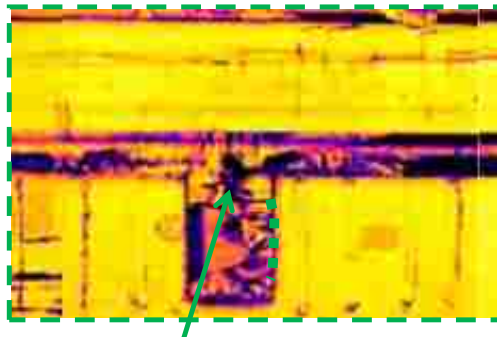
Built-up section Delamination
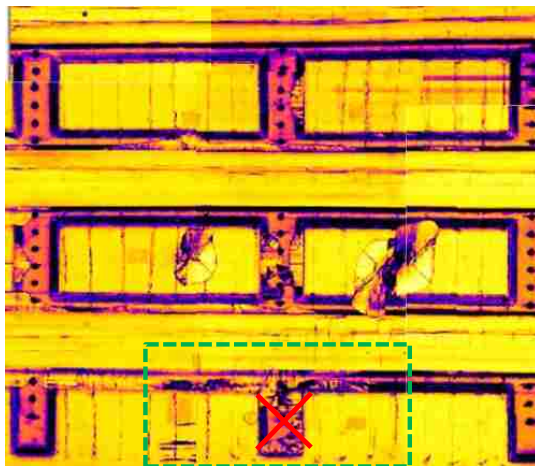
UT Resonance X-Plot

UT Amplitude C-Scan
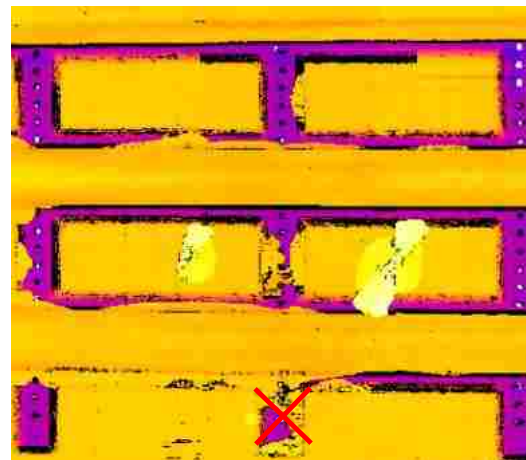
UT Time of Flight C-Scan

✕ Impact Location

Quadrant 3
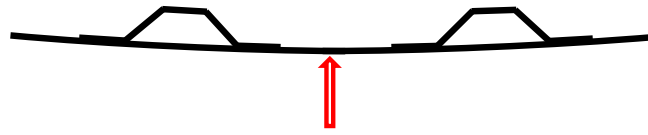
Skin Impact
Max Impact Energy: 996.7 ft lbs, 735.1 Joules
Max Impact Velocity: 383.9 ft/s, 117 m/s
Visual Indication: No front side surface visual indication, 17.5" stringer delamination crack visible on backside
Damage Area: I.D. 20.01, S.D. 29.82 in^2
Type of Damage: Interply delamination in the skin, full length stringer disbond, and partial delamination in the shear tie built-up pad section

Interply Delamination
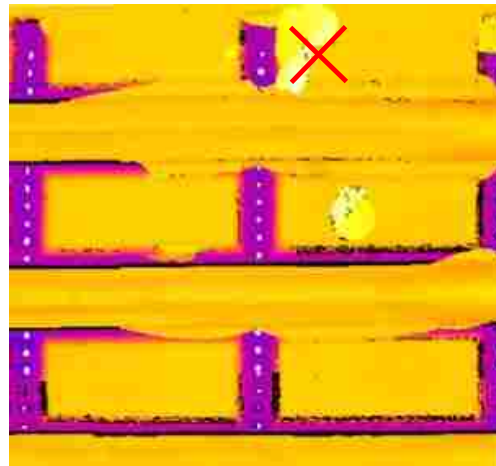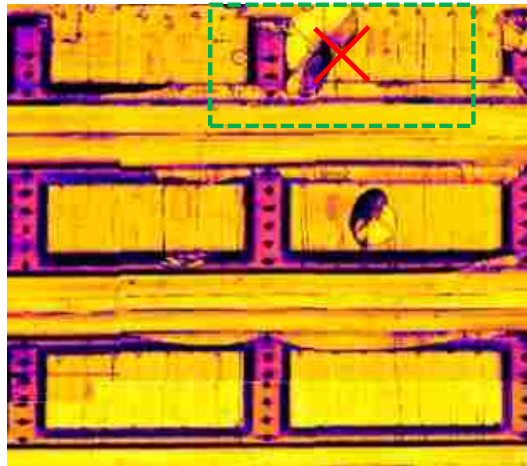
Stringer Disbond

UT Resonance X-Plot

UT Amplitude C-Scan

UT Time of Flight C-Scan

✕ Impact Location   Quadrant 2

155

www.manaraa.com
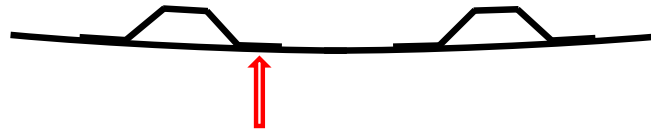
Center of Stringer Flange
Max Impact Energy: 519.6 ft lbs, 383.2 Joules
Max Impact Velocity: 284.1 ft/s, 86.8 m/s
Visual Indication: No front side surface visual indication, 6" stringer flange crack visible on backside of panel
Damage Area: I.D. 0.0, S.D. 16.09 in^2
Type of Damage: Stringer flange disbond

Stringer Disbond

UT Resonance X-Plot

UT Amplitude C-Scan
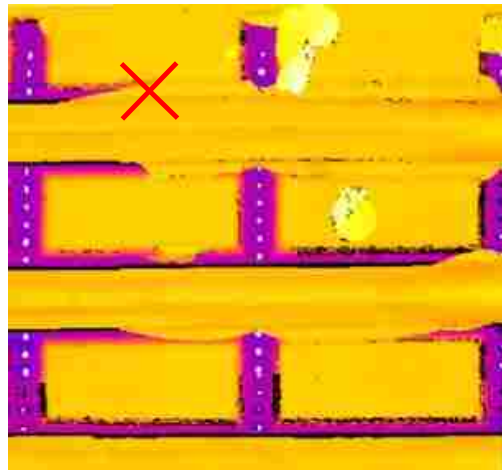
UT Time of Flight C-Scan

$\times$ Impact Location

Quadrant 2
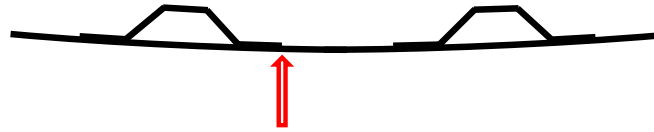
Edge of Stringer Flange (Not Stringer Side)
Max Impact Energy: 573.8 ft lbs, 423.2 Joules
Max Impact Velocity: 291.7 ft/s, 88.9 m/s
Visual Indication: No front side surface visual indication, 4.5" stringer flange crack visible on backside of panel
Damage Area: I.D. 0.0, S.D. 8.41 in^2
Type of Damage: Stringer flange disbond

Stringer Disbond

UT Resonance X-Plot

UT Amplitude C-Scan

UT Time of Flight C-Scan

✕ Impact Location

Quadrant 2

Skin Impact
Max Impact Energy: 902.9 ft lbs, 666.0 Joules
Max Impact Velocity: 364.2 ft/s, 111.0 m/s
Visual Indication: No front side surface visual indication, 15.5" stringer flange crack visible on backside of panel
Damage Area: I.D. 12.55 , 40.23 S.D. in^2
Type of Damage: Interply delamination in the skin, full length stringer disbond

Interply Delamination
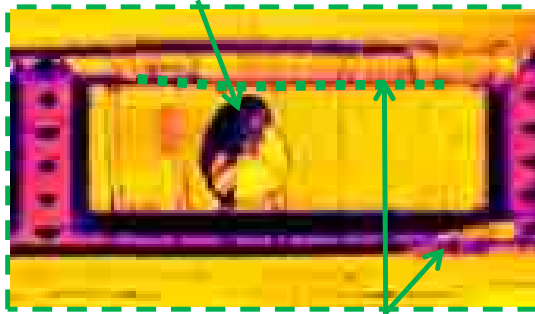
Stringer Disbond

UT Resonance X-Plot

UT Amplitude C-Scan

UT Time of Flight C-Scan

✕ Impact Location   Quadrant 2
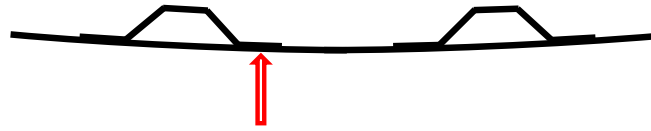
Center of Stringer Flange
Max Impact Energy: 552.9 ft lbs, 407.8 Joules
Max Impact Velocity: 291.7 ft/s, 88.9 m/s
Visual Indication: No front side surface visual indication, two, 2.5" stringer flange cracks visible on backside of panel
Damage Area: I.D. 0.0, S.D. 9.45 in^2
Type of Damage: Stringer flange disbond
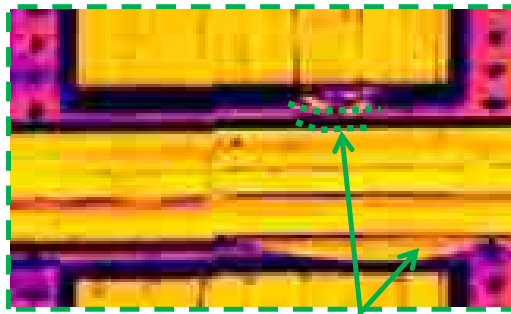
Stringer Disbond

UT Resonance X-Plot

UT Amplitude C-Scan

UT Time of Flight C-Scan

✕ Impact Location

Quadrant 2

159
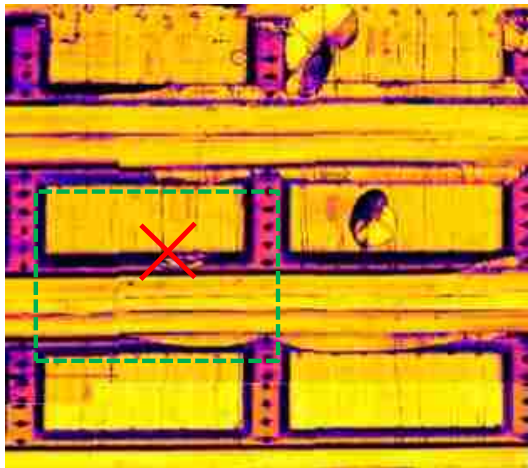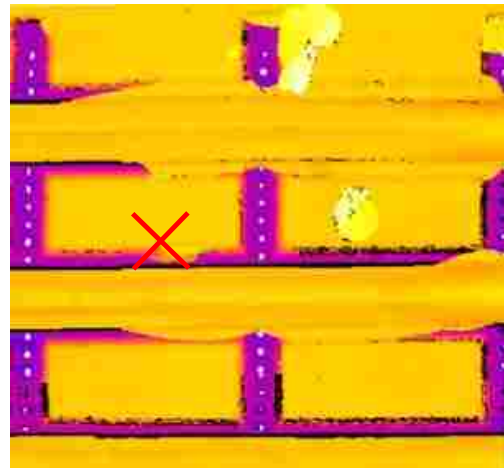
Panel A (Bay 1&2) – Hard Impacts
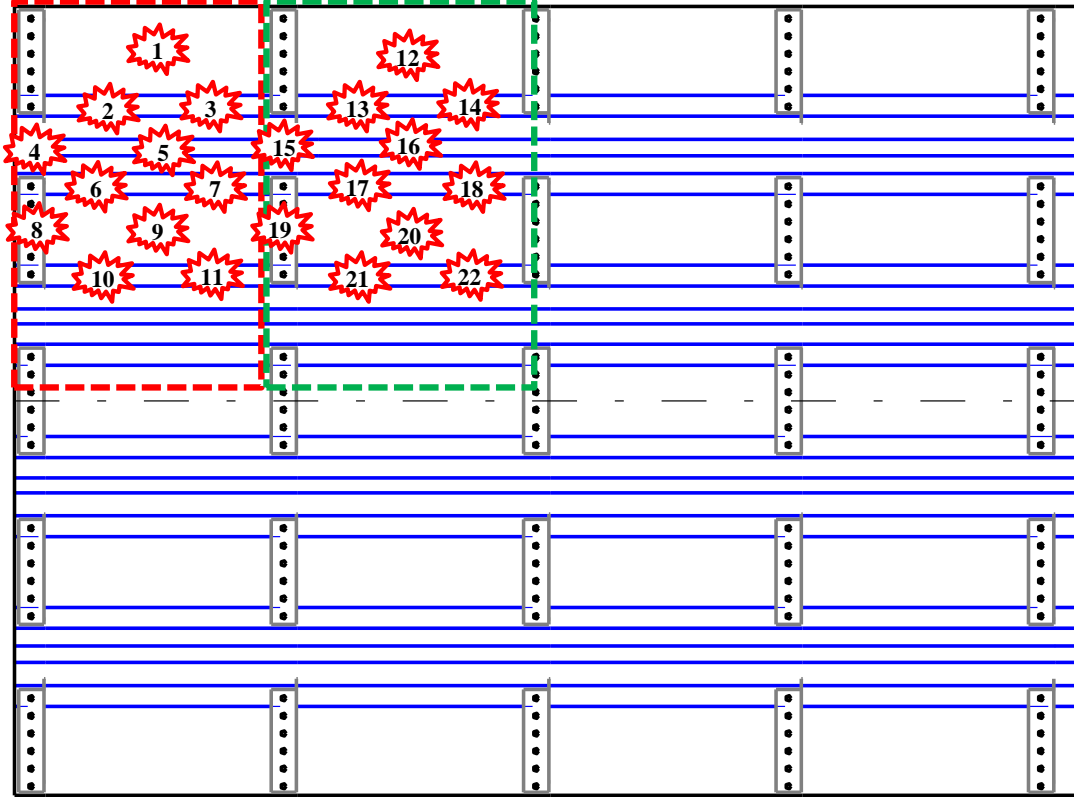
Bay 1 Hard Impacts	Bays 2 Hard Impacts
1 – B1-SK1-ST0-H1	12 – B2-SK1-ST0-H1
2 – B1-SK1-ST1L-H2b	13 – B2-SK1-ST1L-H2a
3 – B1-SK1-ST1R-H2b	14 – B2-SK1-ST1R-H2a
4 – B1-SK0-ST1L-H3	15 – B1/2-SK0-ST1-H3
5 – B1-SK0-ST1-H3	16 – B2-SK0-ST1L-H3
6 – B1-SK2-ST1L-H2c	17 – B2-SK2-ST1L-H2c
7 – B1-SK2-ST1R-H2c	18 – B2-SK2-ST1R-H2c
8 – B1-SK2-ST0-H4	19 –B1/2-SK2-ST0-H4
9 – B1-SK2-ST0-H1	20 – B2-SK2-ST0-H1
10 – B1-SK2-ST2L-H2b	21 – B2-SK2-ST2L-H2b
11 – B1-SK2-ST2R-H2b	22 – B2-SK2-ST2R-H2b

Indicates strain results obtained and presented

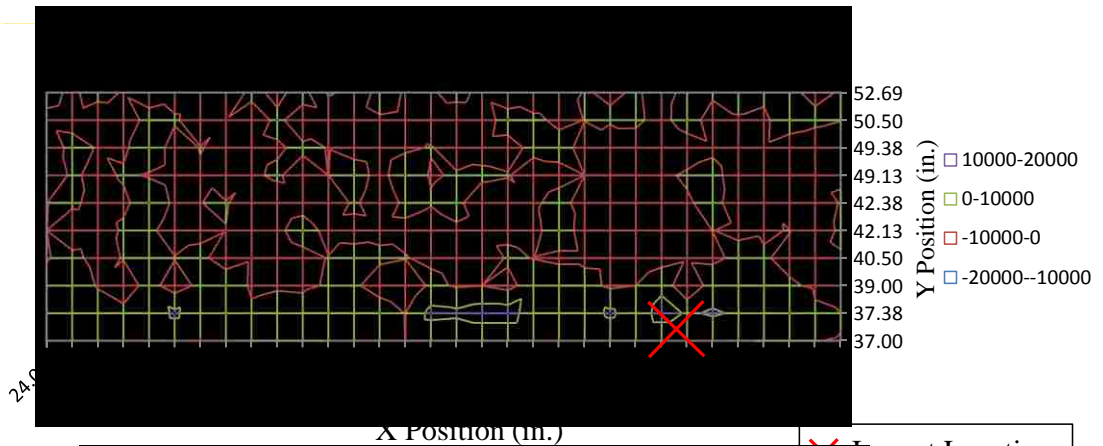Impact Location

--- Fiber Optic

Ultrasonic Amplitude Scan
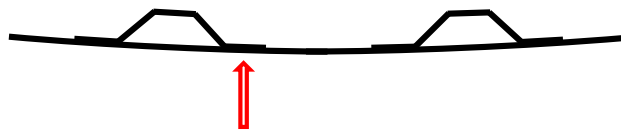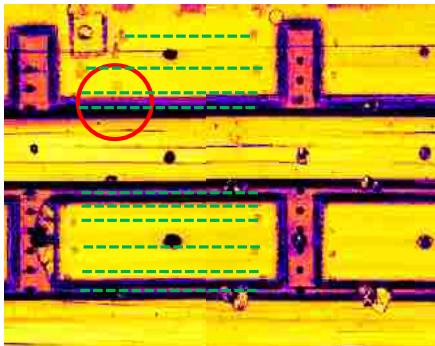
Center of Stringer Flange
Impact Energy: 45 Ft lbs
Damage Area: Could not determine, masked by co-cured flange
Type of Damage: None
Strain Indication: No

	10-20
	0-10
	-10-0
	-20--10

Y Position (in.)

53.06
50.75
49.31
49.13
42.50
42.25
41.06
39.13
37.25
37.06

X Position (in.)

X Impact Location

Micro Strain (*u*e)

	15-20
	10-15
	5-10
	0-5
	-5-0
	-10--5
	-15--10

161

Impact Location ⭕
Fiber Optic - - -

Ultrasonic Amplitude Scan
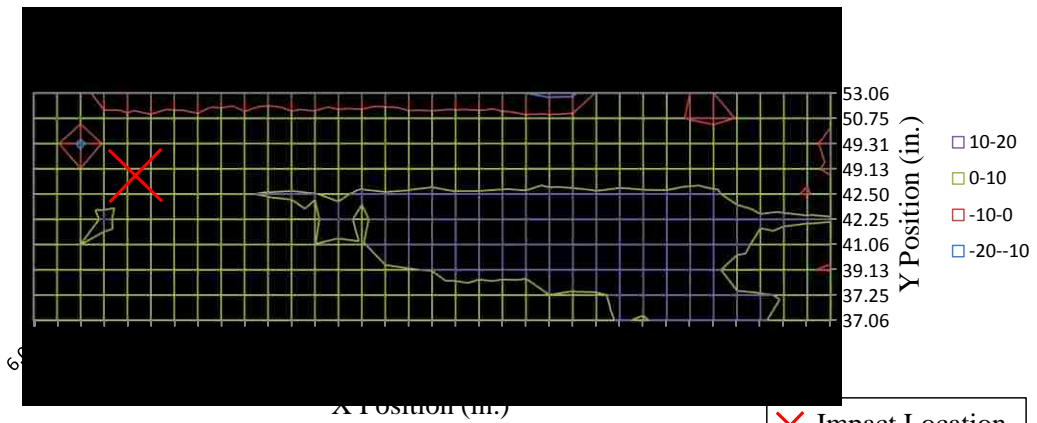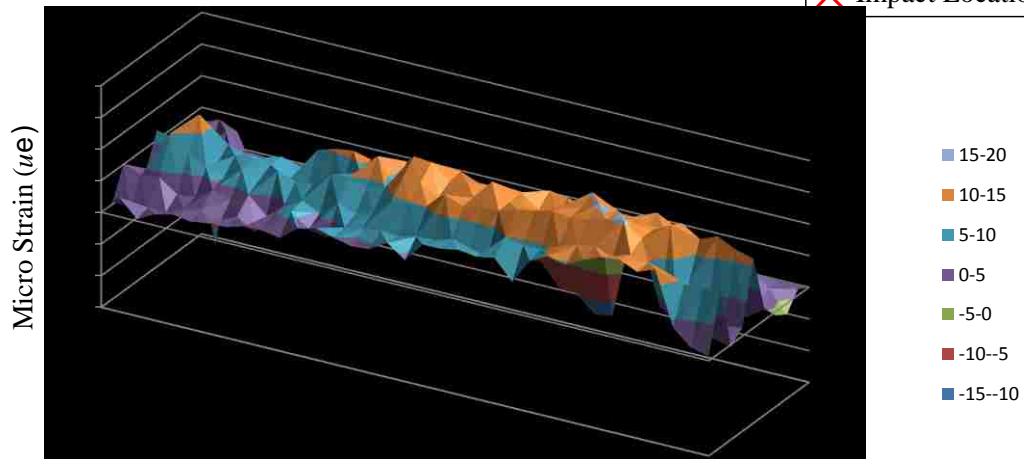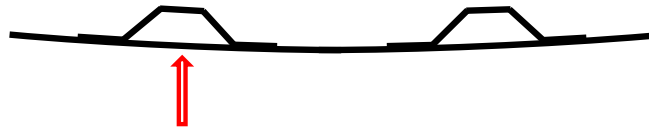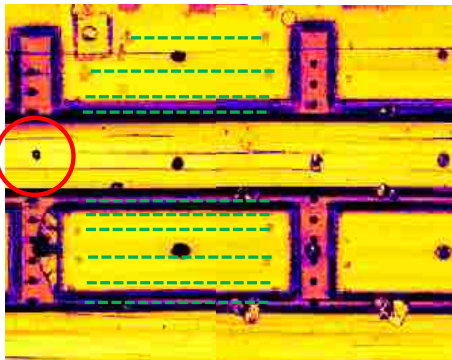
Mid-Stringer on Skin, Between Shear Ties
Impact Energy: 45 Ft lbs
Damage Area: 0.23 in²
Type of Damage: Near surface fiber crushing
Strain Indication: Some strain indication at edge of stringer flange, not detectable
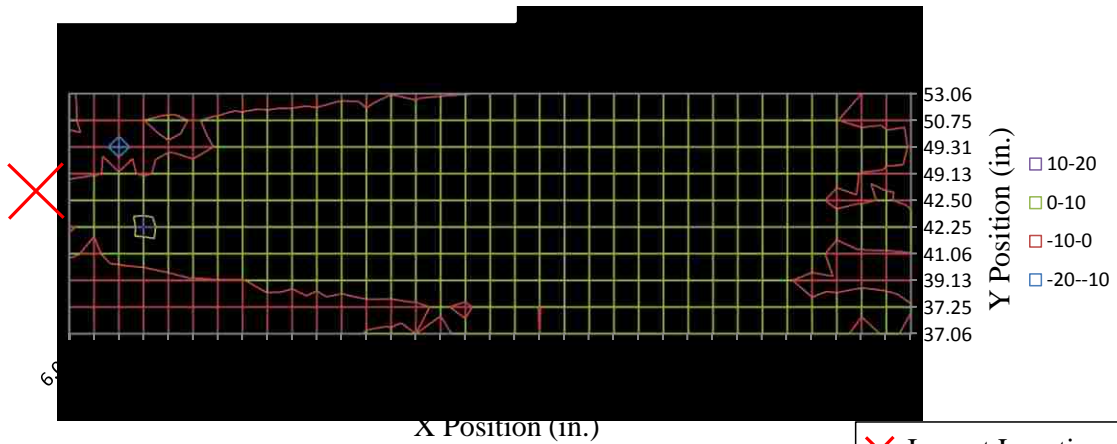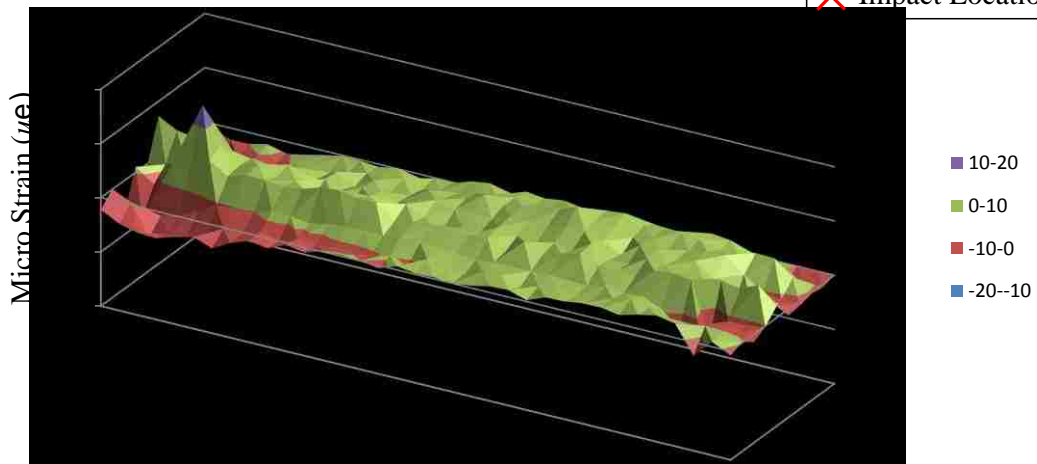
Y Position (in.)
53.06
50.75
49.31
49.13
42.50
42.25
41.06
39.13
37.25
37.06

□ 10-20
□ 0-10
□ -10-0
□ -20--10

X Position (in.)

✕ Impact Location

Micro Strain (μe)

■ 10-20
■ 0-10
■ -10-0
■ -20--10

Impact Location
--- Fiber Optic

Ultrasonic Amplitude Scan

Mid-Stringer Between Flanges
Impact Energy: 45 Ft lbs
Damage Area: 0.47 in^2
Type of Damage: Near surface fiber crushing
Strain Indication: No, possible temperature shift or change in panel loading

Y Position (in.)

53.06
50.75
49.31
49.13
42.50
42.25
41.06
39.13
37.25
37.06

□ 10-20
□ 0-10
□ -10-0
□ -20--10
□ -30--20
□ -40--30

Impact Location

10-20
0-10
-10-0
-20--10
-30--20
-40--30

Micro Strain (*ue*)

163
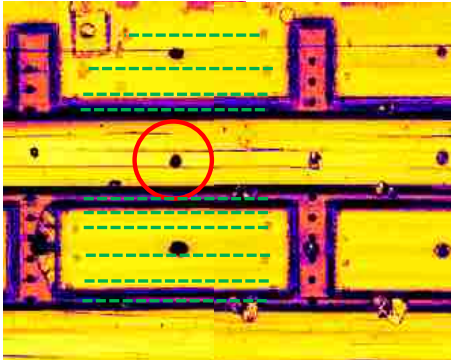
Impact Location
Fiber Optic

Ultrasonic Amplitude Scan
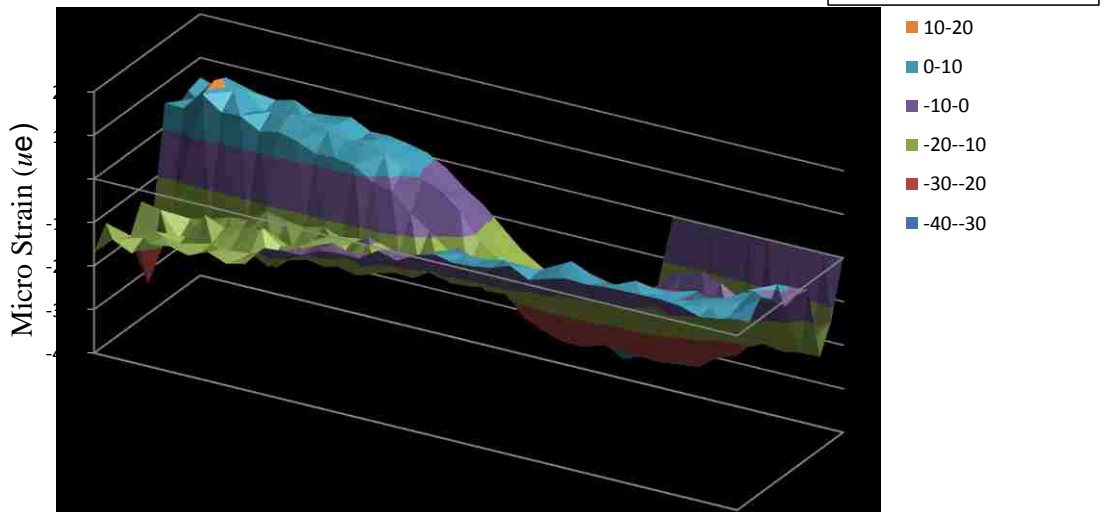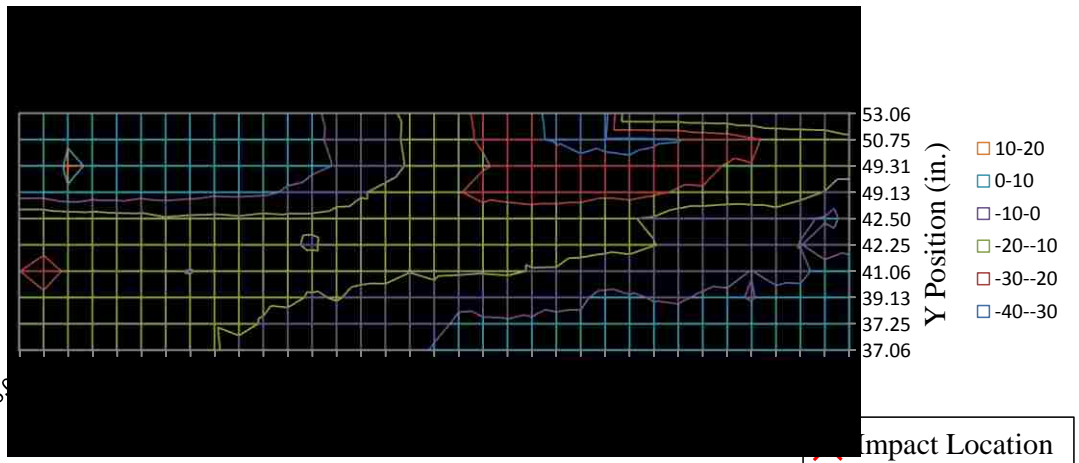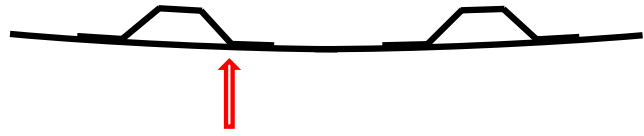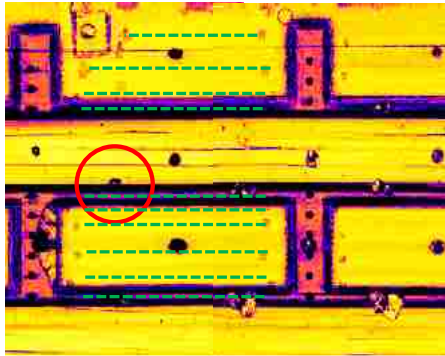
Edge of Stringer Flange (Not Stringer Side)
Impact Energy: 55 Ft lbs
Damage Area: 0.28 in^2
Type of Damage: Near surface fiber crushing
Strain Indication: Minor, local strain increase, not detectable
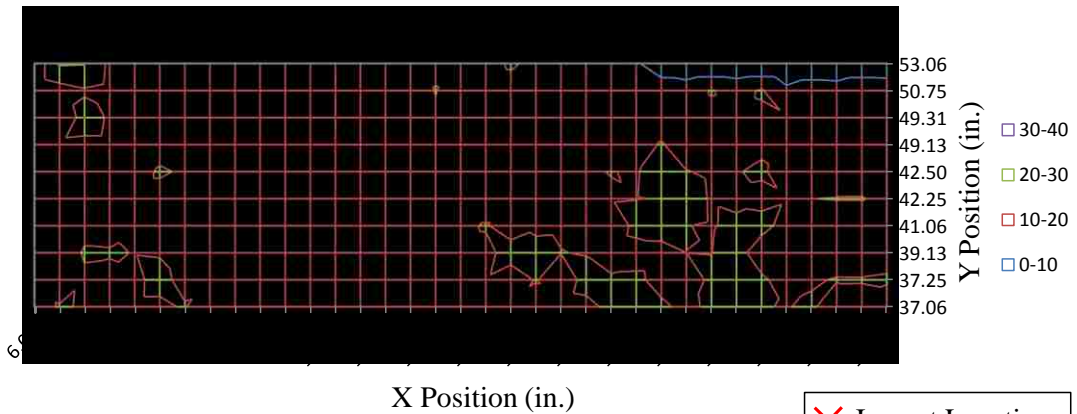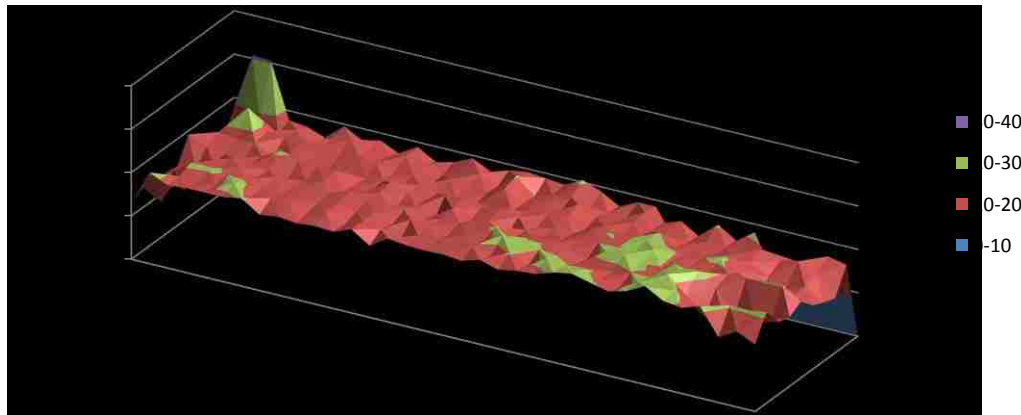
X Position (in.)

Y Position (in.)

□ 30-40
□ 20-30
□ 10-20
□ 0-10

X Impact Location

■ 0-40
■ 0-30
■ 0-20
■ -10

Impact Location
Fiber Optic
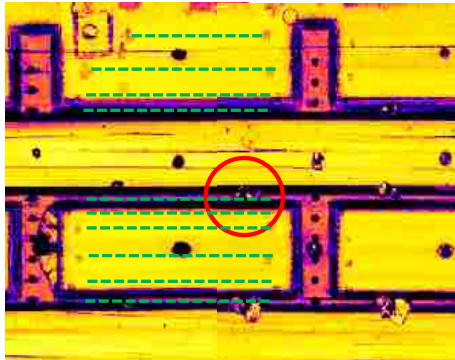
Ultrasonic Amplitude Scan
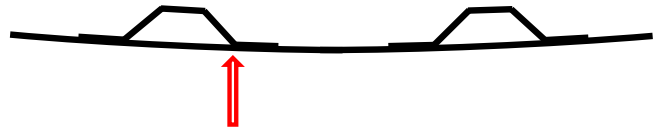
Edge of Stringer Flange (Stringer Side)
Impact Energy: 70 Ft lbs
Damage Area: 1.67 in^2
Type of Damage: Interply delamination
Strain Indication: Yes, Detectable Strain Indication

Y Position (in.)

53.06
50.75
49.31
49.13
42.50
42.25
41.06
39.13
37.25
37.06

50-100
0-50
-50-0
-100--50

X Position (in.)

Location

Micro Strain (*ue*)

50-100
0-50
-50-0
-100--50

165
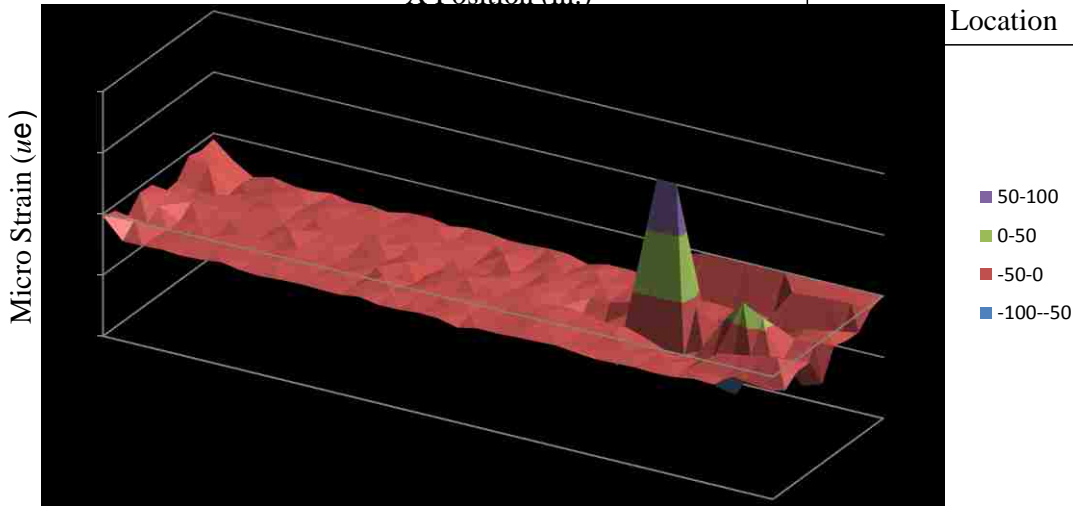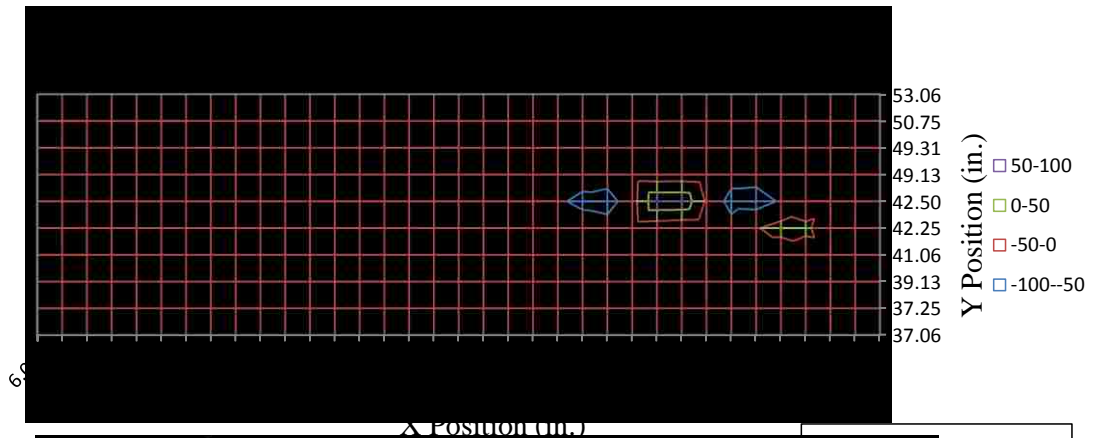
Impact Location
--- Fiber Optic

Ultrasonic Amplitude Scan
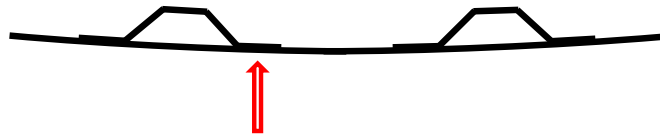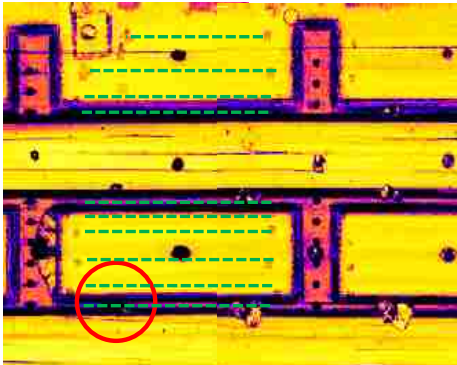
Center of Stringer Flange
Impact Energy: 75 Ft lbs
Damage Area: 1.36 in^2
Type of Damage: Stringer flange delamination
Strain Indication: Yes, detectable strain indication

Y Position (in.)

53.06
50.75
49.31
49.13
42.50
42.25
41.06
39.13
37.25
37.06

150-200
100-150
50-100
0-50
-50-0
-100--50

X Position (in.)

Impact Location

Micro Strain (*ue*)

150-200
100-150
50-100
0-50
-50-0
-100--50

166

○ Impact Location
--- Fiber Optic

Ultrasonic Amplitude Scan

Center of Stringer Flange
Impact Energy: 90 Ft lbs
Damage Area: 2.19 in^2
Type of Damage: Interply delamination
Strain Indication: Yes, detectable strain indication

Y Position (in.)
53.06
50.75
49.31
49.13
42.50
42.25
41.06
39.13
37.25
37.06

□ 150-200
□ 100-150
□ 50-100
□ 0-50
□ -50-0

Micro Strain (*ue*)

■ 150-200
■ 100-150
■ 50-100
■ 0-50
■ -50-0

Legend:
○ Impact Location
--- Fiber Optic
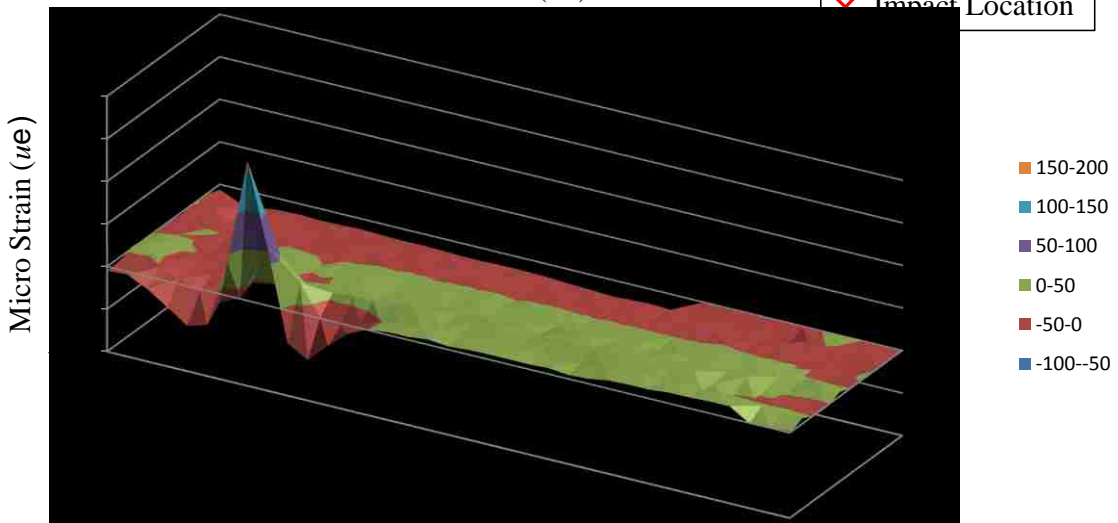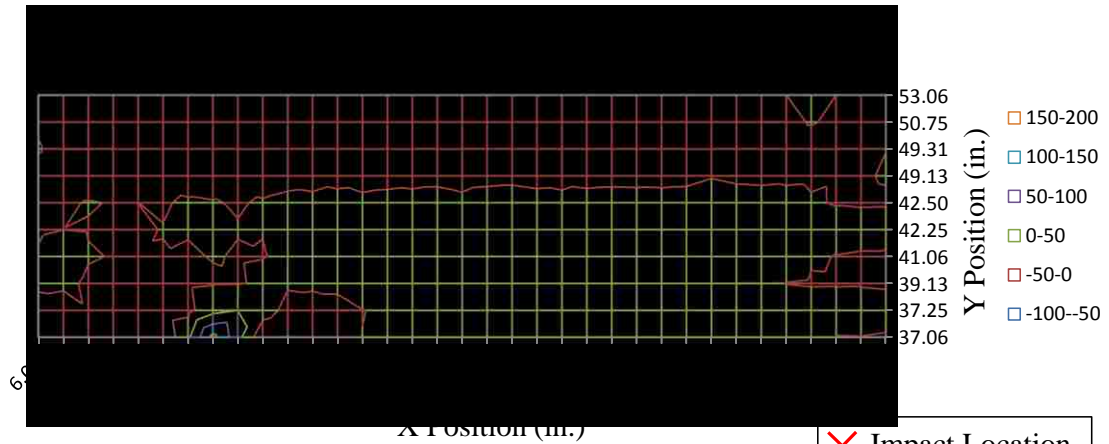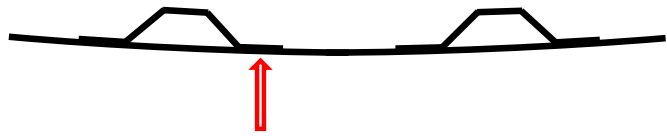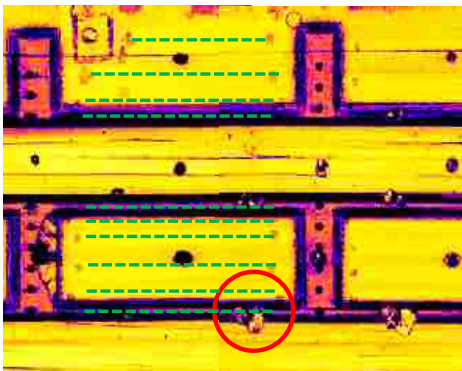
Ultrasonic Amplitude Scan
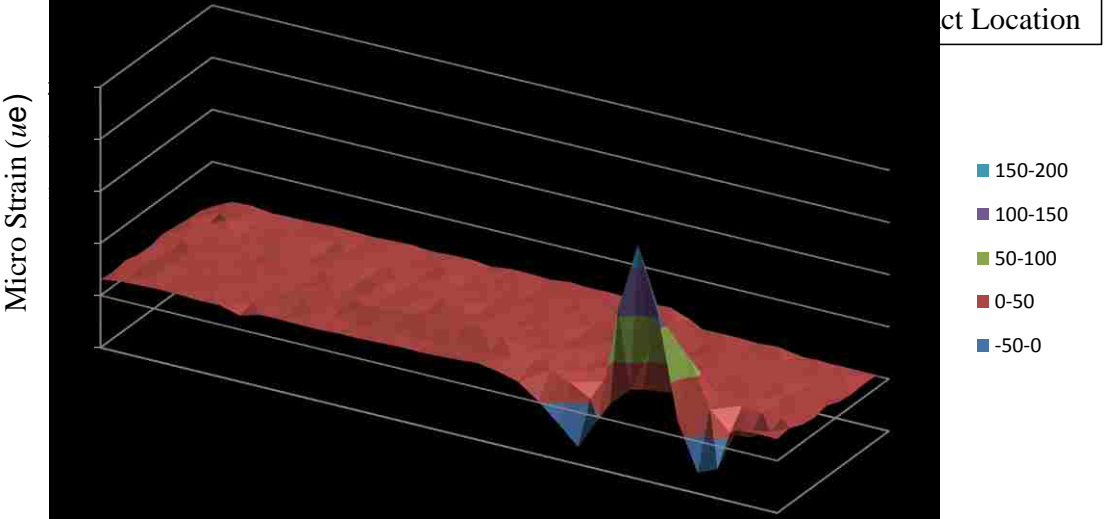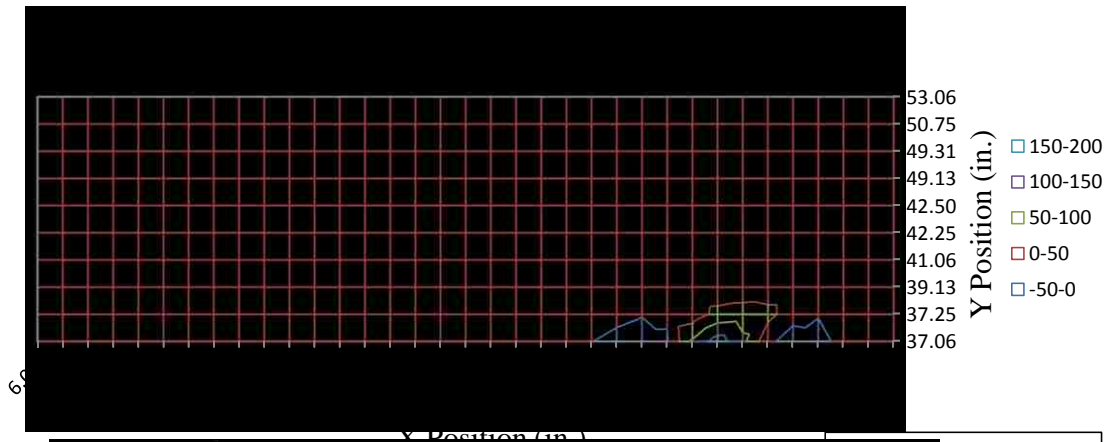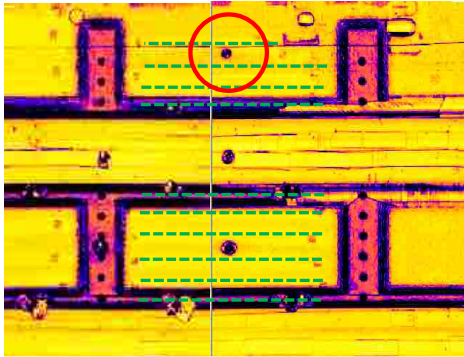
Skin Impact
Impact Energy: 60 Ft lbs
Damage Area: 0.45 in²
Type of Damage: Near surface fiber crushing
Strain Indication: Yes, but caused other indications as well due to high strain levels in the fiber
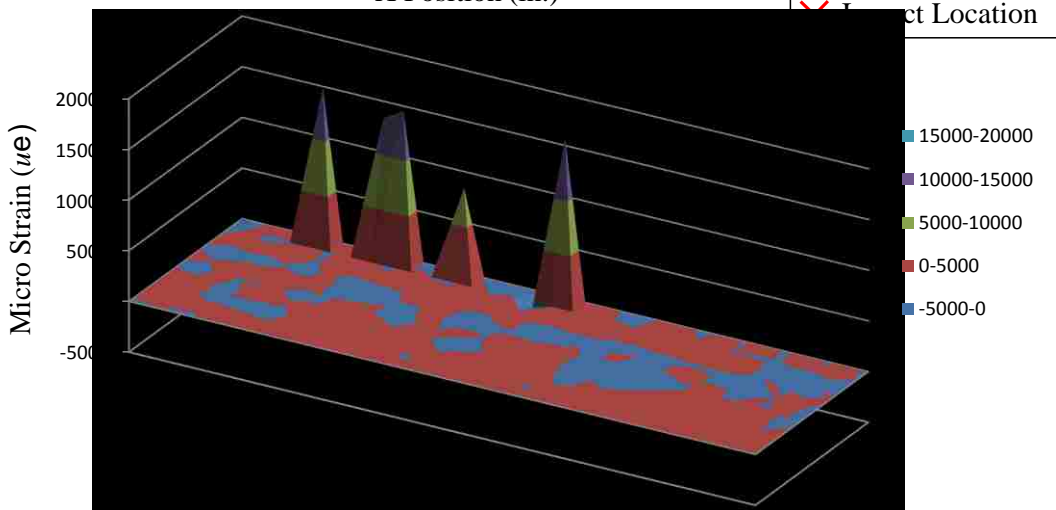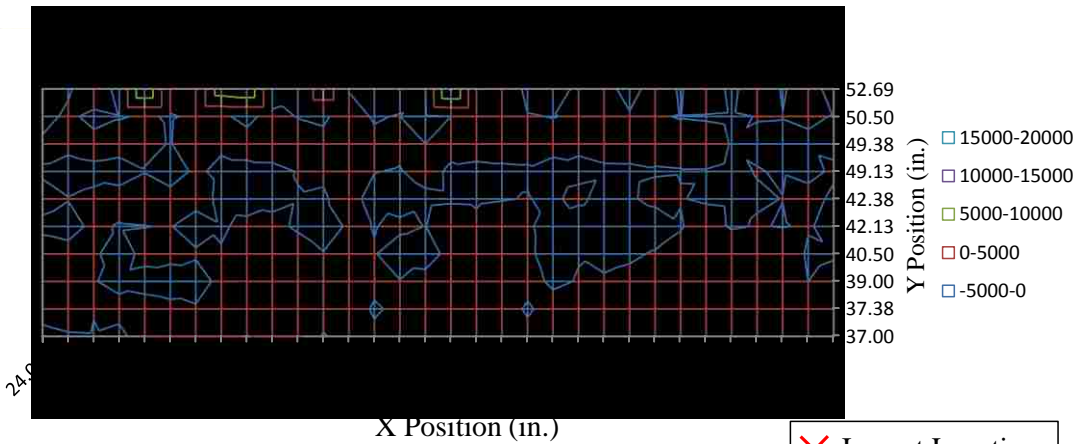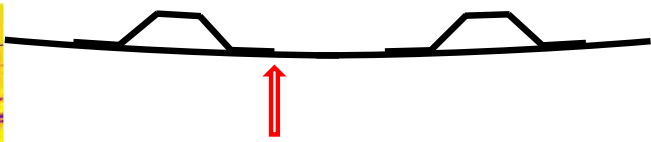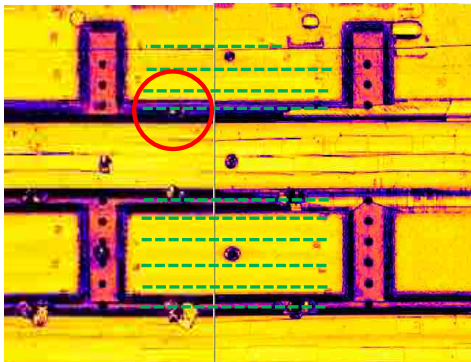
Impact Location
Fiber Optic

Edge of Stringer Flange (Not Stringer Side)
Impact Energy: 60 Ft lbs
Damage Area: 0.93 in^2
Type of Damage: Stringer flange delamination
Strain Indication: No

Ultrasonic Amplitude Scan
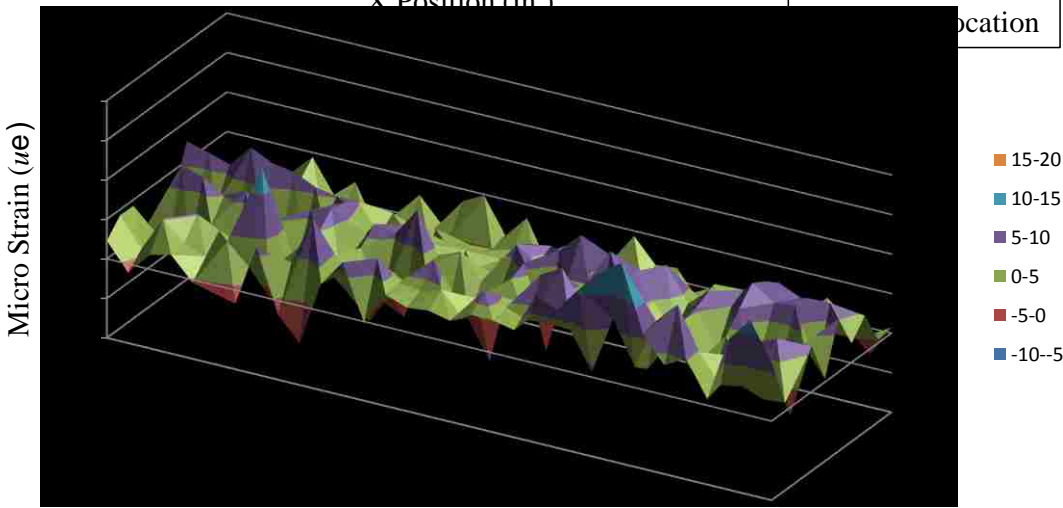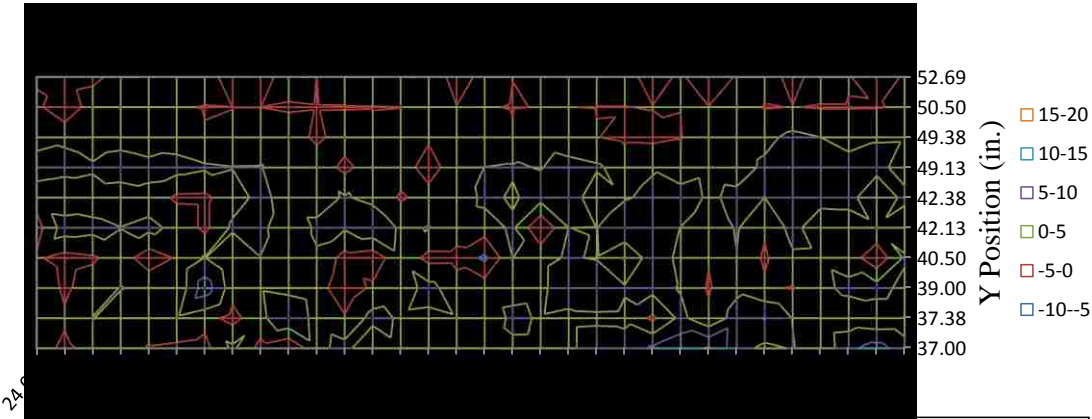
Y Position (in.)

52.69
50.50
49.38
49.13
42.38
42.13
40.50
39.00
37.38
37.00

15-20
10-15
5-10
0-5
-5-0
-10--5

X Position [in.]

Location

Micro Strain (*ue*)

15-20
10-15
5-10
0-5
-5-0
-10--5

169

Impact Location
Fiber Optic
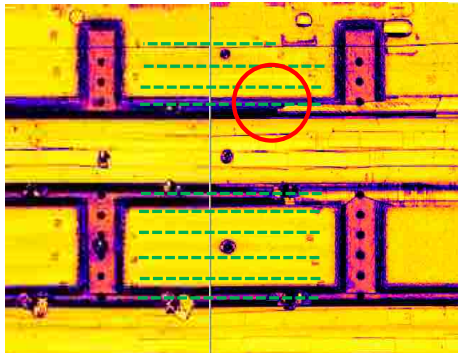
Ultrasonic Amplitude Scan
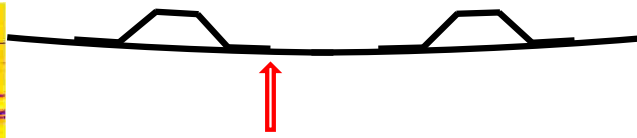
Edge of Stringer Flange (Not Stringer Side)
Impact Energy: 75 Ft lbs
Damage Area: 0.98 in^2
Type of Damage: Interply delamination, and near surface fiber crushing
Strain Indication: Yes, detectable strain indication, but in the other stringer fiber
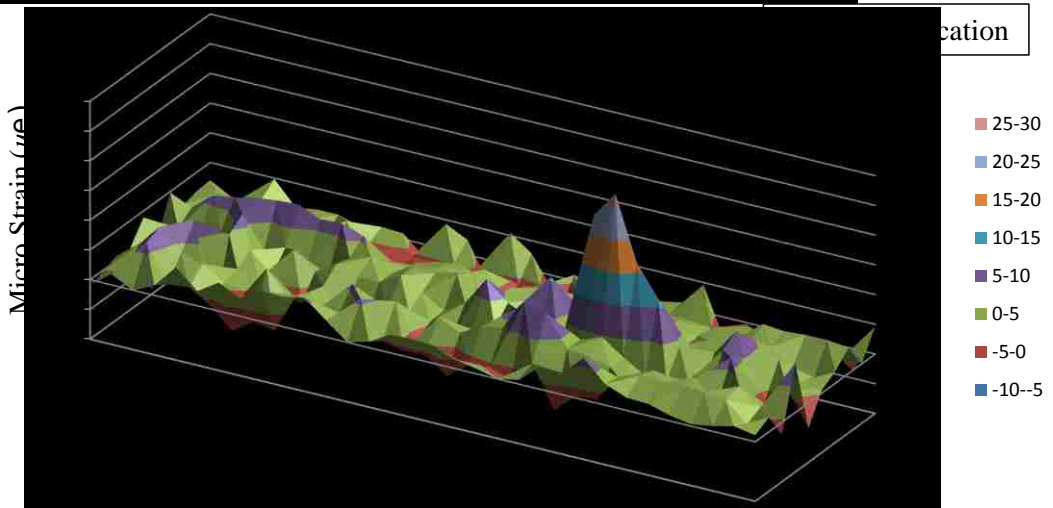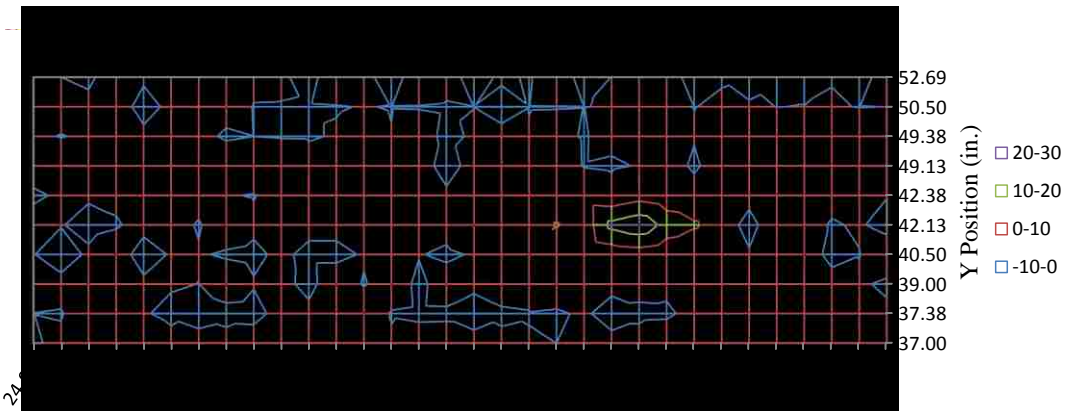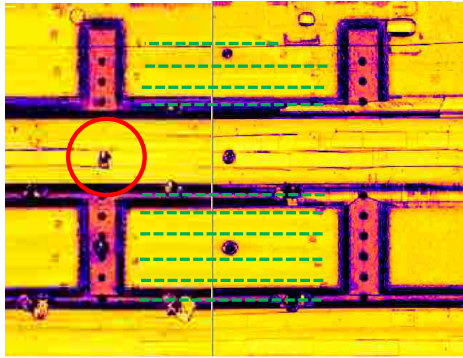
170

Legend:
- ◯ Impact Location
- --- Fiber Optic

Ultrasonic Amplitude Scan
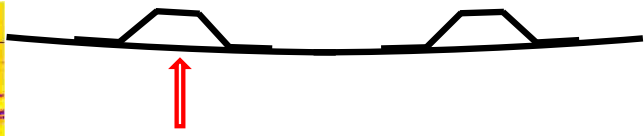
Mid-Stringer Between Flanges (Between Shear ties)
Impact Energy: 60 Ft lbs
Damage Area: 0.93 in²
Type of Damage: Near surface crushed fibers and interply delamination
Strain Indication: Higher strains indicated on stringer flange fibers, not detectable
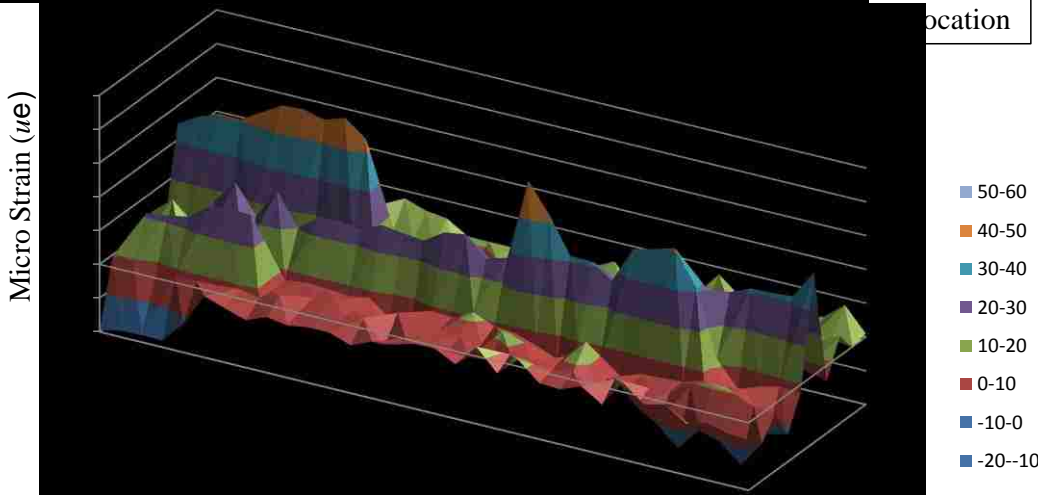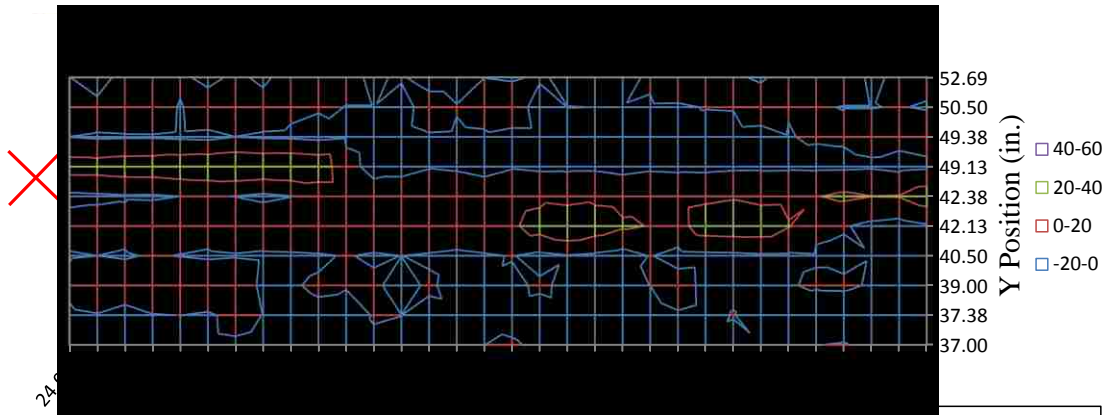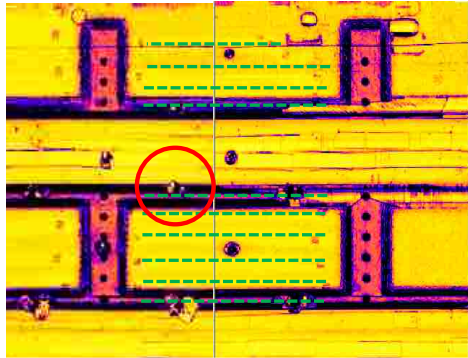
Y Position (in.)

52.69
50.50
49.38
49.13
42.38
42.13
40.50
39.00
37.38
37.00

- ☐ 40-60
- ☐ 20-40
- ☐ 0-20
- ☐ -20-0

ocation

Micro Strain (ue)

- ■ 50-60
- ■ 40-50
- ■ 30-40
- ■ 20-30
- ■ 10-20
- ■ 0-10
- ■ -10-0
- ■ -20--10

Ultrasonic Amplitude Scan
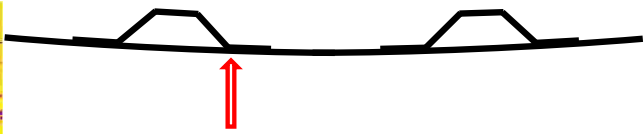
Edge of Stringer Flange (Stringer Side)
Impact Energy: 90 Ft lbs
Damage Area: 1.23 in^2
Type of Damage: Interply delamination
Strain Indication: Yes, spikes in strain data (negative and positive) adjacent to impact location

Ultrasonic Amplitude Scan

Edge of Stringer Flange (Stringer Side)
Impact Energy: 105 Ft lbs
Damage Area: 2.24 in^2
Type of Damage: Stringer flange delamination
Strain Indication: Yes, clear strain decrease and subsequent increase at impact location

○ Impact Location
--- Fiber Optic
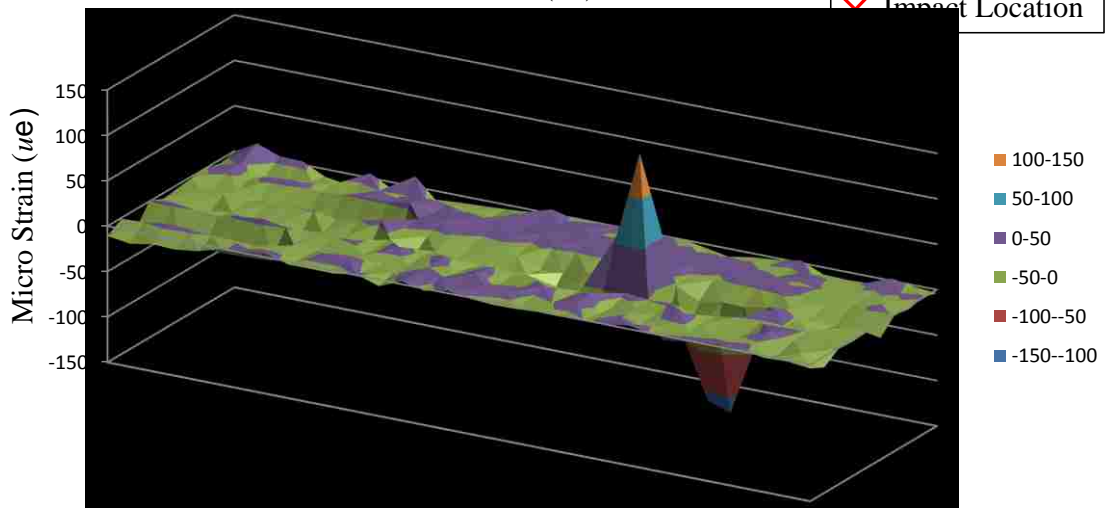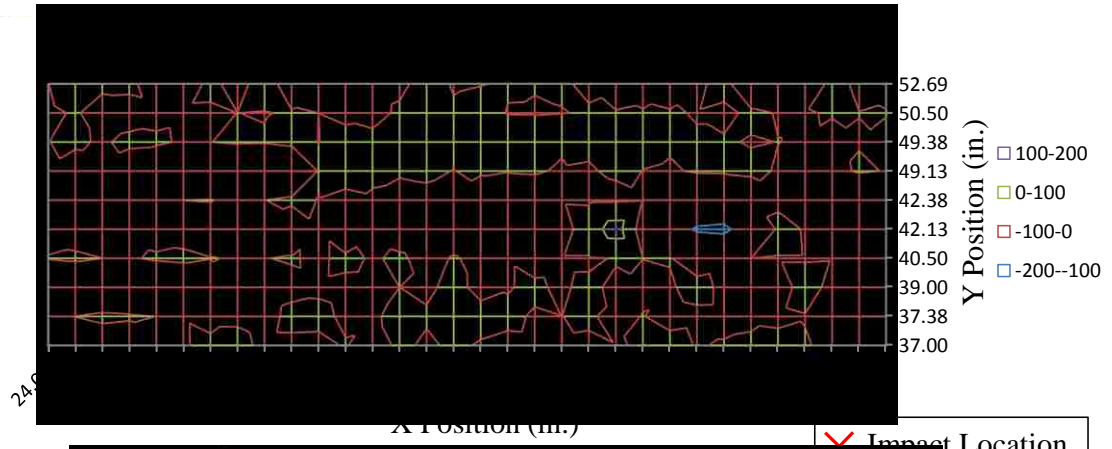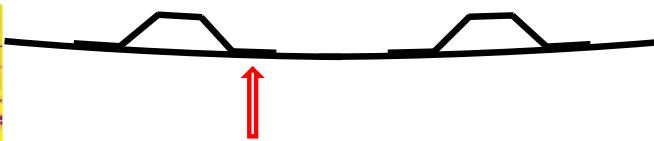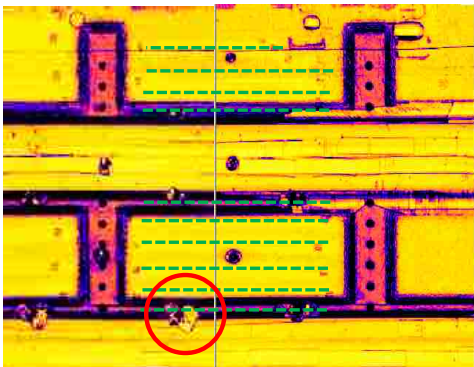
Ultrasonic Amplitude Scan

Center Bay Over Skin
Impact Energy: 60 Ft lbs
Damage Area: 0.75 in^2
Type of Damage: Near surface fiber crushing and slight interply delamination
Strain Indication: No

Y Position (in.)

52.69
50.50
49.38
49.13
42.38
42.13
40.50
39.00
37.38
37.00

□ 10-15
□ 5-10
□ 0-5
□ -5-0
□ -10--5
□ -15--10

X Position (in.)

✕ Impact Location

Micro Strain (µε)

■ 10-15
■ 5-10
■ 0-5
■ -5-0
■ -10--5
■ -15--10

174

Impact Location

--- Fiber Optic

Center of Stringer Flange
Impact Energy: 90 Ft lbs
Damage Area: 3.46 in^2
Type of Damage: Interply delamination
Strain Indication: Yes, clear detectable strain indication

Ultrasonic Amplitude Scan

Y Position (in.)

52.69
50.50
49.38
49.13
42.38
42.13
40.50
39.00
37.38
37.00

☐ 100-150
☐ 50-100
☐ 0-50
☐ -50-0
☐ -100--50

X Position (in.)

Location

Micro Strain (*ue*)

■ 100-150
■ 50-100
■ 0-50
■ -50-0
■ -100--50
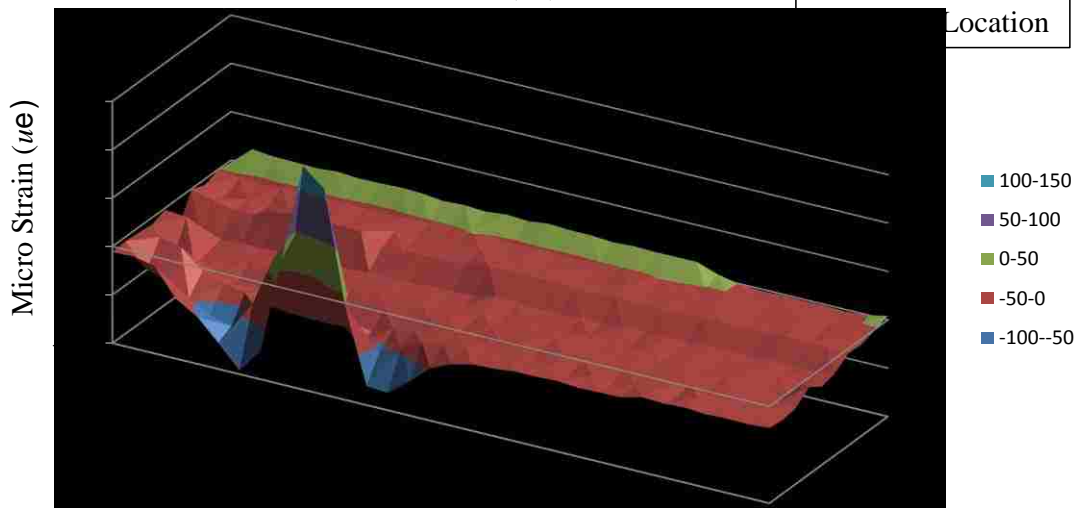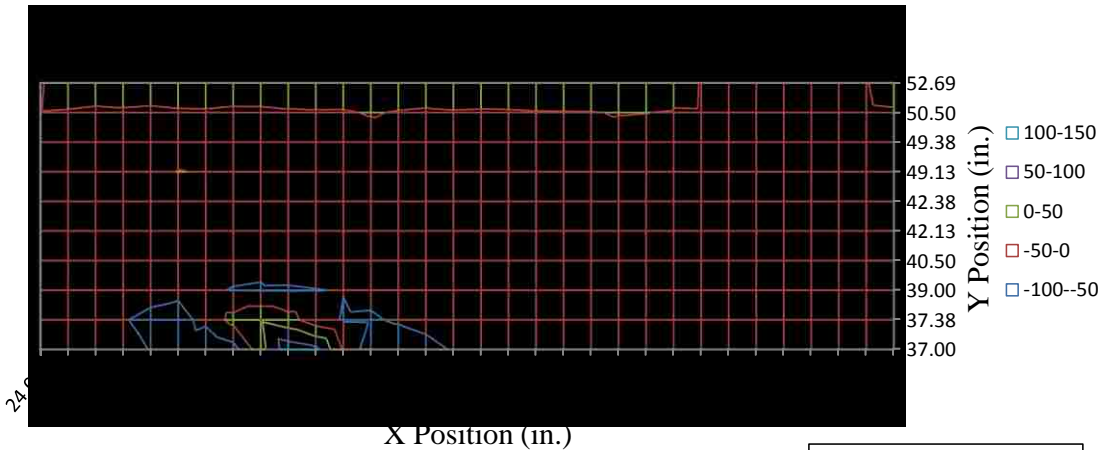
Impact Location
--- Fiber Optic
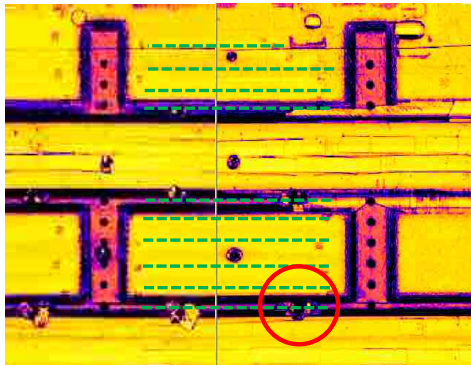
Ultrasonic Amplitude Scan
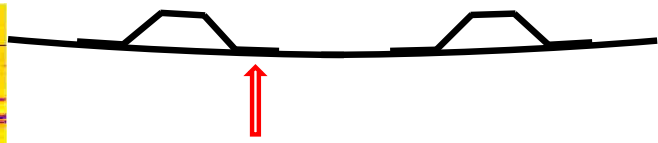
Center of Stringer Flange
Impact Energy: 112.5 Ft lbs
Damage Area: 2.19 in^2
Type of Damage: Interply delamination
Strain Indication: High strains detected at impact location (strains much higher than typically observed), not detectable

X Position (in.)

Y Position (in.)

- 10000-20000
- 0-10000
- -10000-0
- -20000--10000

Impact Location

Micro Strain (ue)

- 15000-20000
- 10000-15000
- 5000-10000
- 0-5000
- -5000-0
- -10000--5000
- -15000--10000

176
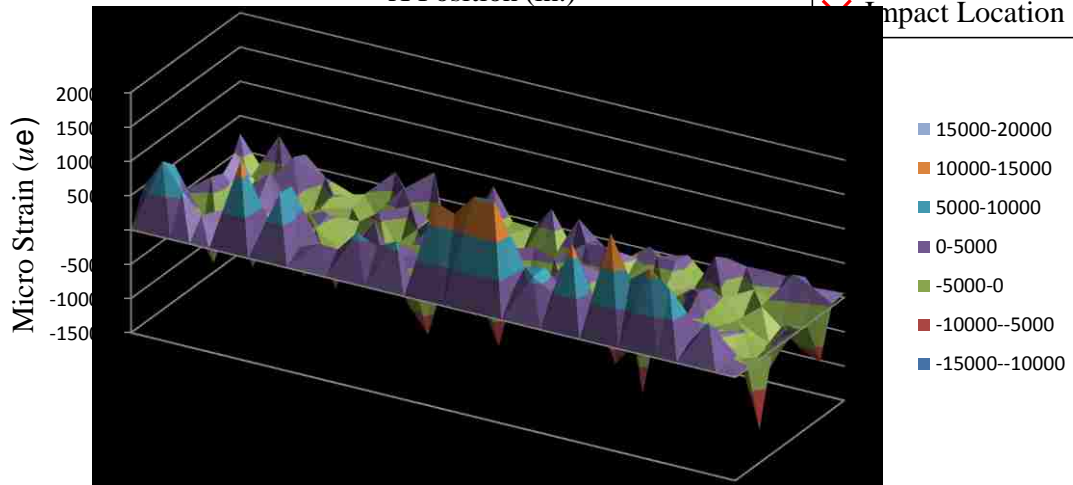
Ultrasonic Amplitude Scan

1 - B1-SK1-ST0-H1
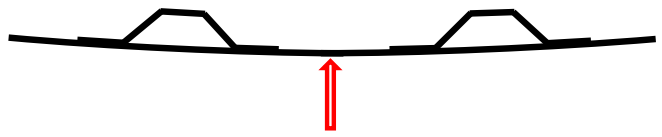
Center Bay Over Skin
Impact Energy: 90 Ft lbs
Damage Area: 0.52 in^2
Type of Damage: Near surface crushed fibers

3 - B1-SK1-ST1R-H2b
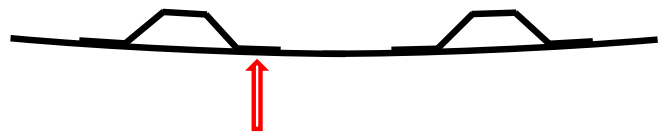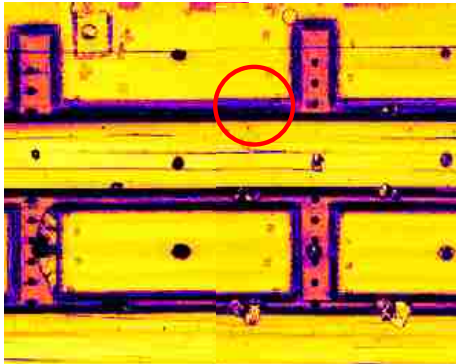
Center of Stringer Flange
Impact Energy: 60 Ft lbs
Damage Area: Could Not Determine, masked by co-cured flange
Type of Damage: None

8 - B1-SK2-ST0-H4
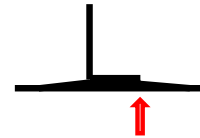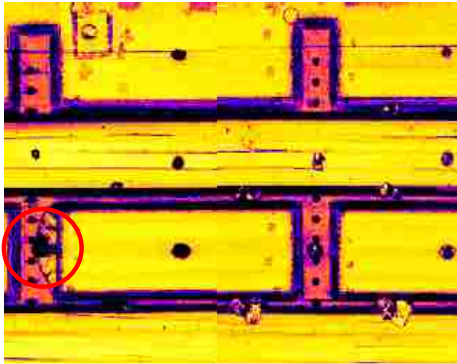
Center of Shear Tie
Impact Energy: 75 Ft lbs
Damage Area: 4.35 in^2
Type of Damage: Delamination of shear tie tapered section build up to skin interface
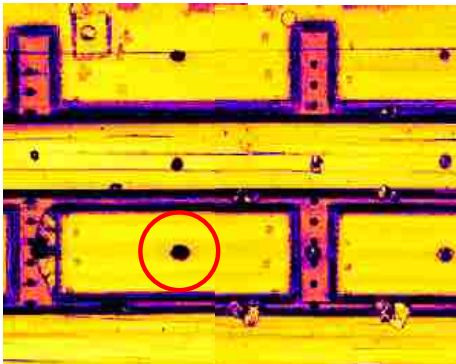
Impact Location
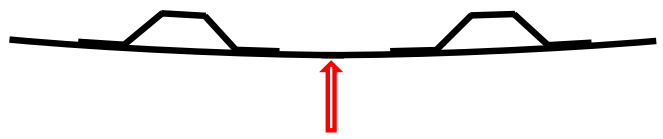
9 - B1-SK2-ST0-H1

Center Bay Over Skin
Impact Energy: 75 Ft lbs
Damage Area: 0.85 in^2
Type of Damage: Near surface crushed fibers

Ultrasonic Amplitude Scan

16 - B2-SK0-ST1L-H3
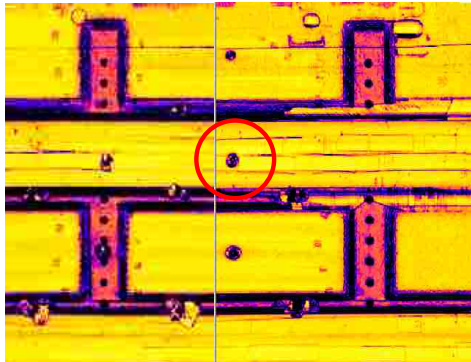
Center of Stringer Between Flanges
Impact Energy: 75 Ft lbs
Damage Area: 0.81 in^2
Type of Damage: Near surface crushed fibers, small interply delamination
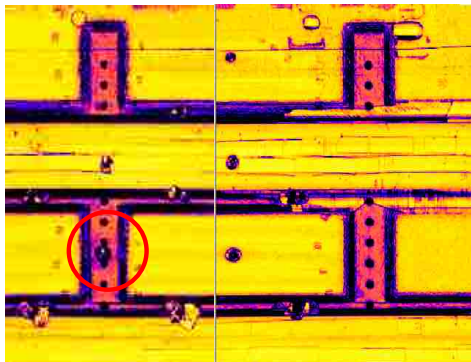
19 - B1/2-SK2-ST0-H4
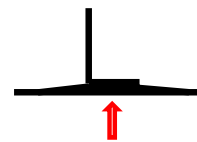
Center of Shear Tie
Impact Energy: 90 Ft lbs
Damage Area: 0.85 in^2
Type of Damage: Interply delamination

178

Panel A (Bay 3&4) – Hard Impacts
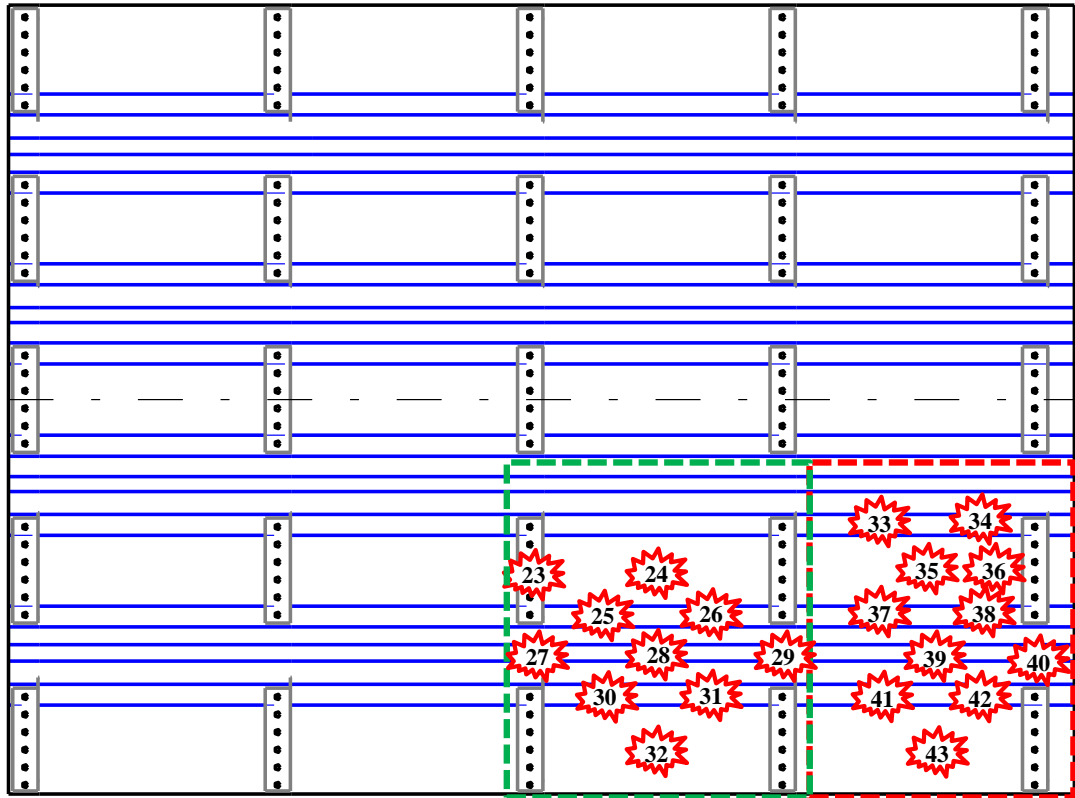
Bay 3 Hard Impacts	Bays 4 Hard Impacts
23 – B2/3-SK4-ST0-H4	33 – B4-SK4-ST3L-H2c
24 – B3-SK4-ST0-H1	34 – B4-SK4-ST3R-H2c
25 – B3-SK4-ST4L-H2a	35 – B4-SK4-ST0-H1
26 – B3-SK4-ST4R-H2a	36 – B4-SK4R-ST0-H1
27 – B2/3-SK0-ST3-H3	37 – B4-SK4-ST4L-H2a
28 – B3-SK0-ST4-H3	38 – B4-SK4-ST4R-H2a
29 – B3/4-SK0-ST4-H3	39 – B4-SK0-ST4-H3
30 – B3-SK5-ST4L-H2b	40 – B4-SK0-ST4R-H3
31 – B3-SK5-ST4R-H2b	41 – B4-SK5-ST4L-H2b
32 – B3-SK5-ST0-H1	42 – B4-SK5-ST4R-H2b
	43 – B4-SK5-ST0-H1

Indicates strain results obtained and presented

179

23 – B2/3

☐ 100-150	
☐ 50-100	
☐ 0-50	
☐ -50-0	
☐ -100--50	

Y Position (in.)

18.11
17.32
16.54
15.75
14.96
14.18
13.39
11.17
7.50
6.71
5.93
5.14
4.36
3.57
2.79
2.00

42.18

✕ Impact Location
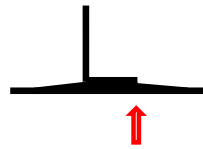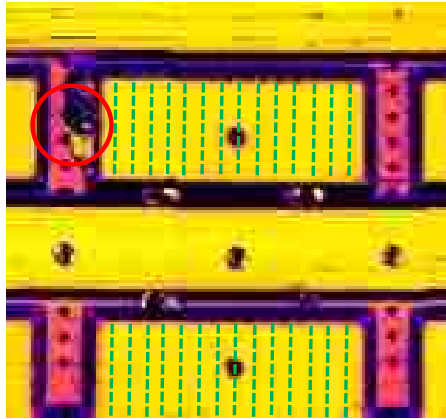
Edge of Shear Tie
Impact Energy: 90 Ft lbs
Damage Area: 10.37 in^2
Type of Damage: Delamination at the shear tie built-up skin interface. Back side visible crack at interface.
Strain Indication: Yes, strain increase in closest fiber section
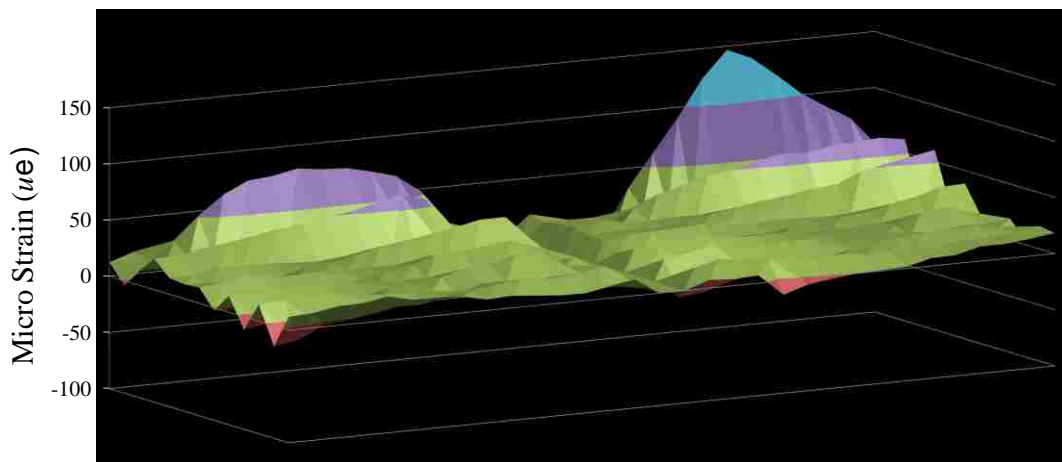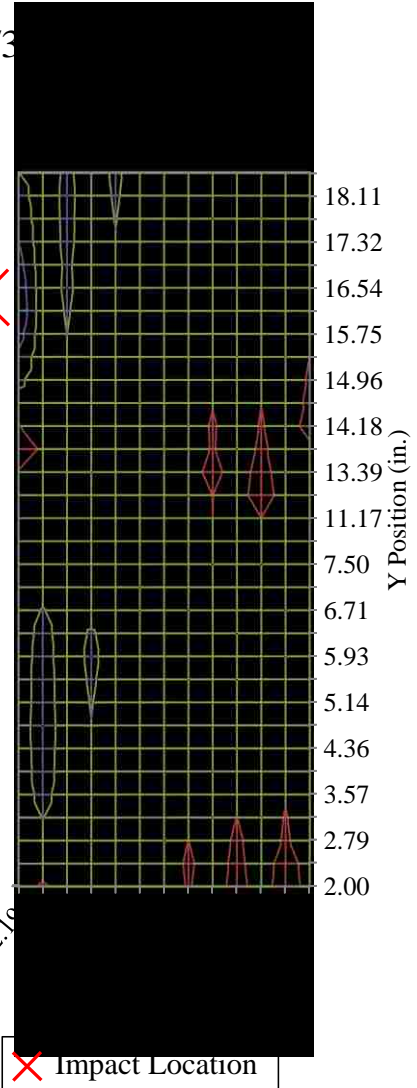
Impact Location
Fiber Optic

200-300
100-200
0-100
-100-0

Y Position (in.)

18.11
17.32
16.54
15.75
14.96
14.18
13.39
11.17
7.50
6.71
5.93
5.14
4.36
3.57
2.79
2.00

42.1
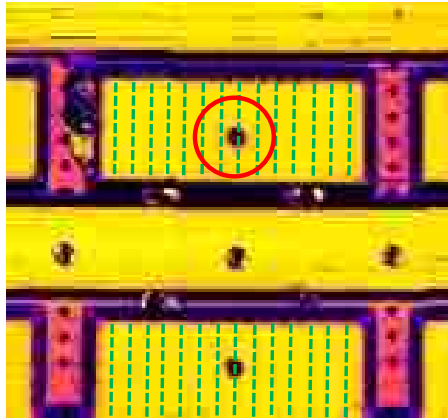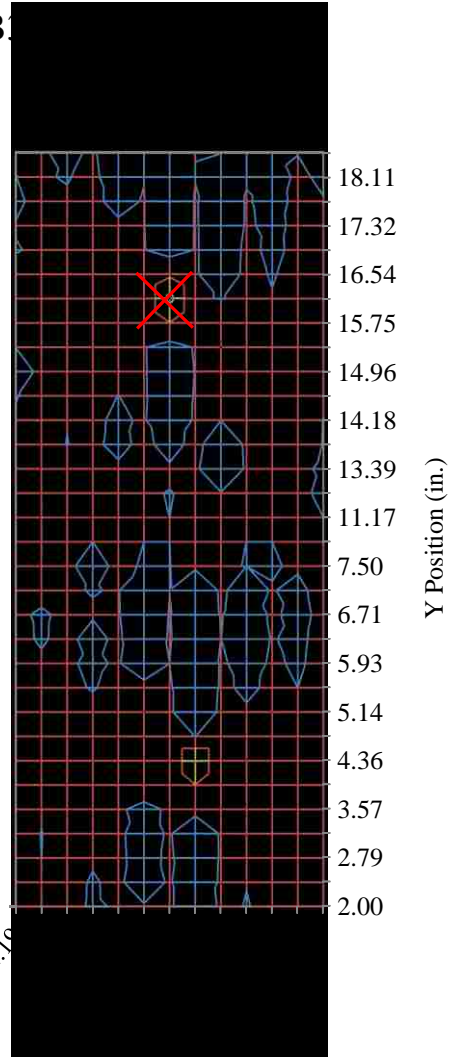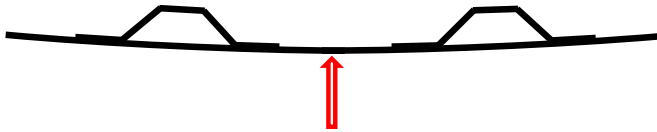
Center Bay Over Skin
Impact Energy: 60 Ft lbs
Damage Area: 0.89 in^2
Type of Damage: Near surface fiber crushing
Strain Indication: Yes, strain indication, but second indication not at the location of interest also was induced.

Impact Location

Micro Strain (*ue*)

250
200
150
100
50
0
-50

25 − B3-S

Legend:
- ○ Impact Location
- --- Fiber Optic
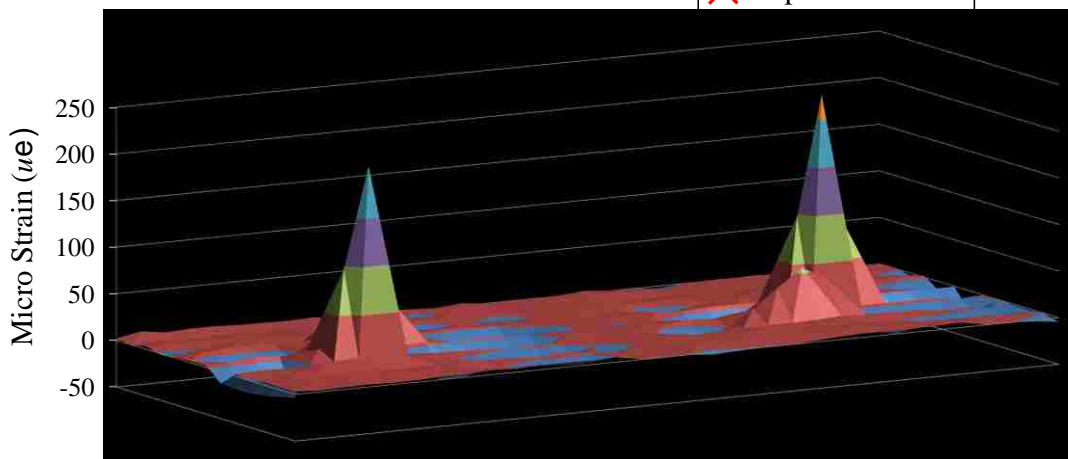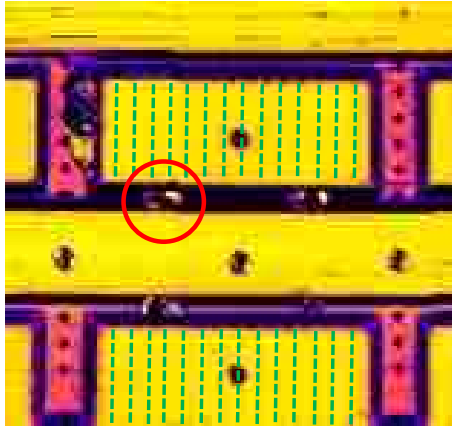
Strain legend:
- □ 100-200
- □ 0-100
- □ -100-0
- □ -200--100
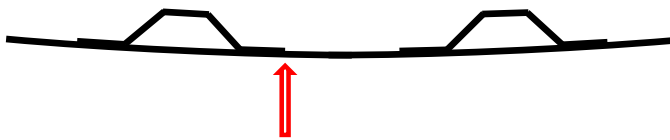
Edge of Stringer Flange (Not Stringer Side)
Impact Energy: 60 Ft lbs
Damage Area: 2.85 in²
Type of Damage: Flange delamination
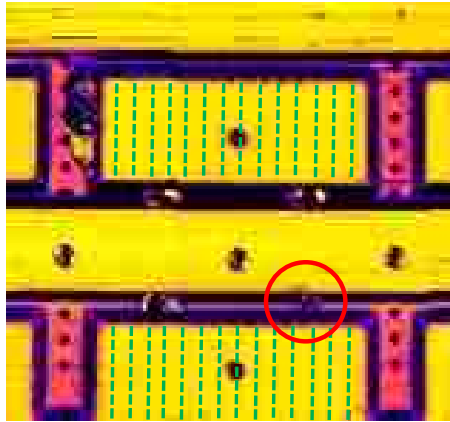**Strain Indication**: Yes, compressive strain indication

Y Position (in.): 18.11, 17.32, 16.54, 15.75, 14.96, 14.18, 13.39, 11.17, 7.50, 6.71, 5.93, 5.14, 4.36, 3.57, 2.79, 2.00

Micro Strain (ue): 150, 100, 50, 0, -50, -100, -150, -200
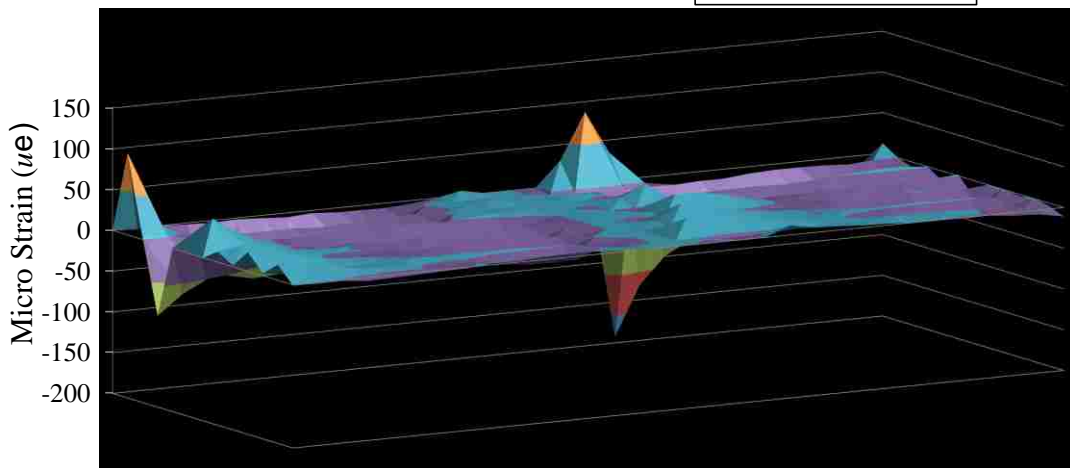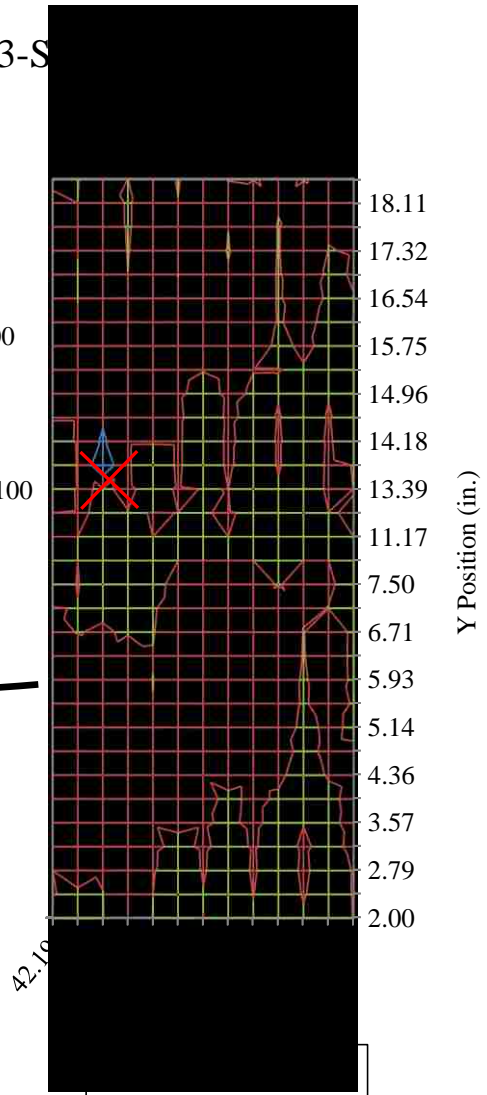
26 – B3-SK4-ST4B-H2

- Impact Location
- --- Fiber Optic
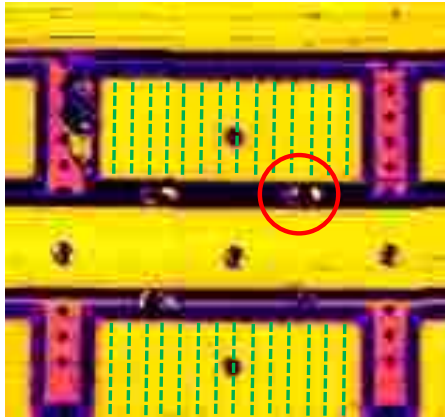
- □ 100-200
- □ 0-100
- □ -100-0
- □ -200--100
- □ -300--200
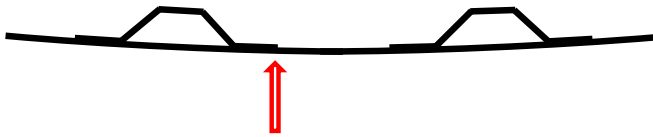
Edge of Stringer Flange (Not Stringer Side)
Impact Energy: 105 Ft lbs
Damage Area: 2.43 in^2
Type of Damage: Flange delamination, visible crack on surface paint
Strain Indication: Yes, compressive strain indication
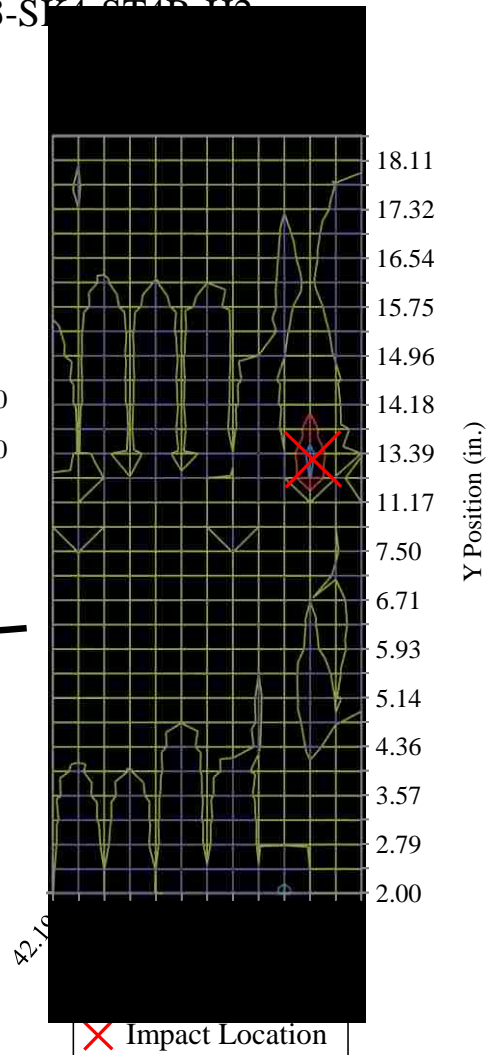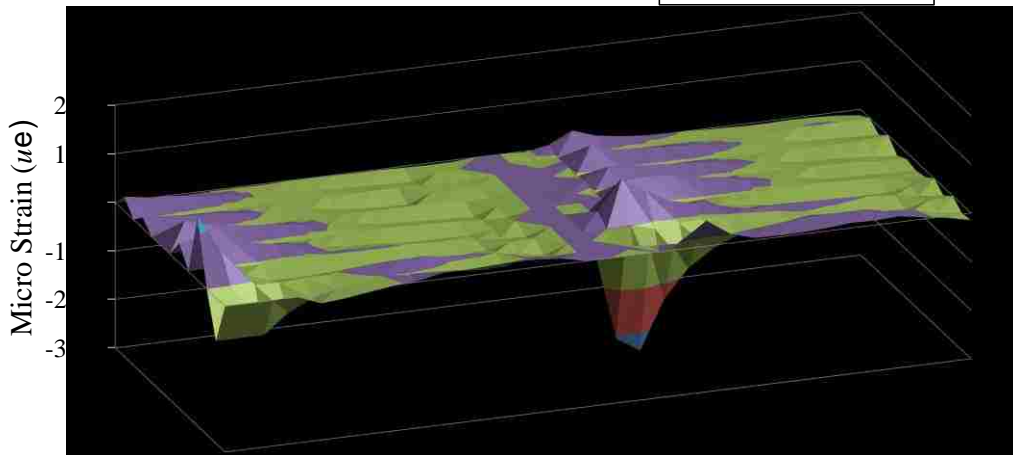
Y Position (in.)

18.11
17.32
16.54
15.75
14.96
14.18
13.39
11.17
7.50
6.71
5.93
5.14
4.36
3.57
2.79
2.00

✕ Impact Location

Micro Strain (ue)

183

27 − B2/3

○ Impact Location
--- Fiber Optic

□ 10-20
□ 0-10
□ -10-0
□ -20--10

✕ Impact Location

Y Position (in.)

18.11
17.32
16.54
15.75
14.96
14.18
13.39
11.17
7.50
6.71
5.93
5.14
4.36
3.57
2.79
2.00
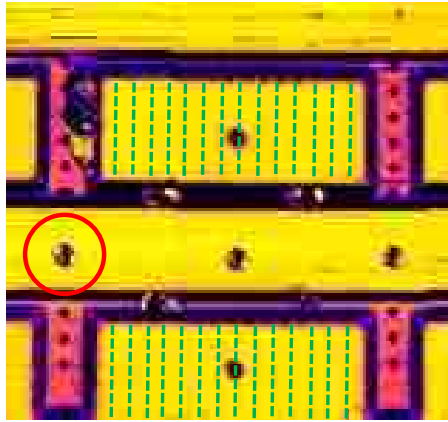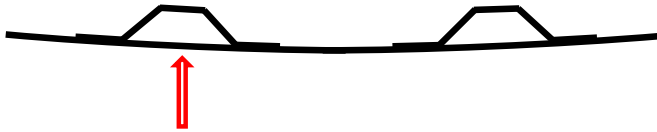
Center of Stringer Between Flanges (Between Shear ties)
Impact Energy: 90 Ft lbs
Damage Area: 1.07 in^2
Type of Damage: Near surface fiber crushing and interply delamination
Strain Indication: No

Micro Strain (*ue*)

15
10
5
0
-5
-10
-15
-20
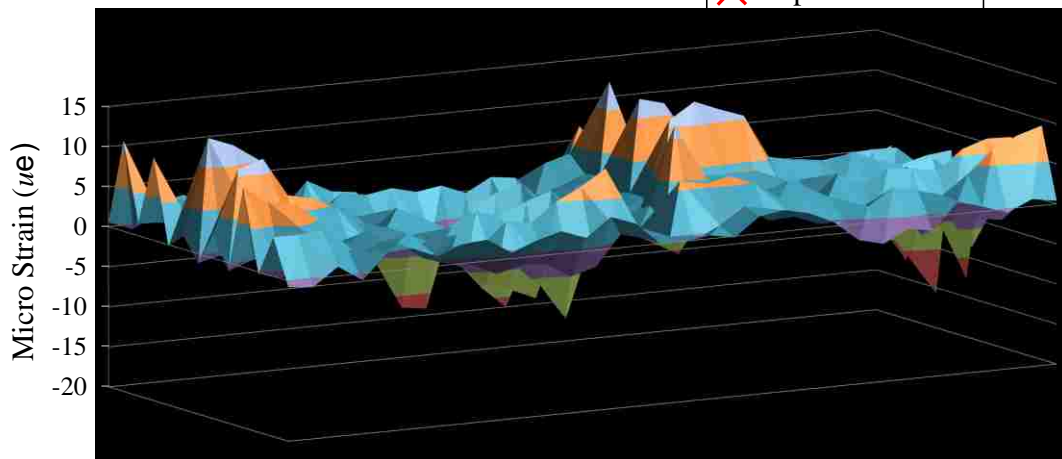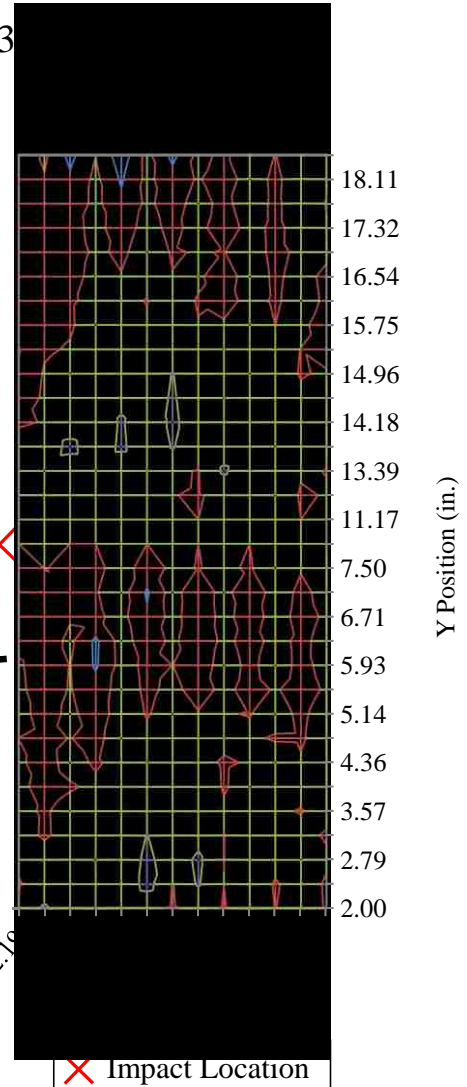
Impact Location

--- Fiber Optic
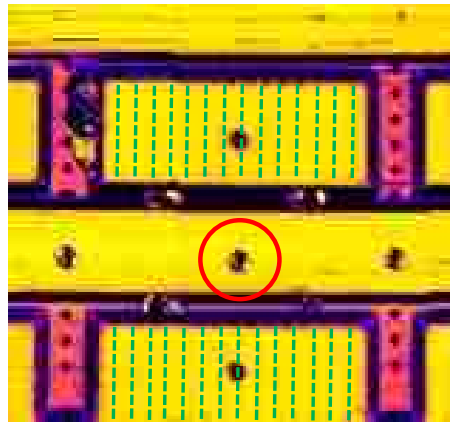
- 0-10
- -10-0
- -20--10
- -30--20
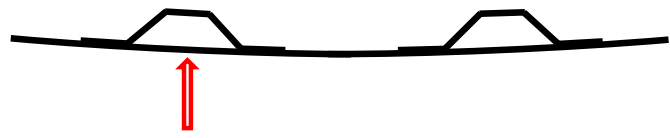
Center of Stringer Between Flanges
Impact Energy: 90 Ft lbs
Damage Area: 1.17 in²
Type of Damage: Interply delamination
Strain Indication: Increased compressive strains at fibers nearest to the stringer flange, not detectable

Y Position (in.)

18.11
17.32
16.54
15.75
14.96
14.18
13.39
11.17
7.50
6.71
5.93
5.14
4.36
3.57
2.79
2.00

42.10

✗ Impact Location

Micro Strain (*ue*)
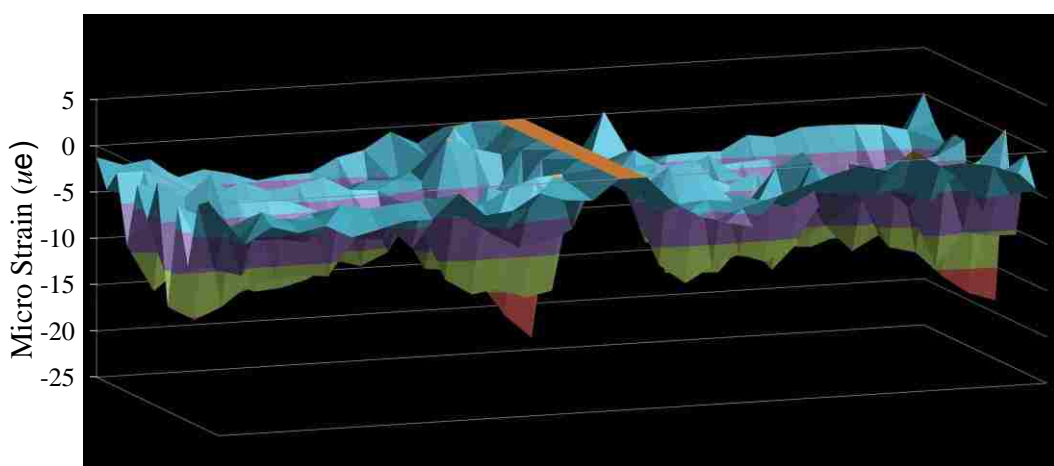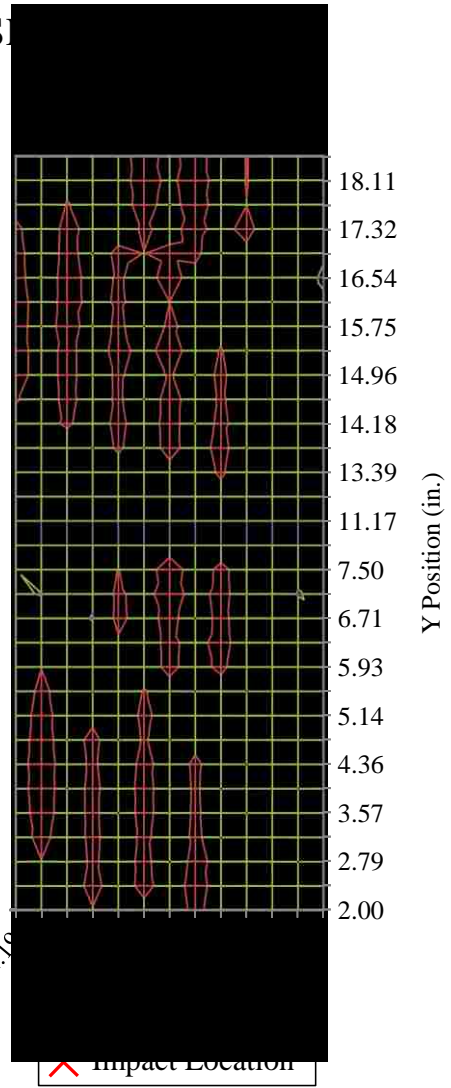
Impact Location
--- Fiber Optic
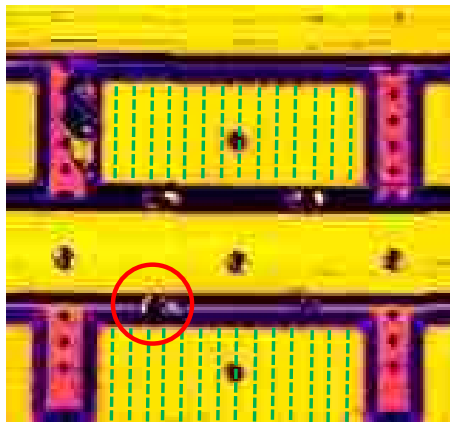
☐ 0-100
☐ -100-0
☐ -200--100
☐ -300--200
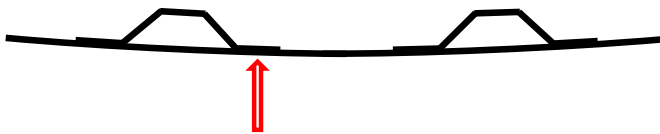
Center of Stringer Flange
Impact Energy: 105 Ft lbs
Damage Area: 3.89 in²
Type of Damage: Interply delamination
Strain Indication: Yes, compressive strain indication

18.11
17.32
16.54
15.75
14.96
14.18
13.39
11.17
7.50
6.71
5.93
5.14
4.36
3.57
2.79
2.00

Y Position (in.)

42.1

✗ Impact Location

Micro Strain (ue)

100
0
-100
-200
-300

186

31 – B3-S

Impact Location (red circle)
Fiber Optic (green dashed)
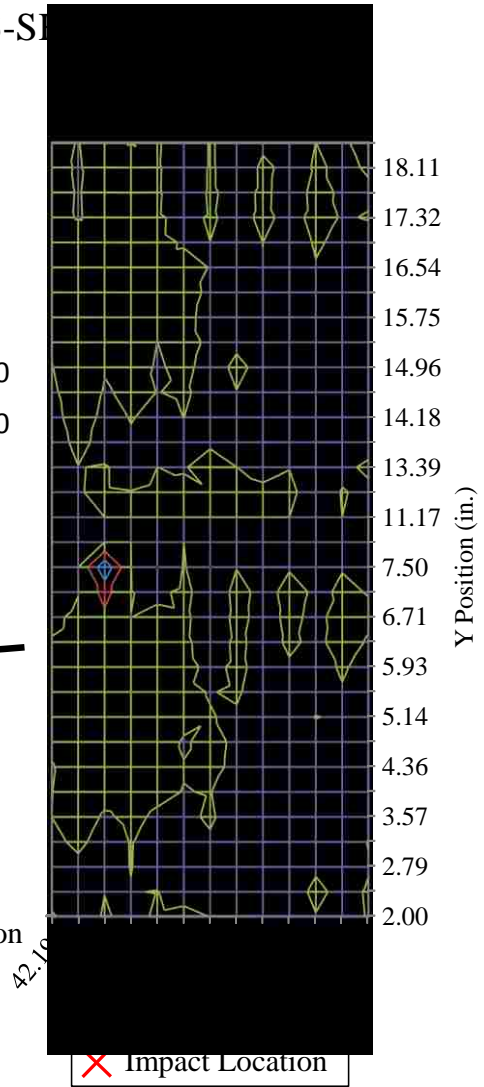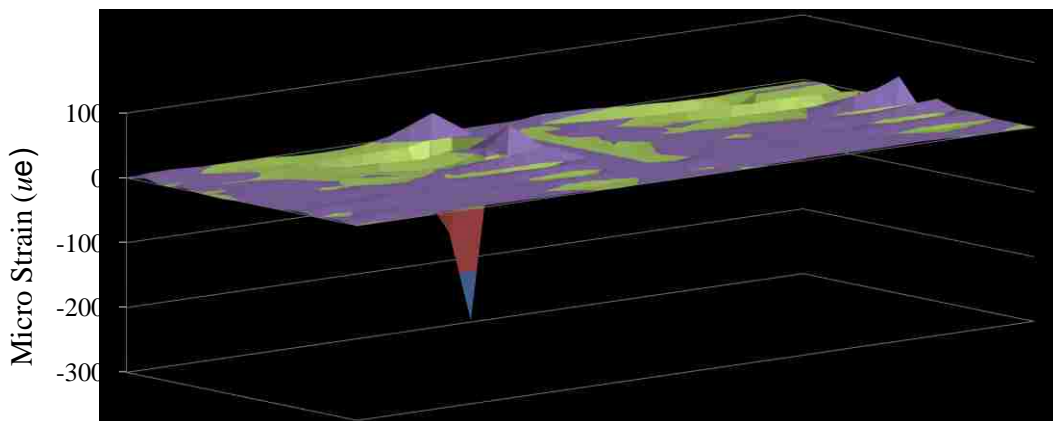
□ 0-20
□ -20-0
□ -40--20
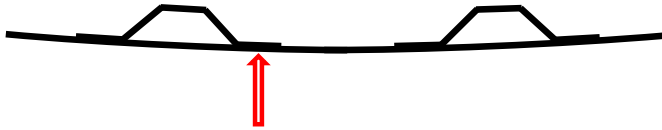
Center of Stringer Flange
Impact Energy: 97.5 Ft lbs
Damage Area: 1.63 in^2
Type of Damage: Interply delamination
Strain Indication: Yes, clear negative strain peak
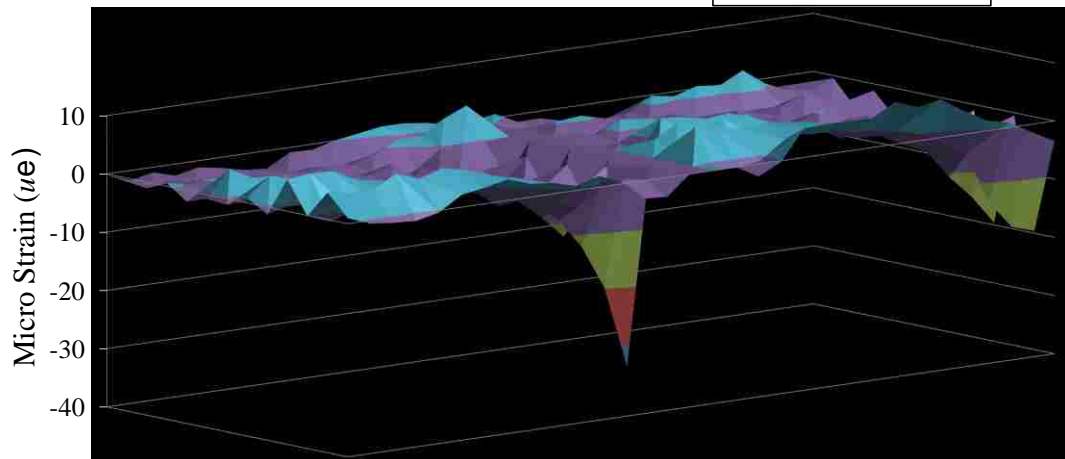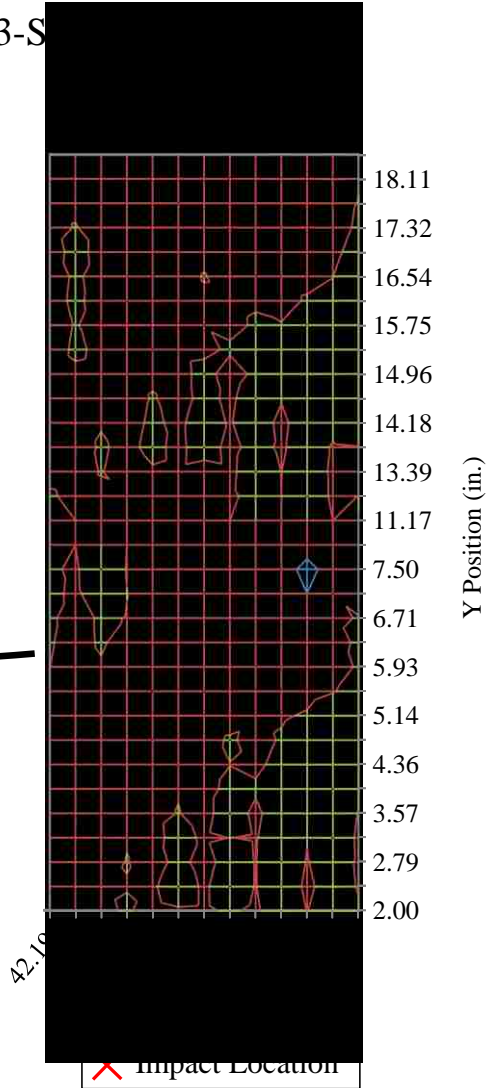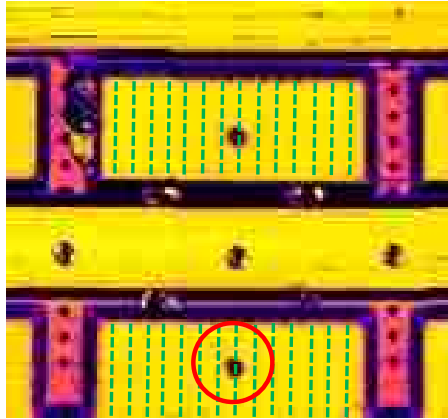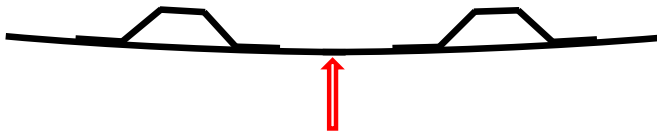
Y Position (in.)

18.11
17.32
16.54
15.75
14.96
14.18
13.39
11.17
7.50
6.71
5.93
5.14
4.36
3.57
2.79
2.00

42.1

X Impact Location

Micro Strain (*ue*)

187

32 – B3-S

Impact Location (○ red circle)
Fiber Optic (--- green dashed)

□ 500-1000
□ 0-500
□ -500-0

Y Position (in.)

18.11
17.32
16.54
15.75
14.96
14.18
13.39
11.17
7.50
6.71
5.93
5.14
4.36
3.57
2.79
2.00

42.18

Center Bay Over Skin
Impact Energy: 105 Ft lbs
Damage Area: 0.81 in^2
Type of Damage: Near surface fiber crushing
Strain Indication: Yes, high strains at impact location

Micro Strain ($u\varepsilon$)

800
600
400
200
0
-200

188
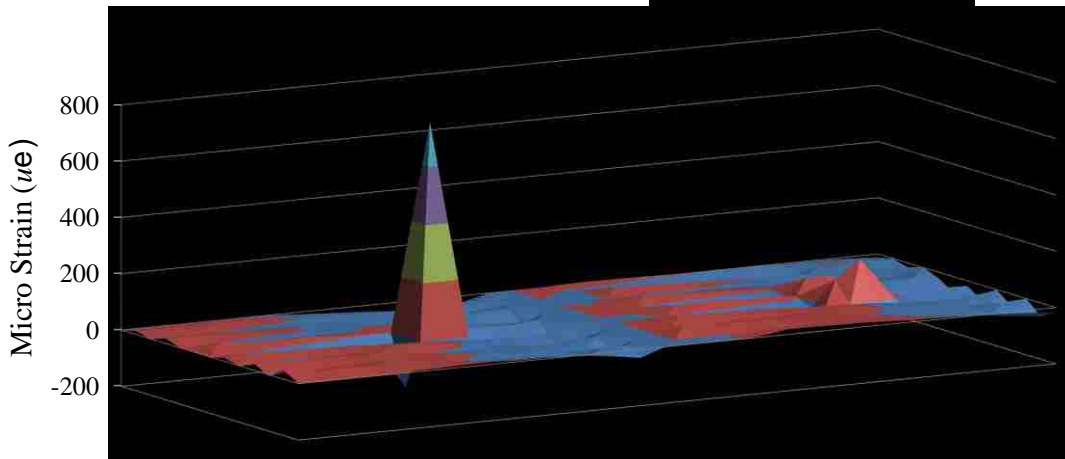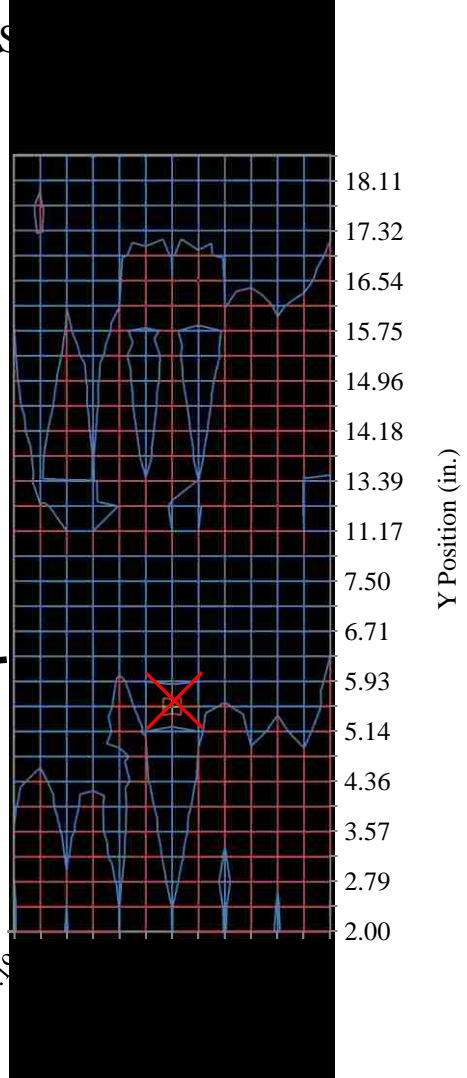
Impact Location
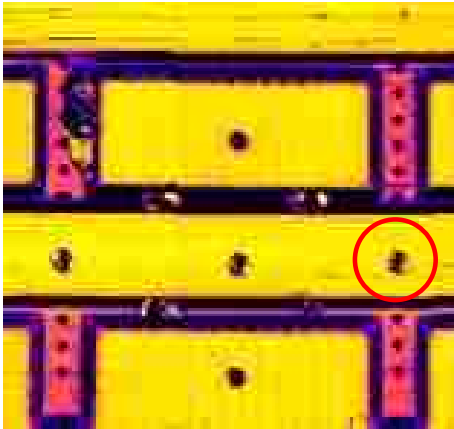
Ultrasonic Amplitude Scan

29 – B3/4-SK0-ST4-H3
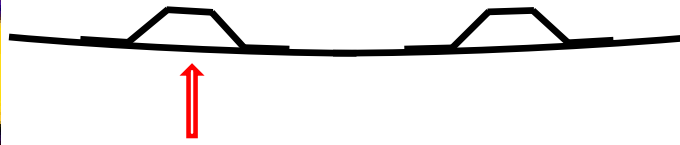
Mid-Stringer Between Flanges
Impact Energy: 75 Ft lbs
Damage Area: 1.18 in^2
Type of Damage: Interply delamination
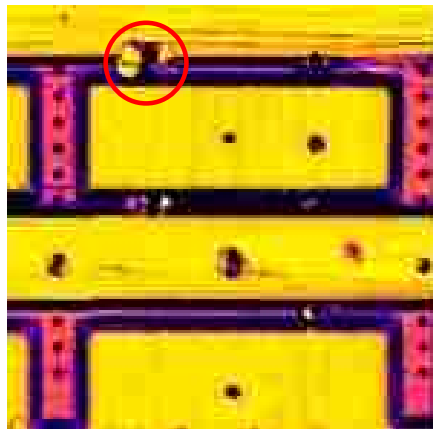
33 – B4-SK4-ST3L-H2c

Edge of Stringer Flange (Stringer Side)
Impact Energy: 97.5 Ft lbs
Damage Area: 5.14 in^2
Type of Damage: Interply delamination
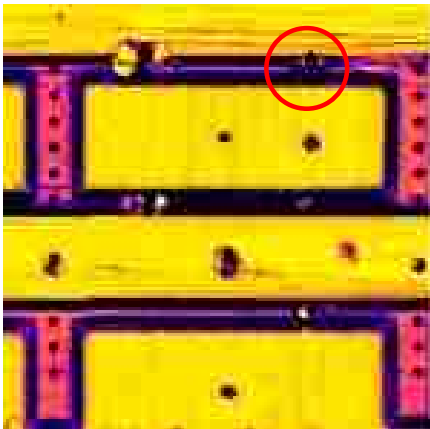
34 – B4-SK4-ST3R-H2c
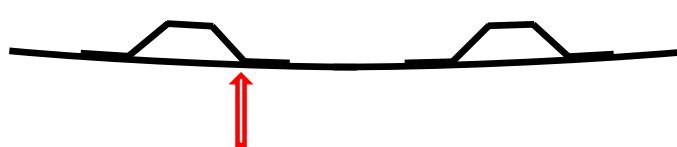
Edge of Stringer Flange (Stringer Side)
Impact Energy: 82.5 Ft lbs
Damage Area: 2.55 in^2
Type of Damage: Interply delamination

189

www.manaraa.com
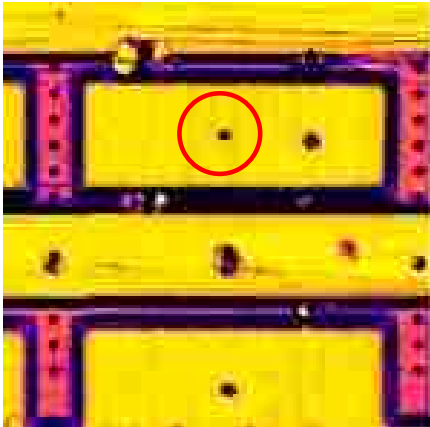
Impact Location
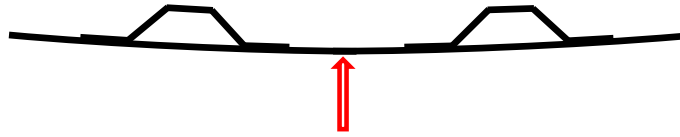
35 – B4-SK4-ST0-H1

Center Bay Over Skin
Impact Energy: 20 Ft lbs
Damage Area: 0.25 in^2
Type of Damage: Near surface crushed fibers

Ultrasonic Amplitude Scan
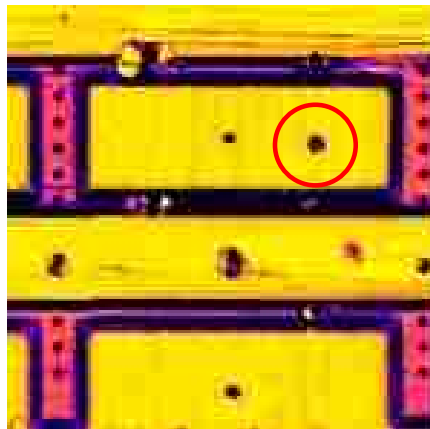
36 – B4-SK4R-ST0-H1
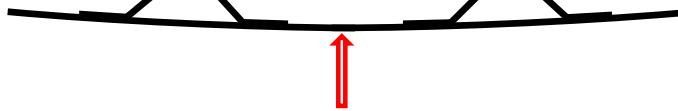
Center Bay Over Skin
Impact Energy: 20 Ft lbs
Damage Area: 0.55 in^2
Type of Damage: Near surface fiber crushing
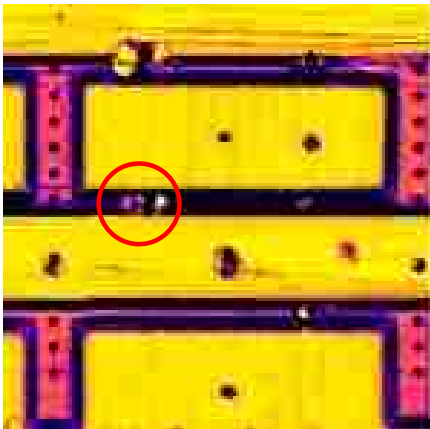
37 – B4-SK4-ST4L-H2a
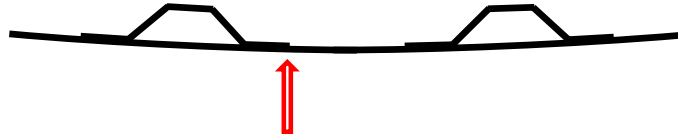
Edge of Stringer Flange (Not Stringer Side)
Impact Energy: 90 Ft lbs
Damage Area: 2.26 in^2
Type of Damage: Interply delamination
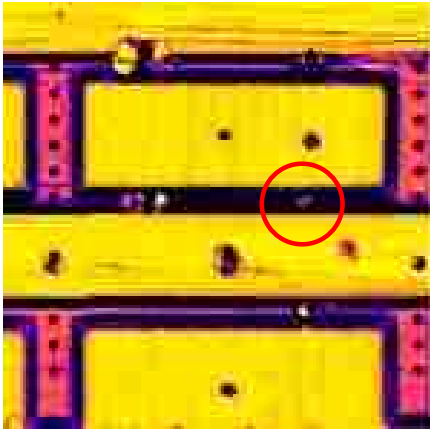
Ultrasonic Amplitude Scan

38 – B4-SK4-ST4R-H2a
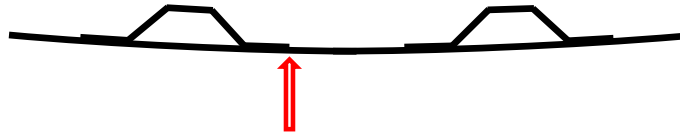
Edge of Stringer Flange (Not Stringer Side)
Impact Energy: 50 Ft lbs
Damage Area: 0.85 in^2
Type of Damage: Interply delamination
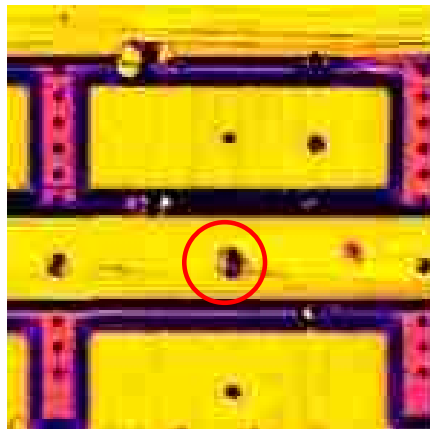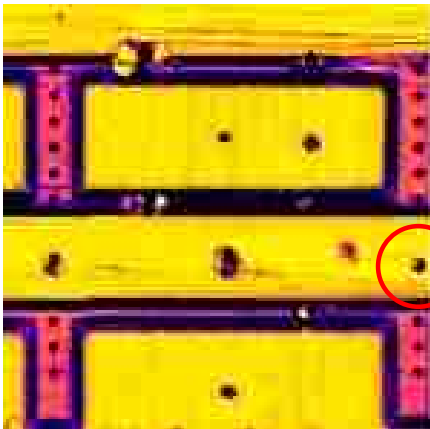

39 – B4-SK0-ST4-H3
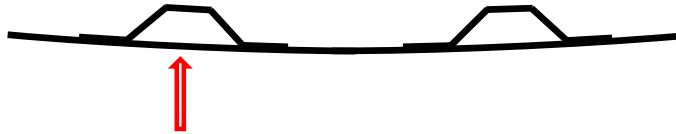
Center Bay Over Skin
Impact Energy: 105 Ft lbs
Damage Area: 1.77 in^2
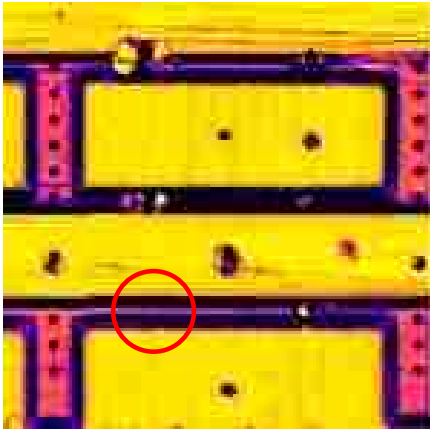**Type of Damage**: Interply delamination

40 – B4-SK0-ST4R-H3

Mid-Stringer Between Flanges (Between Stringers)
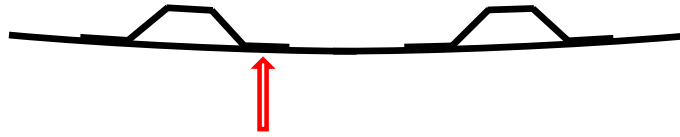**Impact Energy**: 75 Ft lbs
Damage Area: 0.31 in^2
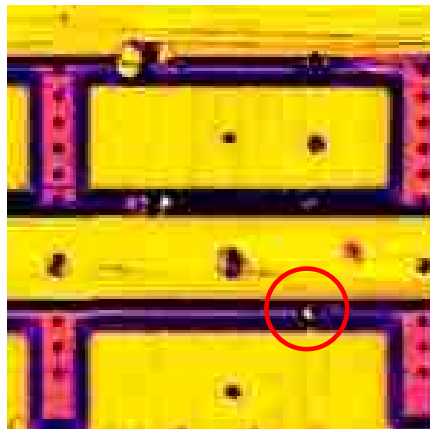**Type of Damage**: Near surface fiber crushing
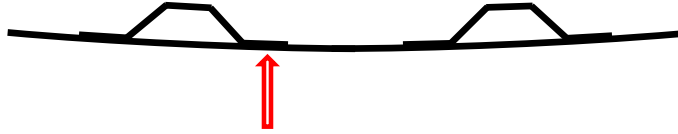
○ Impact Location

Ultrasonic Amplitude Scan

41 – B4-SK5-ST4L-H2b

Center of Stringer Flange
Impact Energy: 60 Ft lbs
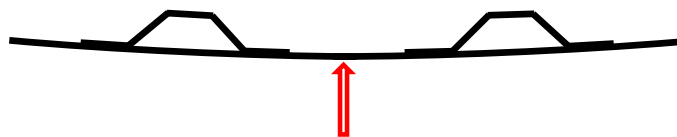**Damage Area**: 0 in^2
Type of Damage: No damage

42 – B4-SK5-ST4R-H2b

Center of Stringer Flange
Impact Energy: 82.5 Ft lbs
Damage Area: 1.68 in^2
Type of Damage: Interply delamination
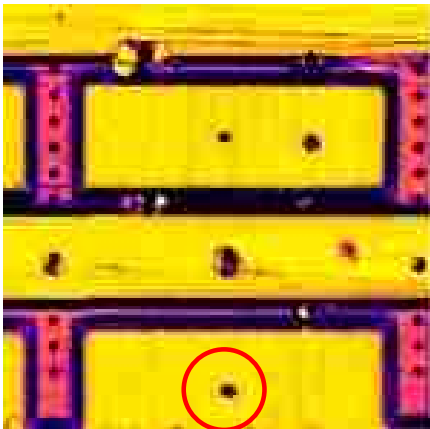
43 – B4-SK5-ST0-H1

Center Bay Over Skin
Impact Energy: 75 Ft lbs
Damage Area: 0.51 in^2
Type of Damage: Near surface fiber crushing